



The  
University  
Of  
Sheffield.

# **Probing Radiation Damage in Fe-doped SrTiO<sub>3</sub> using Micro-contact Impedance Spectroscopy**

**Richard Veazey**

A thesis submitted in partial fulfilment of the requirements for the degree of

Doctor of Philosophy

Supervised by

Prof. Derek C. Sinclair

Dr. Julian S. Dean

Dr. Amy S. Gandy

The University of Sheffield

Faculty of Engineering

Department of Materials Science and Engineering

July 2019

## **Acknowledgements**

Firstly, I would like to thank Prof. Derek C. Sinclair for his outstanding supervision during my PhD. I am very grateful for your support, encouragement, patience and the advice you have provided during my research project. I hope you are rewarded with some well-deserved rest after your tenure as HoD. I would like to thank Dr. Julian S. Dean for his encouragement and the time he has invested in me during my PhD, and Dr Amy S. Gandy for supporting me from the start. My supervisory team was created in unusual circumstances, but I am so happy and lucky that it was, thank you.

Thank you to Mike Bell, Dr. Gavin Williams and particularly Peter Trend for your help and supervision in the clean room. My experimental work benefitted greatly from your help.

Thanks to Seb Lawson for taking me under your wing and providing me with advice on pretty much every aspect of my PhD. Thanks to Adam Fisher for our encouraging discussions throughout. I would also like to thank everyone in the Functional Materials group, the Immobilisation Science Laboratory and the Next Generation Nuclear CDT. I hope we all keep in touch.

I would like to acknowledge the Engineering and Physical Sciences Research Council for funding my PhD and Prof. Karl Whittle for initially showing faith in me.

Finally, thank you to my Mum and Dad for their love and support in all aspects of my life and for always believing in me.

## Abstract

Radiation damage in ceramics has drawn significant attention due to their application as wasteforms for the immobilisation of nuclear waste and a requirement to understand the fundamentals that govern radiation damage tolerance. This project is based on determining whether a novel technique, micro-contact Impedance Spectroscopy, can be employed to characterise radiation damage.

Firstly, a greater understanding of the measurements of local electrical properties using micro-contact measurements is achieved using an in-house finite element modelling package. The electrical response of a single crystal sample based on SrTiO<sub>3</sub> was simulated using different electrode geometries and conditions of confinement. For two micro-contacts on the same surface, the spreading resistance equation overestimates the conductivity at small separations. The accuracy of this equation increases as the contact separation increases and is within 10% error when the contacts are separated by 8 times the micro-contact radius. Further convergence to errors lower than 10% becomes increasingly difficult and requires excessively large separations. The influence of confinement within the sample/electrode arrangements can be an important factor and increases the measured resistance and the spreading resistance equation becomes an underestimate of the conductivity. At extreme levels of confinement, the geometric correction becomes a better approximation for the conductivity. In some cases, the enhancement of conductivity from the close separation of the micro-contacts can counter-balance the reduction in conductivity from confinement producing fortuitously accurate calculated values of conductivity.

The modelling was then extended to include a resistive surface layer of thicknesses ranging from 1 – 50  $\mu\text{m}$ . Equations are proposed to calculate the conductivity of both the surface layer and the underlying bulk phase. If the surface layer is sufficiently thin with respect to the micro-contact size, a geometric factor and the spreading resistance equation produces accurate conductivity values for the surface layer and bulk, respectively. For large surface layer thicknesses, the spreading resistance equation produces an accurate conductivity for the surface layer, however, a bulk conductivity is not obtainable.

Fe-doped SrTiO<sub>3</sub> single crystals were characterised using X-ray diffraction and Impedance Spectroscopy prior to radiation damage studies. The conductivity increased with increasing Fe content, in agreement with previous studies. For micro-contact Impedance Spectroscopy, temperature corrections were made using relationships obtained from conventional Impedance Spectroscopy measurements. These included relationships obtained from the Arrhenius

conductivity behaviour of the sample and also from comparison of the frequency maximum of the  $M''$  Debye peak associated with the bulk response with temperature. The Impedance Spectroscopy signature of a pristine sample included a bulk response and multiple responses at lower frequencies attributed to the sample/electrode interface.

Bulk 5 MeV Au ion implantation of Fe-doped  $\text{SrTiO}_3$  single crystals was undertaken to a fluence of  $5 \times 10^{15}$  ions  $\text{cm}^{-2}$ . Glancing angle X-ray diffraction and cross-sectional transmission electron microscopy (XTEM) confirmed the samples had amorphised. Annealing studies revealed the amorphous surface had partially recrystallised to a polycrystalline perovskite after heating to 400 °C for 30 mins. XTEM confirmed that vacancy-type defects, cracks and regions of high strain still existed in the recrystallised layer after annealing. Cracks were a significant feature on the surface of annealed samples. Conventional Impedance Spectroscopy measurements revealed significant differences between the damaged and pristine samples that could not be easily resolved; however, as micro-contact Impedance Spectroscopy measurements are surface sensitive, these responses were more easily resolved. Two stages of the annealing process were observed. First, an intermediate frequency response initially shifted to higher frequency with a response that was more similar to the bulk response followed by a second stage where the intermediate frequency response shifted to lower frequency and away from the bulk response. The second stage was very sensitive to the number of cracks between the two micro-contacts. The response associated with the first stage of annealing indicates that micro-contact Impedance Spectroscopy may well be a useful tool characterise radiation damage in oxides; however, the changes in physical microstructure associated with the second stage of annealing limited the use of micro-contact Impedance Spectroscopy for characterising radiation damage induced in this study.

# Table of Contents

<b>Acknowledgements.....</b>	<b>2</b>
<b>Abstract.....</b>	<b>3</b>
<b>Chapter 1 : Introduction.....</b>	<b>8</b>
<b>Chapter 2 : Literature Review .....</b>	<b>12</b>
<b>2.1 ABO<sub>3</sub> Perovskite Structure .....</b>	<b>12</b>
<b>2.2 SrTiO<sub>3</sub> .....</b>	<b>13</b>
2.2.1 Defect Chemistry in SrTiO <sub>3</sub> .....	13
<b>2.3 Radiation Damage .....</b>	<b>14</b>
2.3.1 Radiation Damage Processes.....	15
2.3.2 Defects.....	18
2.3.3 Radiation Damage Recovery .....	20
2.3.4 Inducing Damage.....	20
2.3.5 Recrystallisation .....	21
2.3.6 Characterising Radiation Damage .....	22
2.3.7 Electrical Characterisation of Radiation Damage.....	23
2.3.8 Radiation Damage in SrTiO <sub>3</sub> and Related Perovskites.....	24
<b>2.4 Impedance Spectroscopy .....</b>	<b>27</b>
<b>2.5 Micro-contacts .....</b>	<b>29</b>
<b>2.6 Summary and Research Aim .....</b>	<b>34</b>
<b>2.7 References .....</b>	<b>34</b>
<b>Chapter 3 : Experimental Methods.....</b>	<b>45</b>
<b>3.1 Impedance Spectroscopy .....</b>	<b>45</b>
3.1.1 Impedance Spectroscopy Theory.....	45
3.1.2 Simulating Impedance Spectroscopy by Finite Element Modelling .....	48
3.1.3 Model Optimisation .....	48
3.1.4 Analysing Impedance Spectroscopy Data.....	51
<b>3.2 Micro-contact Impedance Spectroscopy.....</b>	<b>54</b>
3.2.1 Micro-contact Fabrication .....	54
<b>3.3 Single Crystal Ceramic Samples.....</b>	<b>56</b>
<b>3.4 X-ray Diffraction (XRD) .....</b>	<b>56</b>

3.4.1	Glancing Angle X-ray Diffraction (GAXRD).....	57
<b>3.5</b>	<b>Cross-sectional Transmission Electron Microscopy (XTEM) .....</b>	<b>57</b>
3.5.1	Sample Preparation.....	58
<b>3.6</b>	<b>Ion Implantation and SRIM.....</b>	<b>60</b>
<b>3.7</b>	<b>References .....</b>	<b>61</b>

## **Chapter 4 : A Finite Element Modelling Study of Spreading**

<b>Resistance and Sample Confinement .....</b>	<b>63</b>	
<b>4.1</b>	<b>Introduction .....</b>	<b>63</b>
<b>4.2</b>	<b>Finite Element Modelling .....</b>	<b>65</b>
<b>4.3</b>	<b>Results .....</b>	<b>66</b>
4.3.1	Top-bottom models.....	66
4.3.2	Top-top models.....	70
4.3.3	Confinement .....	73
<b>4.4</b>	<b>Discussion.....</b>	<b>83</b>
<b>4.5</b>	<b>Conclusions .....</b>	<b>87</b>
<b>4.6</b>	<b>References .....</b>	<b>88</b>

## **Chapter 5 : Measuring the Electrical Properties of Resistive**

<b>Surface Layers by Micro-contact Impedance Spectroscopy .....</b>	<b>91</b>	
<b>5.1</b>	<b>Introduction .....</b>	<b>91</b>
<b>5.2</b>	<b>Model Setup .....</b>	<b>91</b>
<b>5.3</b>	<b>Results .....</b>	<b>93</b>
5.3.1	Full top bottom (FTB).....	93
5.3.2	Micro-top full-bottom (MTFB) .....	100
5.3.3	Micro top top (MTT).....	110
<b>5.4</b>	<b>Discussion.....</b>	<b>115</b>
<b>5.5</b>	<b>Conclusions .....</b>	<b>118</b>
<b>5.6</b>	<b>References .....</b>	<b>119</b>

## **Chapter 6 : Characterisation of Pristine Fe-doped SrTiO<sub>3</sub>**

<b>Single Crystals prior to Irradiations.....</b>	<b>120</b>	
<b>6.1</b>	<b>Introduction .....</b>	<b>120</b>
<b>6.2</b>	<b>Results .....</b>	<b>121</b>

6.2.1	X-ray Diffraction .....	121
6.2.2	Glancing Angle X-ray Diffraction.....	122
6.2.3	Conventional Impedance Spectroscopy .....	124
6.2.4	Micro-contact Impedance Spectroscopy .....	127
6.2.5	Micro-contact / conventional Impedance Spectroscopy comparison .....	133
<b>6.3</b>	<b>Discussion and Conclusions.....</b>	<b>134</b>
<b>6.4</b>	<b>References .....</b>	<b>136</b>

## **Chapter 7 : Characterising Radiation Damage in Fe-doped SrTiO<sub>3</sub> Single Crystals using Micro-contact Impedance Spectroscopy .....**

### **139**

<b>7.1</b>	<b>Introduction .....</b>	<b>139</b>
<b>7.2</b>	<b>Results .....</b>	<b>139</b>
7.2.1	SRIM Calculations.....	139
7.2.2	Glancing Angle X-ray Diffraction & Recovery .....	140
7.2.3	Optical Microscopy.....	142
7.2.4	Cross-sectional Transmission Electron Microscopy.....	143
7.2.5	Conventional Impedance Spectroscopy .....	148
7.2.6	Micro-contact Impedance Spectroscopy .....	149
<b>7.3</b>	<b>Discussion.....</b>	<b>161</b>
7.3.1	Properties of Damaged Samples.....	161
7.3.2	Properties of Damaged and Recrystallised Samples.....	162
7.3.3	Impedance Spectroscopy Measurements .....	165
<b>7.4</b>	<b>Conclusions .....</b>	<b>168</b>
<b>7.5</b>	<b>References .....</b>	<b>169</b>

## **Chapter 8 : Conclusions..... 171**

<b>8.1</b>	<b>Future Work.....</b>	<b>173</b>
<b>8.2</b>	<b>References .....</b>	<b>175</b>

## Chapter 1: Introduction

In an effort to combat climate change, The European Commission outlined a long-term strategy to achieve the goal of limiting global warming by 1.5 °C by 2050<sup>1</sup>. The article confirmed nuclear power will form the backbone of a carbon-free European power system, providing approximately 15% of power. In line with such strategies, the UK outlined an ambitious roadmap to increase the nuclear contribution to power generation to 16 GW by 2025 and 75 GW by 2050<sup>2</sup>. Since the roadmap was created, two nuclear new build projects equating to approximately 6 GW have been put on hold due to rising costs.

Regardless of whether new plants are built, the UK has a large stockpile of nuclear wastes. In 2016, the UK had a high-level waste (HLW) inventory of 3,000 tonnes<sup>3</sup> and an expected 140 tonnes of plutonium on completion of reprocessing operations<sup>4</sup>. These wastes can be radioactive for many years, for example, <sup>237</sup>Np, a fission product, has a half-life of 2 million years<sup>5</sup>. Safe storage of the waste is therefore necessary. The current UK strategy for HLW is to incorporate the waste into borosilicate glass, using a process called vitrification<sup>6</sup>. Vitrification is suitable for complex, multi-component waste streams; however, borosilicate glasses will corrode when in contact with water<sup>7</sup>. Alternative wastefoms are being developed for “simpler” wastes such as separated fission products and weapons-usable plutonium.

Ceramics have received considerable interest due to their ability to incorporate radionuclides into a crystalline structure. These are generally more durable than glasses and more resistant to leaching<sup>8</sup>. A critical concern however is the effects that radiation has on the crystalline phases of the wastefom, which could impact the performance of the wastefom. Self-radiation damage associated with  $\alpha$ -decay of the minor actinides can result in the transformation from a crystalline to an amorphous state<sup>9</sup>. In an ideal wastefom, the physical and chemical properties will not be degraded by radiation produced by the incorporated actinides. Unfortunately, amorphisation is generally accompanied by a degradation in mechanical properties, such as volume swelling, cracking and increasing hardness, and chemical properties, such as increased dissolution rates<sup>10</sup>. As a consequence, understanding radiation damage tolerance in ceramics has received a considerable amount of research. Perovskites have received a large amount of interest due to the chemical flexibility of their composition-structure relationships and it being a main component phase of SYNROC<sup>11</sup>, a proposed nuclear waste form.

Many techniques have been employed to study radiation damage such as X-ray diffraction, Raman spectroscopy, transmission electron microscopy and Rutherford back-scattering. These techniques provide information about the structural characteristics of materials. Electrical

properties are usually significantly more sensitive to defects in a material. For example, small levels of non-stoichiometry in  $\text{Na}_{0.5}\text{Bi}_{0.5}\text{TiO}_3$ , such as  $\text{Na}_{0.5}\text{Bi}_{0.5-x}\text{TiO}_{3-1.5x}$  (where  $x \leq 0.02$ ) can lead to  $\sim 3$  orders of magnitude difference in electrical conductivity<sup>12</sup>, despite all samples appearing structurally identical. The enhanced conductivity is attributed to oxygen vacancies leading to high levels of ionic (oxide-ion) conductivity. Impedance Spectroscopy is a powerful technique widely used to characterise the electrical properties of ceramics<sup>13</sup>. However, it is generally overlooked in its potential to study the effects of radiation damage. Using Impedance Spectroscopy, it is possible to separate contributions from electrically distinct regions, typically the bulk and grain boundaries. One would assume that a damaged or amorphous material would exhibit different electrical properties to its crystalline counterpart.

The damage regions of interest in this thesis are typically  $\sim 1 \mu\text{m}$  in thickness. Conventional Impedance Spectroscopy measurements are averaged across the full sample. An alternative method is making measurements across two photolithographically produced micro-contacts on the same surface. In this setup, 75 % of the response originates from a region that extends 4 times the micro-contact radius from the surface being probed<sup>14</sup>. Considering the radius of these contacts can be as small as  $5 \mu\text{m}$ , the response is significantly more sensitive to surface effects.

The aim of this study is to determine the applicability of micro-contact Impedance Spectroscopy to the characterisation of radiation damage in ceramics. The specific material studied is Fe-doped  $\text{SrTiO}_3$  because a significant amount of research has been carried out on this material in the independent fields of micro-contact Impedance Spectroscopy and radiation damage effects. Single crystals are preferred as grain boundaries generally dominate the impedance response in polycrystalline ceramics.

The structure of this thesis is as follows: Chapter 2 provides a review of radiation damage in materials, with an emphasis on  $\text{SrTiO}_3$ , and the characterisation technique of micro-contact Impedance Spectroscopy. This provides a basic level of understanding to the individual research fields associated with this thesis, although currently there is no overlap between radiation damage and micro-contact Impedance Spectroscopy. Chapter 3 describes the experimental methods and the finite element modelling approach used in this work.

In Chapter 4, a greater understanding of micro-contact measurements is achieved using an in-house finite element software package. Accuracies of commonly used equations are compared and correction factors are suggested for different experimental set-ups. The work in this chapter was published in the Journal of the American Ceramic Society<sup>15</sup>. In Chapter 5, the modelling

is extended to include a resistive surface layer and the accuracy of the commonly used equations are again compared.

Fe-doped SrTiO<sub>3</sub> single crystals are characterised prior to radiation damage studies in Chapter 6. An Impedance Spectroscopy signature is obtained to compare the damage response to the pristine signature. In Chapter 7, radiation damaged samples are characterised with differences observed between the damaged and pristine samples. The simple two-layer models presented in Chapter 5 are not applicable here as additional components (including microstructural changes) are observed which influence the obtained Impedance Spectroscopy response. The chapter highlights there may be potential to use micro-contact Impedance Spectroscopy to characterise radiation damage in oxide-based materials such as SrTiO<sub>3</sub>; however, there are limitations and challenges associated with significant physical microstructures changes as a result of annealing.

In Chapter 8, the results and conclusions are summarised and possibilities for future work are suggested.

## 1.1 References

1. European Commission. A Clean Planet for all: A European strategic long-term vision for a prosperous, modern, competitive and climate neutral economy (2018).
2. Department of Energy and Climate Change. Nuclear Energy Research and Development Roadmap: Future Pathways (2013).
3. Nuclear Decommissioning Authority. Radioactive Wastes in the UK: UK Radioactive Waste Inventory Report (2017).
4. Department for Business, Energy & Industrial Strategy. The United Kingdom's Third National Report on Compliance with the Obligations of the Joint Convention on the Safety of Spent Fuel Management and on the Safety of Radioactive Waste Management (2017).
5. Ewing, R. C. Nuclear waste forms for actinides. *Proc. Natl. Acad. Sci.* **96**, 3432–3439 (1999).
6. Nuclear Decommissioning Authority & Department of Energy and Climate Change. Radioactive Wastes in the UK: A Summary of the 2013 Inventory (2014).
7. Grambow, B. Borosilicate Glass : Future Research Requirements or 'What We Don't Know'. *MRS Bull.* **19**, 20–23 (1994).

8. Lee, W. E., Ojovan, M. I., Stennett, M. C. & Hyatt, N. C. Immobilisation of radioactive waste in glasses, glass composite materials and ceramics. *Adv. Appl. Ceram.* **105**, 3–12 (2006).
9. Ewing, R. C., Weber, W. J. & Clinard, F. W. Radiation effects in nuclear waste forms for high-level radioactive waste. *Prog. Nucl. Energy* **29**, 63–127 (1995).
10. Weber, W. J. & Ewing, R. C. Plutonium Immobilization and Radiation Effects. *Science*. **289**, 2051–2052 (2000).
11. Meldrum, A., Boatner, L. A., Weber, W. J. & Ewing, R. C. Amorphization and recrystallization of the  $ABO_3$  oxides. *J. Nucl. Mater.* **300**, 242–254 (2002).
12. Li, M., Pietrowski, M. J., De Souza, R. A., Zhang, H., Reaney, I. M., Cook, S. N., Kilner, J. A. & Sinclair, D. C. A family of oxide ion conductors based on the ferroelectric perovskite  $Na_{0.5}Bi_{0.5}TiO_3$ . *Nat Mater* **13**, 31–35 (2014).
13. Irvine, J. T. S., Sinclair, D. C. & West, A. R. Electroceramics : Characterization by Impedance Spectroscopy. *Adv. Mater.* **2**, 132–138 (1990).
14. Fleig, J. Local conductivity measurements on AgCl surfaces using microelectrodes. *Solid State Ionics* **85**, 9–15 (1996).
15. Veazey, R. A., Gandy, A. S., Sinclair, D. C. & Dean, J. S. Modeling the influence of two terminal electrode contact geometry and sample dimensions in electro-materials. *J. Am. Ceram. Soc.* Available on-line <https://doi:10.1111/jace.16236> (2018).

## Chapter 2: Literature Review

### 2.1 ABO<sub>3</sub> Perovskite Structure

Perovskite was first named after the Russian mineralogist L. A. Perovskiy, in 1839, when the first material with this structure was discovered, CaTiO<sub>3</sub><sup>1</sup>. The perovskite structure has the general formula ABX<sub>3</sub> where A and B are cations and X is an anion. Several hundred compositions of perovskites have been synthesised due to the large variety of possible charge combinations of A and B cations<sup>2</sup>. The work in this thesis is concerned with oxide perovskites where the X anion is oxygen. As the oxygen has a charge of -2, the A and B cations combined oxidation state must be equal to 6 giving rise to typical charge configurations of A<sup>1+</sup>B<sup>5+</sup>O<sub>3</sub>, A<sup>2+</sup>B<sup>4+</sup>O<sub>3</sub> and A<sup>3+</sup>B<sup>3+</sup>O<sub>3</sub>.

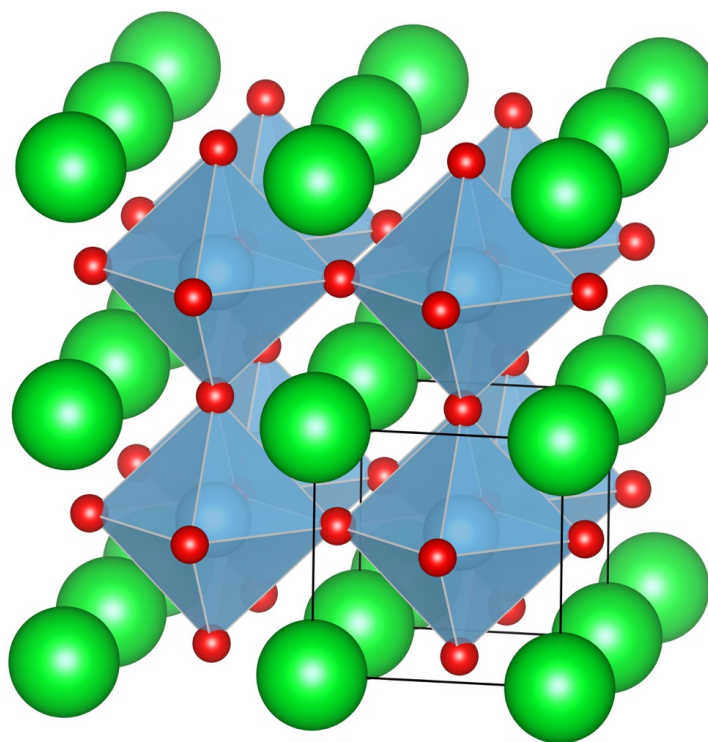


*Figure 2.1. The ideal cubic perovskite structure. Large A cations are shown as green spheres, smaller B cations are shown as blue spheres and the oxygen anions are shown as red spheres. The B cation coordination polyhedra is shown, and the black wire frame represents the unit cell. Image created using Vesta<sup>3</sup>.*

The ideal perovskite structure is cubic with space group  $Pm-3m$  and is shown in Figure 2.1. The coordination of the larger A-site cations is 12 in a cubo-octahedral site whilst the smaller B-site cations are 6 coordinated in an octahedral site. The A-site cations (green spheres) reside at the corners of the unit cell (black wire frame) whilst the B-site cations (blue spheres) are body-centred and the oxygen anions (red spheres) are face-centred, Figure 2.1. Each oxygen anion is shared between two BO<sub>6</sub> octahedra in a linear B-O-B arrangement.

Distortions from the ideal cubic structure described above can occur to accommodate different sized cations within the structure and/or multiple cations occupying either the A or B sites. The Goldschmidt tolerance factor<sup>4</sup>,  $t$ , quantifies this distortion and is given by

$$t = \frac{r_A + r_O}{\sqrt{2}(r_B + r_O)} \quad (2.1)$$

where  $r_A$ ,  $r_B$  and  $r_O$  are the ionic radii of the A and B cations and oxygen, respectively. If  $t = 1$ , the ideal cubic perovskite will form. If  $t < 1$ , the A-site cation is too small for its site and leads to the tilting of the  $BO_6$  octahedra. As the tolerance factor decreases, so too does the crystal symmetry<sup>5</sup>, and the B-O-B arrangements are no longer linear. If  $t > 1$ , the A-site cation is too large for its site and this leads to the distortion of the  $BO_6$  octahedra, reducing the co-ordination of the B cations. Typically, a cubic perovskite will form when  $0.9 < t < 1.0$ <sup>2</sup>. Deformed perovskite structures form for  $t < 0.9$ <sup>6</sup>.

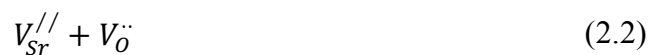
## 2.2 SrTiO<sub>3</sub>

Using Shannon radii<sup>7</sup>, SrTiO<sub>3</sub> has a tolerance factor of  $t = 1.00$  and therefore takes the crystallographic structure of ideal cubic perovskite at room temperature. The structure becomes tetragonal at temperatures below 110 K and orthorhombic below 65 K<sup>8</sup>. It has a lattice parameter of  $a = 0.3905$  nm, a theoretical density of  $5.12$  g cm<sup>-3</sup>, band gap of  $3.25$  eV<sup>9</sup> and a room temperature relative permittivity of  $\epsilon_r \sim 300$ <sup>10</sup>.

### 2.2.1 Defect Chemistry in SrTiO<sub>3</sub>

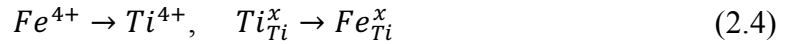
Here we will focus on the defect chemistry of acceptor-doped, specifically Fe, and nominally undoped SrTiO<sub>3</sub>, which is also acceptor-doped by impurities that substitute for Ti<sup>11-13</sup>. Defects can be stoichiometric, non-stoichiometric and/or intrinsic, extrinsic.

A Schottky defect is a cation and anion vacancy pair from lattice positions where a cation and an anion usually reside, whereas a Frenkel defect is an atom that is located in a position that is not a normal crystal structure site, called an interstitial. These defects are stoichiometric and intrinsic. The following (partial) Schottky defects can occur in SrTiO<sub>3</sub> using Kröger-Vink notation<sup>14</sup>

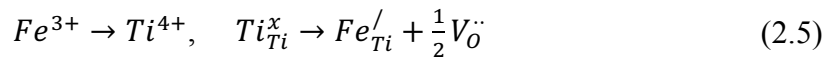


In SrTiO<sub>3</sub>, point defects are far more likely to be vacancies than interstitials given the close packed nature of the perovskite structure<sup>13</sup>.

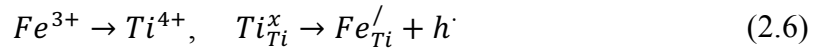
Extrinsic defects are formed by impurities or dopants. A stoichiometric defect is when a dopant of the same charge as the host ion is substituted in the material (isovalent doping), whereas a non-stoichiometric defect is when the dopant has a different charge (aliovalent doping). Fe can cause both stoichiometric and non-stoichiometric defects when substituted onto the Ti site. Stoichiometric doping is simply a straight substitution between the Ti and Fe atom.



However, Fe ions can have mixed oxidation states in the structure (4+/3+)<sup>15-17</sup> and so doping can also lead to non-stoichiometry.



In this case, the Ti site occupied by a Fe ion has an overall negative charge and so oxygen vacancies are produced to compensate for charge balance and is called ionic compensation. Another way that charge compensation can occur is by electronic compensation.



Here, charge balance is achieved by the formation of electron holes and there is no change in stoichiometry. SrTiO<sub>3</sub> is often regarded as a mixed conductor<sup>18</sup>, the oxygen vacancies lead to increased levels of ionic conduction, whilst the formation of holes increases the amount of electronic conduction. Increasing the amount of Fe increases the conductivity due to an increase mainly from the electronic contribution<sup>15</sup>, consistent with a decrease in the band gap<sup>19,20</sup>. In fact, by completely substituting Fe for Ti results in a metallic conductor<sup>17</sup>. It should be noted that for the levels of Fe-doping relevant in this thesis, the room temperature structure is unchanged from the cubic perovskite structure<sup>19</sup>.

### 2.3 Radiation Damage

There has been a considerable amount of research on the use of crystalline ceramic oxides as an alternative wastefrom for the immobilisation of high-level waste (HLW) to borosilicate glasses. The principal sources of radiation in HLW are  $\alpha$ -decay,  $\beta$ -decay and  $\gamma$ -emission. Particles produced in these events can interact and cause atomic displacements in the material through ballistic collisions or ionisation effects. The damage to the crystal structure as a consequence of these interactions is known as radiation damage. The amount of damage

produced in a material can be quantified in terms of the displacements per atom (dpa). This is defined as the number of times each atom has been displaced, due to interactions with radiation, per atom in the system. For example, a damage of 1 dpa is equivalent to every atom in the system being displaced, on average, once.

$\beta$ -decay of short-lived fission products, such as  $^{137}\text{Cs}$  and  $^{90}\text{Sr}$ , produces  $\beta$ -particles with energies  $\sim 0.5$  MeV,  $\gamma$ -rays and low energy recoil nuclei<sup>21</sup>. These recoil nuclei have sufficient energy to produce relatively low levels of radiation damage and are the primary source of radiation damage in the first few hundred years of storage due to their short half-lives (e.g.  $^{137}\text{Cs}$  - 30.2 yr,  $^{90}\text{Sr}$  -28.1 yr)<sup>22</sup>.

$\alpha$ -decay of the actinide elements, such as U, Np, Pu, Am and Cm, produces  $\alpha$ -particles, with energies typically in the range of 4.5 to 5.8 MeV, and  $\alpha$ -daughter recoil nuclei, with energies typically in the range of 70 to 100 keV<sup>23</sup>. For example,  $\alpha$ -decay of  $^{239}\text{Pu}$  produces an  $\alpha$ -particle with an energy of 5.16 MeV and a  $^{235}\text{U}$  recoil nucleus with an energy of 0.086 MeV<sup>24</sup>. The  $\alpha$ -particle has a range of  $\sim 10,000$  nm and displaces a few hundred atoms at the end of its range, whereas the recoil nucleus has a range of  $\sim 10$  nm and can displace several thousand atoms<sup>25</sup>. The actinide elements have much longer half-lives (e.g.  $^{239}\text{Pu}$  –  $2.4 \times 10^4$  yr) and are the primary source of radiation damage after  $\sim 1000$  years<sup>22</sup>.

### 2.3.1 Radiation Damage Processes

Interactions between radiation and atoms in the crystalline lattice produce radiation damage due to transfer of energy from the energetic particle to the atoms within the structure. These interactions can be split into two categories: the transfer of energy to electrons, *electronic stopping*, and the transfer of energy to atomic nuclei, *nuclear stopping*. Electronic stopping occurs when energy is transferred from the incoming particle to the electronic structure through inelastic interactions with the electron cloud. This can cause excitation and ionisation of electrons<sup>26</sup>. Electronic stopping produces little damage, in terms of displacements, over a long range. Nuclear stopping occurs when energy is transferred from the incoming particle through elastic ballistic collisions with atomic nuclei and can lead to significant amounts of atomic displacements. Generally, for high mass particles with low energies, nuclear stopping will dominate, whilst electronic stopping will dominate for low mass particles with high energies. The total energy loss per unit length by the incoming particle can be defined as a sum of the two components<sup>27</sup>:

$$\left(-\frac{dE}{dx}\right)_{total} = \left(-\frac{dE}{dx}\right)_{nuclear} + \left(-\frac{dE}{dx}\right)_{electronic} \quad (2.7)$$

where  $dE/dx$  is the energy transferred per unit length travelled. It should be noted there are also radiation losses but for the energies concerned in this thesis, these are negligible. Whether an incoming particle transfers its energy by electronic or nuclear stopping is determined by a number of factors; the nature of the incoming particle and lattice atom, the energy and mass of the incoming particle, the mass of the lattice atom and density of the material<sup>22</sup>. It is clear that there can be contributions from each stopping mechanism. Hence, it can be beneficial to describe interactions in terms of the electronic to nuclear stopping power ratio (ENSP), to determine which is the dominating mechanism.

$$ENSP = \left( -\frac{dE}{dx} \right)_{\text{electronic}} / \left( -\frac{dE}{dx} \right)_{\text{nuclear}} \quad (2.8)$$

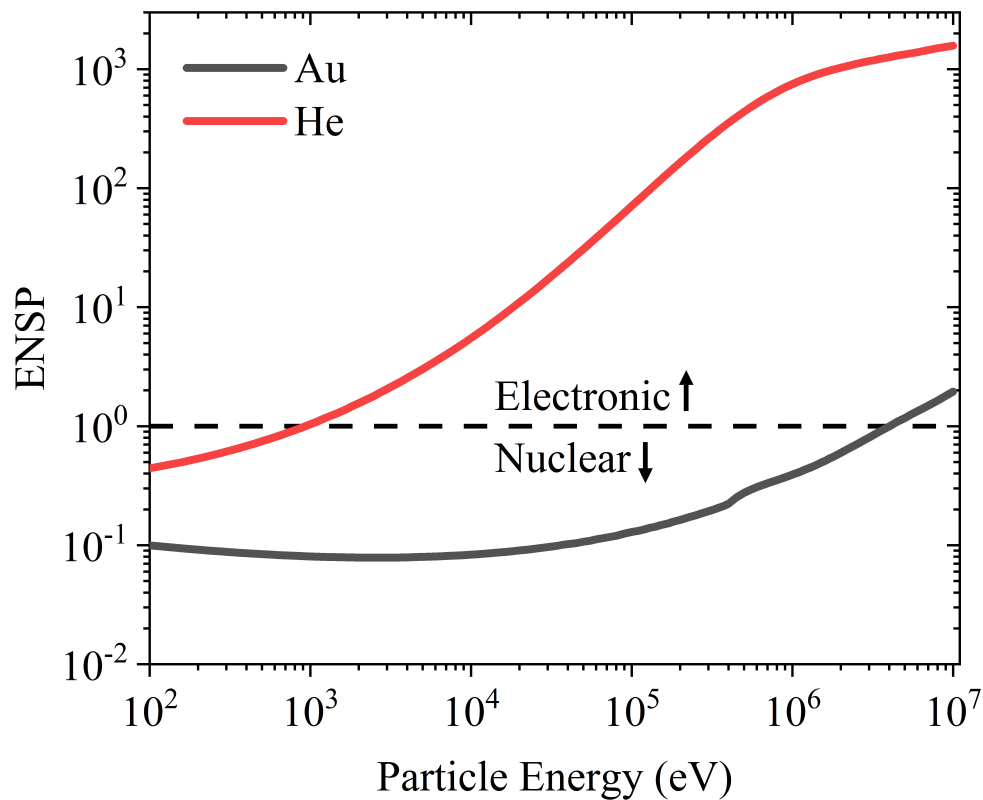


Figure 2.2. The ENSP ratio for Au and He particles implanted in SrTiO<sub>3</sub> in the energy range 0.1 keV – 10 MeV, calculated using SRIM<sup>28</sup> (the Stopping and Range of Ions in Matter, described in Section 3.6). The horizontal line denotes an ENSP of 1.

Au and He are typical elements that are used in implantation studies, which will be discussed later. The ENSP ratio for Au and He implanted in SrTiO<sub>3</sub> is shown in Figure 2.2. Nuclear stopping dominates for Au until very high energies, whereas for He, nuclear stopping dominates at very low energies. Figure 2.3 shows the damage profile of Au and He implanted in SrTiO<sub>3</sub>.

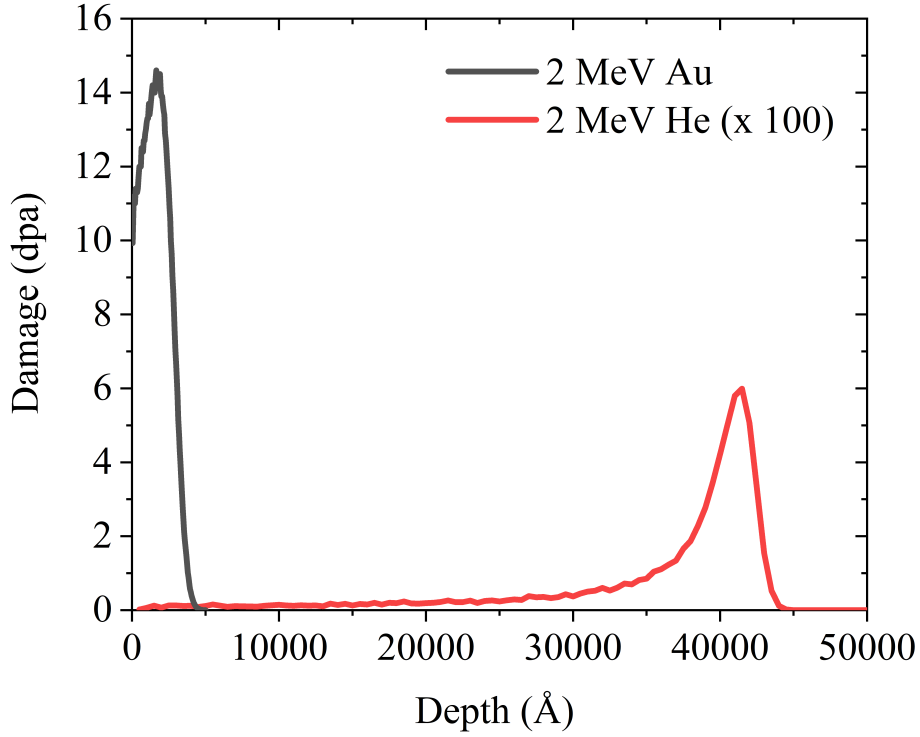


Figure 2.3. The damage profile of 2 MeV Au and He in SrTiO<sub>3</sub>, calculated using SRIM<sup>28</sup>. The amount of damage produced by He has been multiplied by 100 for ease of comparison with Au.

High energy, light particles such as He dissipate the majority of their energy through ionisation processes over a large range in multiple interactions<sup>29</sup>. Towards the end of their range and with lower energies, nuclear stopping dominates, leading to more displacements. It is this decrease in energy that ultimately leads to the increased amount of vacancies at depth in the material, Figure 2.3. Electronic stopping therefore produces low levels of displacements over a large range. Heavier particles such as Au dissipate the majority of their energy via nuclear stopping, producing large amounts of displacements over a much shorter range.

In a ballistic collision, the maximum amount of kinetic energy an incoming particle can transfer to a lattice atom, assuming non-relativistic effects, is given by<sup>30</sup>

$$E_{max} = E_1 \frac{4m_1m_2}{(m_1 + m_2)^2} \quad (2.9)$$

where  $E_1$  is the energy of the incoming particle and  $m_1$  and  $m_2$  are the mass of the incoming particle and lattice atom, respectively. The energy required to displace an atom from its lattice site is known as the displacement energy,  $E_d$ . If the energy transferred is less than  $E_d$ , the atom will not be displaced but will vibrate about its lattice position, heating the surrounding material. If the energy transferred is greater than  $E_d$ , the atom will be displaced, creating a primary knock-on atom (PKA). The PKA can then go on to displace other atoms from their lattice sites

resulting in many displacements in close proximity to each other, producing a *damage cascade*<sup>31</sup>. Similarly, the initial particle will continue to induce further displacements until its energy has reduced to less than  $E_d$ , and the particle will come to rest in the lattice. The Kinchin-Pease model<sup>30</sup> can predict the average amount of displacements created by a PKA of energy  $T$ , summarised as follows:

$$0 \text{ for } T < E_d, \quad (2.10)$$

$$1 \text{ for } E_d < T < 2E_d, \quad (2.11)$$

$$\frac{T}{2E_d} \text{ for } 2E_d < T < E_c \quad (2.12)$$

where  $E_c$  is the cut-off energy for nuclear interactions, above which electronic stopping occurs. This model however is idealistic, and modifications have since been proposed to account for other factors, such as the displacement efficiency and electronic energy losses, which Norgett, Robinson and Torrens proposed in their NRT model<sup>32</sup>.

The displacement energy is dependent on the nature of the atom and the structure of the material and will differ for each sublattice<sup>33</sup>, hence the calculation is complex and usually measured by computer simulations<sup>34</sup>. A wide range of displacement energies have been used for Sr, Ti and O<sup>35-39</sup> when making assumptions about the irradiation conditions. For the sake of simplicity, we assume a displacement energy of 50 eV for each atom when conducting SRIM calculations to estimate the amount of damage produced.

### 2.3.2 Defects

If the incoming particle has sufficient energy, it can displace atoms from their lattice sites, leaving behind a site that is no longer occupied by an atom, called a vacancy. The displaced atom can either recombine with vacancies in the material or it may come to rest at a position that is not a regular lattice site, called an interstitial. Together, these defects are known as a Frenkel pair. Typically, thousands of these defects are produced per  $\alpha$ -decay event<sup>23</sup>. Irradiating particles can also form defects in the structure<sup>40</sup>, by combining with a vacant site or by residing in an interstitial site in the lattice and are called impurities. Frenkel pairs, interstitial and substitutional impurities are known as point defects.

Defects that escape recombination can agglomerate to form larger defects. Interstitials and vacancies can agglomerate to form line defects such as dislocations or volume defects such as voids or regions of different phases called precipitates<sup>42</sup>. Materials that have suffered from the

agglomeration of defects are prone to volume changes such as swelling<sup>43</sup>. A 2D schematic of the point and volume defects described are shown in Figure 2.4.

The end state of the damage process at substantially high doses is amorphisation of the ceramic. There are two main models that describe how a material reaches this end point: defect accumulation and direct-impact<sup>44</sup>. Defect accumulation is a homogeneous amorphisation process where the progressive accumulation of defects eventually leads to a critical dose being achieved and the material spontaneously amorphises. In contrast, direct-impact is a heterogeneous process where each irradiating particle produces an amorphous region directly in the core of its damage cascade<sup>45</sup>. In reality, a combination of both processes can lead to amorphisation (e.g. double cascade overlap<sup>44,46</sup>). Amorphisation is undesirable in a material as it is often accompanied by degradation of mechanical (e.g. swelling and hardness) and chemical properties<sup>47</sup> (e.g. dissolution rates<sup>48,49</sup>).

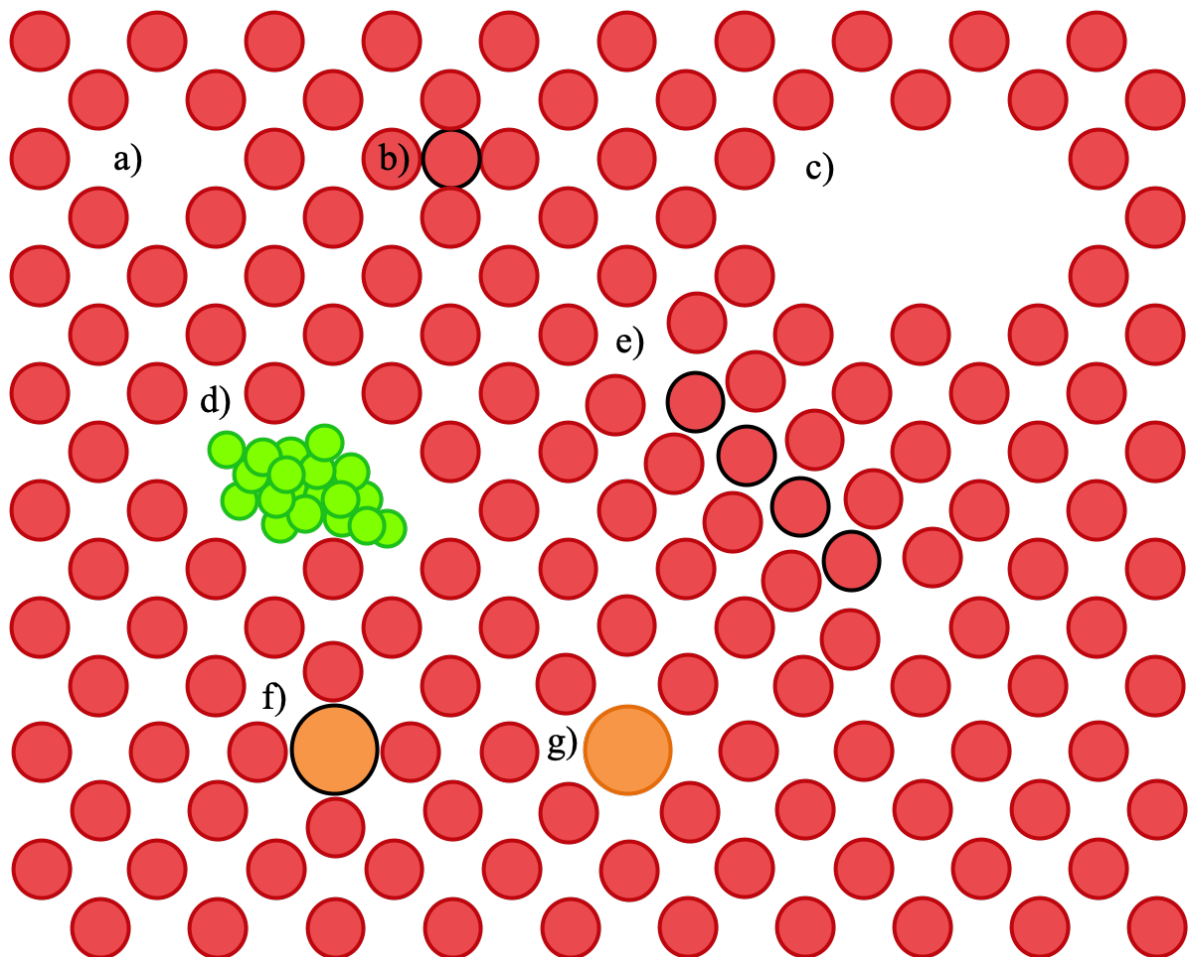


Figure 2.4 - Diagram showing intrinsic and extrinsic defects in a simple crystalline material; a) vacancy, b) self-interstitial, c) void, d) gas-bubble, e) interstitial dislocation loop, f) larger impurity atom in an interstitial site (interstitial impurity) and g) larger impurity atom on a regular lattice site (substitutional impurity).

### 2.3.3 Radiation Damage Recovery

A tolerance to radiation damage can be considered as a systems ability to *recover* the crystalline lattice during irradiation<sup>50</sup>. Defects can receive additional energy from further collisions or an increase in temperature, becoming more mobile. Increased defect mobility can lead to the recombination of vacancies and interstitials, and the lattice is said to have recovered. As previously discussed, defects can migrate to form larger defects which decrease the stored energy in the system and relieve stresses induced by the initial defects<sup>26</sup>. Another form of recombination is when an interstitial recombines with a vacancy from a different sublattice<sup>51</sup>, forming cation antisite defects. Some results suggest materials that are able to accommodate disorder are more tolerant to radiation damage<sup>52</sup>. For example, as a result of damage  $Gd_2Zr_2O_7$  undergoes an irradiation-induced pyrochlore-to-defect fluorite structure transformation. However, Lian et al<sup>53</sup> found the defect fluorite structure is extremely stable even to doses of ~ 100 dpa. How radiation damage evolves over time is determined by the competing processes of damage production and recovery. By increasing the temperature of the material during irradiation increases defect mobility and consequently damage recovery in the material. The critical temperature for amorphisation,  $T_c$ , is the temperature above which a material cannot be amorphised due to thermal recovery processes. At this temperature the rate of recombination becomes greater than the rate of defect production. A material is said to have a greater tolerance to irradiation if its  $T_c$  is lower. It can therefore be useful to describe the critical fluence of amorphisation,  $F_c$ , as a function of the irradiation temperature<sup>54</sup>

$$F_c = F_{c0} / \left\{ 1 - \exp \left[ \left( \frac{E_a}{k_B} \right) \left( \frac{1}{T_c} - \frac{1}{T} \right) \right] \right\} \quad (2.13)$$

where  $F_{c0}$  is the critical fluence at 0 K,  $E_a$  is the activation energy for recovery of radiation damage,  $k_B$  is the Boltzmann constant and  $T$  is the irradiation temperature.

### 2.3.4 Inducing Damage

Inducing radiation damage can be done in a number of ways. One method is actinide doping, where radioactive isotopes are doped into the material. Other methods include placing material in test reactors or characterising natural analogues. Both of these methods require large periods of time for high doses and the material is difficult to handle due to activation.

Ion implantation is the preferred method to induce damage due to its versatility and because it can produce high levels of damage over a short period of time. Charged ions are accelerated in an electric field and directed towards the surface of a sample within a vacuum chamber. The ions penetrate a certain depth into the material depending on the atomic mass of the ion being

accelerated; the energy of the ion; and the material being irradiated. The ion transfers its kinetic energy to atoms in the material, producing defects, until coming to rest in the material, as described in Section 2.3.1. One of the main advantages of ion implantation is that the material is generally not activated, allowing for easier handling and analysis of irradiated samples. Another advantage is that the irradiations can be tuned (irradiating ion and energy) to simulate very specific processes that occur. For example, He implantations are used to simulate the effects of  $\alpha$ -particles in  $\alpha$ -decays<sup>55</sup>; Au implantations are typically used to simulate the recoil nuclei as it is heavy and produces large amounts of displacements that are analogous<sup>56</sup>. One of the main concerns is that the damage rate is much faster than that of a test reactor<sup>57</sup> and is not representative of that found in a wastefrom.

The depth of the damage region is dependent on the irradiating ion, irradiating energy and the composition of the target. In general, ion implantation produces damage within small volumes, typically extending from the surface of the material to a depth of about 1  $\mu\text{m}$ . Because of this small volume, surface sensitive techniques are required to characterise this region. Increasing the energy of the irradiations significantly (typically  $> \text{GeV}$ ), called swift heavy ions, can increase this damage region to thicknesses up to  $\sim 100 \mu\text{m}$ <sup>58,59</sup>, allowing for easier characterisation of damage. At such high energies, the incoming particles lose the majority of their energy by electronic stopping (see Section 2.3.1). How representative such irradiations are to the application of nuclear waste immobilisation is a topic of debate.

### 2.3.5 Recrystallisation

Ion beam amorphised materials can be thermally annealed, leading to recrystallisation of the amorphous volume. In some cases, if medium range order is maintained, precipitates may nucleate and grow from within the amorphous phase<sup>6,60</sup>; however, solid phase epitaxial recrystallisation is the most common way recrystallisation occurs. It is called solid phase as it requires temperatures that are below the melting temperature of the material. The reordering process takes place at the amorphous-crystalline interface and the amorphous material recrystallises, layer by layer (epitaxially), using the underlying crystalline matrix as a template. The driving force for the recrystallisation is the lower free energy of the crystalline phase, relative to the amorphous phase<sup>42</sup>.

As the amorphous-crystalline interface advances, microtwins can form as a result of stacking faults during the recrystallisation process<sup>61</sup>. The stacking faults occur in regions<sup>61</sup> where there are a high concentration of interstitial-type defects, causing a microtwin to nucleate<sup>62</sup>. When the amorphous-crystalline interface reaches the interstitial-type defects, mistakes in the

stacking sequence leads to a change in the orientation of the recrystallised material either side of the stacking fault. Cullis et al.<sup>63</sup> irradiated Si with Ne, Kr and Ar ions and subsequently annealed the samples at 1100 °C. Microtwins had formed at the annealed interface position but the rest of the annealed layer was polycrystalline. They attributed the defects to bonding errors at the moving layer interface.

### 2.3.6 Characterising Radiation Damage

In this thesis, the two main techniques for structural characterisation of radiation damage are glancing angle X-ray diffraction (GAXRD) and transmission electron microscopy (TEM). GAXRD is a non-destructive technique that enables determination of the crystal structure of a material from the surface to depths in the order of several  $\mu\text{m}$ . Using this technique, it is possible to identify: amorphous regions from diffuse scattering with no crystalline peaks; damaged regions from diffuse scattering and crystalline peaks present; swelling from an increase in lattice parameters; and phase transformations as a result of ion implantation. The thickness of damage regions can also be estimated from varying the incidence angle of the X-rays and determining the onset of crystallinity.

TEM is a powerful technique for investigating ion implantation induced damage, including identifying amorphous volumes; vacancy-type defects such as gas bubbles and voids; interstitial-type defects such as dislocations and line defects; and secondary phases such as precipitates. Aughterson et al.<sup>64</sup> irradiated  $\text{Gd}_2\text{TiO}_5$  with 1 MeV Kr ions in-situ in a TEM to observe implantation induced amorphisation and some of their results are shown in Figure 2.5.

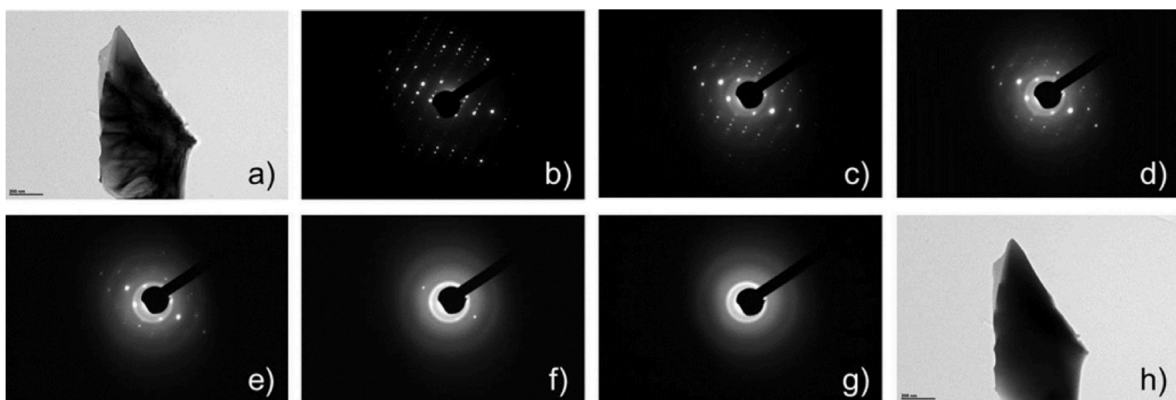


*Figure 2.5. a) Bright-field image of a pristine grain of  $\text{Gd}_2\text{TiO}_5$ , b-g) selected area diffraction patterns of the grain with increasing dose and h) bright-field image of the fully amorphous grain. Reprinted Fig. 3. from Aughterson et al.<sup>64</sup> with permission from Elsevier.*

The bright field image of the pristine sample shows evidence of diffraction contrast across the grain and is due to the electrons diffracting off the planes that satisfy Bragg's law (see Section 3.4). As the dose increases, diffraction spots arising from the crystalline phase decrease in

intensity as diffuse rings appear. In the bright field image of the fully amorphous grain, the diffraction contrast has significantly reduced.

### 2.3.7 Electrical Characterisation of Radiation Damage

The first measurements of radiation induced conductivity (RIC) were made in 1873 where selenium was observed to become more conductive as a function of intensity of light<sup>65</sup>. The selenium returned to its original conductivity instantaneously when the light was removed. There is an extensive amount of literature on RIC in a range of materials<sup>66-69</sup>, by irradiating materials with X-rays,  $\gamma$ -rays, protons and neutrons. RIC is an enhancement of conductivity due to excitation of electrons into the conduction band from the valence band and is dependent on the irradiating flux<sup>70</sup>. Importantly, RIC is a function of ionisation, but not dependent on the irradiating particle or the accumulated dose and the original conductivity is returned after irradiations<sup>71</sup>. Radiation induced electrical degradation (RIED) is similar to RIC, but the irradiations are performed in an electric field and when this is the case, the increased conductivity is permanent. This can significantly impact the use of insulating ceramics in radiation environments, such as fusion applications<sup>41,70</sup>, as increased conductivity can lead to Joule heating in the components employed for reactor maintenance.

Research on GaN suggests that radiation damage by neutrons reduces the conductivity with increasing dose, due to an increase in carrier traps, which significantly degrades device performance<sup>72,73</sup>. Dana et al.<sup>74</sup> irradiated boro-hydro-nitride with X-rays and found the electrical resistivity to decrease with increasing dose and suggested the increase in conductivity is due to the generation of electrically active radiation induced defects. They also noted that the electrical properties were more sensitive at low doses than optical and mechanical measurements.

Ion implantation has been used to increase the conductivity of polymers<sup>75</sup>. Goyal et al.<sup>76</sup> attributed the enhanced conductivity to disordered bonds in an amorphous carbonaceous network, measured by Raman spectroscopy. Martin et al.<sup>77</sup> irradiated quartz with metallic ions and found that Ti irradiations increased the conductivity, whilst Fe and Cu irradiations had no effect on the conductivity and suggested that the surface conductivities were dependent on the chemical reactivity of the irradiating species with quartz. Kobayashi et al.<sup>78</sup> irradiated sapphire with Fe and Ni ions and found the conductivity to increase with increasing dose. They attributed this to metallic conduction from the metal impurities in the sapphire.

Reagor et al.<sup>79</sup> created highly conducting nanolayers on the surface of SrTiO<sub>3</sub> by preferential ion beam etching using argon ions. They measured the electrical properties by a two-point

resistivity measurement before and directly after ion bombardment of different energies and milling times. For 300 keV Ar ion irradiations, they observed the measured resistance decrease with milling time before eventually saturating after 30 mins. They also reported the measured resistance would decrease from an implantation energy of 100 keV down to a minimum at 300 keV, but higher implantation energies up to 700 keV would increase the measured resistance. Cooper et al.<sup>80</sup> created a highly conducting surface, measured by a four-point probe method, on SrTiO<sub>3</sub> by 100 keV boron implantations. They also irradiated with H, Ar, C, Ni, Fe, As, Ta and Nb but reported surface conductivity values several orders of magnitude lower than that of boron, showing that irradiating with boron specifically was significant to conduction.

The radiation damage of focus in this thesis is due to atomic displacements by heavy ions leading to amorphisation. There is little in the literature that attribute changes in electrical properties to this sort of damage. The electrical resistivity of graphite has been measured during swift heavy ion (Au) irradiations<sup>81,82</sup>, by a dc 4-point resistivity measurement. The measured resistance increased with increasing fluence but saturated towards larger doses and the changes were less pronounced for higher irradiation temperatures<sup>81</sup>. Further studies suggested that heavier implanting ions lead to faster increases in resistivity and although electrical properties saturated at high doses, mechanical properties such as hardness continued to increase<sup>82</sup>. Two samples were stacked for the irradiations. The front sample was sufficiently thin that the Au ions would pass through this sample, interacting predominantly through electronic stopping. In the back sample nuclear stopping had a larger effect. The increase in the resistance was larger for the back sample, suggesting nuclear stopping influences changes in resistivity more than electronic stopping. The decrease in conductivity was attributed to a decrease in the mean free path of electrons, arising from defects such as vacancy clusters and dislocation loops and disordering of the graphite structure<sup>82</sup>.

### 2.3.8 Radiation Damage in SrTiO<sub>3</sub> and Related Perovskites

Perovskites, particularly SrTiO<sub>3</sub>, have been extensively studied to investigate their radiation response due to their potential for hosting nuclear wastes such as actinides, and in the case of SrTiO<sub>3</sub> because of its relatively simple cubic structure.

White et al.<sup>83</sup> irradiated single crystals of SrTiO<sub>3</sub> and CaTiO<sub>3</sub> with 540 keV Pb ions and found, using Rutherford back-scattering (RBS) and ion channelling techniques, that the near surface region of both samples became amorphous. After irradiations, they annealed the samples at different temperatures and different times and reported the amorphous to crystalline interface to move towards the surface with increasing annealing time, suggesting solid phase epitaxial

regrowth. Two periods of regrowth were present, a slower induction period followed by a faster linear progression of crystallisation. A later paper by the same authors<sup>84</sup> suggested the length of the induction period decreased with increasing annealing temperature and the velocity of recrystallisation increased. TEM confirmed solid phase epitaxy was occurring but defects were still present in the recrystallised layer.

Meldrum et al.<sup>85</sup> irradiated a number of perovskite compositions in-situ in a TEM using 800 keV Kr ions at a range of temperatures. They found a large range of critical amorphisation temperatures,  $T_c$  (temperature above which a material does not amorphise), of 450 K despite the similar structures of the materials studied. SrTiO<sub>3</sub> had the largest critical amorphisation dose at 0 K of 1.09 dpa and the lowest  $T_c$  of 425 K. They found a weak correlation between  $T_c$  and ENSP and concluded that electronic interactions can enhance defect recombination in these materials. Further studies in the same group<sup>6</sup> found  $T_c$  to decrease with increasing mass of the A-site cation for perovskites with the same B-cation. During annealing, they found that titanate perovskites would recrystallise epitaxially, whereas for niobates and tantalates new crystallites would form from within the amorphous region, suggesting the amorphous material retains some ‘memory’ of the pre-amorphised crystal orientation. The samples were heated in 25 K intervals and held at each temperature for a period of one minute. The authors defined the recrystallisation temperature as the temperature at which observable recrystallisation occurred within the one-minute time frame. They reported that SrTiO<sub>3</sub> would recrystallise at a temperature of 800 K. Irradiations with lighter Ne ions were not able to amorphise SrTiO<sub>3</sub> and they suggest again that electronic energy loss could assist in defect recovery.

Thevuthasan et al.<sup>86</sup> irradiated SrTiO<sub>3</sub> single crystals with 1 MeV Au ions at 170 K and 300 K and characterised the damage using in-situ RBS. They found that the accumulation of disorder exhibits a sigmoidal dependence on ion dose and the Ti sublattice completely disorders at a slightly lower dose than the Sr sublattice. At 170 K, SrTiO<sub>3</sub> amorphised at a dose of 0.8 dpa, whereas at 300 K the dose was 1.1 dpa. Using the same irradiations, Zhang et al.<sup>87</sup> found that the critical amorphisation dose is dependent on the dose rate, obtaining critical amorphisation doses ranging from 0.24 to 0.55 dpa for dose rates of  $8.2 \times 10^{-3}$  dpa/s and  $2.9 \times 10^{-5}$  dpa/s, respectively. Because thermal recovery should be the same, they suggested there is increased dynamic annealing for the higher dose rates, leading to a decreased defect accumulation.

Wang et al.<sup>88</sup> irradiated SrTiO<sub>3</sub> with 2 MeV Au ions at 300 and 975 K and then annealed the samples at 1275 K for 10 hours before observing them in a TEM. 300 K irradiations resulted in an amorphous surface separated from the crystalline bulk by a highly strained layer. After annealing at 1275 K the amorphous surface had epitaxially recrystallised and Au nanoclusters

had formed within this region. The Au nanoclusters exhibited an epitaxial orientation with respect to the surrounding SrTiO<sub>3</sub>. The highly strained layer had also recovered the damage induced and Au nanoclusters had also formed, though the density of these clusters was less than in the amorphous material. Another feature in this region was the formation of cavities and were believed to have formed due to agglomeration of vacancies during Au implantation. Irradiations at 975 K and subsequent annealing formed larger Au clusters and cavities that these clusters seemed to pair with the cavities. They suggested this could occur as the interface between the Au cluster and the SrTiO<sub>3</sub> could act as a sink for the vacancies, leading to preferential nucleation of vacancies at the interface. Further work suggested that Au substituted into a Sr or Ti lattice position, meaning the eventual nucleation of the Au lattice would maintain the same orientation as SrTiO<sub>3</sub><sup>89</sup>. Observations of cavities indicated that vacancy-clustering is the dominant process of vacancy diffusion in Au-implanted SrTiO<sub>3</sub> and prevails over Frenkel pair recombination.

Sabathier et al.<sup>90</sup> irradiated SrTiO<sub>3</sub> single crystals with 320 keV Pb ions and characterised by X-ray absorption spectroscopy and XRD. They concluded irradiations had led to a partial phase transformation from SrTiO<sub>3</sub> to the Ruddlesden-Popper phase Sr<sub>2</sub>TiO<sub>4</sub> and TiO<sub>2</sub>, but no other studies have confirmed this. Further studies on SrTiO<sub>3</sub> and Ruddlesden-Popper phases were examined by Won et al.<sup>39</sup> using Ne irradiations of stoichiometric and non-stoichiometric SrTiO<sub>3</sub> and TEM. By comparing the damage, they concluded that SrTiO<sub>3</sub> with Ruddlesden-Popper faults present were more susceptible to amorphisation than the surrounding stoichiometric SrTiO<sub>3</sub> and the faults lead to the absorption of radiation-induced point defects.

Smith et al.<sup>54</sup> undertook in-situ 1 MeV Kr irradiations of the La<sub>x</sub>Sr<sub>1-3x/2</sub>TiO<sub>3</sub> solid solution using TEM. All samples were amorphised but T<sub>c</sub> passed through a minimum at La<sub>0.2</sub>Sr<sub>0.7</sub>TiO<sub>3</sub>, i.e. the most tolerant composition was in the middle of the solid solution. The trends observed were not consistent with crystal structure differences in the solutions. Instead, they suggested that at La concentrations below the minimum, vacancy enhanced recovery dominates the radiation damage response because of an enhanced mobility of Sr vacancies due to the increasing concentration of A-site vacancies. For greater La concentrations, vacancy enhanced amorphisation occurs and they suggest the O, Sr and La interstitial migration energy is significantly larger leading to migration barriers in the more complex orthorhombic phase.

Zhang et al.<sup>91</sup> irradiated SrTiO<sub>3</sub> with 1 MeV Au ions and characterised the damage with RBS and TEM. They reported that SRIM had underestimated the damage profile of the irradiations with the position of the peak of the simulation being 40% shallower than the depth of the actual peak from the irradiations. They attributed these differences to an overestimation of electronic

stopping in the SRIM prediction. They observed electron beam induced recrystallisation whilst viewing amorphous regions in a TEM and suggested this was due to ionization-induced dynamic recovery.

Li et al.<sup>92</sup> studied the response of SrTiO<sub>3</sub> irradiated with 1 MeV Kr ions as a function of Nb-concentration. Nb-doping in SrTiO<sub>3</sub> significantly enhances the electrical conductivity and can turn it from insulating to semi-conducting or even metallic. Nb-doping, and thus significant increases in conductivity had only a slight improvement on the materials response to amorphisation with T<sub>c</sub> decreasing slightly. The slight improvements in T<sub>c</sub> were suggested to occur because of an increased concentration of Sr vacancies as a result of Nb<sup>5+</sup> substituting for Ti<sup>4+</sup>.

## **2.4 Impedance Spectroscopy**

Conventional two electrode dc measurements of electro-materials yield average electrical properties of multiple components in a material, such as the bulk, grain boundaries, and electrode effects. ac measurements facilitate differentiation between the individual components of the material<sup>93</sup>. In 1969, Bauerle<sup>94</sup> used Impedance Spectroscopy to identify bulk, grain boundary and electrode resistances in ceramics of yttria-stabilised zirconia. An equivalent circuit consisting of two parallel RC elements connected in series was used to describe the system<sup>94</sup>. Since then, Impedance Spectroscopy has been used to characterise a wide range of materials and devices. A summary of Impedance Spectroscopy theory can be found in Chapter 3.

Beekmans and Heyne<sup>95</sup> used a simple boundary layer model, later called the brick layer model (BLM), to describe the equivalent circuit used by Bauerle that consisted of conducting grains (bricks) surrounded by a resistive secondary phase or grain boundaries (mortar). A schematic of the BLM is shown in Figure 2.6 (a).

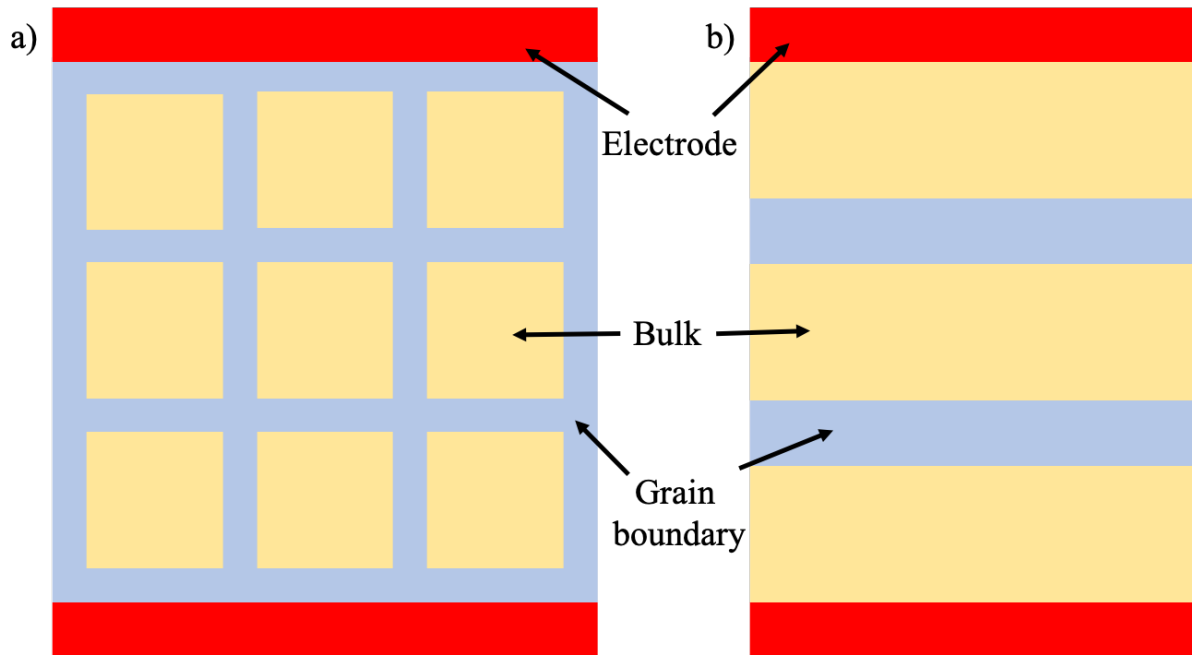


Figure 2.6 a) Schematic of the BLM and b) Beekmans boundary layer model.

As current takes the path of least resistance through a system, there is a preference towards the bulk rather than the resistive grain boundary. Therefore, the system only considers the series path between capping grain boundaries and the bulk and neglects the parallel grain boundary pathway<sup>96</sup>, and the system reduces to Beekmans boundary layer model, Figure 2.6 (b). Each layer of the bulk, grain boundary and the two layers of electrodes can be combined to make a series connection of three parallel RC elements. The conductivity,  $\sigma$ , and relative permittivity,  $\epsilon_r$ , of each component can then be calculated from the extracted R and C values and the following equations

$$R = \frac{GF}{\sigma} \quad (2.14)$$

$$C = \frac{\epsilon_0 \epsilon_r}{GF} \quad (2.15)$$

where GF is a geometric factor taking into account the geometry of the current flow through the system and  $\epsilon_0$  is the permittivity of free space. For conventional measurements such as is shown in Figure 2.6 the geometric factor is given by

$$GF = \frac{l}{A} \quad (2.16)$$

where  $l$  is the thickness of the sample/region and  $A$  is the surface area of the sample/region. When conventional measurements are made it is assumed that current flows homogeneously

through the material. Fleig & Maier<sup>97</sup> showed that a simple BLM does not represent the real microstructure of many ceramics. They undertook 2D finite element modelling (FEM), varying the shapes of the grains from the simple cubic grain shape in the BLM (e.g. hexagonal, triangular, ‘zig-zag’, sloping). They reported grain boundary resistances could increase or decrease depending on the pattern used. They described their findings as a “detour-effect”; the current will detour around blocking grain boundaries if it lowers the impedance. If there is a larger area of grain boundary for the current to pass through, this will lower the resistance of the grain boundary. Fleig<sup>98</sup> modelled a sample exhibiting an inhomogeneous grain size distribution, consisting of 12 large square grains and 4 agglomerates containing 49 smaller grains. Regions with a higher density of grains, and thus a higher density of resistive grain boundaries, had a lower current density than the larger grains. This implies that current takes the path of least resistance through a material.

Heath et al.<sup>99</sup> highlighted a similar effect in core-shell grain structures. They showed the physical microstructure modified the current pathways through the material, with a preference towards the more conductive core. Because of this, the calculated volume fractions from capacitance ratios were unreliable. Dean et al.<sup>100</sup> simulated two idealised structures with the same grain core and grain boundary volume fractions. The first case was a layered structure whereas the second case the grain core was encased in the grain boundary. Despite having the same volume fractions the simulated impedance response was very different. The most notable result was an increase in the full width half maximum of the grain core response in the encased model. This deviation away from an ideal Debye response was as a result of the heterogeneous electrical microstructure produced.

A disadvantage of conventional measurements is that the properties are averaged across the full sample. Micro-contacts allow for localised electrical properties of a material to be calculated<sup>101–103</sup>, or specific regions to be probed and characterised in more detail such as surface layers<sup>104–106</sup>, individual grains or grain boundaries<sup>105,107,108</sup> and thin films<sup>109,110</sup>.

## **2.5 Micro-contacts**

Micro-contacts can be used to extract local electrical properties. The geometric factor in Equation 2.16 is only applicable to electrodes that are the full surface area of a sample (e.g. a pellet sample). To find an equivalent geometric factor suitable for micro-contacts, first consider the simpler case of two hemi-spherical contacts, Figure 2.7.

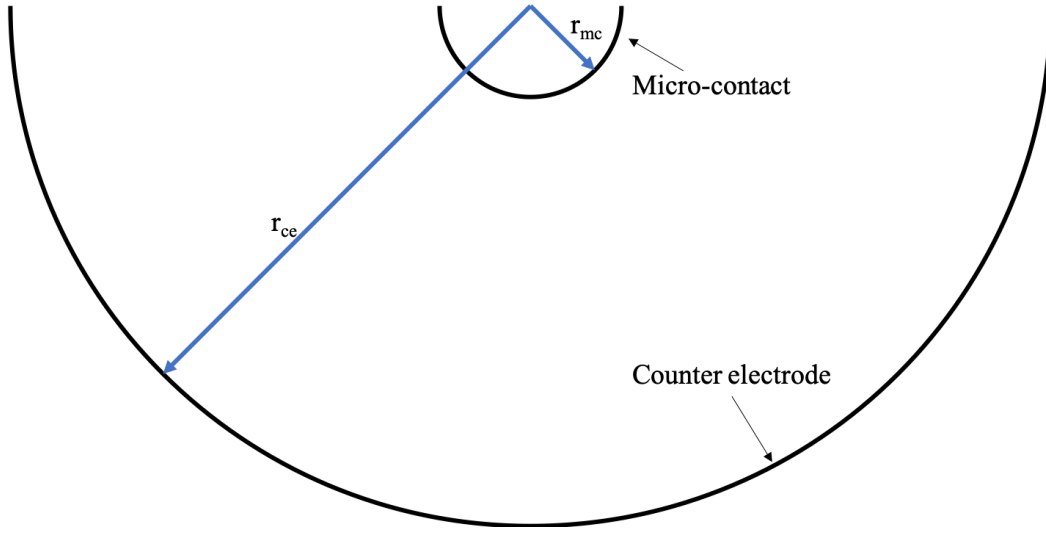


Figure 2.7. Schematic of a sample with two hemi-spherical contacts

The bulk resistance of the sample between the two contacts can be calculated by integrating the infinitesimal resistances of the hemi-spherical shells of radius  $dr$  between  $r_{mc}$  and  $r_{ce}$

$$R = \int_{r_{mc}}^{r_{ce}} \frac{1}{\sigma \cdot 2\pi r^2} dr \quad (2.17)$$

resulting in

$$R = \frac{1}{2\pi r_{mc} \sigma} \left(1 - \frac{r_{mc}}{r_{ce}}\right) \quad (2.18)$$

Considering the measured resistance of each hemi-spherical shell decreases as the separation increases (and surface area increases), the total spreading resistance associated with a single hemi-spherical micro-contact can be calculated in the limit  $r_{ce} \rightarrow \infty$ ,

$$R_{spr} = \frac{1}{2\pi r_{mc} \sigma} \quad (2.19)$$

The derivation for a flat circular micro-contact is more complex but arrives at<sup>11</sup>

$$R_{spr} = \frac{1}{4r_{mc} \sigma} \quad (2.20)$$

thus, the geometric factor for a micro-contact is

$$GF = \frac{1}{4r_{mc}} \quad (2.21)$$

An assumption in the use of this equation is that there are no highly resistive extrinsic regions that exist between the micro-contact and counter electrode that would block the current<sup>112</sup> and the size of the sample is much greater than the size of the micro-contact. From Equation 2.18 it is relatively simple to show the measured resistance drops by 75% at a distance that is equal to  $4r_{mc}$  (i.e. swap  $r_{ce}$  for  $4r_{mc}$ ). This means that 75% of the response originates from this same volume. Hence, micro-contact measurements provide a powerful tool for obtaining local conductivity measurements.

Measurements may also be taken between two micro-contacts, giving the advantage of being able to probe very specific regions of a sample. Because there are two micro-contacts the spreading resistance equation becomes

$$R_{spr} \approx \frac{1}{2r_{mc}\sigma} \quad (2.22)$$

as there is a spreading resistance associated with each micro-contact. A requirement of Equation 2.22 is that the separation between the micro-contacts is sufficiently large<sup>105</sup>,  $> 10r_{mc}$ .

An artefact in micro-contact Impedance Spectroscopy measurements is inductive loops<sup>113,114</sup>. This loop has been attributed to a capacitive coupling between the sample and conductive components in the experimental set-up; this could be the sample holder or heating stage for example. Increasing the distance between the sample and these components reduces the amount of inductance<sup>113</sup>.

Micro-contacts can be experimentally defined in two ways: by mechanically pressing a sharp probe directly into the surface of the sample<sup>101,115</sup>; or by patterning an array of metal contacts onto the surface of the sample which is then contacted by a probe under an optical microscope<sup>116,117</sup>. The first method has an advantage in that no further sample preparation is required, however the size of the contact is poorly defined. For this thesis, photolithographic patterning is the preferred technique as the size of the micro-contact is very well defined. It is possible to achieve micro-contacts that are smaller than 1  $\mu\text{m}$ ; however, these are very difficult to probe under an optical microscope (the smallest micro-contacts used in this thesis are 30  $\mu\text{m}$  in diameter). A section explaining how micro-contacts are prepared can be found in Chapter 3.

An issue with the experimental setup is that the sample is typically asymmetrically heated by means of a heating stage. This induces a temperature gradient across the sample. Further, local temperature gradients are produced by the contacting probe acting as a heat sink<sup>118</sup>. Because of this the exact sample temperature is unknown. Approximations have been made using the following equation<sup>118,119</sup>,

$$T_{spr} = \frac{E_a}{k_B \cdot \ln(\sigma_0 4r_{mc}R)} \quad (2.23)$$

where  $E_a$  is the activation energy of the bulk conductivity of the material and  $k_B$  is the Boltzmann constant. However, this temperature is only an average temperature in the contact region and gradients do exist, even across the contact<sup>118</sup>.

Fleig et al.<sup>107,120</sup> used FEM to study current flow between micro-contacts on adjacent grains. They showed that a large fraction of the current does not flow through the grain boundary of investigation, but through the neighbouring grain boundaries also, resulting in inaccuracies of calculated grain boundary conductivities. The location of the micro-contact within the grain is of minor importance<sup>107,120</sup>. The same studies highlighted how micro-contacts could be used to measure specific regions of a sample. Figure 2.8 shows the response from a grain boundary can be minimised when measurements are taken between two micro-contacts in the same grain.

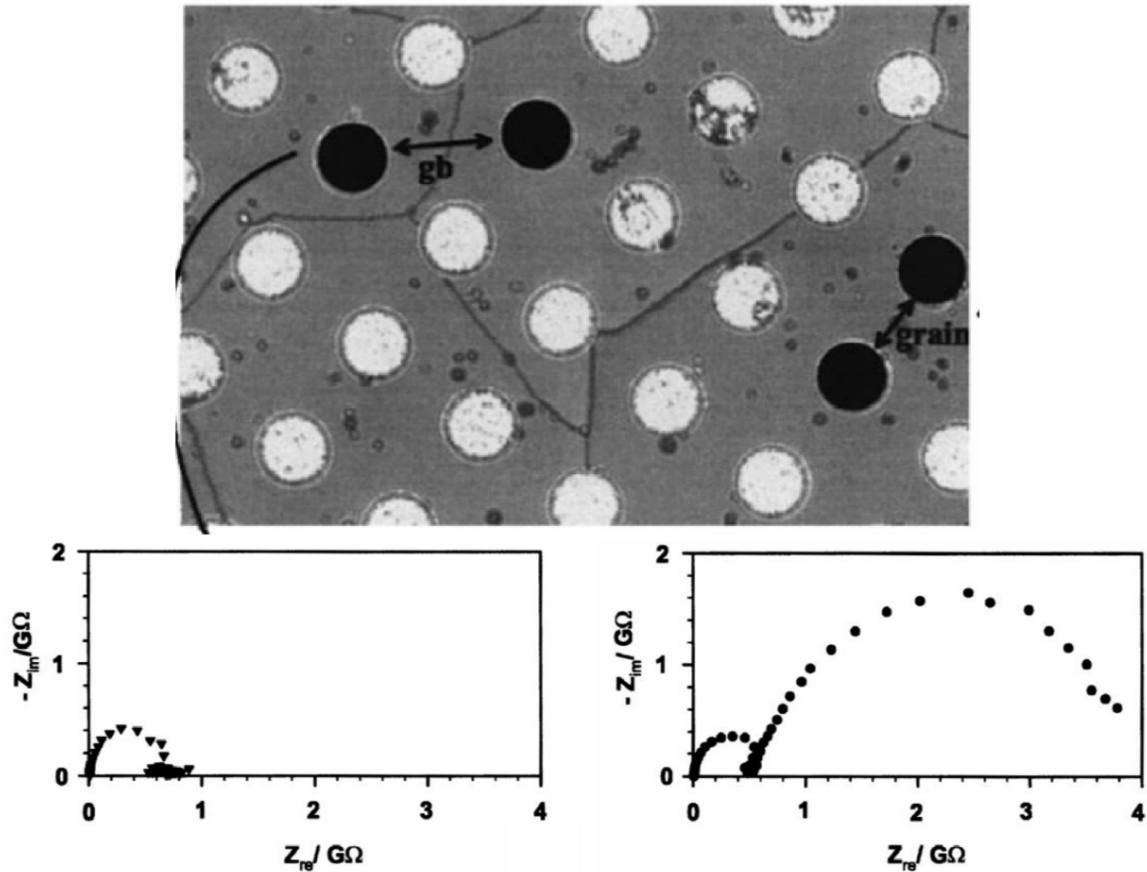


Figure 2.8. (top) Optical microscope image of a polycrystalline sample with 20  $\mu\text{m}$  micro-contacts, (left) impedance spectrum for two micro-contacts in the same grain, (right) impedance spectrum measured across a grain boundary. Reprinted Fig. 6. from Fleig et al.<sup>107</sup> with permission from Elsevier.

Rodewald et al.<sup>103</sup> found excellent agreement in the measured bulk conductivity between micro-contact measurements and the same sample measured by conventional Impedance

Spectroscopy. The main differences between the two measurements was a much larger electrode response and a much higher measured resistance, due to the smaller size of the contacts.

Fleig<sup>104</sup> used micro-contacts to determine the thickness and conductivity of mechanically-produced highly conducting surface layers. Using conventional Impedance Spectroscopy, it would be difficult to measure a conductive surface layer response. With micro-contacts, the measured spreading resistance from the bulk would be smaller with a conductive surface layer present as the current could flow over a larger area than the area defined by the micro-contact, see Figure 2.9.

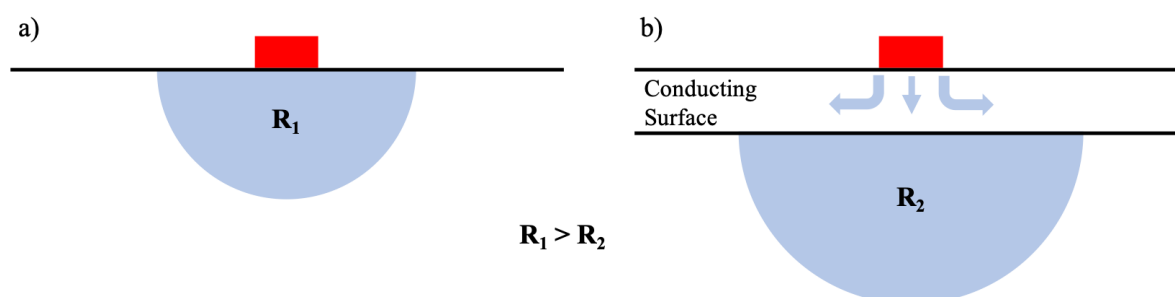


Figure 2.9. a) The 75% hemisphere associated with the spreading resistance of the bulk of a homogeneous sample. b) The 75% hemisphere associated with the spreading resistance of the bulk when there is a conductive surface.

From the measured resistance, an “effective diameter” could be compared to the actual micro-contact size and a surface layer thickness and conductivity could be obtained.

By measuring multiple micro-contacts, conductivity profiles of the sample can be determined<sup>102,103</sup>. Lee et al.<sup>102</sup> measured a conductivity profile that was related to the concentration of nitrogen in zirconia. Rodewald et al.<sup>103</sup> determined an interesting profile in Fe-doped SrTiO<sub>3</sub> after applying an electric field across the sample.

Wachter-Welzl et al.<sup>121</sup> measured the degradation of Li<sub>7</sub>La<sub>3</sub>Zr<sub>2</sub>O<sub>12</sub> after being left for 3 weeks in air. Measurements after 3 weeks showed an increase in the measured resistance for a range of different size micro-contacts. The increase in resistance was greatest for the smaller micro-contact sizes, providing evidence that the degradation was occurring at the surface. In the same study, conductivities obtained from micro-contact measurements were in disagreement with conventional measurements. These differences were attributed to compositional variations in the sample, that were highlighted by the micro-contact measurements, with more conductive regions occurring near the surface.

Rettenwander et al.<sup>122</sup> used micro-contact Impedance Spectroscopy to characterise single crystal Li<sub>1+x</sub>Al<sub>x</sub>Ti<sub>2-x</sub>(PO<sub>4</sub>)<sub>3</sub> embedded in epoxy and FEM to validate their analysis. They

simulated 10 different cases, varying the size and shape of the grain and the position of the micro-contacts within the grain, providing different levels of confinement. Their most confined model revealed inaccuracies of 27% in the calculated conductivity, which was sufficient to validate their experimental results. They noted that small contact separations decreased the measured resistance, whereas the limited size of a single crystal would enhance the resistance, when compared to the ideal formula (Equation 2.22).

## 2.6 Summary and Research Aim

This chapter has discussed the effects of radiation damage in general and then provided a brief summary of important work on SrTiO<sub>3</sub>. A summary of the electrical characterisation technique of micro-contact Impedance Spectroscopy has also been provided. Currently, these research fields are independent and as far as we are aware there is no literature using this technique to characterise radiation damage. Tolerance to radiation damage is usually described in terms of a materials composition or structure. Electrical characterisation could provide an alternative, more sensitive method to describe radiation damage tolerance.

The main research aim of this thesis is to provide a proof of concept for the use of micro-contact Impedance Spectroscopy to characterise radiation damaged surfaces in ceramics. We have used a combination of finite element modelling and experimental work in this study. Modelling was used to help interpret the experimental data obtained; however, the results from our models are applicable to any homogeneous material, such as single crystals (Chapter 4), and any material containing resistive surface layers, such as thin films (Chapter 5).

## 2.7 References

1. Lemanov, V. V, Sotnikov, A. V, Smirnova, E. P., Weihnacht, M. & Kunze, R. Perovskite CaTiO<sub>3</sub> as an incipient ferroelectric. *Solid State Commun.* **110**, 611–614 (1999).
2. West, A. R. *Solid State Chemistry*. (John Wiley & Sons Ltd, 2014).
3. Momma, K. & Izumi, F. VESTA 3 for three-dimensional visualization of crystal, volumetric and morphology data. *J. Appl. Crystallogr.* **44**, 1272–1276 (2011).
4. Goldschmidt, V. M. Die Gesetze der Krystallochemie. *Naturwissenschaften* 477–485 (1926).
5. Reaney, I. M. & Uvic, R. Dielectric and structural characteristics of perovskites and related materials as a function of tolerance factor. *Ferroelectrics* **228**, 23–38 (1999).
6. Meldrum, A., Boatner, L. A., Weber, W. J. & Ewing, R. C. Amorphization and

- recrystallization of the  $ABO_3$  oxides. *J. Nucl. Mater.* **300**, 242–254 (2002).
7. Shannon, R. D. Revised Effective Ionic Radii and Systematic Studies of Interatomic Distances in Halides and Chalcogenides. *Acta Cryst* **32**, 751–767 (1976).
  8. Neville, R. C., Hoeneisen, B. & Mead, C. A. Permittivity of Strontium Titanate. *J. Appl. Phys.* **43**, 2124–2131 (1972).
  9. Benthem, K. V., Elsässer, C. & French, R. H. Bulk electronic structure of  $SrTiO_3$ : Experiment and theory. *J. Appl. Phys.* **90**, 6156–6164 (2001).
  10. Choudhury, B. K., Rao, K. V & Choudhury, R. N. P. Dielectric properties of  $SrTiO_3$  single crystals subjected to high electric fields and later irradiated with X-rays or  $\gamma$ -rays. *J. Mater. Sci.* **24**, 3469–3474 (1989).
  11. Chan, N. H., Sharma, R. K. & Smyth, D. M. Nonstoichiometry in  $SrTiO_3$ . *Solid State Sci. Technol.* **128**, 1762–1769 (1981).
  12. De Souza, R. A., Metlenko, V., Park, D. & Weirich, T. E. Behavior of oxygen vacancies in single-crystal  $SrTiO_3$ : Equilibrium distribution and diffusion kinetics. *Phys. Rev. B - Condens. Matter Mater. Phys.* **85**, 1–11 (2012).
  13. De Souza, R. A. Oxygen Diffusion in  $SrTiO_3$  and Related Perovskite Oxides. *Adv. Funct. Mater.* **25**, 6326–6342 (2015).
  14. Kröger, F. A. & Vink, H. J. Relations between the Concentrations of Imperfections in Crystalline Solids. *Solid State Phys.* **3**, 307–435 (1956).
  15. Da Silva, L. F., M'Peko, J. C., Andres, J., Beltran, A., Gracia, L., Bernardi, M. I. B., Mesquita, A., Antonelli, E., Moreira, M. L. & Mastelaro, V. R. Insight into the effects of Fe addition on the local structure and electronic properties of  $SrTiO_3$ . *J. Phys. Chem. C* **118**, 4930–4940 (2014).
  16. Ghaffari, M., Shannon, M., Hui, H., Tan, O. K. & Irannejad, A. Preparation, surface state and band structure studies of  $SrTi_{(1-x)}Fe_{(x)}O_{(3-\delta)}$  ( $x=0-1$ ) perovskite-type nanostructure by X-ray and ultraviolet photoelectron spectroscopy. *Surf. Sci.* **606**, 670–677 (2012).
  17. Merkle, R. & Maier, J. How is oxygen incorporated into oxides? A comprehensive kinetic study of a simple solid-state reaction with  $SrTiO_3$  as a model material. *Angew. Chemie - Int. Ed.* **47**, 3874–3894 (2008).
  18. Walsh, A., Catlow, C. R. A., Smith, A. G. H., Sokol, A. A. & Woodley, S. M. Strontium

- migration assisted by oxygen vacancies in SrTiO<sub>3</sub> from classical and quantum mechanical simulations. *Phys. Rev. B - Condens. Matter Mater. Phys.* **83**, 1–4 (2011).
19. Steinsvik, S., Bugge, R., Gjønnes, J., Taftø, J. & Norby, T. The defect structure of SrTi<sub>1-x</sub>Fe<sub>x</sub>O<sub>3-y</sub> (x = 0-0.8) investigated by electrical conductivity measurements and electron energy loss spectroscopy (EELS). *J. Phys. Chem. Solids* **58**, 969–976 (1997).
  20. Rothschild, A., Menesklou, W., Tuller, H. L. & Ivers-Tiffée, E. Electronic structure, defect chemistry, and transport properties of SrTi<sub>1-x</sub>Fe<sub>x</sub>O<sub>3-y</sub> solid solutions. *Chem. Mater.* **18**, 3651–3659 (2006).
  21. Weber, W. J., Navrotsky, A., Stefanovsky, S., Vance, E. R. & Vernaz, E. Materials Science of High-Level Immobilization. *MRS Bull.* **34**, 46–53 (2009).
  22. Ewing, R. C., Weber, W. J. & Clinard, F. W. Radiation effects in nuclear waste forms for high-level radioactive waste. *Prog. Nucl. Energy* **29**, 63–127 (1995).
  23. Weber, W. J., Ewing, R. C., Catlow, C. R. A., de la Rubia, T. D., Hobbs, L. W., Kinoshita, C., Matzke, H. J., Motta, A. T., Nastasi, M., Salje, E. K. H., Vance, E. R. & Zinkle, S. J. Radiation Effects In Crystalline Ceramics For The Immobilization Of High-level Nuclear Waste And Plutonium. *J. Mater. Res.* **13**, 1434–1484 (1998).
  24. Weber, W. J. & Ewing, R. C. Radiation Effects in Crystalline Oxide Host Phases for the Immobilization of Actinides. *Mater. Res. Soc. Symp. Proc.* **713**, 1–8 (2002).
  25. Murakami, T., Chakoumakos, B. C., Ewing, R. C., Lumpkin, G. R. & Weber, W. J. Alpha-decay event damage in zircon. *Am. Mineral.* **76**, 1510–1532 (1991).
  26. Ewing, R. C., Weber, W. J. & Lian, J. Nuclear waste disposal-pyrochlore (A<sub>2</sub>B<sub>2</sub>O<sub>7</sub>): Nuclear waste form for the immobilization of plutonium and ‘minor’ actinides. *J. Appl. Phys.* **95**, 5949–5971 (2004).
  27. Was, G. S. *Fundamentals of Radiation Materials Science*. (Springer, 2007).
  28. Ziegler, J. F., Ziegler, M. D. & Biersack, J. P. SRIM - The stopping and range of ions in matter (2010). *Nucl. Instruments Methods Phys. Res. B* **268**, 1818–1823 (2010).
  29. Ewing, R. C. THE DESIGN AND EVALUATION OF NUCLEAR-WASTE FORMS : CLUES FROM MINERALOGY. *J. Mineral. Assoc. Canada* **39**, 697–715 (2001).
  30. Kinchin, G. H. & Pease, R. S. The Displacement of Atoms in Solids by Radiation. *Reports Prog. Phys.* **18**, 1–51 (1955).
  31. Gibbons, J. F. Ion implantation in semiconductors—Part II: Damage production and

- annealing. *Proc. IEEE* **60**, 1062–1096 (1972).
32. Norgett, M. I., Robinson, M. T. & Torrens, I. M. A Proposed Method of Calculating Displacement Dose Rates. *Nucl. Eng. Des.* **33**, 50–54 (1975).
  33. Zinkle, S. J. & Kinoshita, C. Defect production in ceramics. *J. Nucl. Mater.* **251**, 200–217 (1997).
  34. Thomas, B. S., Marks, N. A. & Begg, B. D. Defects and threshold displacement energies in SrTiO<sub>3</sub> perovskite using atomistic computer simulations. *Nucl. Instruments Methods Phys. Res. Sect. B* **254**, 211–218 (2007).
  35. Oyoshi, K., Hishita, S. & Haneda, H. Study of ion beam induced epitaxial crystallization of SrTiO<sub>3</sub>. *J. Appl. Phys.* **87**, 3450–3456 (2000).
  36. Zhang, Y., Wang, C. M., Engelhard, M. H. & Weber, W. J. Irradiation behavior of SrTiO<sub>3</sub> at temperatures close to the critical temperature for amorphization. *J. Appl. Phys.* **100**, 113533 (2006).
  37. Zhuo, M. J., Yan, L., Fu, E. G., Wang, Y. Q., Misra, A., Nastasi, M., Uberuaga, B. P. & Jia, Q. X. Phase transformations and defect clusters in single crystal SrTiO<sub>3</sub> irradiated at different temperatures. *J. Nucl. Mater.* **442**, 143–147 (2013).
  38. Thevuthasan, S., Jiang, W., Shutthanandan, V. & Weber, W. J. Accumulation of ion beam induced disorder in strontium titanate. *Nucl. Instruments Methods Phys. Res. Sect. B Beam Interact. with Mater. Atoms* **206**, 162–165 (2003).
  39. Won, J. *et al.* The role of non-stoichiometric defects in radiation damage evolution of SrTiO<sub>3</sub>. *J. Mat. Chem. A* **1**, 9235–9245 (2013).
  40. Zhang, J. *et al.* Helium irradiation induced micro-swelling and phase separation in pyrochlore Lu<sub>2</sub>Ti<sub>2</sub>O<sub>7</sub>. *Nucl. Instruments Methods Phys. Res. B* **342**, 179–183 (2015).
  41. Hobbs, L. W., Clinard, F. W., Zinkle, S. J. & Ewing, R. C. Radiation effects in ceramics. *J. Nucl. Mater.* **216**, 291–321 (1994).
  42. Nastasi, M. & Mayer, J. W. *Ion Implantation and Synthesis of Materials*. (Springer, 2006).
  43. Li, Y. H., Wang, Y. Q., Valdez, J. A., Tang, M. & Sickafus, K. E. Swelling effects in Y<sub>2</sub>Ti<sub>2</sub>O<sub>7</sub> pyrochlore irradiated with 400keV Ne<sup>2+</sup> ions. *Nucl. Instruments Methods Phys. Res. B* **274**, 182–187 (2012).
  44. Weber, W. J. Models and mechanisms of irradiation-induced amorphization in ceramics.

- Nucl. Instruments Methods Phys. Res. Sect. B Beam Interact. with Mater. Atoms* **166**, 98–106 (2000).
45. Weber, W. J. Alpha-Decay-Induced Amorphization in Complex Silicate Structures. *J. Am. Ceram. Soc.* **76**, 1729–1738 (1993).
  46. Weber, W. J., Ewing, R. C. & Wang, L. M. The radiation-induced crystalline-to-amorphous transition in zircon. *J. Mater. Res.* **9**, 688–698 (1994).
  47. Devanathan, R. Radiation damage evolution in ceramics. *Nucl. Instruments Methods Phys. Res. B* **267**, 3017–3021 (2009).
  48. Begg, B. D. *et al.* Heavy-ion irradiation effects on structures and acid dissolution of pyrochlores. *J. Nucl. Mater.* **288**, 208–216 (2001).
  49. Weber, W. J. & Ewing, R. C. Plutonium Immobilization and Radiation Effects. *Science*. **289**, 2051–2052 (2000).
  50. Trachenko, K. Understanding resistance to amorphization by radiation damage. *J. Phys. Condens. Matter* **16**, R1491–R1515 (2004).
  51. Sickafus, K. E., Grimes, R. W., Valdez, J. A., Cleave, A., Tang, M., Ishimaru, M., Corish, S. M., Stanek, C. R. & Uberuaga, B. P. Radiation-induced amorphization resistance and radiation tolerance in structurally related oxides. *Nat. Mater.* **6**, 217–223 (2007).
  52. Whittle, K. R., Blackford, M. G., Smith, K. L., Lumpkin, G. R. & Zaluzec, N. J. Radiation Tolerance and Disorder - Can They Be Linked? *Mater. Res. Soc. Symp. Proc.* **1215**, (2010).
  53. Lian, J. *et al.* Ion-irradiation-induced amorphization of  $\text{La}_2\text{Zr}_2\text{O}_7$  pyrochlore. *Phys. Rev. B* **66**, 054108 (2002).
  54. Smith, K. L., Lumpkin, G. R., Blackford, M. G., Colella, M. & Zaluzec, N. J. In situ radiation damage studies of  $\text{La}_x\text{Sr}_{1-3x/2}\text{TiO}_3$  perovskites. *J. Appl. Phys.* **103**, 08351 (2008).
  55. Taylor, C. A., Patel, M. K., Aguiar, J. A., Zhang, Y., Crespillo, M. L., Wen, J., Xue, H., Wang, Y. & Weber, W. J. Bubble formation and lattice parameter changes resulting from He irradiation of defect-fluorite  $\text{Gd}_2\text{Zr}_2\text{O}_7$ . *Acta Mater.* **115**, 115–122 (2016).
  56. Zhang, Y., Weber, W. J., Shutthanandan, V. & Thevuthasan, S. Non-linear damage accumulation in Au-irradiated  $\text{SrTiO}_3$ . *Nucl. Instruments Methods Phys. Res. Sect. B*

- Beam Interact. with Mater. Atoms* **251**, 127–132 (2006).
57. Was, G. S., Jiao, Z., Getto, E., Sun, K., Monterrosa, A. M., Maloy, S. A., Anderoglu, O., Sencer, B. H. & Hackett, M. Emulation of reactor irradiation damage using ion beams. *Scr. Mater.* **88**, 33–36 (2014).
  58. Park, S., Lang, M., Tracy, C. L., Zhang, J., Zhang, F., Trautmann, C., Kluth, P., Rodriguez, M. D. & Ewing, R. C. Swift heavy ion irradiation-induced amorphization of  $\text{La}_2\text{Ti}_2\text{O}_7$ . *Nucl. Instruments Methods Phys. Res. Sect. B Beam Interact. with Mater. Atoms* **326**, 145–149 (2014).
  59. Lang, M., Zhang, F., Li, W., Severin, D., Bender, M., Klaumünzer, S., Trautmann, C. & Ewing, R. C. Swift heavy ion-induced amorphization of  $\text{CaZrO}_3$  perovskite. *Nucl. Instruments Methods Phys. Res. Sect. B Beam Interact. with Mater. Atoms* **286**, 271–276 (2012).
  60. Meldrum, A., Zinkle, S. J., Boatner, L. A. & Ewing, R. C. Heavy-ion irradiation effects in the  $\text{ABO}_4$  orthosilicates : Decomposition , amorphization , and recrystallization. *Phys. Rev. B* **59**, 3981–3992 (1999).
  61. Beaufort, M. F., Pizzagalli, L., Gandy, A. S., Oliviero, E., Eyidi, D. & Donnelly, S. E. Solid-phase epitaxial regrowth of amorphous silicon containing helium bubbles. *J. Appl. Phys.* **104**, 094905 (2008).
  62. Gandy, A. S., Donnelly, S. E., Beaufort, M. F., Oliviero, E. & Fichtner, P. F. P. The interaction of cavities in silicon with moving amorphous-crystalline interfaces. *Nucl. Instruments Methods Phys. Res. Sect. B* **257**, 177–180 (2007).
  63. Cullis, A. G., Seidel, T. E. & Meek, R. L. Comparative study of annealed neon-, argon, and krypton-ion implantation damage in silicon. *J. Appl. Phys.* **49**, 5188–5198 (1978).
  64. Aughterson, R. D., Lumpkin, G. R., Ionescu, M., Reyes, M. D. L., Gault, B., Whittle, K. R., Smith, K. L. & Cairney, J. M. Ion-irradiation resistance of the orthorhombic  $\text{Ln}_2\text{TiO}_5$  ( $\text{Ln} = \text{La, Pr, Nd, Sm, Eu, Gd, Tb and Dy}$ ) series. *J. Nucl. Mater.* **467**, 683–691 (2015).
  65. Smith, W. Effect of light on selenium during the passage of an electric current. *Nature* **7**, 303 (1873).
  66. Zinkle, S. J. & Hodgson, E. R. Radiation-induced changes in the physical properties of ceramic materials. *J. Nucl. Mater.* **191–194**, 58–66 (1992).

67. Hodgson, E. R. & Clement, S. Dose rate dependence of the radiation-induced electrical conductivity in MgO. *J. Nucl. Mater.* **155–157**, 357–360 (1988).
68. Hodgson, E. R. General radiation problems for insulating materials in future fusion devices. *J. Nucl. Mater.* **258–263**, 226–233 (1998).
69. Snead, L. L. Limits on irradiation-induced thermal conductivity and electrical resistivity in silicon carbide materials. *J. Nucl. Mater.* **329–333**, 524–529 (2004).
70. Hodgson, E. R. Challenges for insulating materials in fusion applications. *Nucl. Instruments Methods Phys. Res. Sect. B Beam Interact. with Mater. Atoms* **191**, 744–751 (2002).
71. Hunn, J. D., Stoller, R. E. & Zinkle, S. J. In-situ measurement of radiation-induced conductivity of thin film ceramics. *J. Nucl. Mater.* **219**, 169–175 (1995).
72. Pearton, S. J., Deist, R., Ren, F., Liu, L., Polyakov, A. Y. & Kim, J. Review of radiation damage in GaN-based materials and devices. *J. Vac. Sci. Technol. A Vacuum, Surfaces, Film.* **31**, 050801 (2013).
73. Pearton, S. J., Ren, F., Patrick, E., Law, M. E. & Polyakov, A. Y. Review—Ionizing Radiation Damage Effects on GaN Devices. *ECS J. Solid State Sci. Technol.* **5**, Q35–Q60 (2016).
74. Dana, S. S., Batey, J., Maldonado, J. R., Vladimirsky, O., Fair, R. & Viswanathan, R. ELECTRICAL RESISTIVITY AND RADIATION DAMAGE IN BORO-HYDRO-NITRIDE X-RAY LITHOGRAPHY MASK SUBSTRATES. *Microelectron. Eng.* **6**, 233–240 (1987).
75. Bridwell, L. B., Giedd, R. E., Wang, Y. Q., Mohite, S. S., Jahnke, T., Brown, I. M., Bedell, C. J. & Sofield, C. J. Ion implantation of polymers for electrical conductivity enhancement. *Nucl. Inst. Methods Phys. Res. B* **56–57**, 656–659 (1991).
76. Goyal, P. K., Kumar, V., Gupta, R., Mahendia, S., Sharma, T. & Kumar, S. Change in the Electrical Conductivity of N<sup>+</sup> Ion Implanted Polycarbonate. *Adv. Appl. Sci. Res.* **2**, 227–231 (2011).
77. Martin, P., Dufour, M., Ermolieff, A., Marthon, S., Pierre, F. & Dupuy, M. Electrical surface conductivity in quartz induced by ion implantation. *J. Appl. Phys.* **72**, 2907–2911 (1992).
78. Kobayashi, T. & Terai, T. Electrical property of high-fluence metal ion implanted

- sapphire and its thermal annealing effects. *Nucl. Instruments Methods Phys. Res. Sect. B Beam Interact. with Mater. Atoms* **141**, 441–445 (1998).
79. Reagor, D. W. & Butko, V. Y. Highly conductive nanolayers on strontium titanate produced by preferential ion-beam etching. *Nat. Mater.* **4**, 593–596 (2005).
  80. Cooper, C. M., Nayar, P. S., Hale, E. B. & Gerson, R. Conductive strontium titanate layers produced by boron-ion implantation. *J. Appl. Phys.* **50**, 2826–2831 (1979).
  81. Fernandes, S., Pellemoine, F., Tomut, M., Avilov, M., Bender, M., Boulesteix, M., Krause, M., Mittig, W., Schein, M., Severin, D. & Trautmann, C. In-situ electric resistance measurements and annealing effects of graphite exposed to swift heavy ions. *Nucl. Instruments Methods Phys. Res. Sect. B Beam Interact. with Mater. Atoms* **314**, 125–129 (2013).
  82. Hubert, C., Voss, K. O., Bender, M., Kupka, K., Romanenko, A., Severin, D., Trautmann, C. & Tomut, M. Swift heavy ion-induced radiation damage in isotropic graphite studied by micro-indentation and in-situ electrical resistivity. *Nucl. Instruments Methods Phys. Res. Sect. B Beam Interact. with Mater. Atoms* **365**, 509–514 (2015).
  83. White, C. W., Boatner, L. A., Rankin, J. & Aziz, M. J. Ion Implantation and Annealing of SrTiO<sub>3</sub> and CaTiO<sub>3</sub>. *Mater. Res. Soc. Symp. Proc.* **93**, 9–14 (1987).
  84. White, C. W., Boatner, L. A., Sklad, P. S., Mchargue, C. J., Rankin, J., Farlow, G. C. & Aziz, M. J. Ion Implantation and Annealing of Crystalline Oxides and Ceramic Materials. *Nucl. Inst. Methods Phys. Res. B* **32**, 11–22 (1988).
  85. Meldrum, A., Boatner, L. A. & Ewing, R. C. Effects of ionizing and displacive irradiation on several perovskite structure oxides. *Nucl. Instruments Methods Phys. Res. Sect. B Beam Interact. with Mater. Atoms* **141**, 347–352 (1998).
  86. Thevuthasan, S., Jiang, W., Shutthanandan, V. & Weber, W. J. Accumulation and thermal recovery of disorder in Au<sup>2+</sup>-irradiated SrTiO<sub>3</sub>. *J. Nucl. Mater.* **289**, 204–209 (2001).
  87. Zhang, Y., Lian, J., Wang, C. M., Jiang, W., Ewing, R. C. & Weber, W. J. Ion-induced damage accumulation and electron-beam-enhanced recrystallization in SrTiO<sub>3</sub>. *Phys. Rev. B - Condens. Matter Mater. Phys.* **72**, 1–8 (2005).
  88. Wang, C. M., Shutthanandan, V., Zhang, Y., Thomas, L. E., Baer, D. R. & Thevuthasan, S. Precipitation of Au nanoclusters in SrTiO<sub>3</sub> by ion implantation. *J. Appl. Phys.* **95**, 5060–5068 (2004).

89. Wang, C. M., Shutthanandan, V., Zhang, Y., Thevuthasan, S. & Duscher, G. Direct observation of substitutional Au atoms in SrTiO<sub>3</sub>. *Phys. Rev. B - Condens. Matter Mater. Phys.* **70**, 1–4 (2004).
90. Sabathier, C., Chaumont, J., Rouzière, S. & Traverse, A. Characterisation of Ti and Sr atomic environments in SrTiO<sub>3</sub> before and after ion beam irradiation by X-ray absorption spectroscopy. *Nucl. Instruments Methods Phys. Res. Sect. B* **234**, 509–519 (2005).
91. Zhang, Y., Lian, J., Zhu, Z., Bennett, W. D., Saraf, L. V., Rausch, J. L., Hendricks, C. A., Ewing, R. C. & Weber, W. J. Response of strontium titanate to ion and electron irradiation. *J. Nucl. Mater.* **389**, 303–310 (2009).
92. Li, W., Rodriguez, M. D., Kluth, P., Lang, M., Medvedev, N., Sorokin, M., Zhang, J., Afra, B., Bender, M., Severin, D., Trautmann, C. & Ewing, R. C. Effect of doping on the radiation response of conductive Nb-SrTiO<sub>3</sub>. *Nucl. Inst. Methods Phys. Res. B* **302**, 40–47 (2013).
93. Cole, K. S. & Cole, R. H. Dispersion and absorption in dielectrics I. Alternating current characteristics. *J. Chem. Phys.* **9**, 341–351 (1941).
94. Bauerle, J. E. Study of solid electrolyte by a complex admittance. *J. Phys. Chem. Solids* **30**, 2657–2670 (1969).
95. Beekmans, N. M. & Heyne, L. Correlation Between Impedance, Microstructure and Composition of Calcia-Stabilized Zirconia. *Electrochim. Acta* **21**, 303–310 (1976).
96. Kidner, N. J., Perry, N. H., Mason, T. O. & Garboczi, E. J. The brick layer model revisited: Introducing the nano-grain composite model. *J. Am. Ceram. Soc.* **91**, 1733–1746 (2008).
97. Fleig, J. & Maier, J. A Finite Element Study on the Grain Boundary Impedance of Different Microstructures. *J. Electrochem. Soc.* **145**, 2081 (1998).
98. Fleig, J. Impedance spectroscopy on solids: The limits of serial equivalent circuit models. *J. Electroceramics* **13**, 637–644 (2004).
99. Heath, J. P., Dean, J. S., Harding, J. H. & Sinclair, D. C. Simulation of Impedance Spectra for Core-Shell Grain Structures Using Finite Element Modeling. *J. Am. Ceram. Soc.* **98**, 1925–1931 (2015).
100. Dean, J. S., Harding, J. H. & Sinclair, D. C. Simulation of Impedance Spectra for a Full

- Three-Dimensional Ceramic Microstructure Using a Finite Element Model. *J. Am. Ceram. Soc.* **97**, 885–891 (2014).
101. Fleig, J. & Maier, J. Point contacts in solid state ionics: Finite element calculations and local conductivity measurements. *Solid State Ionics* **86–88**, 1351–1356 (1996).
  102. Lee, J. S., Fleig, J., Maier, J., Kim, D. Y. & Chung, T. J. Local conductivity of nitrogen-graded zirconia. *J. Am. Ceram. Soc.* **88**, 3067–3074 (2005).
  103. Rodewald, S., Fleig, J. & Maier, J. Measurement of conductivity profiles in acceptor-doped strontium titanate. *J. Eur. Ceram. Soc.* **19**, 797–801 (1999).
  104. Fleig, J. Local conductivity measurements on AgCl surfaces using microelectrodes. *Solid State Ionics* **85**, 9–15 (1996).
  105. Fleig, J. Microelectrodes in solid state ionics. *Solid State Ionics* **161**, 279–289 (2003).
  106. Rupp, G. M., Opitz, A. K., Nenning, A., Limbeck, A. & Fleig, J. Real-time impedance monitoring of oxygen reduction during surface modification of thin film cathodes. *Nat. Mater.* **16**, 640–645 (2017).
  107. Fleig, J., Rodewald, S. & Maier, J. Spatially resolved measurements of highly conductive and highly resistive grain boundaries using microcontact impedance spectroscopy. *Solid State Ionics* **136–137**, 905–911 (2000).
  108. Fleig, J. & Maier, J. Microcontact impedance measurements of individual highly conductive grain boundaries: General aspects and application to AgCl. *Phys. Chem. Chem. Phys.* **1**, 3315–3320 (1999).
  109. Kubicek, M., Taibl, S., Navickas, E., Hutter, E., Fafilek, G. & Fleig, J. Resistive states in strontium titanate thin films: Bias effects and mechanisms at high and low temperature. *J. Electroceramics* **39**, 197–209 (2017).
  110. Navickas, E., Gerstl, M., Friedbacher, G., Kubel, F. & Fleig, J. Measurement of the across-plane conductivity of YSZ thin films on silicon. *Solid State Ionics* **211**, 58–64 (2012).
  111. Holm, R. *Electric Contacts*. (Springer, 1967).
  112. Fleig, J. in *Advances in Electrochemical Science and Engineering* (ed. Alkire, R. C.) **8**, 1–79 (Wiley-VCH, 2002).
  113. Fleig, J., Jamnik, J., Maier, J. & Ludvig, J. Inductive Loops in Impedance Spectroscopy Caused by Electrical Shielding. *J. Electrochem. Soc.* **143**, 3636–3641 (1996).

114. Taibl, S., Fafilek, G. & Fleig, J. Impedance spectra of Fe-doped SrTiO<sub>3</sub> thin films upon bias voltage: Inductive loops as a trace of ion motion. *Nanoscale* **8**, 13954–13966 (2016).
115. Lauret, H. & Hammou, A. Localization of oxygen cathodic reduction zone at lanthanum manganite/zirconia interface. *J. Eur. Ceram. Soc.* **16**, 447–451 (1996).
116. Lee, J. S., Fleig, J., Maier, J., Chung, T. J. & Kim, D. Y. Microcontact impedance spectroscopy in nitrogen-graded zirconia. *Solid State Ionics* **176**, 1711–1716 (2005).
117. Rodewald, S., Fleig, J. & Maier, J. Microcontact Impedance Spectroscopy at Single Grain Boundaries in Fe-Doped SrTiO<sub>3</sub> Polycrystals. *J. Am. Ceram. Soc.* **84**, 521–530 (2001).
118. Huber, T. M., Opitz, A. K., Kubicek, M., Hutter, H. & Fleig, J. Temperature gradients in microelectrode measurements: Relevance and solutions for studies of SOFC electrode materials. *Solid State Ionics* **268**, 82–93 (2014).
119. Opitz, A. K. & Fleig, J. Investigation of O<sub>2</sub> reduction on Pt/YSZ by means of thin film microelectrodes: The geometry dependence of the electrode impedance. *Solid State Ionics* **181**, 684–693 (2010).
120. Fleig, J., Rodewald, S. & Maier, J. Microcontact impedance measurements of individual highly resistive grain boundaries: General aspects and application to acceptor-doped SrTiO<sub>3</sub>. *J. Appl. Phys.* **87**, 2372 (2000).
121. Wachter-Welzl, A., Wagner, R., Rettenwander, D., Taibl, S., Amthauer, G. & Fleig, J. Microelectrodes for local conductivity and degradation measurements on Al stabilized Li<sub>7</sub>La<sub>3</sub>Zr<sub>2</sub>O<sub>12</sub> garnets. *J. Electroceramics* 1–6 (2016). doi:10.1007/s10832-016-0058-6
122. Rettenwander, D., Welzl, A., Pristat, S., Tietz, F., Taibl, S., Redhammer, G. J. & Fleig, J. A microcontact impedance study on NASICON-type Li<sub>1+x</sub>Al<sub>x</sub>Ti<sub>2-x</sub>(PO<sub>4</sub>)<sub>3</sub> (0 ≤ x ≤ 0.5) single crystals. *J. Mater. Chem. A* **4**, 1506–1513 (2016).

## Chapter 3: Experimental Methods

### 3.1 Impedance Spectroscopy

Impedance Spectroscopy is the main characterisation technique in this thesis, so a detailed discussion of the theory is presented here.

#### 3.1.1 Impedance Spectroscopy Theory

Impedance Spectroscopy is a versatile technique for characterising the electrical properties of a wide range of materials<sup>1</sup>. Typically, it is used to obtain resistance and capacitance values for different regions of a sample, as a function of temperature. In Impedance Spectroscopy an ac voltage is applied across a sample. First, we will consider a dc measurement.

When a dc voltage ( $f = 0$  Hz) is applied across a sample, the resistance,  $R$ , of the sample can usually be calculated using Ohms law,

$$R = \frac{V}{I} \quad (3.1)$$

where  $V$  is the applied voltage and  $I$  is the measured current. The resistance determined is the *total* resistance of the sample. From this measurement, it cannot be determined what regions of the sample (such as grains, grain boundaries, secondary phases etc.) are contributing to the resistance. In fact, some measurements may be dominated by electrode effects meaning the resistance measurement isn't reflective of the sample itself and is more representative of the sample-electrode interface.

Impedance is the ac analogue of resistance. Typically, as the frequency of an applied voltage increases, the impedance,  $Z$ , of a sample decreases. The ac analogue of Ohms law is given by,

$$Z^* = \frac{V(t)}{I(t)} = \frac{V_{max} \cdot \sin(\omega t)}{I_{max} \cdot \sin(\omega t + \theta)} \quad (3.2)$$

where  $V_{max}$  is the magnitude of the applied voltage,  $I_{max}$  is the magnitude of the measured current,  $\omega$  is the angular frequency and is equal to  $2\pi f$  (where  $f$  is the radial frequency in Hz),  $t$  is the time and  $\theta$  is the phase difference between the applied voltage and measured current. The difference between Equation 3.2 and Ohms law (Equation 3.1) is the incorporation of the phase difference between the measured current and the applied voltage<sup>2</sup>. The phase difference is dependent on the material properties. Perfect resistors obey Ohms law and there is no phase difference between the measured current and applied voltage ( $\theta = 0^\circ$ ). In a pure capacitor, the

current leads the voltage by  $\theta = 90^\circ$  and in a pure inductor, the current lags the voltage by  $\theta = -90^\circ$ . The impedance of each of these components is given by

$$Z_R^* = R \quad (3.3)$$

$$Z_C^* = -\frac{j}{\omega C} \quad (3.4)$$

$$Z_L^* = j\omega L \quad (3.5)$$

where  $j = \sqrt{-1}$ . From this it can be seen that for a resistor, the impedance is frequency independent and remains constant; for a capacitor impedance decreases with increasing frequency; and for an inductor the impedance increases with increasing frequency. In reality, most materials are a combination of resistive, capacitive and inductive components. Materials concerned with this thesis generally can be described by a combination of resistors and capacitors, so we will not discuss inductors further here. However, as was seen in Chapter 2, inductances can significantly affect impedance measurements, specifically when making micro-contact measurements. This will be discussed further in the relevant chapter(s). Impedance data are generally analysed using a complex impedance ( $Z^*$ ) plot, also referred to as a Nyquist plot, as shown in Figure 3.1. It is therefore beneficial to define impedance in its complex cartesian co-ordinates also,

$$Z^* = Z' - jZ'' \quad (3.6)$$

where  $Z'$  and  $Z''$  are the real and imaginary components of impedance, respectively.

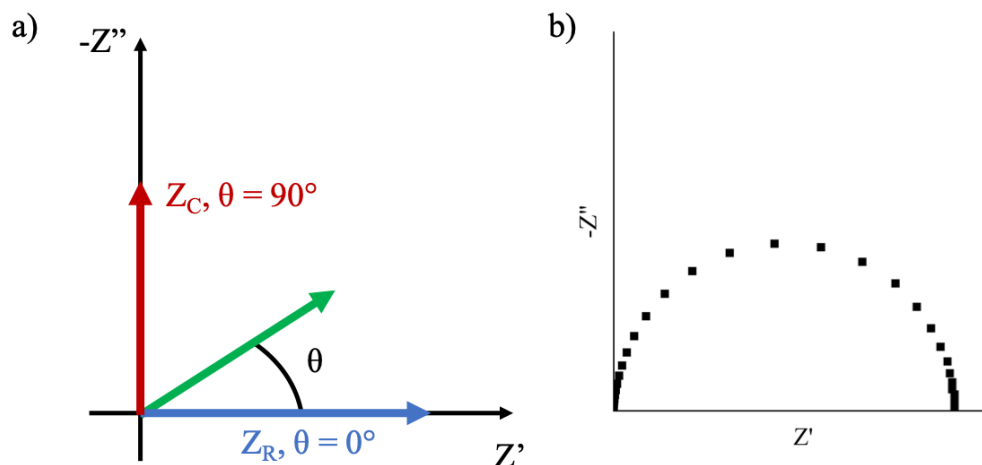


Figure 3.1. a) Impedance measurements represented as vectors on a Nyquist plot and b) as discrete data points at selected frequencies on a Nyquist plot.

Individual impedance measurements of a single frequency can be represented by a vector on a  $Z^*$  plot. As the phase difference for a pure resistor is  $0^\circ$ , the measurement of impedance is always on the real axis, blue arrow in Figure 3.1 (a). For a capacitor, the phase difference is  $+90^\circ$  so is always on the imaginary axis, red arrow in Figure 3.1 (a). (For an inductor,  $\theta = -90^\circ$  so is on the imaginary axis but below the real axis). Real materials have a phase difference between the applied voltage and measured current of  $0^\circ < \theta < 90^\circ$ , i.e. they have both resistive and capacitive components meaning they have real and imaginary components, respectively, green arrow in Figure 3.1 (a). By repeating measurements over a range of frequencies, a Nyquist or  $Z^*$  plot can be constructed, Figure 3.1 (b). However, this is only one of many ways that impedance data can be presented. There are four immittance formalisms that can be used to plot data and these are all interrelated. For example, the complex electric modulus ( $M^*$ ) is related to  $Z^*$  via the relationship  $M^* = j\omega Z^*$ . For the majority of this thesis, spectroscopic plots of the imaginary components of  $Z^*$  (i.e.  $Z''$ ) and the electric modulus,  $M^*$ , (i.e.  $M''$ ) are preferred, as shown in Figure 3.2. Also shown in the inset is an equivalent circuit (described in Section 3.1.4) that is typically used to model impedance spectroscopy data.

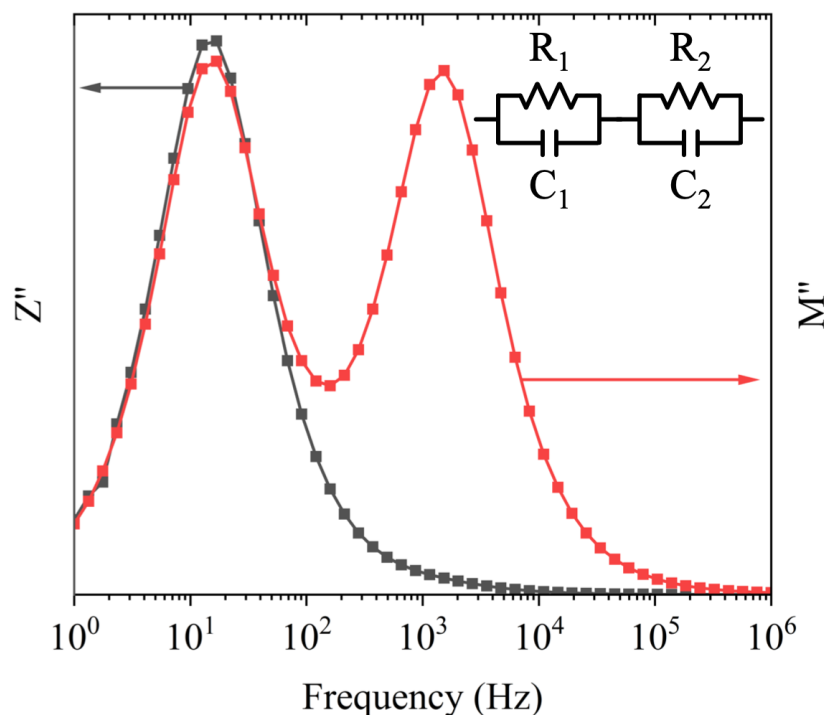


Figure 3.2. Overlaid  $Z''$  and  $M''$  spectroscopic plot. An equivalent circuit that is typically used to model impedance spectroscopy data is shown in the inset.

It can be seen how important it is to view impedance data in different formalisms, as information can be missed if only one formalism is used. In Figure 3.2 there are clearly two

components in the  $M''$  spectrum, however, if the data was only viewed in the  $Z''$  spectrum, only the response of the lower frequency component would be evident.

### 3.1.2 Simulating Impedance Spectroscopy by Finite Element Modelling

In this thesis, an in-house developed code, called EICer<sup>3</sup> (Electro-Ceramics), that solves Maxwell's equations<sup>4</sup> in space and time has been employed to simulate the electrical response of various electrical microstructures and/or electrode contact geometries. A detailed description of how this is achieved is available in Dean et al<sup>3</sup>, and other examples of the code being utilised<sup>5-8</sup> for various electrical microstructures.

Firstly, a 3D micro-structure is generated. A series of points define lines and then in turn define surfaces and volumes. These distinct regions are then meshed with tetrahedral elements using open-source software Gmsh<sup>9</sup>. An extra volume representing a pure resistor is then added to the top surface as a 'reference layer', which is used to interrogate the current from the applied voltage. The different volumes are each assigned a unique conductivity and relative permittivity. Boundary conditions are then assigned over the model which consist of; a Dirichlet boundary condition used to set the electric potential to known applied voltages where the electrodes are defined; a Neumann boundary condition used to set the current density to zero at the remaining surfaces that are not defined as electrodes, confining the current density to the model; and an internal boundary condition that allows current to flow between individual elements within the model.

After the model is constructed, EICer is then used to interrogate the impedance response of the model over a defined frequency range. As the materials defined in the micro-structure have conductivity and permittivity values, the current flowing through the electrode will be frequency dependent. For each time step, the difference in phase between the measured current integrated over the reference layer, and the applied voltage can be calculated and, combined with the ratio of the magnitudes, used to find the impedance. This process is repeated over the frequency range defined and an impedance spectrum can then be constructed. Using EICer it is also possible to obtain a steady state simulation of the dc response (single frequency at 0 Hz) which provides a single current measurement.

### 3.1.3 Model Optimisation

The majority of the work in this thesis simulates the effect of the electrical microstructure and impedance spectra from the use of micro-contacts. When simulating micro-contact measurements, it has been shown that 75% of the current density originates from a volume that is approximately four times the micro-contact radius<sup>10</sup>. Because of this, it is important that the

mesh size is small in the vicinity near the local contact to ensure the solution is mesh-independent. By optimising this region, it allows the rest of the model to be meshed coarser. Attractors are a tool in Gmsh that allow this localised meshing and a 2D representation of how they work is shown in Figure 3.3.

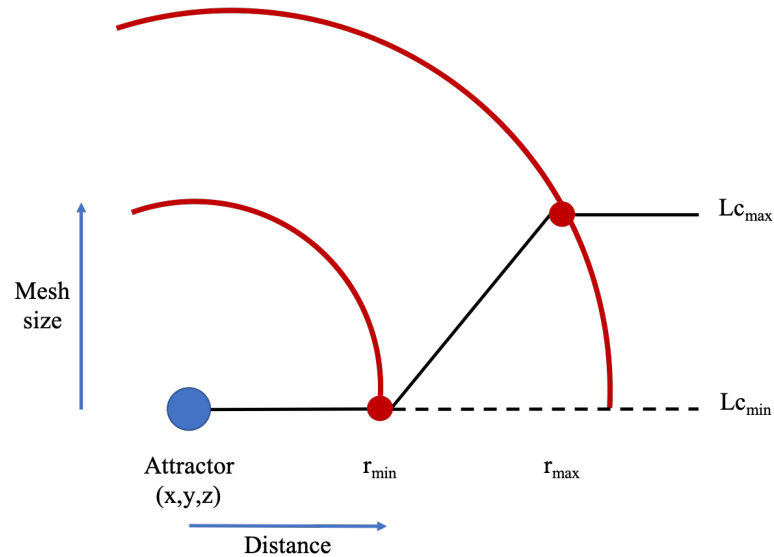


Figure 3.3. 2D representation of how attractors work in Gmsh.

An attractor is defined as a point in the model, which can be anywhere but in this case is the centre of a micro-contact. A characteristic length ( $L_{c_{min}}$ ) is defined up to a certain radius ( $r_{min}$ ) where the mesh takes this size between the attractor and that radius, in 3 dimensions. A second characteristic length ( $L_{c_{max}}$ ) and radius ( $r_{max}$ ) is defined, where past this radius the mesh takes this larger mesh size. Between the two defined radii, the mesh slowly increases in size from  $L_{c_{min}}$  to  $L_{c_{max}}$ . Attractors can also be applied to lines in a similar way. An example of the meshing using an attractor around a micro-contact is shown in Figure 3.4. The different colours in Figure 3.4 represent the boundary conditions described previously (red – Dirichlet, light blue – Neumann, dark blue – internal).

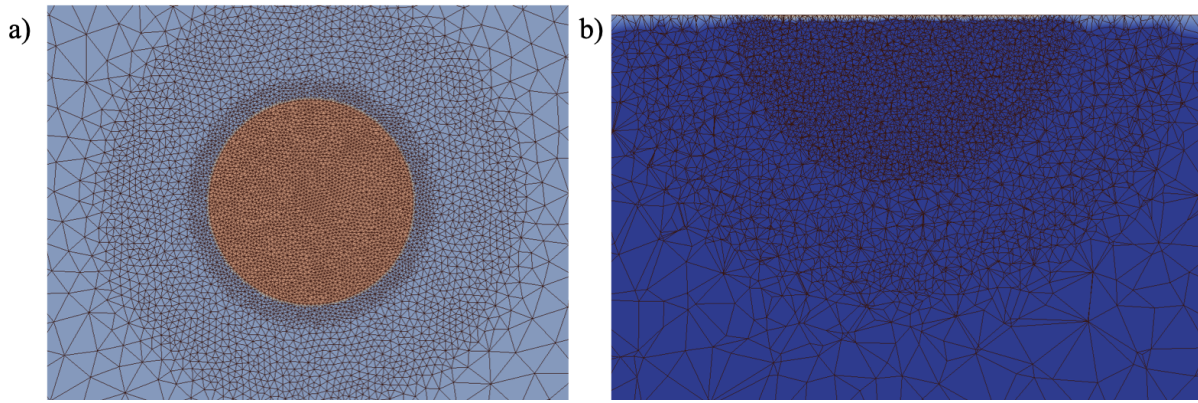


Figure 3.4. a) A top view of the surface and b) cross-section of a model with a micro-contact and the mesh overlaid where the mesh has been generated using attractors at the centre of the micro-contact.

In order to find a suitable mesh for the micro-structures and geometries studied, convergence studies were performed. Examples of the convergence studies are shown in Figure 3.5.

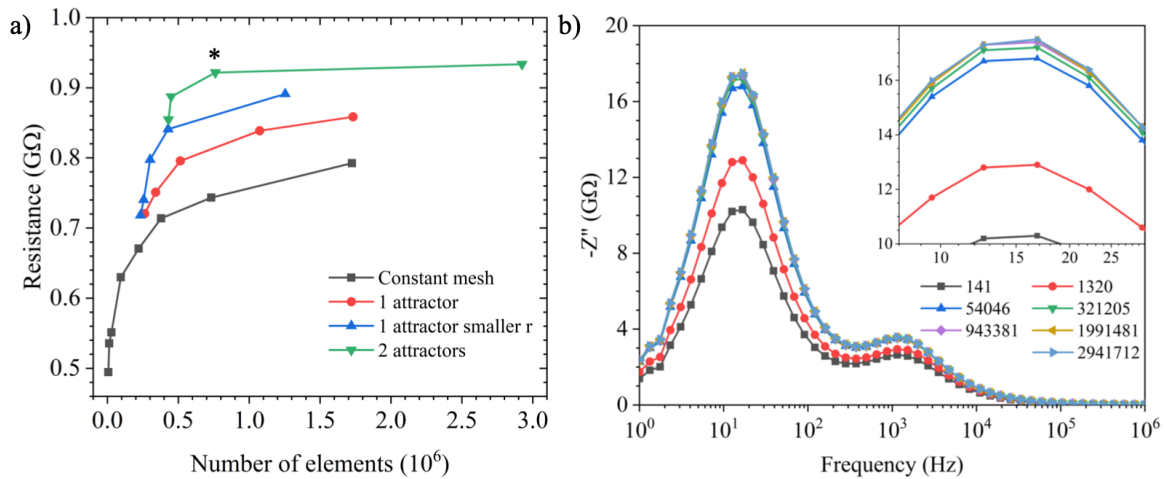


Figure 3.5. Convergence studies for a) a single material and b) a two layer material (legend specifies the number of elements in the model). The lines between data points in a) are to be used as a guide and are not fits to the data points. The inset in (b) shows an expanded scale for the larger  $Z''$  peak in the spectrum.

For the micro-structures involving a single material, the dc response was simulated, and the calculated resistance compared for models with a varying number of elements. Using a constant mesh shows that significant increases in the calculated resistance are occurring with an increasing number of elements, even after 1.5 million elements meaning the model is some way off convergence, black squares in Figure 3.5 (a). By introducing a single attractor, red circles in Figure 3.5 (a), helps the resistance value converge quicker and decreasing  $r_{\min}$  and  $r_{\max}$  also helps as a smaller mesh size can be used for a similar number of elements, blue up triangles in Figure 3.5 (a). By introducing a second attractor (i.e. attractor at same point but second set of  $L_c$  and  $r$ ) allows the resistance values to converge even faster, green down

triangles in Figure 3.5 (a). The increase in accuracy for the final point is small compared to the number of extra elements required, so the previous data point (labelled by \*) was taken for subsequent models.

For models with two materials, a dc measurement is not sufficient as an increase in resistance may be the result of an increase in accuracy for one region but not the other. Instead convergence studies were implemented by comparing the simulated impedance response. Convergence is obtained if insignificant differences in the response arise from significant differences in the number of elements in the model. In Figure 3.5 (b) the converged value was chosen as the yellow left triangle plot as the next model with ~ 1 million more elements made little change to the response. Once a model has been chosen as the converged value, it is more important to remain consistent with all following models to observe the trends, as trends would therefore not be dependent on the mesh.

Full details on the specific micro-structures and geometries can be found in the methods section of the relevant chapters.

#### 3.1.4 Analysing Impedance Spectroscopy Data

To extract electrical properties from a measurement, it is essential to model the experimental data using an equivalent circuit, generally consisting of a combination of resistors and capacitors connected in parallel and/or series<sup>11</sup>. This can be done by assuming an equivalent circuit from visual inspection of the data and then extracting resistance and capacitance values by a hand-fitting procedure. Alternatively, the data can be modelled using an equivalent circuit, extracting R and C values from the best fit to the data and is typically modelled using software such as ZView® (Scribner Associates Inc, USA). A common equivalent circuit used to model electroceramics is a resistor and capacitor connected in parallel. The real and imaginary components of impedance of the circuit can be calculated using Equation 3.3 and 3.4 and the different immittance formalisms to arrive at

$$Z' = R \frac{1}{1 + (\omega RC)^2} \quad (3.7)$$

$$Z'' = R \frac{\omega RC}{1 + (\omega RC)^2} \quad (3.8)$$

By considering the frequency limits of Equations 3.7 and 3.8 we can visualise the impedance plots the equivalent circuit will obtain. When  $\omega \rightarrow 0$  -  $Z' \rightarrow R$  and  $Z'' \rightarrow 0$ , when  $\omega \rightarrow \infty$  -  $Z' \rightarrow 0$  and  $Z'' \rightarrow 0$ . Also, the second part of Equation 3.8 is a Debye function and is at a maximum

value when  $\omega RC = 1$ . At the Debye frequency,  $Z'' = R/2$ . The graphical representation of these are shown in Figure 3.6.

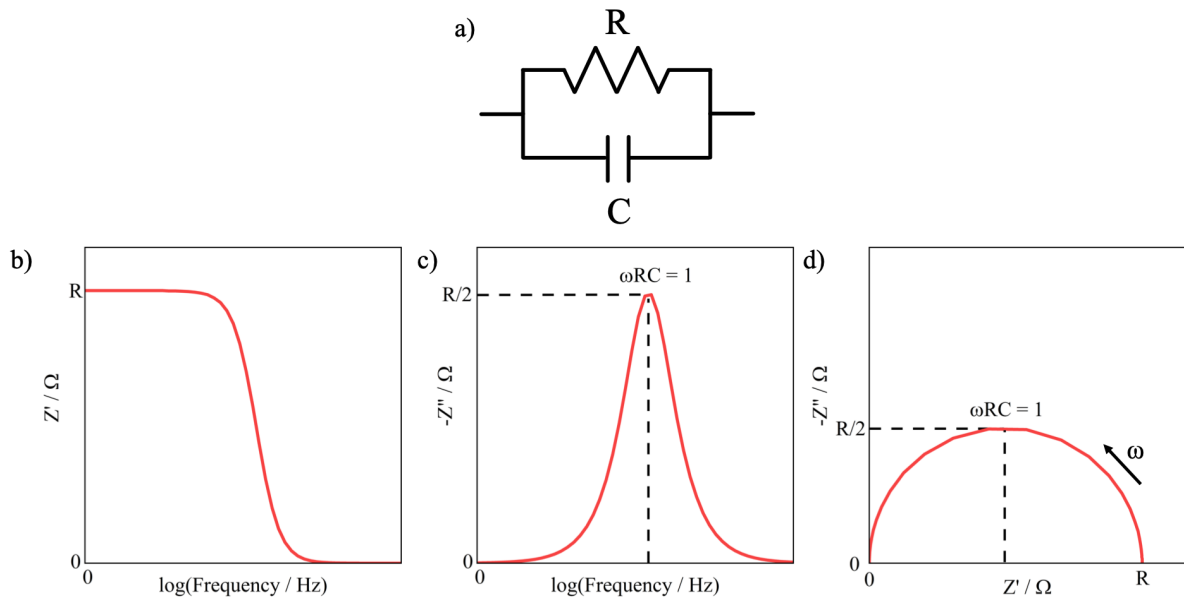


Figure 3.6. a) Equivalent circuit of a parallel RC element and the corresponding b) real impedance ( $Z'$ ) spectroscopic plot, c) imaginary impedance ( $Z''$ ) spectroscopic plot and d) complex impedance Nyquist plot.

Similar results to Figure 3.6 are obtained for  $M''$  spectroscopic plots. Using Figure 3.2 as an example, the equivalent circuit that best represents the data is two parallel RC elements connected in series (see inset of Figure 3.2), meaning resistance and capacitance values can be easily extracted from the Debye peaks using the following equations,

$$Z''_{max} = \frac{R}{2} \quad (3.9)$$

$$M''_{max} = \frac{1}{2C} \quad (3.10)$$

Calculating the resistance and capacitance is simple for the low frequency response in Figure 3.2, however, finding the resistance of the higher frequency response from Equation 3.9 appears more difficult. Each region of the sample has a characteristic time constant given by,

$$\tau = RC \quad (3.11)$$

This is related to the frequency at which the maximum of the regions' response occurs by

$$\omega_{max}\tau = 1 \quad (3.12)$$

where  $\omega_{\max}$  is equal to  $2\pi f_{\max}$  and  $f_{\max}$  is the frequency of the maximum in the Debye peak. The resistance of the intermediate frequency response can be calculated using Equation 3.10 followed by Equation 3.12. After the resistance and capacitance of each region has been determined, the intrinsic properties of each region can be calculated. The conductivity,  $\sigma$ , and relative permittivity,  $\epsilon_r$ , can be determined from the following equations

$$R = GF \cdot \frac{1}{\sigma} \quad (3.13)$$

$$C = \frac{\epsilon_0 \epsilon_r}{GF} \quad (3.14)$$

where  $\epsilon_0$  is the permittivity of free space and GF is a geometric factor. At this point, careful consideration of how current flows through the sample, and the individual regions in the sample, is required – i.e. individual regions may require different geometric factors. For a conventional impedance measurement, the full top and bottom surfaces of a sample are electrodes. Current flows homogeneously over the surface area of the sample,  $A$ , through the thickness of the sample,  $l$ . The geometric factor in this case is

$$GF = \frac{l}{A} \quad (3.15)$$

If micro-contacts are used, current spreads out heterogeneously from the micro-contact into the sample<sup>12</sup> and the geometric factor is related to the micro-contact radius,  $r_{mc}$ , for each micro-contact used (i.e. double Equation 3.16 if measurements are taken between two micro-contacts). It should be noted that when micro-contacts are used, calculated permittivities are termed effective rather than relative due to the uncertainty in the geometry correction.

$$GF = \frac{1}{4r_{mc}} \quad (3.16)$$

In this study, samples were coated with Au-paste electrodes and fired at 850 °C for 2 hours. Impedance Spectroscopy measurements were undertaken using an Agilent E4980A Precision LCR meter with an applied ac voltage of 100 mV, over a frequency range of 1 Hz – 1 MHz. Samples were held at the measurement temperature for a minimum of 30 minutes to allow for thermal equilibrium before measurements were recorded. IS data were corrected for sample geometry and analysed using ZView®.

## 3.2 Micro-contact Impedance Spectroscopy

### 3.2.1 Micro-contact Fabrication

Circular micro-contacts were prepared by a photolithographic lift-off process in a clean room environment. Grease, dust particles and drying stains can prevent the adhesion of metal to the sample surface creating a poor contact, so cleaning of the sample is very important. The whole photolithographic lift-off process can be visualised in Figure 3.7 and described in detail below.

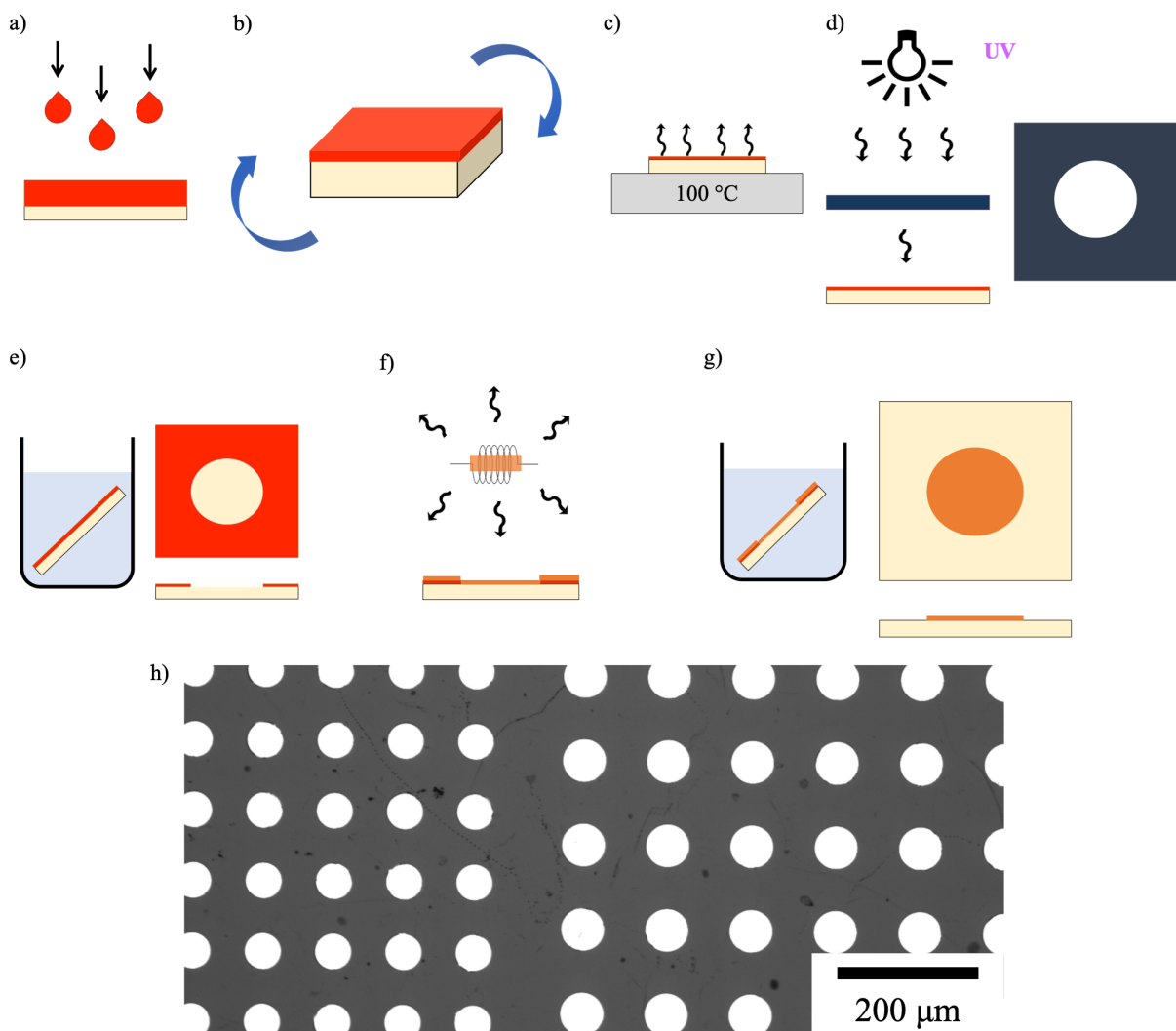


Figure 3.7. Images describing each step in the photolithographic lift-off process. a) Layer of AZ1514H photoresist applied to surface, b) sample spun at 4000 rpm, c) sample baked on a hot plate at 100 °C for 1 min, d) UV radiation incident on sample through a mask with the desired micro-contact pattern, e) sample developed for 1 min, f) metal evaporation, g) sample submerged in acetone to remove remaining photoresist and h) an optical microscope image of a resulting array of micro-contacts with radii of 20 and 30 μm.

The samples are cleaned and degreased first using n-butyl acetate heated to ~ 100 °C and a cotton tip bud. The sample is then submerged in acetone to remove the acetate and finally into

isopropanol. The isopropanol is then blown off the sample using nitrogen gas, preventing drying stains.

After cleaning, the sample is dehydrated on a hot plate at 100 °C for 1 minute to remove any remaining solvent or water. The sample is then placed on a spinner, covered in AZ1514H photoresist and spun at 4000 rpm for 30 seconds leaving a uniform layer of photoresist that is approximately 1 µm thick. The sample is then returned to the hot plate and the photoresist is baked at 100 °C for 1 minute, removing the majority of the solvent in the photoresist. (Figure 3.7 (a → c)).

The sample is then aligned under a mask with the required micro-contact pattern and exposed to a UV lamp for ~ 8 seconds. The sample is then transferred to an AZ developer solution for 1 minute and then rinsed with de-ionised water. Regions of the photoresist layer that were exposed to the UV light develop approximately 1000 times faster than the unexposed photoresist. This creates a “negative pattern” of the required micro-contact arrangement. (Figure 3.7 (d and e)).

The sample is then transferred to a metal evaporator and the chamber pumped to a vacuum of  $10^{-6}$  mbar. Wires of Ti (~ 1 cm) and Au (~ 6 cm) are placed in the centre of tungsten filaments above the samples. When current passes through the filament it heats, melting and then evaporating the metal in all directions. Firstly, a thin layer ~ 150 nm of Ti is evaporated, followed by a thicker layer ~ 300 nm of Au. The thin film of Ti is required to improve the adhesion of Au to the surface. The sample is then immersed in acetone and agitated to remove the remaining photoresist leaving the array of micro-contacts on the surface of the sample. (Figure 3.7 (f → h)).

Micro-contact impedance spectroscopy measurements were undertaken using a Solartron ModuLab XM MTS with an applied ac voltage of 100 mV, over a frequency range of 0.1 Hz – 1 MHz. The sample was placed on a slab of sapphire on a Linkam THMS600 heating stage connected to a Linkam TMS94 controlling unit. Water was circulated through the heating stage using an EHEIM water cooler and the electrodes contacted by two tungsten probes (1 µm tip radius, Signatone) that are positioned by micro-manipulators (Signatone) under an optical microscope. The experimental setup is shown in Figure 3.8.

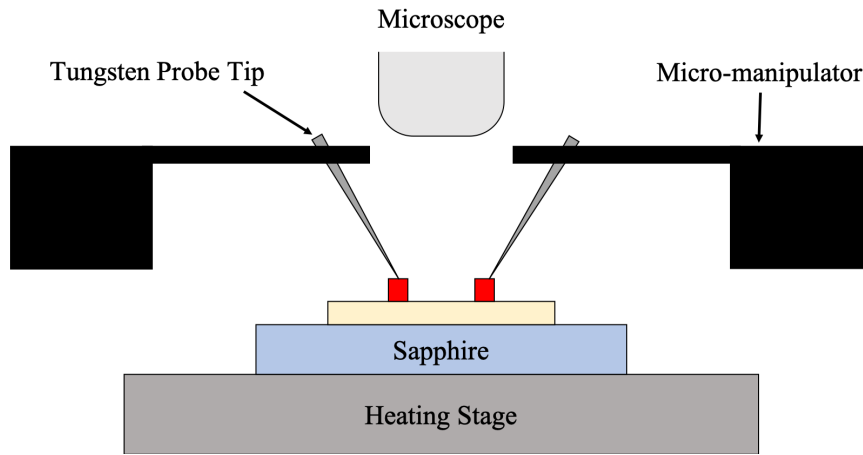


Figure 3.8. Experimental setup for micro-contact Impedance Spectroscopy measurements.

### 3.3 Single Crystal Ceramic Samples

Single crystals of Fe-doped SrTiO<sub>3</sub>, purchased from PI-KEM (Tamworth, UK), were grown by the Verneuil technique with a (001) orientation and a purity of 99.9995%. The substrates were 10 x 10 x 1 mm, with one side epi polished and the other side with a rough finish. The single crystals had compositions that were either undoped, 0.022 wt% Fe-doped, 0.2 wt% Fe-doped or 1 wt% Fe-doped. All samples were annealed at 1000 °C for 24 hours prior to any characterisation or irradiations.

### 3.4 X-ray Diffraction (XRD)

XRD is a powerful technique used widely to determine the crystal structures of materials. All crystalline materials can be thought of as sets of parallel planes of atoms, separated by an inter-planar spacing  $d$ , defined by Miller indices. When X-rays are incident on a material, diffraction occurs at each crystal plane. In most cases, this diffraction will lead to destructive interference of the waves. However, at certain angles, the difference in path length of the incoming waves will be equal to an integer number of wavelengths and the waves will remain in-phase after diffraction. This will cause the waves to interact constructively, leading to an increase in the detected intensity. The Bragg equation defines the angles at which this interaction occurs,

$$n\lambda = 2d \cdot \sin\theta \quad (3.17)$$

where  $n$  is a positive integer,  $\lambda$  is the wavelength of the X-ray beam,  $d$  is the distance between planes and  $\theta$  is the angle of reflection. Once a diffraction pattern has been obtained, it is possible to index the peaks and calculate the size of the unit cell. For a cubic structure, the lattice parameter  $a$  can be calculated using the following equation,

$$\frac{1}{d^2} = \frac{h^2 + k^2 + l^2}{a^2} \quad (3.18)$$

where h, k and l are the Miller indices. This equation becomes more complex as the structure becomes less symmetrical.

In this study a Bruker D2 Phaser was used to obtain XRD data using Cu K<sub>α</sub> radiation (λ=1.5406 Å) generated at 30 kV and 10 mA. The data were collected over the 2θ range of 5 – 80 ° with a step size of 0.02 ° and step time of 0.1 s. A 1 ° divergence slit and a Ni K<sub>β</sub> filter was employed. The sample was rotated at 15 rev/min.

### 3.4.1 Glancing Angle X-ray Diffraction (GAXRD)

GAXRD is a modification that allows for the characterisation of surface regions that would be difficult to detect by conventional methods. By fixing the angle of incidence, the same depth into the material can be probed throughout the experiment. Shallow incident angles lead to less penetration into the material, hence the name Glancing Angle X-Ray Diffraction (GAXRD). The penetration depth that X-rays probe into a material as a function of incidence angle can be calculated with the following equation

$$x = 3\mu \cdot \sin\alpha \quad (3.19)$$

where x is the depth of penetration, μ is the attenuation length and α is the incidence angle. The attenuation length is defined as the distance into the material where the intensity of X-rays drops to 1/e of the value at the surface and is dependent on the material and the X-ray energy. The attenuation length of the samples were obtained from the X-ray database<sup>13</sup>.

GAXRD patterns were collected using a Philips PANalytical X'Pert<sup>3</sup> Powder diffractometer in glancing angle parallel beam configuration using Cu - Kα<sub>1</sub> (λ=1.5406 Å) X-rays at room temperature. Data were collected over the 2θ range of 20 - 55 ° and an incident beam angle of α = 0.5, 2, 5 and 10 °. The step size was 0.02 ° with a step time of 3.5 s. A 1/2 ° divergent slit and a 4 mm beam mask was employed with both incident and diffracted beams passing through 0.04 rad Soller slits. The sample was rotated at 0.25 rev/s.

### 3.5 **Cross-sectional Transmission Electron Microscopy (XTEM)**

TEM uses an accelerated electron beam which is focused by magnetic lenses onto a sample. The electrons from the beam pass through the sample and are scattered by atoms in the sample. After passing through the sample, more magnetic lenses are then used to focus the electrons onto a fluorescent screen or CCD camera. Altering the strength of the lenses manipulates the

beam to form either an image or a diffraction pattern on the screen. In imaging mode, in a sample of constant thickness, any changes in contrast are due to elemental changes in the sample as the different elements scatter electrons differently. In diffraction mode, the principle is the same as that in XRD and Equation 3.17. That is at very discrete scattering angles, constructive interference gives rise to strong beams of electrons. Diffraction patterns allow information about the unit cell to be obtained and whether a material is crystalline or amorphous.

TEM was undertaken using an FEI Tecnai F20 operating at 200 keV in bright-field mode. Images and diffraction patterns were acquired using a CCD camera.

### 3.5.1 Sample Preparation

A requirement of TEM is that a sample needs to be sufficiently thin for high energy electrons to be transmitted through the sample. To study the surface, cross-sectional samples were prepared by the following method.

Samples were prepared, Figure 3.9, by slicing a 10 x 10 x 1 mm sample into 2 mm strips using a diamond slow saw. The strip was then cut in half and the irradiated surfaces cleaned thoroughly with acetone and isopropanol using a cotton tip bud. A generous layer of M-bond 610 was then spread on one of the irradiated surfaces and the irradiated surface of the other strip was placed on top, such that from top to bottom the cross-section consists of bulk<sub>1</sub> - irradiated surface<sub>1</sub> - M-bond - irradiated surface<sub>2</sub> - bulk<sub>2</sub>. The sample was then placed in a teflon clamp to ensure the sample surfaces were compact together. The clamp and sample were then placed in an oven at 180 °C for 2 – 4 hours to cure the glue and then left at room temperature overnight. The sample was then removed from the clamp and then sliced into smaller samples using a diamond slow saw.

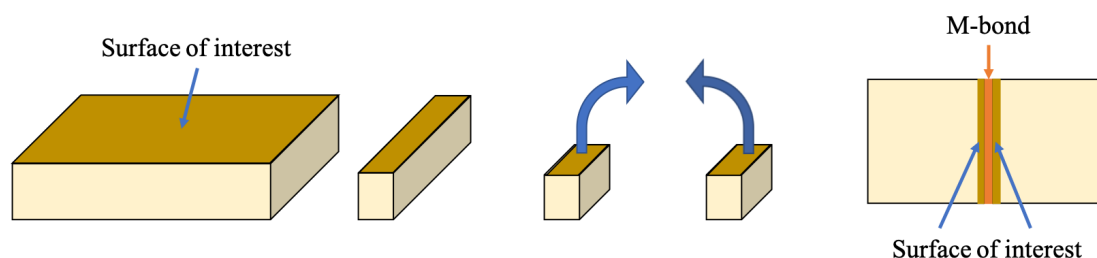


*Figure 3.9. First stage of cross-sectional sample prep. The sample is cut into slices and then the slices are glued together by the surface of interest.*

The sample was then mounted to an aluminium stub using CrystalBond (Gatan) and then mechanically ground using a Buehler EcoMet 250 grinder polisher unit and P1200 and P2500 silicon carbide grinding paper (Buehler). The samples were then polished using 6, 3 and 1  $\mu\text{m}$

water-based diamond suspension (MetaDi). The sample was then turned over, and the process repeated on the opposite side ensuring the final thickness of the sample was between 40 – 70  $\mu\text{m}$ .

The sample was then thinned further using a Gatan dimple grinding unit. The sample was rotated while a phosphor bronze wheel, lapped with 1  $\mu\text{m}$  diamond paste, rotates on the cross-section creating a dimple in the sample. The dimple grinding process produces a large amount of thin area in the centre of the sample surrounded by a thicker rim, giving mechanical stability for the subsequent sample preparation steps, Figure 3.10. Once the thickness of the sample at the centre of the dimple is 10 - 30  $\mu\text{m}$  thick, the bronze wheel is replaced with a felt wheel and polished with the 1  $\mu\text{m}$  diamond paste. Final polishing is achieved using 250 nm alumina suspension. The sample was then mounted to a copper TEM slot (AGAR) using M-bond.

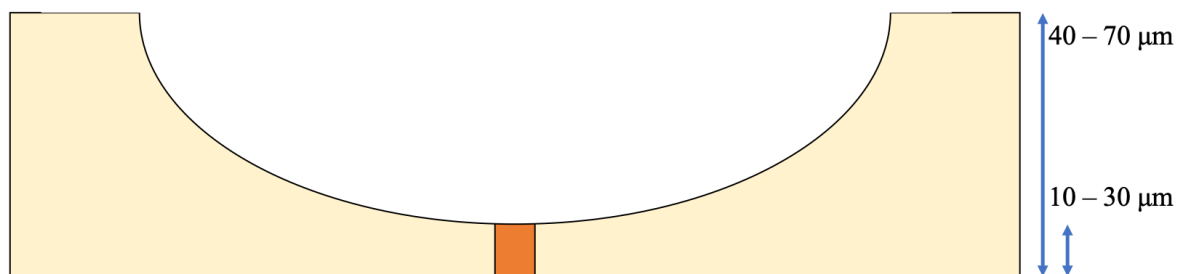


*Figure 3.10. Side view of a cross-sectional sample after dimple grinding.*

Final thinning is achieved by ion beam milling where an ion beam is incident on a sample, sputtering material until electron transparency is achieved. Ar ions are generally used as they are heavy and inert; meaning they produce a good sputtering yield and minimise chemical interactions with the sample. The sample is rotated to achieve uniform thinning and dual beams are employed to decrease the milling times. The Ar beam is incident on a large area of the sample but milling is faster at the centre where the two beams overlap. A consequence of the technique is that the regions close to the surface are subsequently damaged and amorphised by this process. Lowering the angles of the guns and the energies can decrease this effect but leads to longer milling times. Using lower angles and energies for the final stages of ion milling helps reduce the surface damage. The ion milling process and an example of a sample after milling is shown in Figure 3.11.

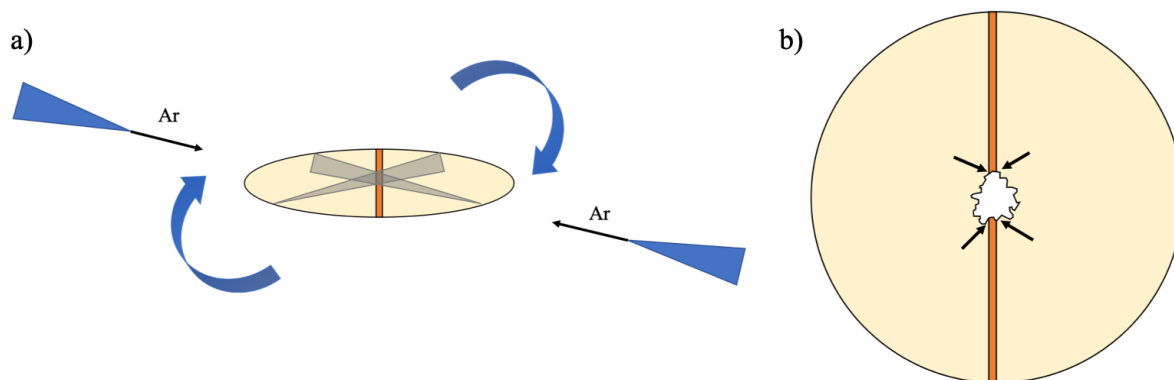


Figure 3.11. a) Schematic of the ion milling setup for a rotating sample. The grey triangles indicate where the argon beam is incident on the surface and there is a larger intensity where the beams overlap in the centre; the blue triangles represent the Ar guns. b) The sample after ion milling with a hole on the cross-section. The four arrows indicate where the surface should be electron transparent and can be observed by TEM.

Electron transparent samples were achieved using a Gatan Precision Ion Polishing System II. An Ar ion beam with energy of 5 keV and gun angle of  $8^\circ$  was used to thin the sample to perforation, ideally at the location of the cross-section. If perforation occurred away from the interface, milling was continued until the perforation reached the interface. The beam energy was then decreased to 3, 1 and 0.5 keV at angles of  $6^\circ$ ,  $4^\circ$  and  $4^\circ$ , respectively, to thin the edges of the hole further and to reduce surface damage from milling. This creates 4 possible viewing points for TEM analysis of the damaged region of the sample.

### 3.6 Ion Implantation and SRIM

Bulk ion implantation was undertaken at the Helmholtz Zentrum Dresden Rossendorf Ion Beam Centre. Samples were implanted with 5 MeV  $^{197}\text{Au}^+$  ions to a total fluence of  $5 \times 10^{15}$  ions  $\text{cm}^{-2}$  at room temperature at an incident angle that was  $7^\circ$  from the surface normal. The implantation was carried out at room temperature on a water-cooled sample holder. The vacuum pressure of the chamber was below  $3 \times 10^{-6}$  mbar.

Prior to irradiations, SRIM (the Stopping and Range of Ions in Matter)<sup>14</sup> was used to simulate the damage profile for  $\text{SrTiO}_3$  allowing for estimates of the ion implantation range and damage produced to be calculated. SRIM is a group of programs which calculate stopping powers, energy loss values, stopping range, displacements and others from analytical and Monte Carlo calculations. ‘Detailed Calculations with Full Damage Cascades’ with displacement energies of 50 eV for Sr, Ti, Fe and O were used.

### 3.7 References

1. Irvine, J. T. S., Sinclair, D. C. & West, A. R. Electroceramics : Characterization by Impedance Spectroscopy. *Adv. Mater.* **2**, 132–138 (1990).
2. Kidner, N. J., Perry, N. H., Mason, T. O. & Garboczi, E. J. The brick layer model revisited: Introducing the nano-grain composite model. *J. Am. Ceram. Soc.* **91**, 1733–1746 (2008).
3. Dean, J. S., Harding, J. H. & Sinclair, D. C. Simulation of Impedance Spectra for a Full Three-Dimensional Ceramic Microstructure Using a Finite Element Model. *J. Am. Ceram. Soc.* **97**, 885–891 (2014).
4. Maxwell, J. C. *A Treatise on Electricity and Magnetism*. (Cambridge University Press, 2010).
5. Dale, G., Strawhorne, M., Sinclair, D. C. & Dean, J. S. Finite element modeling on the effect of intra-granular porosity on the dielectric properties of BaTiO<sub>3</sub> MLCCs. *J. Am. Ceram. Soc.* **101**, 1211–1220 (2018).
6. Heath, J. P., Harding, J. H., Sinclair, D. C. & Dean, J. S. Electric field enhancement in ceramic capacitors due to interface amplitude roughness. *J. Eur. Ceram. Soc.* **39**, 1170–1177 (2018).
7. Naderi, S., Heath, J. P. & Dean, J. S. Morphology characterisation of inclusions to predict the breakdown strength in electro-ceramic materials: Microstructure modelling. *Ceram. Int.* **45**, 361–368 (2018).
8. Heath, J. P., Dean, J. S., Harding, J. H. & Sinclair, D. C. Simulation of Impedance Spectra for Core-Shell Grain Structures Using Finite Element Modeling. *J. Am. Ceram. Soc.* **98**, 1925–1931 (2015).
9. Geuzaine, C. & Remacle, J. F. Gmsh: a three-dimensional finite element mesh generator with built-in pre- and post-processor facilities. *Int. J. Numer. Methods Eng.* **79**, 1309–1331 (2009).
10. Fleig, J. Local conductivity measurements on AgCl surfaces using microelectrodes. *Solid State Ionics* **85**, 9–15 (1996).
11. Abram, E. J., Sinclair, D. C. & West, A. R. A Strategy for Analysis and Modelling of Impedance Spectroscopy Data of Electroceramics: Doped Lanthanum Gallate. *J. Electroceramics* **10**, 165–177 (2003).
12. Veazey, R. A., Gandy, A. S., Sinclair, D. C. & Dean, J. S. Modeling the influence of two terminal electrode contact geometry and sample dimensions in electro-materials. *J. Am. Ceram. Soc.* Available on-line <https://doi.org/10.1111/jace.16236> (2018).

13. Henke, B. L., Gullikson, E. M. & Davis, J. C. X-Ray Interactions: Photoabsorption, Scattering, Transmission, and Reflection at  $E = 50\text{--}30,000$  eV,  $Z = 1\text{--}92$ . *At. Data Nucl. Data Tables* **54**, 181–342 (1993).
14. Ziegler, J. F., Ziegler, M. D. & Biersack, J. P. SRIM - The stopping and range of ions in matter (2010). *Nucl. Instruments Methods Phys. Res. B* **268**, 1818–1823 (2010).

# Chapter 4: A Finite Element Modelling Study of Spreading Resistance and Sample Confinement

*This chapter contains material published in the Journal of the American Ceramic Society<sup>1</sup>.*

## 4.1 Introduction

The use of single crystals, thin & thick films and bulk ceramics for electrical applications requires careful consideration of how current flows through the sample. In many cases, the electrical response is dominated by the ‘bulk’ material properties (conductivity and permittivity); however, in others, surface layers, grain boundaries and/or non-ohmic sample/electrode interfaces play a dominant or significant role. Impedance Spectroscopy<sup>2,3</sup> is a useful technique to identify various electro-active regions in a sample and to extract various bulk and interface parameters for a wide range of materials and devices.

Two general electrode configurations are used. The first type is where contacts are located on the top and bottom surfaces of the sample and we refer to this as a top-bottom configuration. The second type is where both contacts are defined on the same surface, referred to as top-top. Electroceramics are conventionally measured by Impedance Spectroscopy using top-bottom macroscopic contacts, where full surfaces are coated with electrodes. Applying a geometric factor (Equation 4.1) using the sample thickness and electrode area to the resulting response allows the bulk conductivity,  $\sigma_{bulk}$ , to be calculated from the measured resistance by<sup>4,5</sup>

$$\sigma_{bulk} = \frac{s}{A} \frac{1}{R_{bulk}} \quad (4.1)$$

where  $R_{bulk}$  is the measured resistance,  $s$  is the separation of the electrodes (e.g. the thickness of the sample) and  $A$  is the surface area of the electrodes (e.g. the area of the major faces of the sample). Current flow through such a system is typically homogeneous, providing the physical microstructure is relatively simple<sup>6</sup>.

In some situations, full coating of the top and bottom surfaces of a sample is undesirable, for example when local properties are required. The electrical response of a sample may then differ significantly depending on the electrode configuration employed. Microscopic contacts allow for localised electrical properties of a material to be calculated<sup>7-9</sup>, or specific regions to be probed and characterised in more detail such as surface layers<sup>10-12</sup> and individual grains or grain boundaries<sup>9,11,12</sup>. In each case, specific spreading resistance equations are required to describe the electrode geometry and hence current flow through a sample. Significant errors

can be generated in the measurement of intrinsic ‘bulk’ properties if the wrong equation is used or applied incorrectly due to limitations in the assumptions on current flow.

The electrical response from micro-contacts is determined by the sample properties in the vicinity directly beneath the micro-contacts. Fleig<sup>10</sup> has shown that 75% of the electrical response between a circular micro-contact and a full surface counter electrode originates from a volume directly beneath the micro-contact. This region of high current density has a radius approximately four times the micro-contact radius and thus the size of the micro-contact determines the volume being probed. The spreading resistance,  $R_{spr}$ , of a circular micro-contact of electrode radius,  $r$ , can be calculated by<sup>15</sup>,

$$R_{spr} = \frac{1}{4r\sigma} \quad (4.2)$$

where  $\sigma$  is the conductivity of the sample. An assumption in the use of this equation is there are no highly resistive extrinsic regions that exist between the micro-contact and counter electrode that would block the current<sup>16</sup>.

A less common contact geometry uses a micro-contact on the top and bottom surfaces of the sample. Such micro-contact geometries are used in electromotive force measurements to determine the oxygen ion transport numbers in oxide-ion solid electrolytes<sup>17,18</sup>. These typically use electrodes which cover approximately 50% of the top and bottom surface areas of the sample. The spreading resistance approximation in this configuration becomes,

$$R_{spr} = \frac{1}{2r\sigma} \quad (4.3)$$

This approximation is double the value of the previous equation, as it is assumed there is a spreading resistance associated with each micro-contact. This equation has also been shown to be a good approximation for top-top configurations where two micro-contacts are located on the same surface. This contact geometry has benefits of measuring specific (or local) regions within a sample, such as individual grains and across individual grain boundaries<sup>19,20</sup>. Bulk conductivities<sup>21</sup> and conductivity profiles<sup>8</sup> have been successfully determined using this method. An assumption made in the spreading resistance approximation is the size of the micro-contacts is much smaller than the size of the sample. Rettenwander et al.<sup>21</sup> found that limiting the size of the sample (confinement) would increase the measured resistance. With 30  $\mu\text{m}$  diameter micro-contacts they simulated a range of top-top contact separations from 30  $\mu\text{m}$  up to  $\sim 40$  times greater than the contact diameter with a variety of model sizes. This revealed

inaccuracies of only  $\sim 30\%$ ; however, detailed confinement studies have not been performed. As a consequence, a full analysis of electrode geometry and space confinement remains to be established.

In this chapter we apply an in-house developed code Elcer<sup>4</sup> that uses Maxwell's equations to simulate the electrical response of various electrical microstructures and electrode contact geometries and also consider the influence of confinement (i.e. sample size with respect to electrode size and separation). Each of the electrode geometries described above are simulated for an electrically homogeneous sample to represent an 'ideal' single crystal and analysed to extract the intrinsic 'bulk' properties using the different equations. The results are compared to the input intrinsic properties to highlight the benefits and limitations of the equations for each electrode configuration and also to consider the influence of confinement on the extracted conductivity values. In addition, to extend the analysis to polycrystalline samples we consider confinement arising from an individual grain being surrounded by a resistive grain boundary or embedded in an epoxy glue.

## 4.2 Finite Element Modelling

Using FEM, we have studied the main types of top-bottom and top-top configurations. For the top-bottom models, a cylinder with a radius of  $33.851\ \mu\text{m}$  (surface area of  $3600\ \mu\text{m}^2$ ) was used to represent typical ceramic disc geometry. The thickness of the model was varied from  $10\ \mu\text{m}$  to  $100\ \mu\text{m}$  to study the influence of contact separation. Electrodes were initially defined as the full top and bottom (FTB) surfaces of the model, Figure 4.1 (a). The size of the top contact was then decreased to create a circular micro-contact on the top surface (i.e. only part of the surface was covered) and a full contact on the bottom surface. These models will be referred to as micro-top full-bottom, MTFB, as shown in Figure 4.1 (b). Finally, the size of the bottom contact was decreased such that circular micro-contacts were defined on both surfaces. These models will be defined as micro-top-bottom, MTB, as shown in Figure 4.1 (c). The micro-contact radius was varied to be 75, 50, 25, 10 and 1% of the model radius. Thicknesses much smaller and much larger than the micro-contact radius were then simulated to study the effects of confinement at 'extreme' separations.

For the top-top geometry, two micro-contacts were defined on the top surface of a slab of material initially of side length  $1500\ \mu\text{m}$  and thickness  $500\ \mu\text{m}$  (micro-top-top - MTT), Figure 4.1 (d), representing typical single crystal, thin film and ceramic bar geometries. Although, the size and shape of the model was larger in this case, the micro-contact surface area was consistent with the previous models. The influence of contact separation was again studied and

to investigate the influence of boundary effects (confinement) on the electrical response, the size of the model was then decreased in all directions. Experimental dimensions taken from Rodewald et al.<sup>20</sup> were then used to examine realistic size effects of confinement. A second material with a conductivity three orders of magnitude lower than the bulk was then defined around one of the confined models to simulate the influence of a resistive grain boundary or a supporting epoxy glue surrounding a single grain, such as in Rettenwander et al<sup>21</sup>.

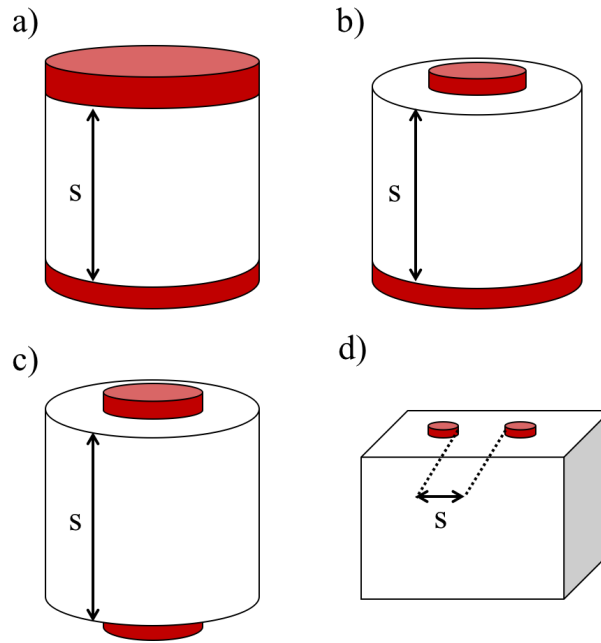


*Figure 4.1. Schematic of the circular electrode models for a) FTB - contacts are the full top and bottom surfaces, b) MTFB – micro-contact on the top surface and full contact on the bottom surface, c) MTB – micro-contact on the top and bottom surfaces and d) MTT – two micro-contacts on a single surface. Electrodes are shown in red and this is consistent throughout all figures.*

In all models, the contact separation was defined as the shortest distance between the contacts. The sample was assigned a conductivity of  $\sigma = 13.6 \mu\text{S m}^{-1}$  and a relative permittivity of  $\epsilon_r = 162$ . These values were selected as they were experimentally determined ‘bulk’ values for a  $\text{SrTiO}_3$  single crystal at  $300 \text{ }^\circ\text{C}$  with macroscopic top and bottom electrodes as measured by conventional Impedance Spectroscopy. Between 800,000 and 1,500,000 elements were used. Current density plots and line scans of the solved structure were visualised using ParaView<sup>22</sup>.

## 4.3 Results

### 4.3.1 Top-bottom models

The electrical response for the top-bottom models was simulated for a range of separations. The conductivity was then calculated using the geometric factor and the spreading resistance equation for each of the solved structures and compared to the input values. The calculated

conductivity values using the geometric factor for the differing types of top-bottom models are shown in Figure 4.2. Due to accuracy with the FEM method and extraction of the intrinsic values, we assume the extracted value is in agreement with the input value if it is  $\pm 10\%$  of the input value (grey box in following figures).

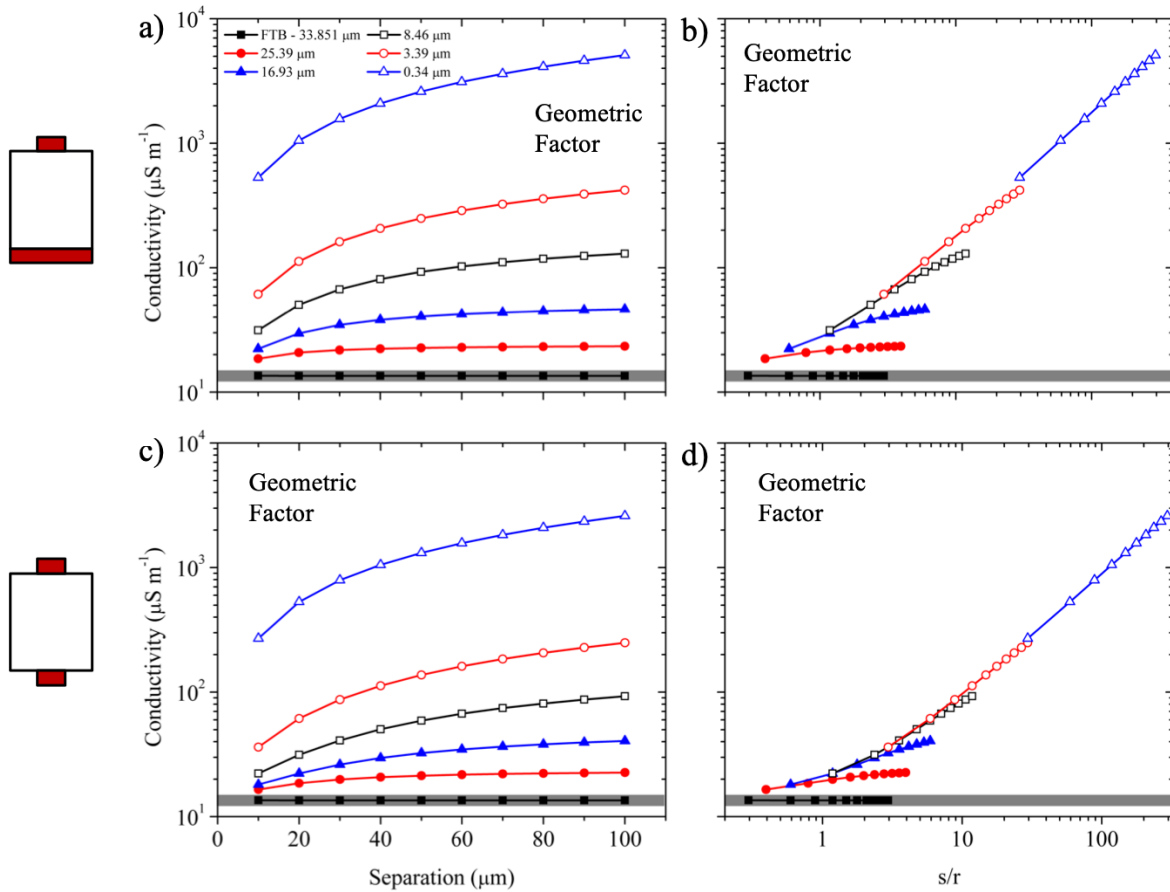


Figure 4.2. Calculated conductivity using the geometric factor plotted against contact separation and the ratio of the contact separation,  $s$ , over the micro-contact radius,  $r$ , for a, b) MTFB and c, d) MTB models. The grey box represents the input conductivity  $\pm 10\%$ . Models are labelled by the radius of the micro-contacts.

As expected, the FTB models (conventional measurements) return the correct conductivity using the geometric factor at all separations modelled, filled black squares in Figure 4.2. As the surface area of the micro-contact decreases with respect to the model surface area, the reliability of this equation decreases. In both the MTFB and MTB cases, the extracted conductivity produces an overestimate of the input value at all separations. However, when the micro-contact radius was 25.39  $\mu\text{m}$ , covering 56.25% of the model surface, the calculated conductivity was within  $\pm 100\%$  of the input value, filled red circles in Figure 4.2. When the micro-contacts radius was 0.34  $\mu\text{m}$ , covering 0.01% of the surface, the calculated conductivity exceeds the input conductivity by over two orders of magnitude, open blue triangles in Figure

4.2. When micro-contacts are used, small  $s/r$  values and large micro-contact sizes are required for the most accurate approximations using the geometric factor.

The calculated conductivity using the spreading resistance equation for the top-bottom models is shown in Figure 4.3. In both the MTFB and MTB cases, the conductivity is overestimated at small separations and underestimated at large separations. As the contact size decreases, the spreading resistance equations become better approximations for each separation, giving the input conductivity when the micro-contact radius reduces to  $0.34 \mu\text{m}$ , covering  $0.01\%$  of the sample surface. In contrast to the geometric factor, large  $s/r$  values and small micro-contact sizes are required for accurate approximations of the conductivity using the spreading resistance equation.

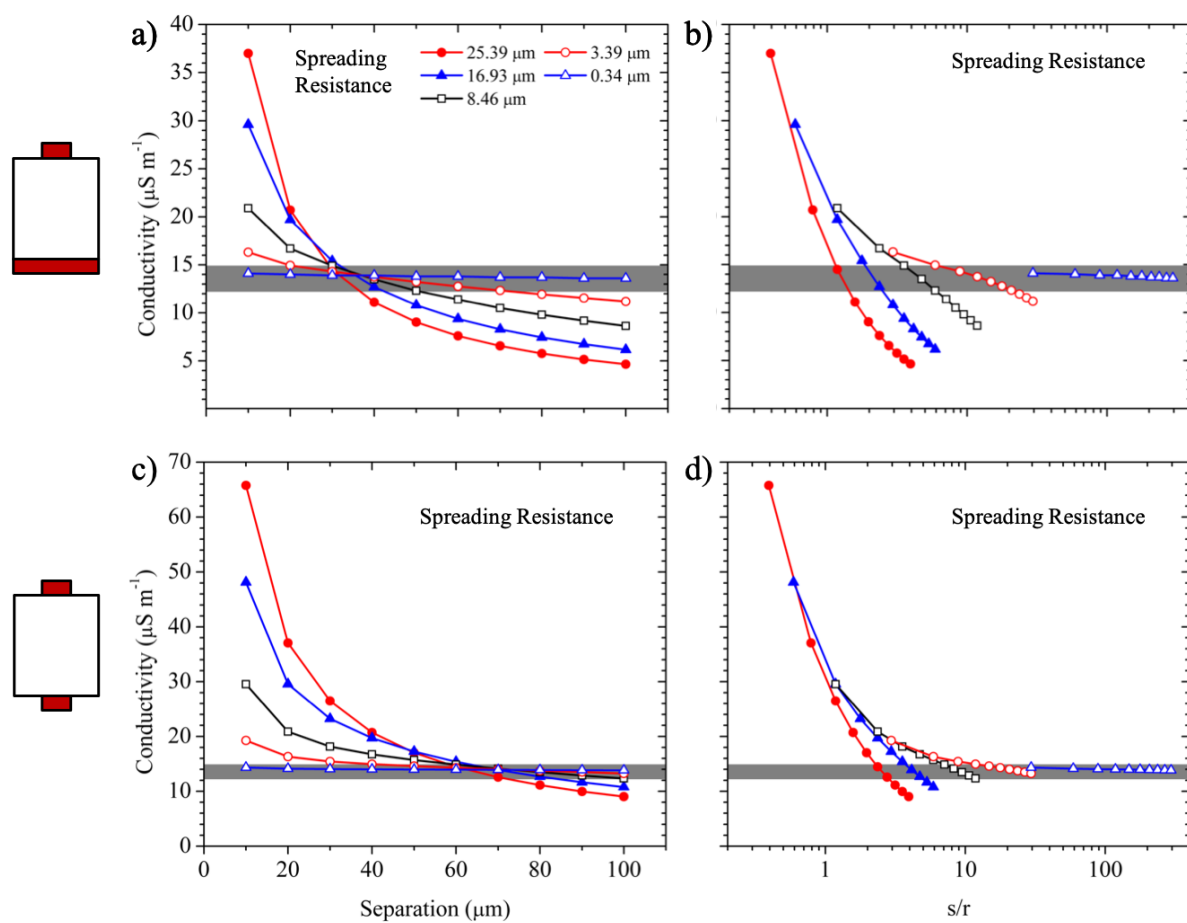


Figure 4.3. Calculated conductivity using the spreading resistance equations plotted against contact separation and the ratio of the contact separation,  $s$ , over the micro-contact radius,  $r$ , for a, b) MTFB and c, d) MTB models. The grey box represents the input conductivity  $\pm 10\%$ . Models are labelled by the radius of the micro-contacts. (Model radius –  $33.851 \mu\text{m}$ ).

Current density plots were generated for the top-bottom models and are shown in Figure 4.4. Red indicates a region of large current density and blue represents a region of low current density. For the FTB model, the conduction pathways are straight with a constant distance

between them and the current density is homogeneous, Figure 4.4 (a). As the size of the micro-contact decreases the current density becomes more heterogeneous as the curvature of the conduction pathway trajectories increases and the distance between each trajectory decreases, Figure 4.4 (b)-(g). For the MTB models, Figure 4.4 (e)-(g), as both top and bottom surfaces are micro-contacts, there are heterogeneities in the current density at both surfaces.

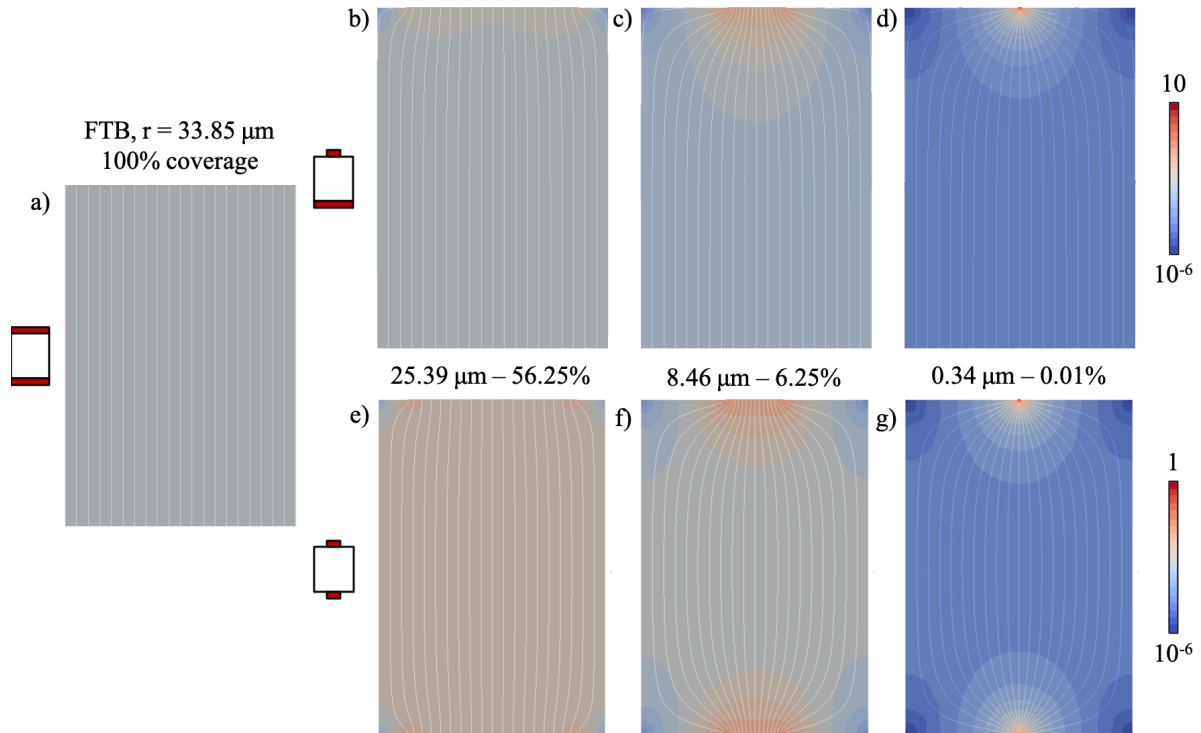


Figure 4.4. Simulated current density plots for a) FTB, b-d) MTFB and e-g) MTB models, with a contact separation of  $100 \mu\text{m}$ . Plots include overlaid simulated conduction pathway trajectories. Scale bars are in units of  $\text{A}/\text{m}^2$ .

The current density measured at a number of points along the central z-axis of the models are shown in Figure 4.5. When the contacts are defined as the full surfaces, the current density is constant throughout, filled black squares in Figure 4.5. For micro-contacts the current density is greatest at the surface of the micro-contact. As the micro-contact size decreases, the current density becomes increasingly dominated by the region close to the micro-contact. For a micro-contact radius of  $0.34 \mu\text{m}$ , covering 0.01% of the surface, and separation of  $100 \mu\text{m}$ , over 90% of the current density arises from a region approximately  $2 \mu\text{m}$  (MTFB) or  $3 \mu\text{m}$  (MTB) from the micro-contacts, open blue triangles in Figure 4.5 (a) and (b). At a separation of  $10 \mu\text{m}$  and micro-contact radius of  $0.34 \mu\text{m}$ , the current density is heterogeneous, open blue triangles in Figure 4.5 (c). For larger micro-contact radii ( $25.39$ ,  $16.93$  and  $8.46 \mu\text{m}$ ) the current density remains homogeneous, Figure 4.5 (c), in contrast to the models with a separation of  $100 \mu\text{m}$  where small heterogeneities can be observed, Figure 4.5 (b).

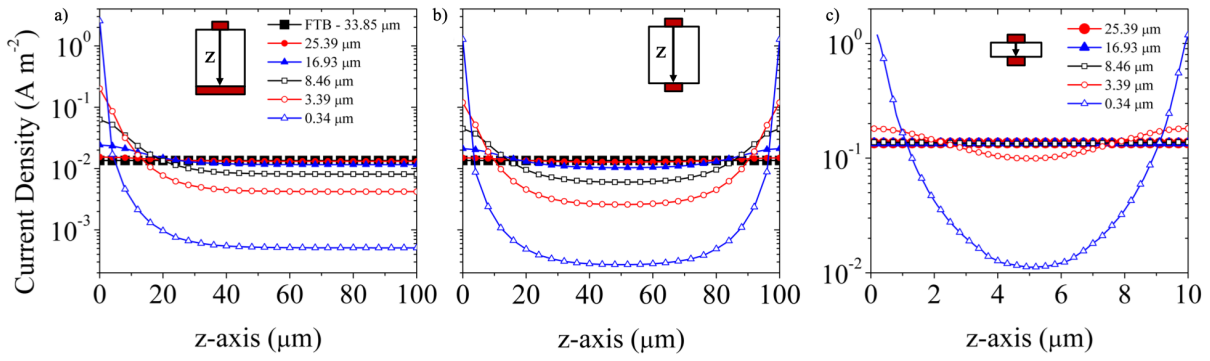


Figure 4.5. Current density measured along the central z-axis for a) MTFB and b) MTB cases at a separation of 100  $\mu\text{m}$  and c) the MTB case at a separation of 10  $\mu\text{m}$ .

#### 4.3.2 Top-top models

Calculations were then performed for top-top models. The calculated conductivity using the geometric factor for the top-top models is shown in Figure 4.6. Three models give accurate conductivities at an  $s/r \sim 1.2$ , although there is no convergence towards the input conductivity. At lower  $s/r$  values the conductivity is underestimated for these models. At higher  $s/r$  values, the calculated conductivity is overestimated and increases linearly.

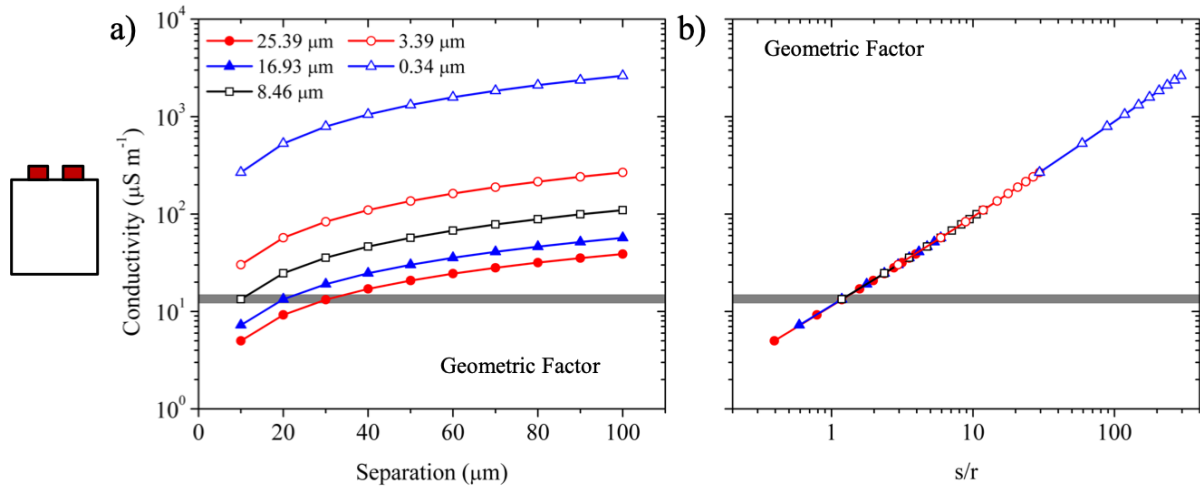


Figure 4.6. Calculated conductivity using the geometric factor plotted against contact separation and the ratio of contact separation,  $s$ , over micro-contact radius,  $r$ , for the MTT models. The grey box represents the input conductivity  $\pm 10\%$ .

The calculated conductivity using the spreading resistance equation for the top-top models is shown in Figure 4.7. The larger contact sizes overestimate the conductivity. In contrast, as the contact size decreases the calculated conductivity approaches the input value, Figure 4.7 (a). A clear trend is observed where the calculated conductivity converges to within 10% of the input value at  $s/r \sim 8$ , Figure 4.7 (b). As  $s/r$  increases, the rate the calculated conductivity converges to the input value decreases. Thus, to gain significant improvement in the accuracy

of the results, substantially larger micro-contact separations are required. For example, an  $s/r \sim 28$  is required for a calculated conductivity within 5% error.

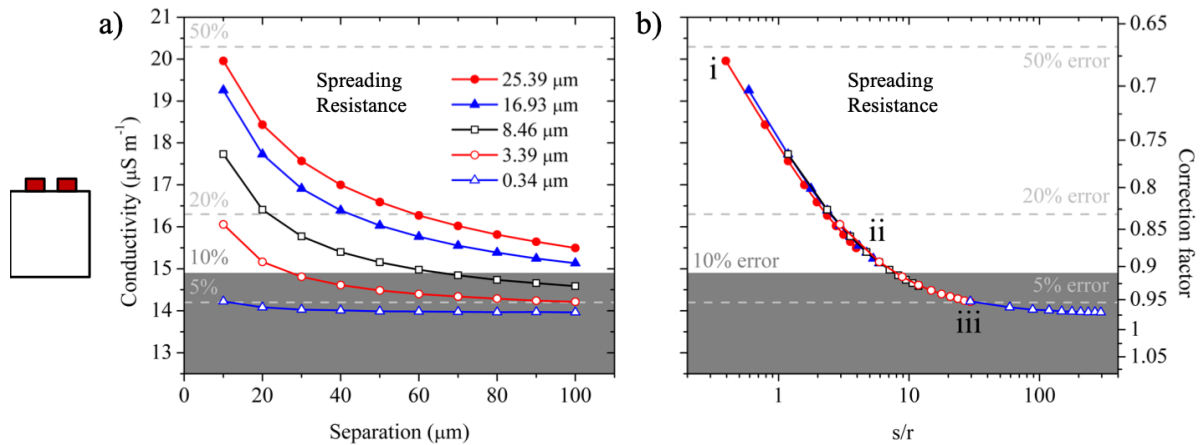


Figure 4.7. Calculated conductivity using the spreading resistance equation plotted against a) contact separation and b) the ratio of the contact separation,  $s$ , over the micro-contact radius,  $r$ , for the MTT models of a cube of side length  $1500 \mu\text{m}$  and thickness of  $500 \mu\text{m}$ . The secondary axis in b) is the required correction factor to the calculated conductivity to account for contact interference. The dark grey box represents the input conductivity  $\pm 10\%$ . Dashed light grey lines represent different errors from the input conductivity. Points labelled i, ii and iii are models with  $s/r = 0.4, 4$  and  $28$ , respectively, and are explored further in Figure 4.8 and Figure 4.9.

Due to the universal trend for the calculated conductivity versus  $s/r$ , irrespective of the micro-contact size, Figure 4.7 (b), a correction factor for unconfined model dimensions could be applied to compensate for the overestimation of conductivity due to contact interference. For example, an  $s/r$  of 2 and 4 could produce overestimates of the conductivity by 23% and 15%, requiring correction factors of 0.81 and 0.87.

Current density plots for top-top models with a micro-contact radius of  $25.39 \mu\text{m}$ , and with  $s/r$  labelled i, ii and iii in Figure 4.7, are shown in Figure 4.8. These show current flow is heterogeneous throughout the full model for top-top models.

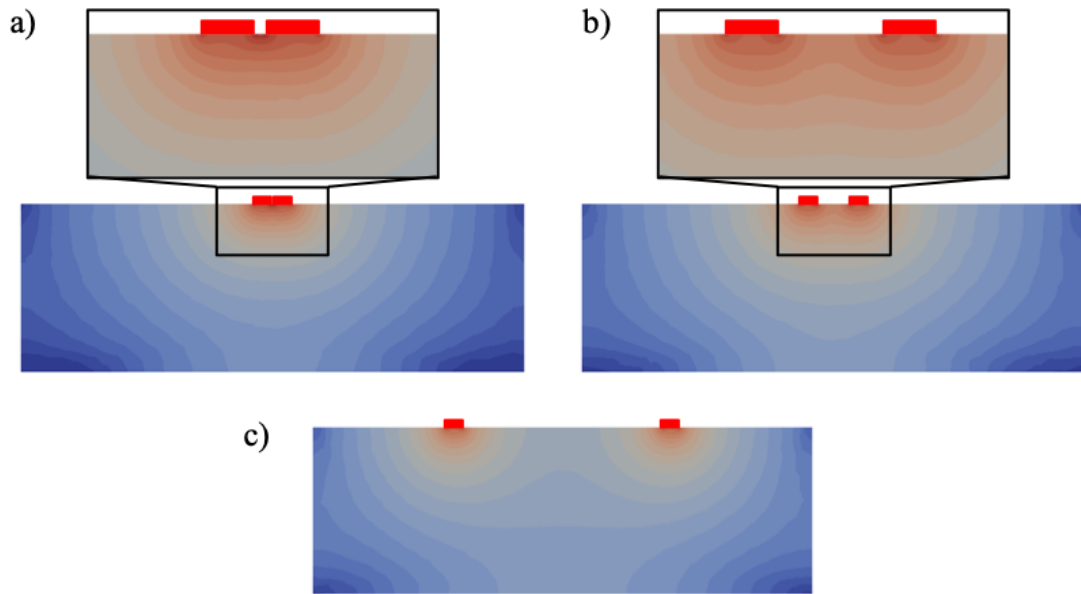


Figure 4.8. Simulated current density plots for the MTT models with a micro-contact radius of  $25.39 \mu\text{m}$  and contact separation of a)  $10 \mu\text{m}$  ( $s/r = 0.4$ ), b)  $100 \mu\text{m}$  ( $s/r = 4$ ) and c)  $700 \mu\text{m}$  ( $s/r = 28$ ).

Current density line scans along the x-axis of the MTT models with a micro-contact radius of  $25.39 \mu\text{m}$  at different depths from the top surface ( $z$ ) is shown in Figure 4.9. The current density is smallest towards the edges of the models ( $\sim 1 - 10 \mu\text{A}/\text{m}^2$ ) and is negligible compared to the response directly beneath the micro-contacts ( $\sim 0.1 \text{ A}/\text{m}^2$ ), highlighting the localising effect of the micro-contacts. The line scan closest to the micro-contacts (located  $1 \mu\text{m}$  below the top surface, black line in Figure 4.9) shows sharp peaks in the current density. These occur at the position of the edges of the micro-contacts. For contacts with an  $s/r = 0.4$  the current density is greatest between the contacts showing evidence of interference between the two electrodes, Figure 4.9 (a). The current density is observed to reduce by a factor of  $\sim 3$  directly beneath the centre of the micro-contact. As the line scan moves deeper into the model (increasing  $z$ ), the current density decreases rapidly; approximately one order of magnitude at  $50 \mu\text{m}$  from the surface and two orders of magnitude at  $150 \mu\text{m}$  from the surface. The responses from the two micro-contacts merge to an apparently single response in the current density. This is due to interference and gives rise to the overestimation of the conductivity at small separations, Figure 4.7. As the contacts move further apart,  $s/r = 4$  (Figure 4.9 (b)), a minimum is generated in the current density between the contacts which becomes more pronounced at larger separation, Figure 4.9 (c). At larger separations, the minimum at the midpoint of the electrodes can be seen deeper into the material. This signifies the interference between the electrodes has reduced to a point where each contact behaves as an isolated element. As each electrode becomes more isolated the accuracy of the spreading resistance equation increases.

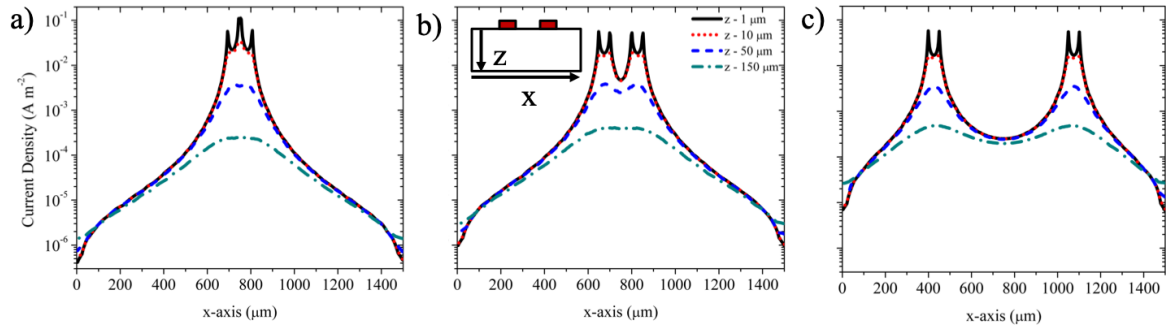


Figure 4.9. Current density line scans along the  $x$ -axis at various distances from the top surface for a micro-contact radius of  $25.39 \mu\text{m}$  and contact separation of a)  $10 \mu\text{m}$  ( $s/r = 0.4$ ), b)  $100 \mu\text{m}$  ( $s/r = 4$ ) and c)  $700 \mu\text{m}$  ( $s/r = 28$ ).

### 4.3.3 Confinement

Confinement has been studied in both of the micro-contact geometries discussed above. Firstly, top-bottom models with micro-contact radii of  $25.39$ ,  $8.46$  and  $0.34 \mu\text{m}$  were studied further. The separation of the contacts, or thickness of the model, was increased or decreased to much larger or smaller values than the contact size. The calculated conductivity for the three different micro-contact sizes for the MTFB case are shown in Figure 4.10. The conductivity was calculated using the geometric factor and spreading resistance equations. For the geometric factor, the conductivity was calculated using both the micro-contact surface area and the model surface area, black squares and red circles in Figure 4.10, respectively.

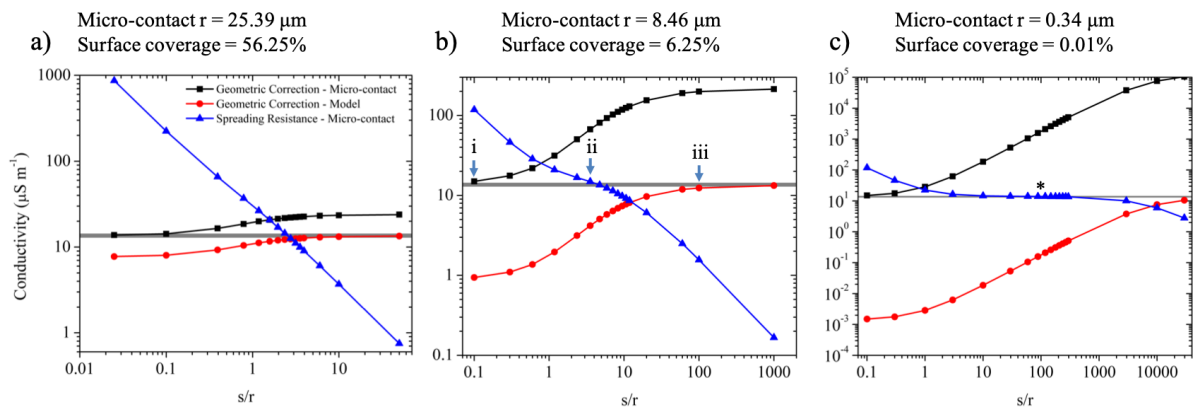


Figure 4.10. Calculated conductivity using the geometric factor and spreading resistance equations for the MTFB models for a micro-contact radius of a)  $25.39 \mu\text{m}$ , b)  $8.46 \mu\text{m}$  and c)  $0.34 \mu\text{m}$  plotted against the ratio of the contact separation,  $s$ , over the micro-contact radius,  $r$ . The range of  $s/r$  is much larger than in previous figures. The grey box represents the input conductivity  $\pm 10\%$ . Current density plots for the points labelled i, ii and iii are shown in Figure 4.11.

At small  $s/r$  values, the geometric factor using the micro-contact surface area gives the best approximation for each micro-contact size, black squares in Figure 4.10. The trends observed suggest this equation will give increasingly more accurate conductivities at increasingly smaller  $s/r$  values. Such  $s/r$  values are representative of thin film geometries. At large  $s/r$  values

the geometric factor using the model surface area gives the best approximation, red circles in Figure 4.10. At intermediate  $s/r$  values the spreading resistance equation gives the best approximation of the input conductivity, blue triangles in Figure 4.10. The size of this intermediate region is very small for the models with a micro-contact radius of  $25.39\ \mu\text{m}$  covering 56.25% of the surface, Figure 4.10 (a). In contrast, when the micro-contact radius is  $0.34\ \mu\text{m}$ , covering 0.01% of the surface, the spreading resistance equation gives the best approximation over approximately four orders of magnitude in  $s/r$ , Figure 4.10 (c). When using the MTFB geometry a micro-contact radius approximately  $10\ \mu\text{m}$  is typically used on a sample that is 1 mm thick ( $s/r = 100$ ) and of the order of mm in size. For this geometry and size, the spreading resistance equation will give the best approximation for the conductivity, star in Figure 4.10 (c). Current density plots for the MTFB models labelled i, ii and iii in Figure 4.10 are shown in Figure 4.11.

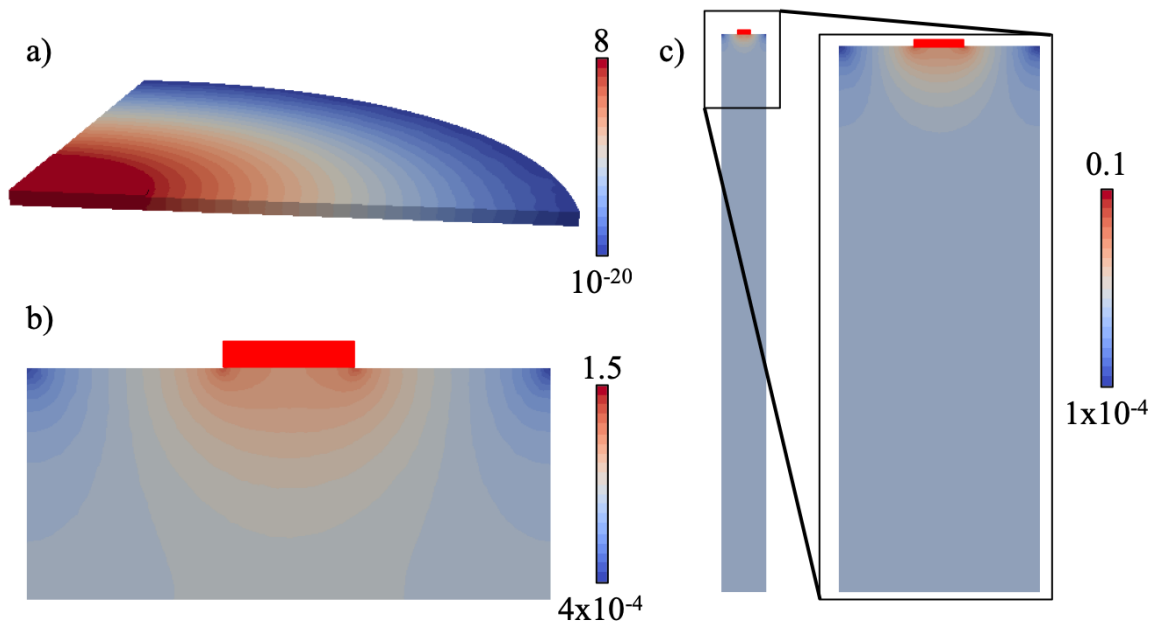


Figure 4.11. Simulated current density plots for the MTFB models with a micro-contact radius of  $25.39\ \mu\text{m}$  with  $s/r$  values of a) 0.1, b) 3.5 and c) 100. Scale bar is in units of  $\text{A}/\text{m}^2$ .

At an  $s/r$  value of 0.1, Figure 4.11 (a), the current is concentrated in the region directly beneath the micro-contact and appears to flow mainly over an area equal to the micro-contact area. Although the lower surface is a full contact, the current is not evenly distributed on this surface. The current density decreases rapidly away from the micro-contact and is 20 orders of magnitude smaller at the edge of the model. As a consequence, the geometric factor using the micro-contact area gives the best estimation of the conductivity, Figure 4.10. At an  $s/r$  value of 3.5, Figure 4.11 (b), there is enough space for the current to fill the model and the current density remains heterogeneous and therefore the spreading resistance equation gives the best

estimation of the conductivity. For large  $s/r$  values such as 100, Figure 4.11 (c), the current density is heterogeneous in the vicinity of the micro-contact but is homogeneous for the majority of the model and therefore the geometric factor using the model area gives the best estimation of the conductivity.

To study the effects of confinement using a top-top geometry, a cubic model initially of side length  $500\ \mu\text{m}$ , with  $s/r = 1, 2$  and  $4$ , was decreased in size until the contacts were  $2.5\ \mu\text{m}$  from the sides on the top surface and the conductivity calculated using the spreading resistance equation, Figure 4.12.

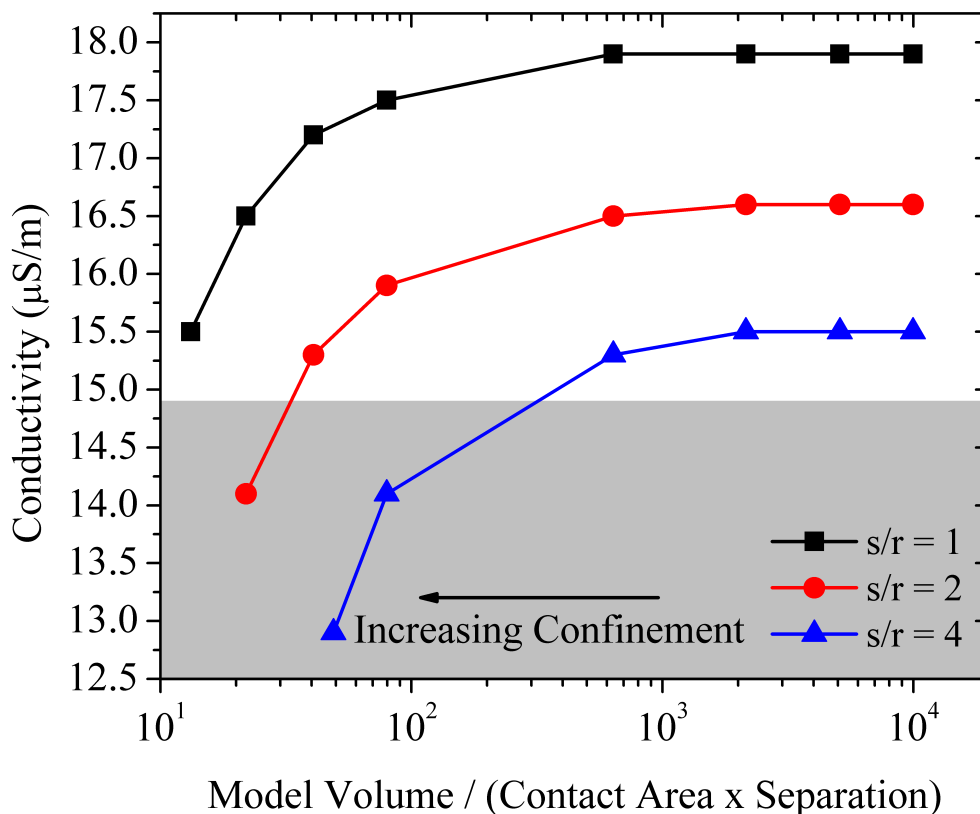


Figure 4.12. Calculated conductivity for cubic MTT models using the spreading resistance equation plotted against the confinement provided by the size of the model. The grey box represents the input conductivity  $\pm 10\%$ .

Initially as the grains decrease in size (from right to left) there is no effect on the calculated conductivity as the effect of confinement is very small, Figure 4.12. Eventually, the size of the model starts to have an effect on the response, decreasing the calculated conductivity. Keeping the grains cubic limits the amount of confinement that can be simulated. To simulate higher levels of confinement, the size of the grains was then decreased in each direction sequentially.

Again,  $s/r$  values of 1, 2 and 4 were used as these were comparable to those used in previous studies<sup>19,21,23</sup> and also compared to an  $s/r = 30$ , giving conductivities within 5% of the input

conductivity for an unconfined case. The change in calculated conductivity with the level of confinement provided by the size of the model is shown in Figure 4.13. Confinement in each direction was changed sequentially. The models were initially shrunk in the x-direction, then in y- and finally in the z-direction (from right to left in Figure 4.13). It was previously shown that at small separations with respect to the micro-contact size ( $s/r$ ) and when confinement has no effect on the response, Figure 4.7 (b) and far right in Figure 4.13 (a), the conductivity is overestimated using the spreading resistance equation. Initially as the size decreases the calculated conductivity does not change until confinement starts to influence the response. The calculated conductivity first starts decreasing when the distance to the edge of the model is 1.5 times the micro-contact radius. With increasing confinement, the calculated conductivity continues to further decrease below the input conductivity. In contrast, if the geometric factor using the cross-sectional area of the model and the contact separation is used, Figure 4.13 (b), the conductivity is initially underestimated and approaches the input conductivity with increasing confinement. The approximation is within  $\pm 10\%$  of the input conductivity for the most confined model considered with  $s/r = 30$ , filled turquoise triangles in Figure 4.13 (b).

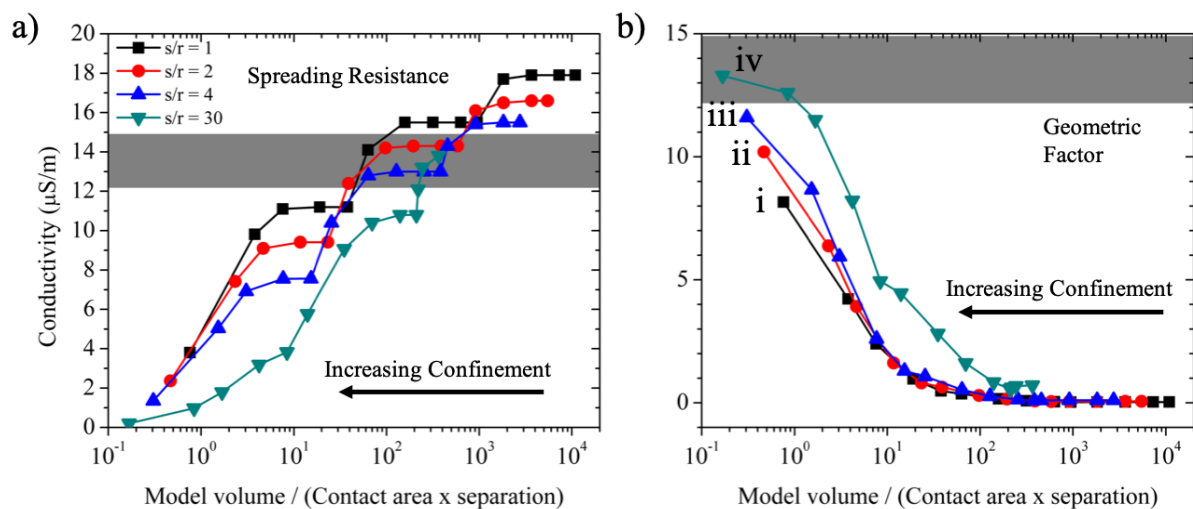


Figure 4.13. Calculated conductivity for MTT models using a) the spreading resistance equation and b) the geometric factor plotted against the confinement provided by the size of the model. The grey box represents the input conductivity  $\pm 10\%$ . The points labelled i-iv in b) are the models used in Figure 4.14 and Figure 4.15.

Current density plots for the models with  $s/r = 1$  and 30 highlighted in Figure 4.13 (b) are shown in Figure 4.14. The current density is heterogeneous across the micro-contacts and is greatest at the close edges of the contacts. At  $s/r = 1$  where the model shows both confinement and interference, Figure 4.14 (a), the current density remains heterogeneous between the micro-contacts. In contrast at  $s/r = 30$  which shows confinement only, Figure 4.14 (b), the current density is homogeneous between the micro-contacts.

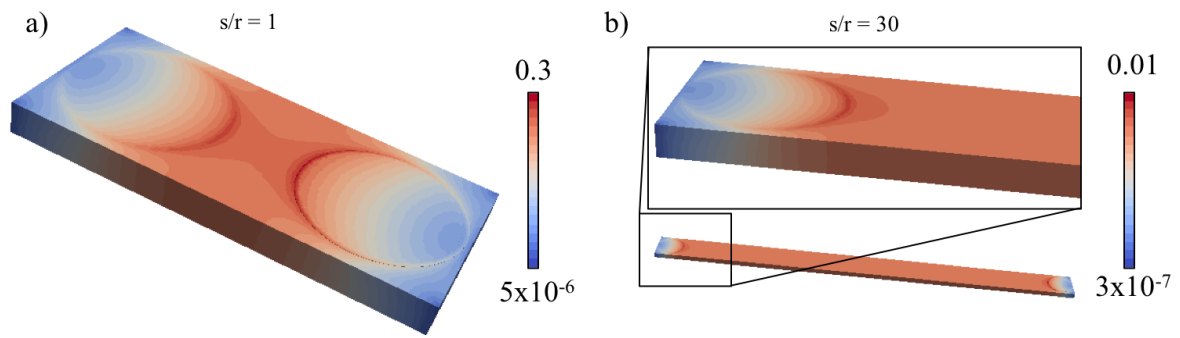


Figure 4.14. Simulated current density plots of models i and iv in Figure 4.13 with a)  $s/r = 1$  and b)  $s/r = 30$ . Scale bar is in units of  $A/m^2$ .

The change in current density along the x-axis through the centre of the cross section for the most confined models (points labelled i-iv in Figure 4.13) is shown in Figure 4.15. The models had a height of  $10\ \mu\text{m}$  and a width of  $60\ \mu\text{m}$ . The length,  $x$ , of each model was 130, 160, 210 and  $865\ \mu\text{m}$  for the models with  $s/r = 1, 2, 4$  and 30, respectively (micro-contact radius  $25.39\ \mu\text{m}$ ). The current density is plotted against the normalised x-axis for ease of comparison. The current density is negligible at the edges of the model compared to between the micro-contacts and peaks at the close edges of the micro-contacts. As  $s/r$  increases, the current density becomes more homogeneous between the micro-contacts as interference is reduced.

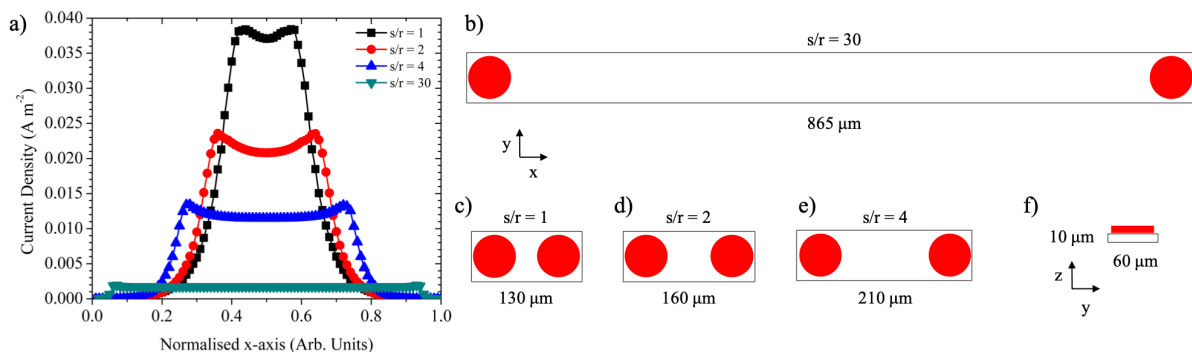
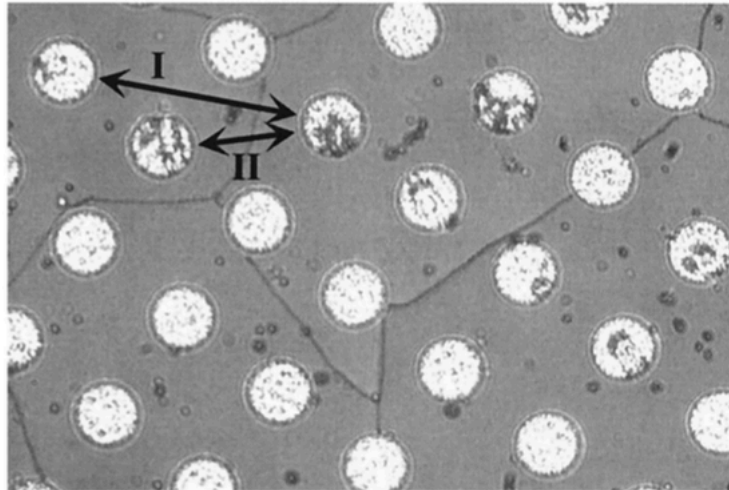


Figure 4.15. a) Current density plotted along a line through the centre of the cross-sectional area of the most confined models (points labelled i-iv in Figure 4.13). Schematics of the most confined models for  $s/r$  of b) 30, c) 1, d) 2 and e) 4. f) Cross-section of models b-e).

Although the effects of confinement presented above are clear, many of the simulated systems would be challenging to measure experimentally; therefore, realistic grain sizes were modelled to determine the effects of confinement. Rodewald et al.<sup>20</sup> measured the impedance response of Fe-doped  $\text{SrTiO}_3$  polycrystals using a top-top configuration. Their samples had a mean grain size of  $56\ \mu\text{m}$  and they employed micro-contacts with a  $20\ \mu\text{m}$  diameter and separation. An image taken from Rodewald et al.<sup>20</sup> is shown in Figure 4.16.



*Figure 4.16. Image showing a sample region used to measure impedance spectra in Rodewald et al.<sup>20</sup>. Micro-contacts have a diameter of 20  $\mu\text{m}$ . Reprinted Fig. 1 (c) from Rodewald et al.<sup>20</sup> with permission from John Wiley and Sons.*

There will be a distribution of grain sizes in polycrystalline samples so although the mean grain size is 56  $\mu\text{m}$ , there will be grains much larger than this. In order to fit two 20  $\mu\text{m}$  diameter micro-contacts within the same grain with the same separation, a minimum grain size of around 65  $\mu\text{m}$  is required (leaving 2.5  $\mu\text{m}$  between each contact and the grain boundary). 140  $\mu\text{m}$  grains are the largest grains Rodewald et al.<sup>20</sup> measured, assuming Figure 4.16 shows the largest grains. Thus, cubic grains with a size of 65 and 140  $\mu\text{m}$  with two 20  $\mu\text{m}$  diameter micro-contacts were simulated at different separations that could fit the two contacts within the same grain. The contacts were located such that the centre of the surface was also the mid-point between the contacts and the distance to the edge of the model was at least 2.5  $\mu\text{m}$ . The calculated conductivity plotted against  $s/r$  for the grain sizes described above are shown in Figure 4.17 and compared to when confinement effects are negligible, such as in a single crystal (black squares).

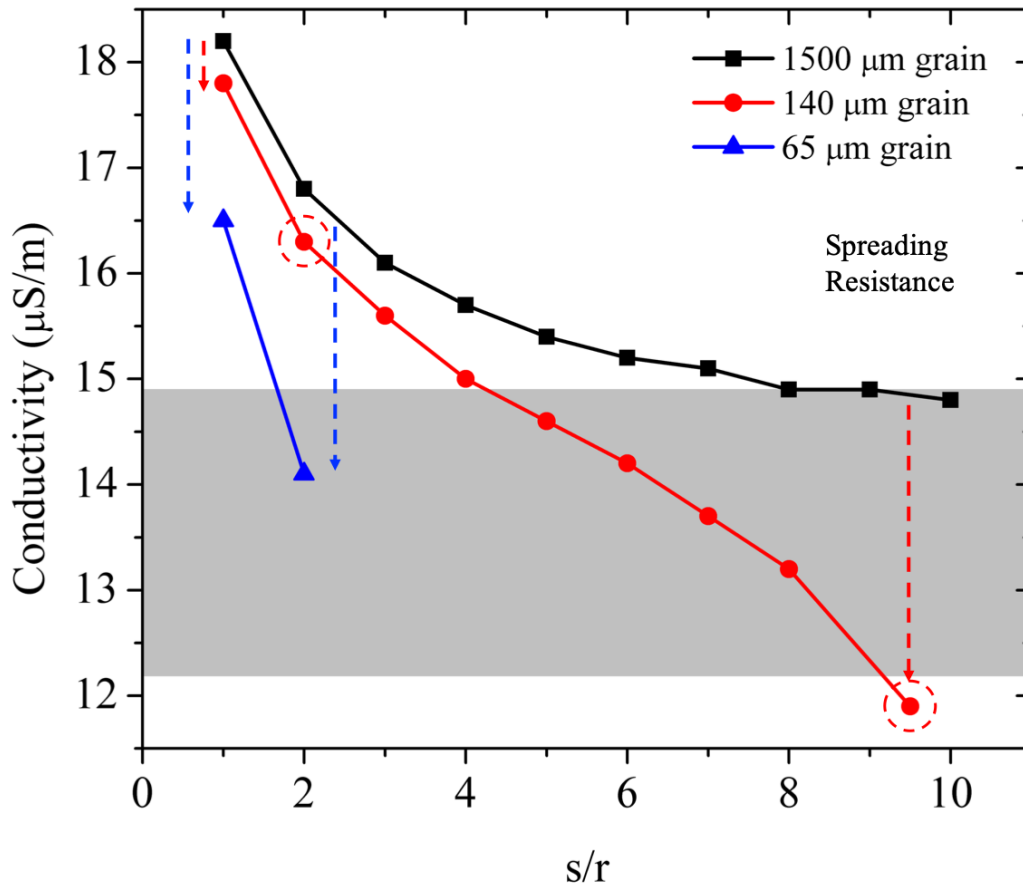


Figure 4.17. Calculated conductivity using the spreading resistance equation plotted against the ratio of contact separation,  $s$ , over the micro-contact radius,  $r$ , for cubic grains that are 140 and 65  $\mu\text{m}$  in size and a micro-contact radius of 10  $\mu\text{m}$ . Also plotted is when the grain is 1500  $\mu\text{m}$ , when effects of confinement are negligible. The grey box represents the input conductivity  $\pm 10\%$ . Circled points are the models shown in Figure 4.18. Dashed arrows show the difference in the calculated conductivity between the models with significant confinement effects and the model with negligible confinement effects.

The calculated conductivity for the single crystal data, when confinement effects from the size of the model are negligible (black squares in Figure 4.17), converges to the input conductivity at  $s/r \sim 8$ , as in Figure 4.7. Extra resistances arise in smaller grains due to the limited size of the grain, decreasing the calculated conductivity. At  $s/r = 1$ , the calculated conductivity in the 140  $\mu\text{m}$  grain is only slightly lower than in the single crystal. The conductivity decreases further for the 65  $\mu\text{m}$  grain, shown by the dashed red and blue arrows, respectively in Figure 4.17. As  $s/r$  increases and the contacts approach the edges of the grains, the amount the calculated conductivity deviates from the single crystal increases.

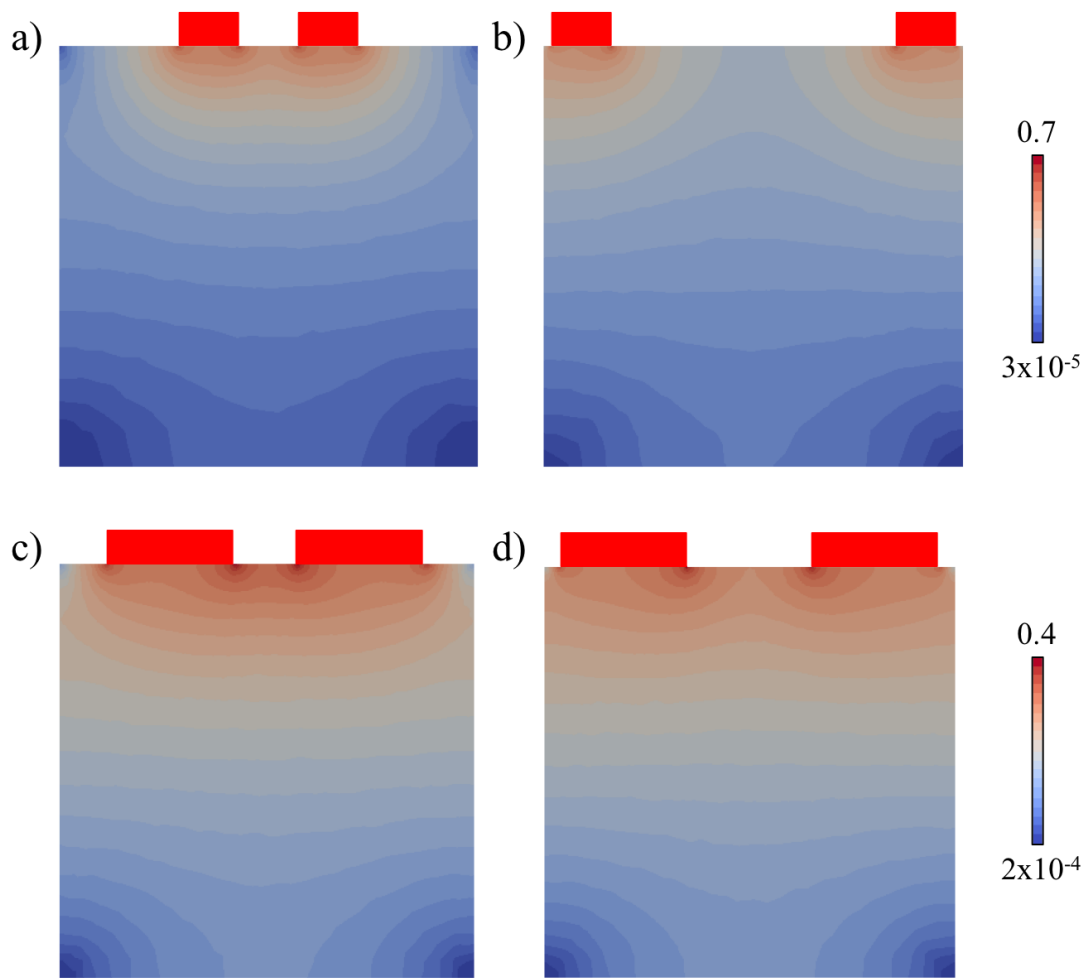


Figure 4.18. Simulated current density plots of MTT models with a, b) 140  $\mu\text{m}$  grain and c, d) 65  $\mu\text{m}$  grain and 20  $\mu\text{m}$  diameter micro-contacts with separations of a) 20  $\mu\text{m}$ , b) 95  $\mu\text{m}$ , c) 10  $\mu\text{m}$  and d) 20  $\mu\text{m}$ . Scale bar is in units of  $\text{A}/\text{m}^2$ .

Current is able to spread out in all directions when the micro-contacts are not close to the edges of the model, Figure 4.18 (a). When the contacts approach the edges of the model, current flow is limited and not able to spread out in all directions, Figure 4.18 (b). Accurate conductivities ( $\pm 10\%$  input conductivity) are extracted with 20  $\mu\text{m}$  diameter contacts with a separation of 20  $\mu\text{m}$  in 65  $\mu\text{m}$  grains, the smallest grains that could reasonably be measured by Rodewald et al.<sup>20</sup>, because of the reduction in the calculated conductivity from confinement. Similarly, an  $s/r$  of 4-9 is required for accurate conductivities in the largest grains (140  $\mu\text{m}$ ) simulated here.

The amount of confinement in the x-y plane can be directly observed; however, confinement in the z-plane is unknown. The thickness of the cubic grains was then decreased (for a 140  $\mu\text{m}$  grain, thicknesses of 140, 70, 35 and 10  $\mu\text{m}$  were simulated and for the 65  $\mu\text{m}$  grain, thicknesses of 65, 30 and 10  $\mu\text{m}$ ) to simulate this effect and the conductivity calculated for the smallest and largest contact separation of each grain size modelled in Figure 4.17, Figure 4.19.

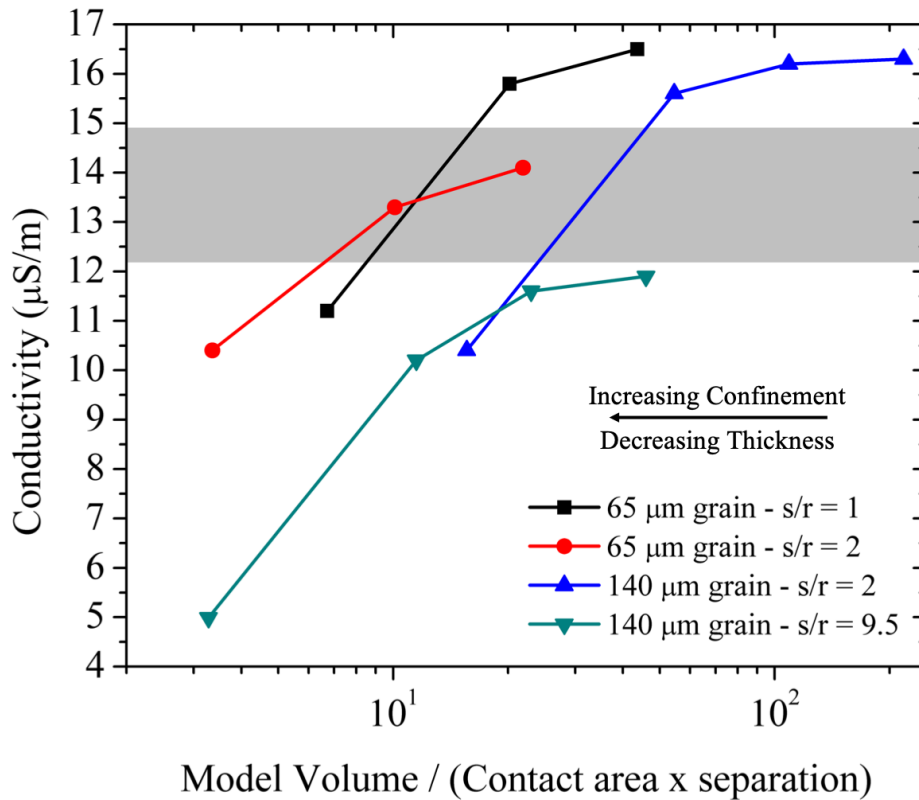


Figure 4.19. Calculated conductivity using the spreading resistance equation plotted against the confinement provided by the size of the model. The grey box represents the input conductivity  $\pm 10\%$ .

For each data set in Figure 4.19, the point furthest right on the plot represents the models with cubic grains. As the thickness of each model decreases (right to left in Figure 4.19), the calculated conductivity decreases. As the thickness of a grain cannot be measured, the amount of confinement is unknown when taking micro-contact measurements on a polycrystalline sample, meaning significant deviations from the actual (input) conductivity can arise, Figure 4.19.

Above, the confinement is produced by the limited size of the model. However, confinement could be generated by other effects such as insulating grain boundaries or secondary phases. To confirm this a second material with a conductivity three orders of magnitude lower ( $\epsilon_r$  assumed to be the same as the grain) was defined around the model (to mimic a grain embedded in an epoxy such as shown in Rettenwander et al.<sup>21</sup> and in Figure 4.20) with a grain size of 65  $\mu\text{m}$  and micro-contact diameter and separation of 20  $\mu\text{m}$  ( $s/r = 2$ ) and the impedance response simulated. The thickness of the epoxy was varied from 1 to 50  $\mu\text{m}$ .

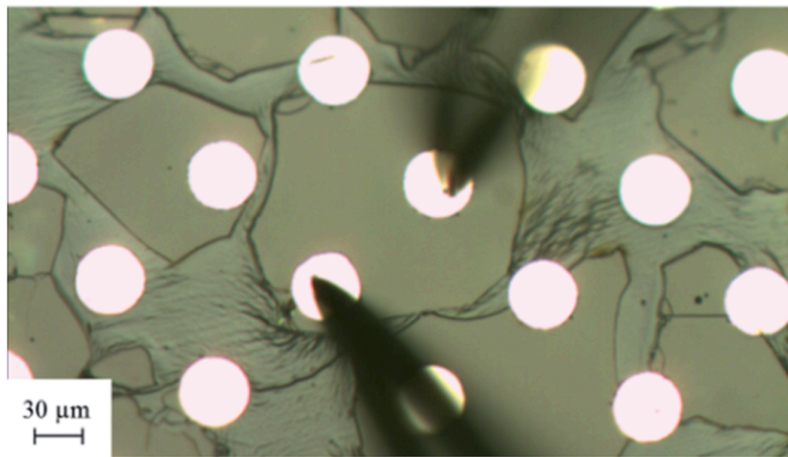


Figure 4.20. Image showing a sample region of embedded and polished single crystals with patterned electrodes  $30\ \mu\text{m}$  in diameter, used to measure the impedance in Rettenwander et al.<sup>21</sup>. Reprinted Fig. 2 from Rettenwander et al.<sup>21</sup> with permission from the Royal Society of Chemistry.

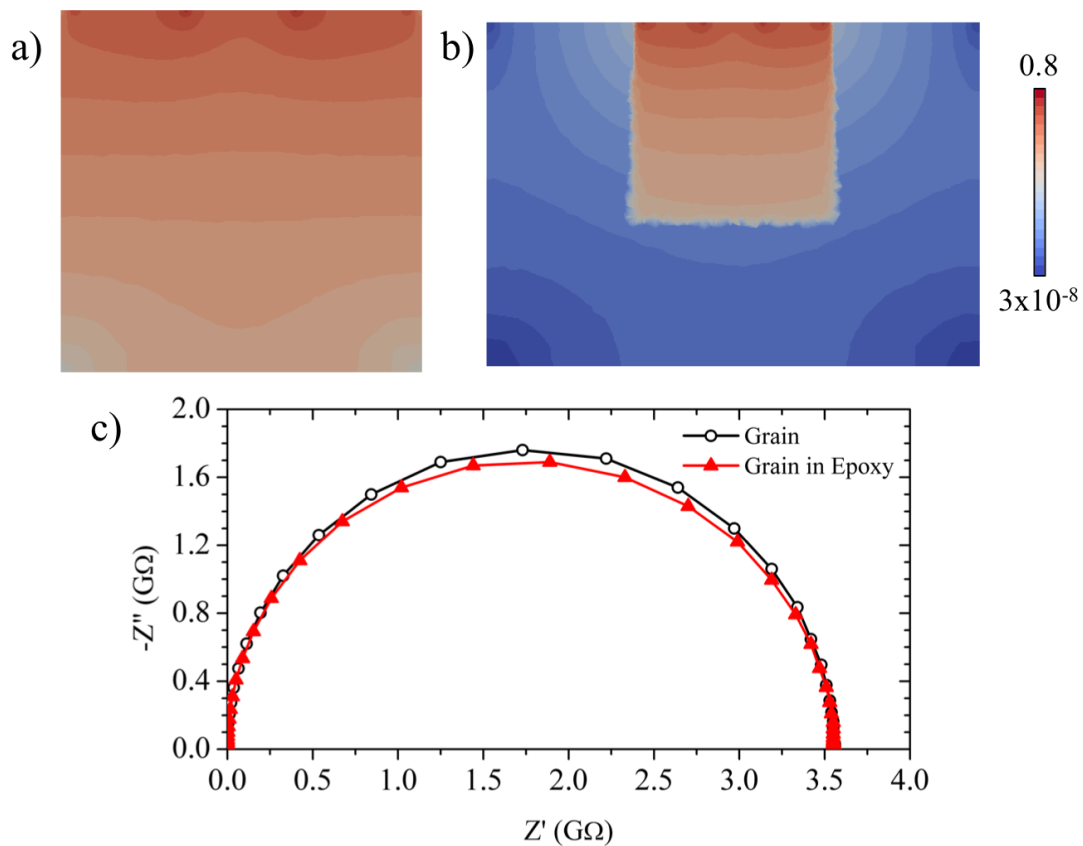


Figure 4.21. Simulated current density plots for a MTT model with a  $65\ \mu\text{m}$  cubic grain and micro-contact diameter and separation of  $20\ \mu\text{m}$  which is a) confined by the limited size of the model and b) the same grain confined by a second resistive material which has a thickness of  $50\ \mu\text{m}$ , representing a grain embedded in epoxy. Scale bar is in units of  $A/m^2$ . c) Complex impedance plots for the models in a) and b).

The simulated current density and impedance response for the models described above are shown in Figure 4.21. The current density within the grain looks similar whether it is confined

by the size of the model, Figure 4.21 (a), or by an insulating epoxy, Figure 4.21 (b). The magnitude of the current density is much lower in the epoxy. The arc in the complex impedance crosses the real axis at the same point in both models and no extra response from the epoxy can be resolved, Figure 4.21 (c). This was true for all epoxy thicknesses modelled. The main difference in the complex impedance plot is there is a non-ideal response, shown by the slight depression in the arc for the model embedded in epoxy. The non-ideality occurred for all epoxy thicknesses modelled but was most pronounced when it was 50  $\mu\text{m}$  thick.

#### 4.4 Discussion

Using the geometric factor, Equation 4.1, for the FTB models allows us to validate our FEM approach. At all separations, the calculated conductivity of the sample corresponds to the input value of conductivity, Figure 4.2. As expected, current flow is homogeneous through the sample, Figure 4.4 (a) and Figure 4.5, in agreement with previous studies<sup>6</sup>, and so these measurements obtain average electrical properties.

The geometric factor assumes a cylinder of constant volume defined by the micro-contact area and distance of separation; however, the current within the sample spreads out over a larger effective area compared to that defined by the micro-contact(s) and thus there is a reduction in the measured resistance. The geometric factor, Equation 4.1, therefore overestimates the conductivity when using micro-contacts, Figure 4.2. When the micro-contact radius was 25.39  $\mu\text{m}$ , covering 56.25% of the surface, the geometric factor provides a good approximation of the conductivity to within 100% of the input value, Figure 4.2. This is because the current flow is still relatively homogeneous as shown in Figure 4.4 (b) and (e) and Figure 4.5. The approximation is particularly accurate at small separations. The majority of the electrical response originates from a region directly beneath the micro-contact<sup>9,10,14</sup>, defined here as a region of high current density. This region has a radius four times the micro-contact radius<sup>10</sup>. In the models with large contacts and small separations, this region (theoretically) extends further than the separation of the contacts, Figure 4.22 (a) and (b). Due to this, spreading from the micro-contact is limited and so current flow is more homogeneous, Figure 4.5 (c).

As the separation of the contacts increases, the region of high current density becomes fully contained within the model, Figure 4.22 (d) and (e) and heterogeneities in the current flow become more pronounced. This suggests the spreading resistance is now the dominant effect in the electrical response. For this reason, the geometric factor no longer provides an accurate approximation.

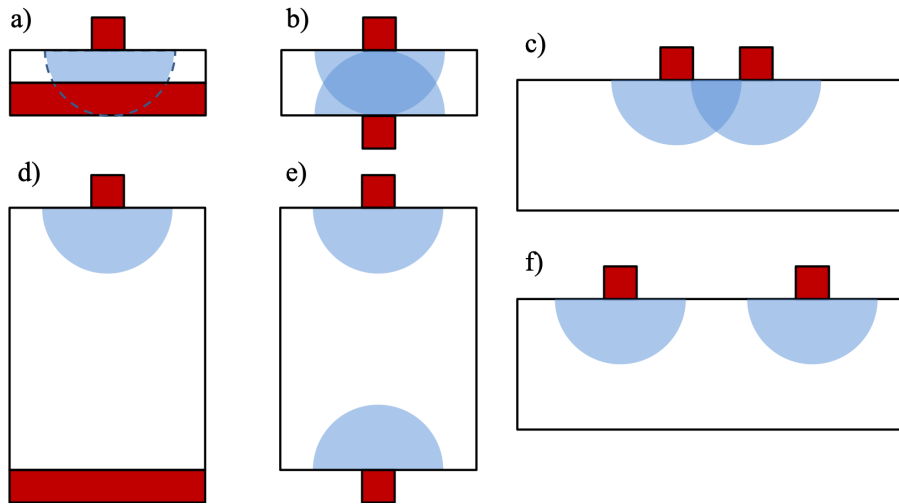


Figure 4.22. Schematic showing the region of high current density (blue hemisphere) for a) MTFB, b) MTB and c) MTT at small separation and d) MTFB, e) MTB and f) MTT at large separation.

When the micro-contact radius was  $0.34\ \mu\text{m}$ , covering 0.01% of the surface, the heterogeneity in the current density is most pronounced, Figure 4.4 (d) and (g) and Figure 4.5. The spreading resistance therefore provides an accurate approximation of the input conductivity (to within 10% error). That is not to say there is no homogeneous current flow present but its contribution is negligible compared to the response in the vicinity of the micro-contact due to the spreading resistance. This can be observed in the conduction pathway trajectories in Figure 4.4 (d) and (g), where close to the micro-contacts there is a lot of curvature but away from the contacts the trajectory is much more linear and also in Figure 4.5 where the current density is greatest at the surface and decreases rapidly (i.e. is heterogeneous) until remaining relatively constant (homogeneous) after a depth of  $\sim 40\ \mu\text{m}$ . Over 90% of the current density originates in a region that is  $\sim 2\ \mu\text{m}$  (MTFB) and  $3\ \mu\text{m}$  (MTB) from the micro-contacts, open blue triangles in Figure 4.5 (a) and (b), and thus obtain local electrical properties.

In summary, the geometric factor gives the best approximation for homogeneous current flow, providing average electrical properties and the spreading resistance equation gives the best approximation for heterogeneous current flow, providing local electrical properties.

In the models with two micro-contacts on the top surface (MTT), the geometric factor does not accurately represent the current flow, Figure 4.6, because there is insignificant homogeneous current flow, Figure 4.8 and Figure 4.9. Due to the heterogeneous current flow, the spreading resistance equation provides the best approximation of the conductivity. The response is dominated by the small volume directly beneath the micro-contacts, evident by the regions of high current density in Figure 4.8 and Figure 4.9.

The four sharp peaks in the current density plot occur at the edges of the micro-contacts, Figure 4.9, suggesting the majority of the conduction of current occurs through the circumference of the micro-contact, in agreement with previous studies<sup>24</sup>. When the separation between the micro-contacts is small the peaks in current density from the edge of the contacts merge and the calculated conductivity is overestimated, Figure 4.7. This is attributed to contact interference<sup>15</sup> which occurs when the regions of high current density overlap, Figure 4.22 (c). The current density away from the micro-contacts is negligible at all separations, again supporting the suggestion that micro-contact geometries provide local electrical properties.

When making micro-contact measurements, the most important factor to take into account is the ratio of the separation over the radius of the micro-contacts (not simply the size or separation alone). Due to the heterogeneous current flow, the spreading resistance equation provides the best approximation of the conductivity, converging to the input conductivity at larger  $s/r$ , Figure 4.7. At small  $s/r$ , the conductivity is overestimated because of contact interference. Small increases in  $s/r$  significantly improve the accuracy of the spreading resistance equation and calculated conductivities can be within 10% error at  $s/r \sim 8$ , Figure 4.7. For further increases in  $s/r$ , the gain in accuracy becomes less significant with increasing  $s/r$  and to achieve a conductivity within 5% error requires an  $s/r \sim 28$ . Such large separations may not be experimentally feasible. Previous studies<sup>20,21</sup> have used  $s/r$  of 2 and 4 which will overestimate the conductivity by 23 and 15%, respectively. To account for the overestimate of conductivity due to contact interference, we suggest applying a correction factor of 0.81 and 0.87, respectively. The correction factors suggested in Figure 4.7 are only applicable to an unconfined case.

Confinement occurs when the electrical properties of a material can be calculated by a geometric factor because of some limitation in the current flow through the model or sample. An example is when the contacts are the full top and bottom surfaces of the sample. Current flow is homogeneous, Figure 4.4 (a) and flows through the cross-sectional area of the sample over the thickness of the sample. However, confinement can also occur with micro-contacts in a top-bottom geometry. With micro-contacts, at separations much smaller than the micro-contact radius the current does not have the space required to spread into the rest of the sample. As a consequence, most of the current will pass straight to the second electrode homogeneously with little spreading, Figure 4.11, meaning the geometric factor using the micro-contact area provides the most accurate approximation for the conductivity, Figure 4.10.

Alternatively, if the separation is very large, the current spreads out to fill the model and then remains homogenous for the majority of the sample, Figure 4.11 (c), meaning as the separation

increases, the effect of spreading resistance becomes negligible. Hence, at very large separations the geometric factor using the model area gives the best approximation for the conductivity, despite using micro-contacts, Figure 4.10. The  $s/r$  value required for this to be true increases as the micro-contact size decreases.

Thus, there are two confinement regimes. Confinement at very small and very large  $s/r$  values. At intermediate  $s/r$  values the spreading resistance provides the most accurate approximation. At these values, current flow remains heterogeneous throughout the model, Figure 4.11 (b). The size of this intermediate region is dependent on the size of the micro-contact and increases as the micro-contact size decreases. Experimental measurements using the MTFB geometry would typically use micro-contacts that are 10s of  $\mu\text{m}$  in size, where the sample surface area is much larger (unconfined for single crystals) and thicknesses (contact separation) of  $\sim 1$  mm. Because of this, measurements will generally be within the intermediate spreading regime, Figure 4.10 (c), so the spreading resistance equation will give the most accurate conductivities and effects of confinement will be negligible.

Confinement can also occur using the top-top geometry and acts in a similar way to that described above at large  $s/r$  values. This only occurs at extreme cases of confinement, such as in Figure 4.15 (b)-(f). In these cases, the spreading resistance equation becomes less reliable and the geometric factor becomes a better approximation for the conductivity, see Figure 4.13 (b). This occurs because the current spreads out to fill the full model, and then flows homogeneously between the two micro-contacts. The geometric factor is most accurate at large  $s/r$  values with large amounts of confinement, Figure 4.13 (b, turquoise triangles) and Figure 4.15, because the current flow is predominantly homogeneous. At smaller  $s/r$  values, black squares in Figure 4.15, the current density between the micro-contacts remains heterogeneous as the separation is too small for the current to fill the model and flow homogeneously, Figure 4.14. The current density drops close to zero behind the micro-contact, Figure 4.14 and Figure 4.15, showing current does not spread out in all directions; instead it only flows between the micro-contacts.

The top-top models described above are very extreme cases of confinement and are not representative of realistic situations experimentally. Their purpose is to aid in understanding how confinement can affect the electrical response of materials. Confinement will occur when using micro-contacts but not to such extreme amounts where a geometric factor can be used to describe the current flow in a system. Instead, confinement will only partially influence the current flow, changing the measured resistance in modest but significant amounts. When cubic grains with realistic dimensions<sup>20</sup> were modelled, the calculated conductivity was lower than

equivalent  $s/r$  values in a model with negligible confinement, Figure 4.17. The conductivity decreased further as the micro-contacts approach the edges of the model. This occurs because the current is unable to spread out in all directions in equal amounts, confining the current flow in certain directions, Figure 4.18. For a single crystal (unconfined) we suggest using an  $s/r \sim 8$  for conductivities within 10% error. For small grains ( $\sim 65 \mu\text{m}$ ) using an  $s/r$  of 2 gives accurate conductivities and for relatively large grains ( $\sim 140 \mu\text{m}$ )  $s/r > 4$  is required (both based on resistive grain boundaries with conductivity 3 orders of magnitude lower than the grain). When the thickness of the grains (a quantity unobservable in experimental measurements based on an optical probe station) was decreased, the calculated conductivity decreased further because of an increasing amount of confinement, Figure 4.19. It is therefore evident that although small  $s/r$  values ( $\sim 2$ ) would overestimate the conductivity, confinement from the size of the grain can decrease the calculated conductivity, providing fortuitously accurate results<sup>9,20,21</sup>. Careful consideration of the physical microstructure must therefore be taken into account when such measurements are performed. Whilst confinement on the surface (in the  $x$ - $y$  plane) can be directly observed in a probe station, it is not possible (optically) to determine the confinement under the micro-contact, in the  $z$ -plane.

If measurements are to be performed within a single grain in a film or ceramic, insulating grain boundaries or epoxies can produce confinement. Current density plots, Figure 4.21 (a) and (b), show limited current flow through the insulating epoxy as compared to the grain. Although the response will be non-ideal, using the low frequency intercept in the complex impedance plane plot will obtain a grain resistance which can be analysed as the grain conductivity, Figure 4.21 (c), and an arc representing the insulating epoxy is not observed.

## 4.5 Conclusions

The electrical response of a sample has been simulated for different electrode geometries. The geometric factor gives the best approximation for the conductivity when there is homogeneous current flow. For heterogeneous current flow, the spreading resistance equation gives the best approximation. Confinement, where a geometric factor can be used to describe the current flow, occurs for micro-top full-bottom geometries at very large or very small separations compared to the size of the micro-contact. For very large separations, the current is able to fill the model and flow homogeneously throughout the majority of the model. For very small separations, the current does not have enough room to spread out to fill the model, so the majority of current flow is over an area equal to the micro-contact area.

For measurements between two micro-contacts on the same surface, because the current density is predominantly heterogeneous, the spreading resistance equation produces the most reliable approximation, particularly at separations exceeding 8 times the micro-contact radius. Limiting the separation of the contacts overestimates the calculated conductivity. When the separation is twice the micro-contact radius, the calculated conductivity is greater than the input conductivity by 23%, requiring a correction factor of 0.81 to account for contact interference. Shrinking the size of the model and thus increasing the confinement decreases the calculated conductivity. In some cases, the reduction in the calculated conductivity from confinement can counter-balance the enhancement of the calculated conductivity from the close separation of the micro-contacts, obtaining what appears to be accurate conductivities. Insulating grain boundaries or epoxies can produce confinement and grain conductivities can be calculated from the intercept in complex impedance plots. If making measurements of a single grain using an optical probe station, care must be taken as the amount of confinement in the z-plane is unknown.

#### 4.6 References

1. Veazey, R. A., Gandy, A. S., Sinclair, D. C. & Dean, J. S. Modeling the influence of two terminal electrode contact geometry and sample dimensions in electro-materials. *J. Am. Ceram. Soc.* Available on-line <https://doi.org/10.1111/jace.16236> (2018).
2. Irvine, J. T. S., Sinclair, D. C. & West, A. R. Electroceramics: Characterization by Impedance Spectroscopy. *Adv. Mater.* **2**, 132–138 (1990).
3. Sinclair, D. C. Characterization of Electro-materials using ac Impedance Spectroscopy. *Bol. La Soc. Esp. Ceram. y Vidr.* **34**, 55–66 (1995).
4. Dean, J. S., Harding, J. H. & Sinclair, D. C. Simulation of Impedance Spectra for a Full Three-Dimensional Ceramic Microstructure Using a Finite Element Model. *J. Am. Ceram. Soc.* **97**, 885–891 (2014).
5. Hwang, J. H., Kirkpatrick, K. S., Mason, T. O. & Garboczi, E. J. Experimental Limitations in Impedance Spectroscopy: Part IV. Electrode Contact Effects. *Solid State Ionics* **98**, 93–104 (1997).
6. Heath, J. P., Dean, J. S., Harding, J. H. & Sinclair, D. C. Simulation of Impedance Spectra for Core-Shell Grain Structures Using Finite Element Modeling. *J. Am. Ceram. Soc.* **98**, 1925–1931 (2015).
7. Fleig, J. & Maier, J. Point contacts in solid state ionics: Finite element calculations and

- local conductivity measurements. *Solid State Ionics* **86–88**, 1351–1356 (1996).
8. Lee, J. S., Fleig, J., Maier, J., Kim, D. Y. & Chung, T. J. Local conductivity of nitrogen-graded zirconia. *J. Am. Ceram. Soc.* **88**, 3067–3074 (2005).
  9. Rodewald, S., Fleig, J. & Maier, J. Measurement of conductivity profiles in acceptor-doped strontium titanate. *J. Eur. Ceram. Soc.* **19**, 797–801 (1999).
  10. Fleig, J. Local conductivity measurements on AgCl surfaces using microelectrodes. *Solid State Ionics* **85**, 9–15 (1996).
  11. Fleig, J. Microelectrodes in solid state ionics. *Solid State Ionics* **161**, 279–289 (2003).
  12. Rupp, G. M., Opitz, A. K., Nenning, A., Limbeck, A. & Fleig, J. Real-time impedance monitoring of oxygen reduction during surface modification of thin film cathodes. *Nat. Mater.* **16**, 640–645 (2017).
  13. Fleig, J., Rodewald, S. & Maier, J. Spatially resolved measurements of highly conductive and highly resistive grain boundaries using microcontact impedance spectroscopy. *Solid State Ionics* **136–137**, 905–911 (2000).
  14. Fleig, J. & Maier, J. Microcontact impedance measurements of individual highly conductive grain boundaries: General aspects and application to AgCl. *Phys. Chem. Chem. Phys.* **1**, 3315–3320 (1999).
  15. Holm, R. *Electric Contacts*. (Springer, 1967).
  16. Fleig, J. in *Advances in Electrochemical Science and Engineering* (ed. Alkire, R. C.) **8**, 1–79 (Wiley-VCH, 2002).
  17. Li, M., Pietrowski, M. J., De Souza, R. A., Zhang, H., Reaney, I. M., Cook, S. N., Kilner, J. A. & Sinclair, D. C. A family of oxide ion conductors based on the ferroelectric perovskite  $\text{Na}_{0.5}\text{Bi}_{0.5}\text{TiO}_3$ . *Nat Mater* **13**, 31–35 (2014).
  18. Li, L., Li, M., Zhang, H., Reaney, I. M. & Sinclair, D. C. Controlling mixed conductivity in  $\text{Na}_{1/2}\text{Bi}_{1/2}\text{TiO}_3$  using A-site non-stoichiometry and Nb-donor doping. *J. Mater. Chem. C* **4**, 5779–5786 (2016).
  19. Fleig, J., Rodewald, S. & Maier, J. Microcontact impedance measurements of individual highly resistive grain boundaries: General aspects and application to acceptor-doped  $\text{SrTiO}_3$ . *J. Appl. Phys.* **87**, 2372 (2000).
  20. Rodewald, S., Fleig, J. & Maier, J. Microcontact Impedance Spectroscopy at Single Grain Boundaries in Fe-Doped  $\text{SrTiO}_3$  Polycrystals. *J. Am. Ceram. Soc.* **84**, 521–530

- (2001).
21. Rettenwander, D. , Welzl, A., Pristat, S., Tietz, F., Taibl, S., Redhammer, G. J. & Fleig, J. A microcontact impedance study on NASICON-type  $\text{Li}_{1+x}\text{Al}_x\text{Ti}_{2-x}(\text{PO}_4)_3$  ( $0 \leq x \leq 0.5$ ) single crystals. *J. Mater. Chem. A* **4**, 1506–1513 (2016).
  22. ParaView Homepage <https://www.paraview.org/> (accessed 01/2016).
  23. Lee, J. S., Fleig, J., Maier, J., Chung, T. J. & Kim, D. Y. Microcontact impedance spectroscopy in nitrogen-graded zirconia. *Solid State Ionics* **176**, 1711–1716 (2005).
  24. Nakamura, M. Constriction Resistance of Conducting Spots. *IEEE Trans. Components, Hybrids, Manuf. Technol.* **16**, 339–343 (1993).

# **Chapter 5: Measuring the Electrical Properties of Resistive Surface Layers by Micro-contact Impedance Spectroscopy**

## **5.1 Introduction**

In the previous chapter the electrical response of a homogeneous material using micro-contacts was simulated to understand how best to analyse data and to understand the effects of confinement and contact interference. In this chapter, the simulations are extended to include a second material to understand how these effects differ and the best method for extracting accurate intrinsic properties of both a surface layer and the underlying bulk material.

Micro-contact Impedance Spectroscopy has previously been used to characterise surface layers in materials. Work performed by Fleig<sup>1</sup> measured mechanically-produced highly conducting surface layers in AgCl using micro-contacts; however, the analysis infers a surface layer conductivity from changes in the bulk measurement, rather than measuring the surface layer itself. Navickas et al.<sup>2</sup> measured Yttria Stabilised Zirconia (YSZ) thin films (20-90 nm in thickness) on a silicon substrate by micro-contact impedance measurements, in which they used a geometric factor to determine the layer conductivity and the spreading resistance equation to calculate the Si conductivity. The size of the micro-contacts (80 – 200  $\mu\text{m}$ ) were much larger than the thickness of the YSZ layer in this case.

The surface layers of interest in this project are damage regions induced by ion implantation. As these surface layers are thin, typically 1  $\mu\text{m}$  of a 1 mm thick sample, the response from the surface layer would be difficult to measure by conventional Impedance Spectroscopy measurements, which obtain measurements across the full sample thickness.

This chapter aims to justify the use of micro-contacts for Impedance Spectroscopy measurements of resistive surface layers, particularly for a thickness of 1  $\mu\text{m}$ , and provide a method for analysing data to find the conductivity of the surface layer. This is extended to larger surface layer thicknesses to determine how the method of analysis changes. The impedance response of resistive surface layers in the range of 1 – 50  $\mu\text{m}$  were simulated and the geometric factor and spreading resistance equations used to calculate the conductivity of the surface layer and the bulk, determining the validity of each equation.

## **5.2 Model Setup**

The two electrode geometries studied in this chapter are Micro Top Full Bottom (MTFB) and Micro Top Top (MTT). Firstly, the MTFB geometry was studied. For the simulated response

to be independent of mesh size, it is important there is a sufficient number of mesh elements in the surface layer. Increasing the number of elements raises issues in computational time and memory requirements. To alleviate this, we take advantage of symmetry and simulate a quarter of the cylinder. This was compared to a full cylinder response to ensure the quarter cylinder returns comparable results to the full cylinder. This was tested for a single and a two-layer material. Current density plots and the impedance response of a full cylinder and a quarter cylinder are compared in Figure 5.1. The blue rectangles in the top image in Figure 5.1 (a) and (b) show where the current density slices are taken from in the full and quarter models. The meshing and the current density plots of the full and quarter model are very similar. Simulating the impedance response of a full and quarter model and then correcting for the surface area returns the same impedance spectra, Figure 5.1 (c), validating the use of a quarter cylinder for the MTFB geometries.

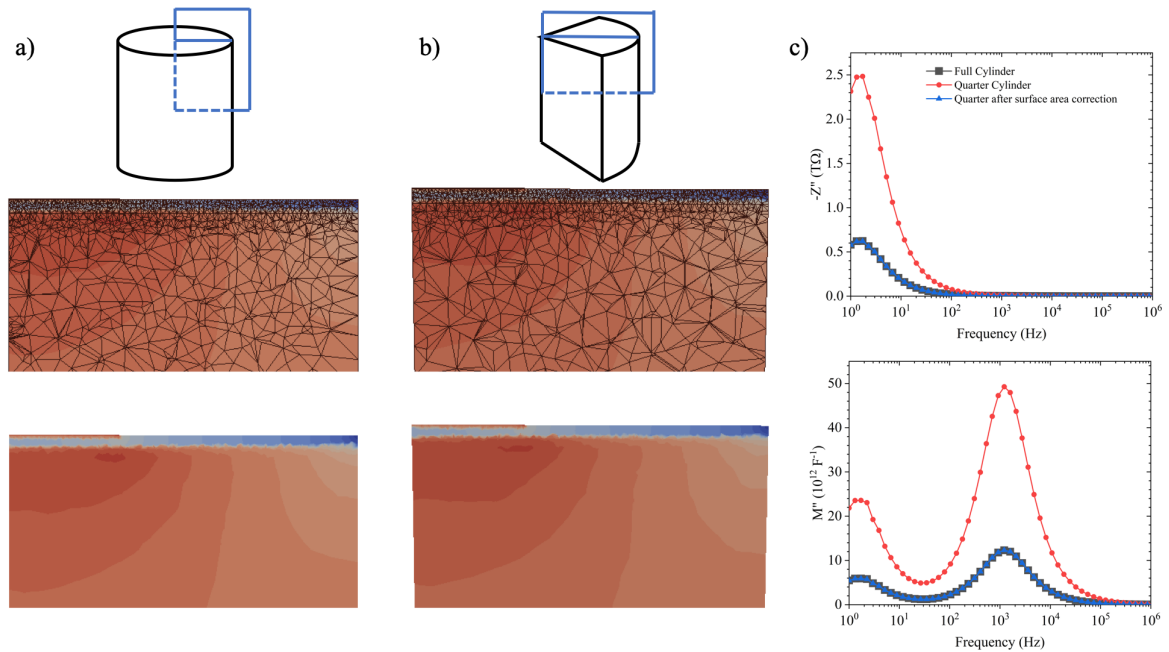


Figure 5.1. a) Current density plots of a full cylinder and b) a quarter cylinder. Top - illustration of where the slice is taken from in the models, middle – current density plot with the mesh overlaid, bottom – current density plot. c) Simulated Impedance ( $Z''$ ) and Modulus ( $M''$ ) spectroscopic plots for the full and quarter cylinder and the correction for the surface area of the quarter model.

A quarter cylindrical model with radius  $50 \mu\text{m}$  and thickness of  $100 \mu\text{m}$  was used. Within this thickness two materials were defined; the bulk and a surface layer. The bulk was assigned a conductivity  $\sigma_b = 13.6 \mu\text{S m}^{-1}$  and relative permittivity  $\epsilon_r = 162$ . These values were determined experimentally by conventional impedance measurements with full electrode contacts on a  $\text{SrTiO}_3$  single crystal at a temperature of  $300 \text{ }^\circ\text{C}$ . The surface layer had the same relative permittivity but its conductivity was lower than the bulk, e.g.  $\sigma_s = \sigma_b/10, \sigma_b/100, \sigma_b/1000$ . The

thickness of the surface layer,  $\tau_s$ , was varied such that the thickness of the bulk was then  $\tau_b = 100 \mu\text{m} - \tau_s$ . The bottom surface connected to the bulk was then defined as a full surface electrode whilst a micro-contact was defined on the top surface connected to the surface layer. The size of the micro-contact was varied such that it covered 75, 50, 25, 10 and 1 % of the model surface (100 % coverage was also simulated, i.e. conventional Impedance measurement/ Full Top Bottom). A convergence study was performed to ensure the simulated response was independent of the mesh size and all models had approximately 2 million elements.

For the MTT geometry, a cube of side length  $200 \mu\text{m}$  was used and the thickness of the surface layer and bulk varied in a similar way to above. Two micro-contacts were defined on the top surface connected to the surface layer with a diameter of  $10 \mu\text{m}$  and the contact separation varied. The midpoint between the two contacts was defined as the centre of the surface. The size of the micro-contacts was also varied ( $5$  and  $20 \mu\text{m}$  diameter). The two micro-contact geometries are shown in Figure 5.2. For analysis, an equivalent circuit of two parallel RC elements, representing the bulk and the surface layer, connected in series was assumed.

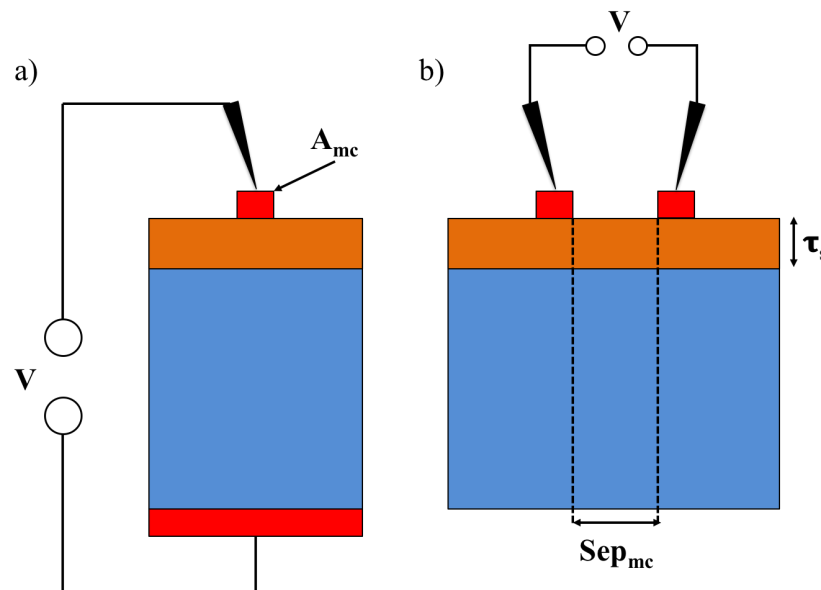


Figure 5.2. Schematic of the circular electrode models for a) MFTB - micro-contact on the top surface and full contact on the bottom surface, and b) MTT – two micro-contacts on the same surface. Electrodes are shown in red and this is consistent throughout all figures.

## 5.3 Results

### 5.3.1 Full top bottom (FTB)

For contacts that cover the full top and bottom surface (i.e. a conventional Impedance Spectroscopy measurement), the expected response can be solved analytically because the

current flows homogeneously through the model. The resistance, R, and capacitance, C, of each region can be calculated individually, using

$$R = \frac{l}{A\sigma} \quad (5.1)$$

$$C = \epsilon_0\epsilon_r \frac{A}{l} \quad (5.2)$$

where l is the thickness of the region, A is the surface area of the electrodes, and  $\epsilon_0$  is the permittivity of free space. The expected  $M''$  and  $Z''$  values of each region can then be calculated using

$$-Z''_{max} = \frac{R}{2} \quad (5.3)$$

$$M''_{max} = \frac{1}{2C} \quad (5.4)$$

and this is shown graphically in Figure 5.3. The analytical solution for a surface layer which is 100 times more resistive than the bulk is shown in Table 5.1.

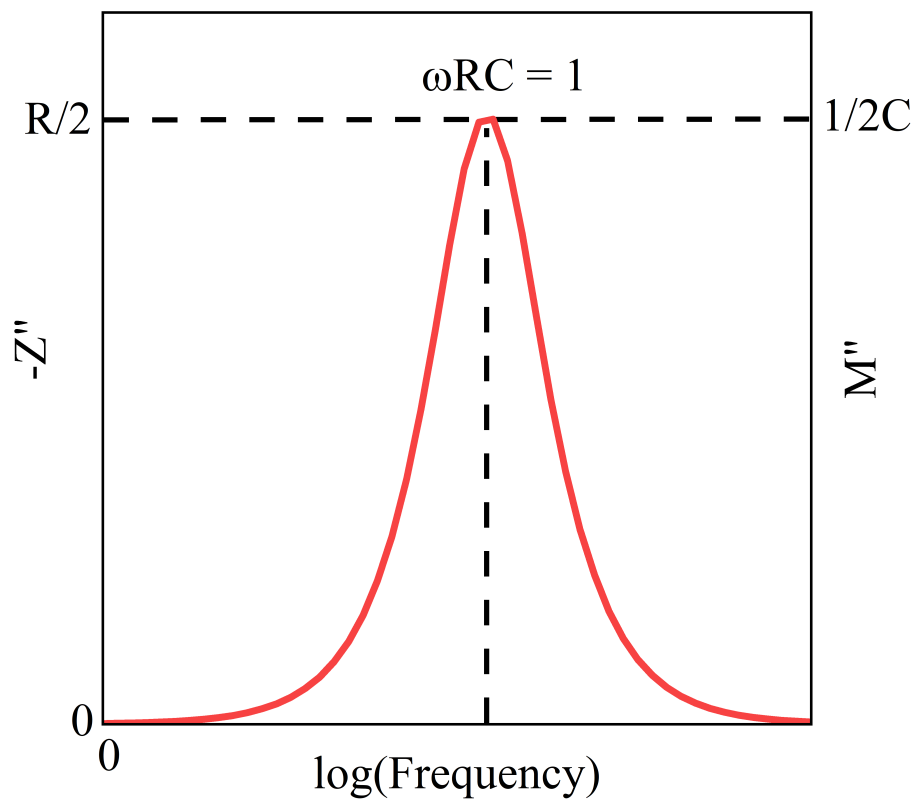


Figure 5.3.  $Z''$  and  $M''$  spectroscopic plots for a parallel RC element.

Table 5.1. Table showing the analytical solution for the electrical properties of a two-layer cylinder where the surface layer is 100 times more resistive than the bulk. The cylinder has a total thickness of 100  $\mu\text{m}$  and a radius of 50  $\mu\text{m}$  and the contacts are defined as the full top and bottom surfaces.

$\tau_{\text{Surface}}$ ( $\mu\text{m}$ )	$\tau_{\text{Bulk}}$ ( $\mu\text{m}$ )	Surface R ( $\text{M}\Omega$ )	Bulk R ( $\text{M}\Omega$ )	Surface $Z''$ ( $\text{M}\Omega$ )	Bulk $Z''$ ( $\text{M}\Omega$ )	Surface $Z''$ (% of total)	Bulk $Z''$ (% of total)	Surface C (pF)	Bulk C (pF)	Surface $M''$ ( $\text{pF}^{-1}$ )	Bulk $M''$ ( $\text{pF}^{-1}$ )	Surface $M''$ (% of total)	Bulk $M''$ (% of total)
1	99	939.7	930.3	469.8	465.1	50	50	11.29	0.11	0.04	4.38	1	99
2	98	1879.3	920.9	939.7	460.4	67	33	5.65	0.12	0.09	4.34	2	98
5	95	4698.3	892.7	2349.2	446.3	84	16	2.26	0.12	0.22	4.21	5	95
10	90	9396.6	845.7	4698.3	422.8	92	8	1.13	0.13	0.44	3.99	10	90
20	80	18793.2	751.7	9396.6	375.9	96	4	0.56	0.14	0.89	3.54	20	80
50	50	46983.0	469.8	23491.5	234.9	99	1	0.23	0.23	2.21	2.21	50	50

The first two columns of Table 5.1 define the model. The surface layer and bulk resistance and capacitances are then calculated individually using  $\tau$  as l in Equations 5.1 and 5.2 followed by Equations 5.3 and 5.4 to find the expected  $Z''$  and  $M''$  values. The percentage that each region of the sample contributes to the total response was calculated by dividing that region response by the sum of each response. For example, the percentage of the response that the surface layer contributes in  $M''$  is given by

$$M''_{Surface} \% = \frac{M''_{Surface}}{M''_{Surface} + M''_{Bulk}} \quad (5.5)$$

Because both regions of the sample have been assigned the same relative permittivity ( $\epsilon_r = 162$ ), calculating the percentage of the  $M''$  response from each region gives an indication of the electrical volume fraction of that region. When full surface contacts are used, current flows homogeneously through the material so there is no localisation of the response (see Chapter 4). The electrical volume fraction can be easily compared to the physical volume fraction of the material. As both regions have the same surface area, the only factor that determines the physical volume fractions is the thickness of each region. In the first row of Table 5.1 the physical volume fraction of the surface layer and bulk is 1% and 99%, respectively. Comparing this to the electrical volume fractions (in  $M''$ ) shows that these should be equal. In contrast the response in  $Z''$  does not equal the physical volume fraction as  $Z''$  is related to the conductivity of each region, which in this case are different. The simulated response for the models described in Table 5.1 are shown in Figure 5.4 and the calculated electrical volume fractions from the simulated data are compared to the physical volume fractions in Figure 5.5.

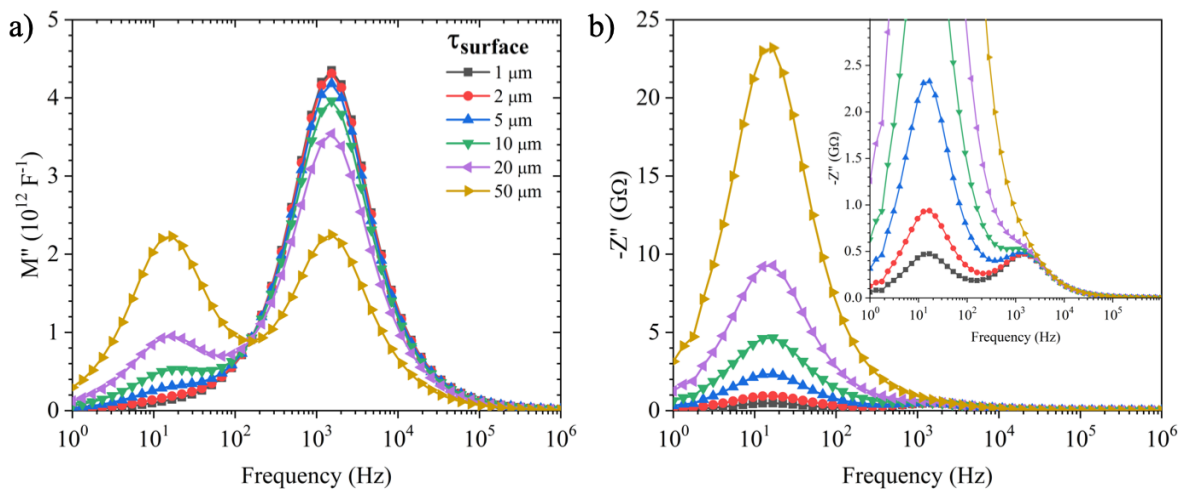


Figure 5.4. Simulated a)  $M''$  and b)  $Z''$  spectroscopic plots for the models defined in Table 5.1 with full surface electrodes (FTB).

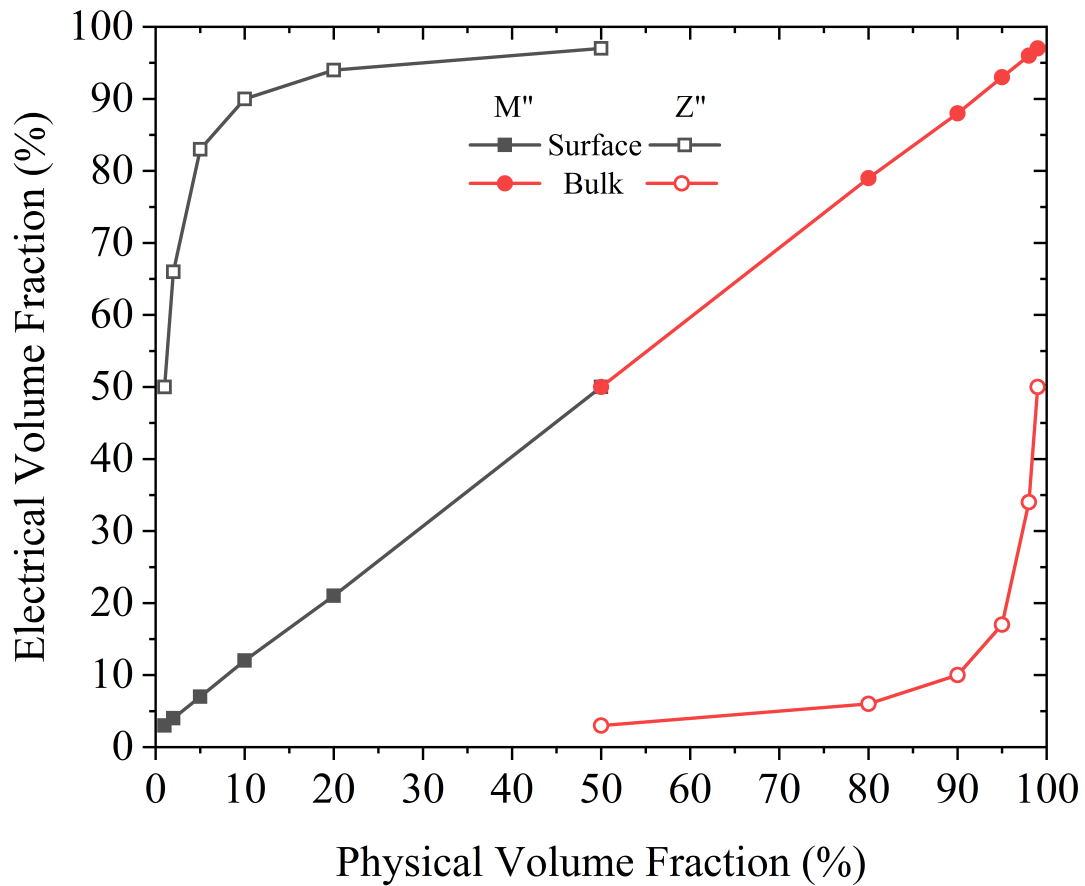


Figure 5.5.  $M''$  and  $Z''$  electrical volume fraction plotted against the physical volume fraction for the bulk and surface layer response from the simulated data defined in Table 5.1 with FTB.

The  $M''$  electrical volume fraction is equal to the physical volume fraction for all FTB models simulated, solid symbols in Figure 5.5. As predicted above, the  $Z''$  volume fraction is not equal to the physical volume fraction as  $Z''$  is related to the conductivity of the region.

When calculating the electrical properties from impedance data, the calculations described above are completed in reverse. For example, take the values of the peak maxima, to calculate R and C using Equations 5.3 and 5.4, followed by Equations 5.1 and 5.2 to find the conductivity and permittivity. The measured peaks from Figure 5.4 and calculated electrical properties are summarised in Table 5.2. Going from left to right in Table 5.2 is the order that the properties were obtained/calculated.

Table 5.2. Table showing the calculated electrical properties of a two-layer cylinder where the surface layer is 100 times more resistive than the bulk. The properties are calculated from the peaks in either  $M''$  or  $Z''$ . The cylinder has a total thickness of  $100\ \mu\text{m}$  and a radius of  $50\ \mu\text{m}$  and the contacts are defined as the full top and bottom surfaces.

M'' Spectroscopic plot analysis															
$\tau_{\text{Surface}}$ ( $\mu\text{m}$ )	$\tau_{\text{Bulk}}$ ( $\mu\text{m}$ )	$f_{\text{max,Surface}}$ (Hz)	$f_{\text{max,Bulk}}$ (Hz)	Surface $M''$ ( $\text{pF}^{-1}$ )	Bulk $M''$ ( $\text{pF}^{-1}$ )	Surface $M''$ (% of total)	Bulk $M''$ (% of total)	Surface C (pF)	Bulk C (pF)	Surface $\epsilon_r$	Bulk $\epsilon_r$	Surface R (M $\Omega$ )	Bulk R (M $\Omega$ )	Surface $\sigma$ ( $\mu\text{S/m}$ )	Bulk $\sigma$ ( $\mu\text{S/m}$ )
1	99	16.8	1526.4	0.14	4.31	3	97	3.52	0.12	50.7	165.4	2694.7	897.9	0.047	14.038
2	98	16.8	1526.4	0.18	4.31	4	96	2.71	0.12	77.9	163.6	3506.8	898.5	0.073	13.887
5	95	16.8	1526.4	0.31	4.18	7	93	1.60	0.12	114.9	163.5	5940.2	871.5	0.107	13.879
10	90	16.8	1526.4	0.53	3.96	12	88	0.95	0.13	136.7	163.3	9992.9	826.7	0.127	13.861
20	80	16.8	1526.4	0.95	3.54	21	79	0.52	0.14	150.9	162.8	18097.4	737.3	0.141	13.816
50	50	16.8	1526.4	2.23	2.25	50	50	0.22	0.22	161.0	160.2	42410.3	468.2	0.150	13.597

Z'' Spectroscopic plot analysis															
$\tau_{\text{Surface}}$ ( $\mu\text{m}$ )	$\tau_{\text{Bulk}}$ ( $\mu\text{m}$ )	$f_{\text{max,Surface}}$ (Hz)	$f_{\text{max,Bulk}}$ (Hz)	Surface $Z''$ (M $\Omega$ )	Bulk $Z''$ (M $\Omega$ )	Surface $Z''$ (% of total)	Bulk $Z''$ (% of total)	Surface R (M $\Omega$ )	Bulk R (M $\Omega$ )	Surface $\sigma$ ( $\mu\text{S/m}$ )	Bulk $\sigma$ ( $\mu\text{S/m}$ )	Surface C (pF)	Bulk C (pF)	Surface $\epsilon_r$	Bulk $\epsilon_r$
1	99	16.8	1526.4	474.8	471.0	50	50	949.6	942.0	0.134	13.381	9.99	0.11	143.8	157.7
2	98	16.8	1526.4	938.6	475.7	66	34	1877.1	951.5	0.136	13.114	5.06	0.11	145.5	154.5
5	95	16.8	1526.4	2329.0	489.9	83	17	4658.0	979.8	0.137	12.345	2.04	0.11	146.6	145.4
10	90	16.8	1526.4	4645.4	513.0	90	10	9290.8	1025.9	0.137	11.170	1.02	0.10	147.0	131.6
20	80	16.8	1526.4	9277.3	558.6	94	6	18554.6	1117.1	0.137	9.118	0.51	0.09	147.2	107.4
50	50	16.8	1526.4	23167.0	695.7	97	3	46334.0	1391.4	0.137	4.575	0.20	0.07	147.4	53.9

The percentage of the total  $M''$  response from each region scales with the thicknesses of each region. This is because the permittivity of each region is equal and so the percentages give approximate values of the volume fractions. In this case, the electrical volume fractions are approximately equal to the physical volume fraction. When taking the values calculated using  $M''$  spectroscopic plots, the calculation of the bulk relative permittivity is very accurate. The accuracy of the surface layer relative permittivity increases as its thickness increases. The calculated bulk conductivity using the  $M''$  peaks is within 5% of the input value for all thicknesses modelled. However, the calculated surface layer conductivity is initially underestimated and becomes more accurate with increasing thickness. It is worth noting that the surface layer response is difficult to resolve in the  $M''$  spectroscopic plot for a thickness of 1, 2 and 5  $\mu\text{m}$ , Figure 5.4 (a), which contributes to the less accurate calculations of the electrical properties.

When using  $Z''$  spectroscopic plots, the percentage of the total response is not representative of the physical volume fractions. The calculated conductivity is within 5% of the input value for the surface layer at all thicknesses. The calculated bulk conductivity is most accurate when the bulk thickness is largest, and the accuracy decreases as the thickness decreases. The surface layer permittivity is within around 10% of the input value for all thicknesses modelled. The bulk permittivity is most accurate when the bulk is very large and the accuracy decreases as its thickness decreases. The bulk response can be resolved for a surface layer thickness of 1, 2, 5 and 10  $\mu\text{m}$  but is harder to resolve for thicknesses of 20 and 50  $\mu\text{m}$  where the surface layer dominates the response. The inaccuracies of the permittivity measurements have been attributed to errors in the readings of the frequency and magnitude of the response peaks. Simply reading the values from the plots was used for convenience; however, equivalent circuit fitting would have obtained more accurate measurements.

By comparing Table 5.1 and Table 5.2 it can be seen that the analysis from the models are for the most part consistent with the analytical solution. However, there are some discrepancies between the input electrical properties and the calculated properties. It is clear that in the FTB case to obtain accurate electrical properties of the surface layer, one should use the  $Z''$  formalism. In contrast, to obtain accurate bulk properties, one should use the  $M''$  formalism.

Similar results were found for when the surface layer conductivity was 1000 and 10 times more resistive than the bulk.

### 5.3.2 Micro-top full-bottom (MTFB)

The size of the top contact was then decreased, such that 75, 50, 25, 10 and 1% of the surface was covered, creating a micro-contact on the top surface. Models where the surface layer conductivity was 100 times more resistive than the bulk are shown in the following figures, however conductivities of 1000 and 10 times more resistive were simulated also, obtaining similar results. Results can be compared by fixing the surface layer thickness to see the effect of micro-contact size on the response, Figure 5.6, or by fixing the micro-contact size to see the effect of surface layer thickness on the response, Figure 5.7.

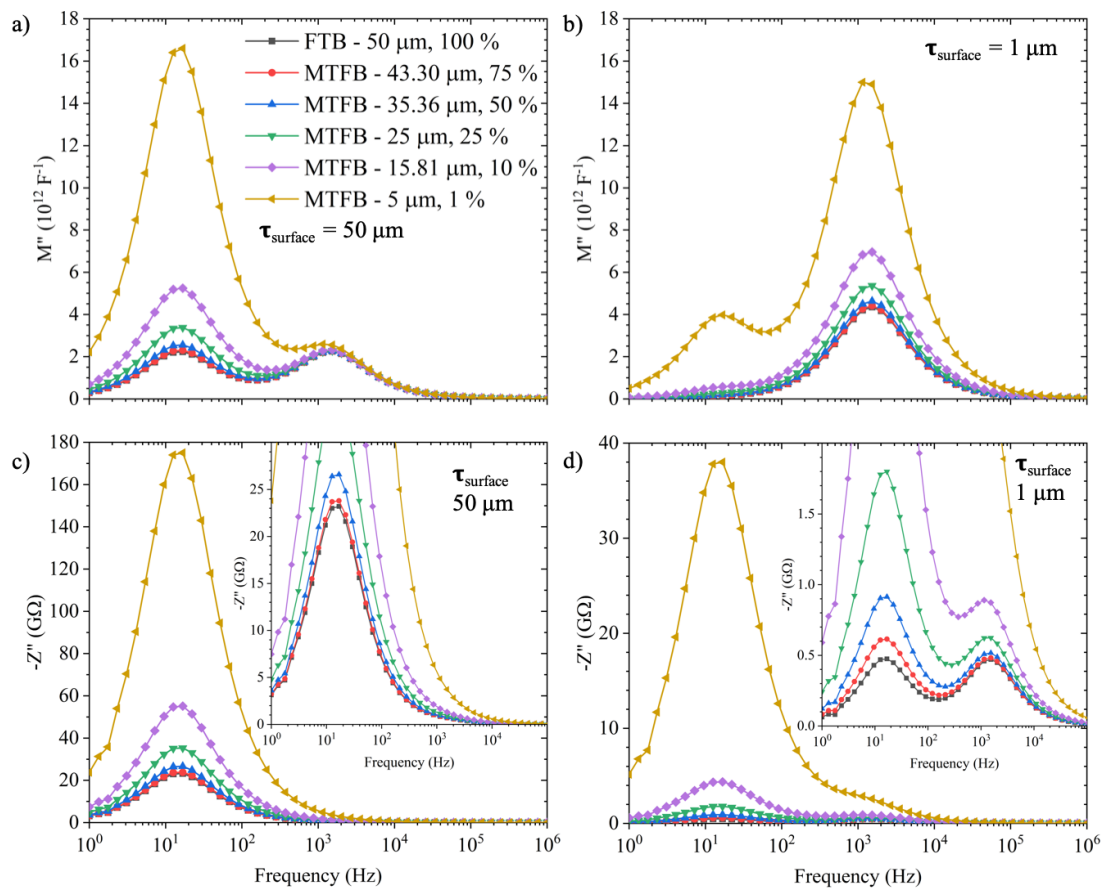


Figure 5.6.  $M''$  and  $Z''$  spectroscopic plots for a  $50 \mu\text{m}$  radius and  $100 \mu\text{m}$  thick cylinder with a surface layer that is 100 times more resistive than the bulk. Surface layer thickness of a, c)  $50 \mu\text{m}$  and b, d)  $1 \mu\text{m}$ . Models are labelled by the size of the micro-contact and the percent of the surface they cover. The inset of c) and d) is the same plot on a smaller  $Z''$  scale to highlight the intermediate frequency response (bulk).

When the thickness of the surface layer is  $50 \mu\text{m}$ , the same as the bulk, two responses can be clearly resolved in  $M''$  spectroscopic plots for all contact sizes modelled, Figure 5.6 (a). The response from the surface layer is the same as the bulk for full surface contacts. As the size of the top micro-contact decreases, the magnitude of the surface layer response increases. In contrast, the response from the bulk is very similar for all the micro-contact sizes modelled,

suggesting current passes through the bulk in the same manner for any micro-contact size modelled. When the surface layer thickness is 1  $\mu\text{m}$ , its response is small compared to the bulk and difficult to resolve in the  $M''$  plot for larger contact sizes but can be easily resolved when the micro-contact is 5  $\mu\text{m}$ , Figure 5.6 (b). In contrast to the larger surface layer thickness, the bulk response increases significantly with decreasing micro-contact size at this surface layer thickness.

When viewing the data in  $Z''$  spectroscopic plots, Figure 5.6 (c) and (d), the response is mainly dominated by the surface layer. This is because impedance is sensitive to large resistances and as the surface layer is 100 times more resistive than the bulk it dominates the signal. The magnitude of both the bulk and surface layer response increases as the micro-contact size decreases. It is difficult to resolve the response from the bulk when the surface layer thickness is 50  $\mu\text{m}$ , Figure 5.6 (c), but it can be resolved when the thickness is 1  $\mu\text{m}$ , Figure 5.6 (d).

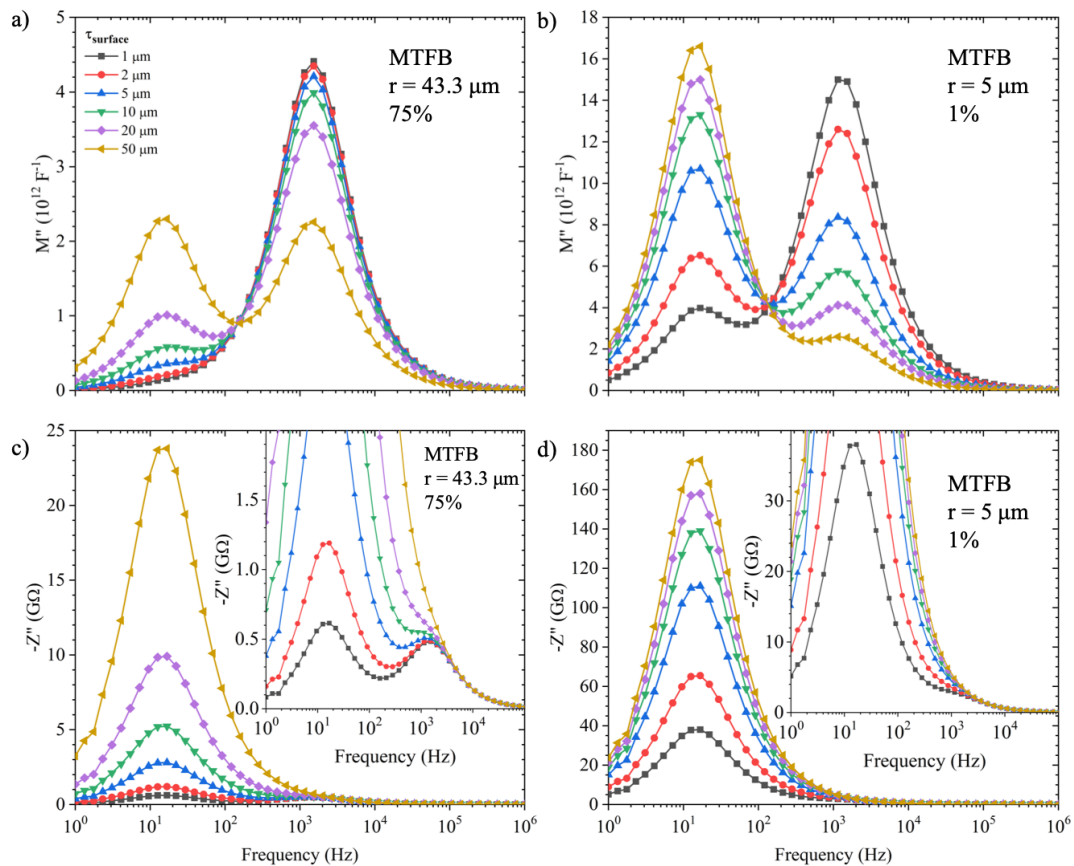


Figure 5.7.  $M''$  and  $Z''$  spectroscopic plots for a 50  $\mu\text{m}$  radius and 100  $\mu\text{m}$  cylinder with a surface layer that is 100 times more resistive than the bulk. The radius of the contact on the top surface is a, c) 43.3  $\mu\text{m}$  covering 75% of the surface and b, d) 5  $\mu\text{m}$  covering 1% of the surface. Models are labelled by the surface layer thicknesses. The inset of c) and d) is the same plot on a smaller  $Z''$  scale to highlight the intermediate frequency response (bulk).

Alternatively, the data can be compared by fixing the contact size and changing the surface layer thickness, Figure 5.7. When the micro-contact radius is 43.3  $\mu\text{m}$ , covering 75% of the surface, Figure 5.7 (a), the bulk response dominates the  $M''$  spectroscopic plot for a surface layer thickness of 1  $\mu\text{m}$ . As the thickness of the surface layer increases, its response increases and the response from the bulk decreases. This is consistent in both Figure 5.7 (a) and (b). When the micro-contact is 5  $\mu\text{m}$ , the surface layer response is easier to resolve even for a thickness of 1  $\mu\text{m}$ , emphasizing the localizing effect of micro-contacts, Figure 5.7 (b).

As the surface layer thickness increases, its response increases in  $Z''$  spectroscopic plots, Figure 5.7 (c) and (d). The response from the bulk can be extracted for small surface layer thicknesses and a micro-contact radius of 43.3  $\mu\text{m}$ , Figure 5.7 (c), but more difficult to resolve for smaller micro-contact sizes, Figure 5.7 (d), or as the surface layer thickness increases.

As the micro-contact size decreases, the electrical volume fraction no longer represents the physical volume fraction of the model. The electrical volume fractions of  $M''$  and  $Z''$  for the MTFB models are shown in Figure 5.8. When the contact covers the full top and bottom surface,  $M''$  electrical volume fractions give accurate physical volume fractions as discussed above (solid black square and red circle far right points in Figure 5.8). As the size of the top surface electrode decreases (from right to left in Figure 5.8) the  $M''$  electrical volume fraction increases for the surface layer response and decreases for the bulk. This highlights the localising effect that micro-contacts have on electrical measurements, in agreement with the findings in Chapter 4. The  $Z''$  electrical volume fraction is greatest for the surface layer response for all models. This is because of a combination of the surface layer having a conductivity which is 100 times smaller than the bulk and also the localising effect of the micro-contact.

The conductivities of the bulk and the surface layer were then calculated using both the spreading resistance equation and the geometric factor, using the micro-contact surface area and the model surface area, and the results are shown in Figure 5.9. For the surface layer analysis, the resistance values were calculated from the magnitude of the low frequency  $Z''$  peaks.

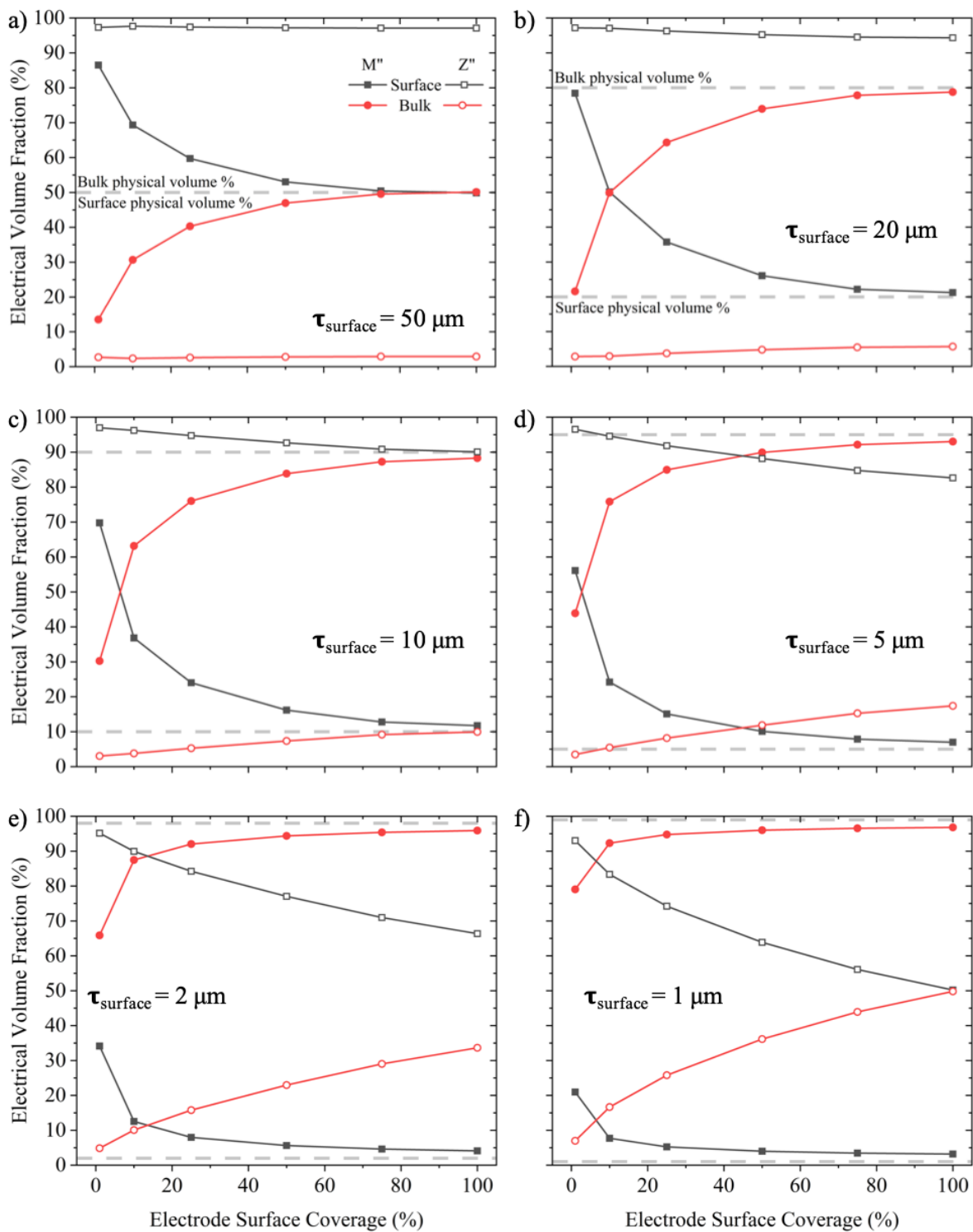


Figure 5.8. Calculated electrical volume fractions for each region of the model for a surface layer thickness of a)  $50 \mu\text{m}$ , b)  $20 \mu\text{m}$ , c)  $10 \mu\text{m}$ , d)  $5 \mu\text{m}$ , e)  $2 \mu\text{m}$  and f)  $1 \mu\text{m}$ . The electrical volume fractions are calculated from the peaks in either the  $M''$  or  $Z''$  formalisms. The grey dotted lines represent the physical volume fraction of the bulk and surface layer.

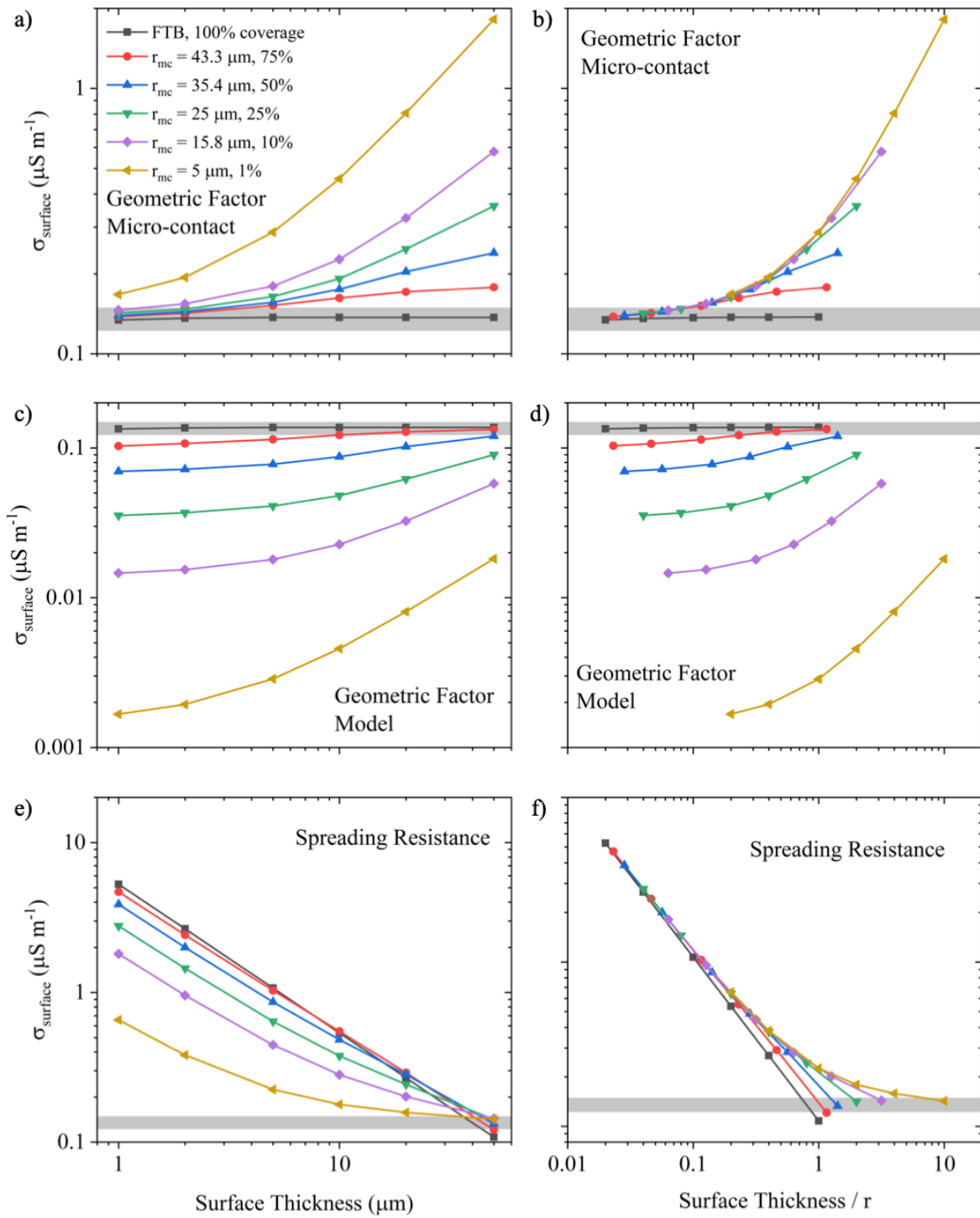


Figure 5.9. Calculated conductivity of a surface layer that is 100 times more resistive than the bulk for the MTFB models using a, b) the geometric factor using the micro-contact area, c, d) the geometric factor using the model area and e, f) the spreading resistance equation. Each are plotted against the surface layer thickness and the ratio of the thickness over the micro-contact radius. The grey box represents the input conductivity  $\pm 10\%$ . All values are shown on a log scale.

The FTB models (macro-contacts) extract the correct conductivity for the surface layer using the geometric factor. This is true for all thicknesses modelled as seen by the black squares in Figure 5.9 (a)-(d).

When the surface layer has a thickness of 1  $\mu\text{m}$ , the geometric factor using the micro-contact area obtains the most accurate approximation of the surface layer conductivity and is within 10% error for five contact sizes modelled, Figure 5.9 (a). However, when the micro-contact radius is 5  $\mu\text{m}$  the calculated conductivity is not within 10% error, but the geometric factor using the micro-contact area still produces the most accurate approximation. If the ratio of the surface layer thickness over the micro-contact radius is smaller than 0.1 the calculated conductivity is within 10% error for all models, Figure 5.9 (b). The accuracy of the geometric factor using the micro-contact area decreases as the thickness of the surface layer increases.

The geometric factor using the model area returns inaccurate conductivities at small separations but as the surface layer thickness increases the calculated conductivities increase in accuracy; however, for the thicknesses modelled only the model with a micro-contact radius of 43.3  $\mu\text{m}$  reaches a conductivity within 10% of the input value, Figure 5.9 (c) and (d). Similarities can be seen between Figure 5.9 (d) and Figure 4.10 in Chapter 4.

The spreading resistance equation is inaccurate at small surface layer thicknesses but works well at larger thicknesses, Figure 5.9 (e) and (f). For a micro-contact radius of 5  $\mu\text{m}$  the calculated conductivity converges to the input value. The other contact sizes modelled appear to reach a converging limit before continuing to decrease linearly. This could be because of the increased confinement in these models. For example, the FTB case (black squares), which is the fully confined case, does not converge at all and decreases linearly.

Clearly the amount of confinement the system possesses has a significant effect on the calculation of the conductivity. In reality, for most MTFB measurements, confinement from the sample size will not be an issue as the micro-contact size will be much smaller than the sample (e.g. for measurements of thin films or single crystals). Figure 5.10 shows the calculated conductivity using the geometric factor and the spreading resistance equation for the least confined model (micro-contact radius = 5  $\mu\text{m}$ ).

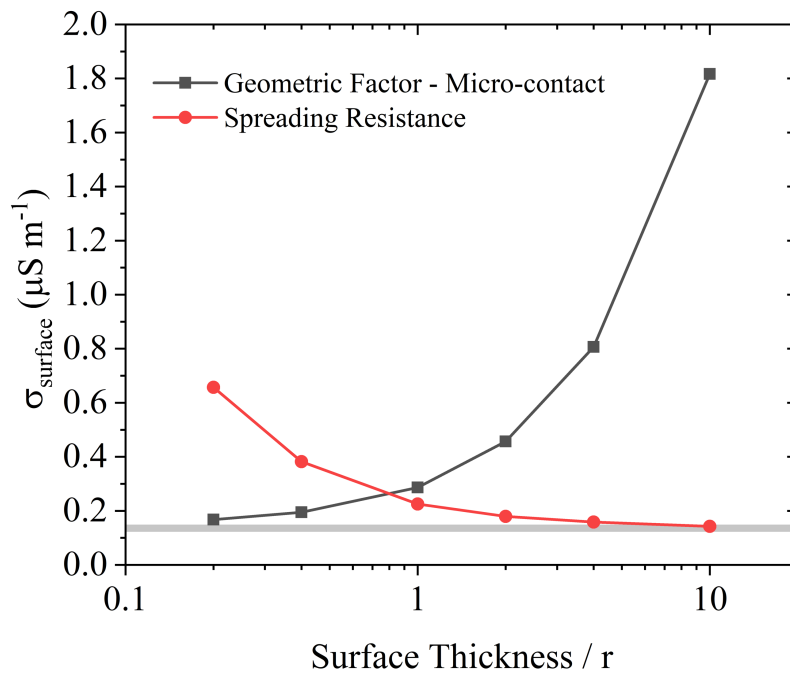


Figure 5.10. Calculated conductivity of a surface layer that is 100 times more resistive than the bulk for the least confined MTFB model (micro-contact radius of 5  $\mu\text{m}$ ), using the geometric factor using the micro-contact area or the spreading resistance equation. The grey box represents the input conductivity  $\pm 10\%$ .

From this analysis, three general comments can now be stated

1. When the surface layer thickness is  $\sim 10$  times smaller than the micro-contact radius, the **geometric factor** using the micro-contact radius obtains the best approximation of the conductivity (black squares in Figure 5.10).
2. When the surface layer thickness is  $\sim 10$  times greater than the micro-contact radius, the **spreading resistance** equation obtains the best approximation of the conductivity (red circles in Figure 5.10).
3. The crossover for where either equation is more accurate is at a surface layer thickness that is  $\sim 0.8$  times the micro-contact radius.

The calculations were then repeated for the bulk response and are shown in Figure 5.11. In this case, the capacitance of the bulk was calculated from the frequency and magnitude of the  $M''$  peak and then converted to resistance, using Equation 5.4 followed by Equation 3.12.

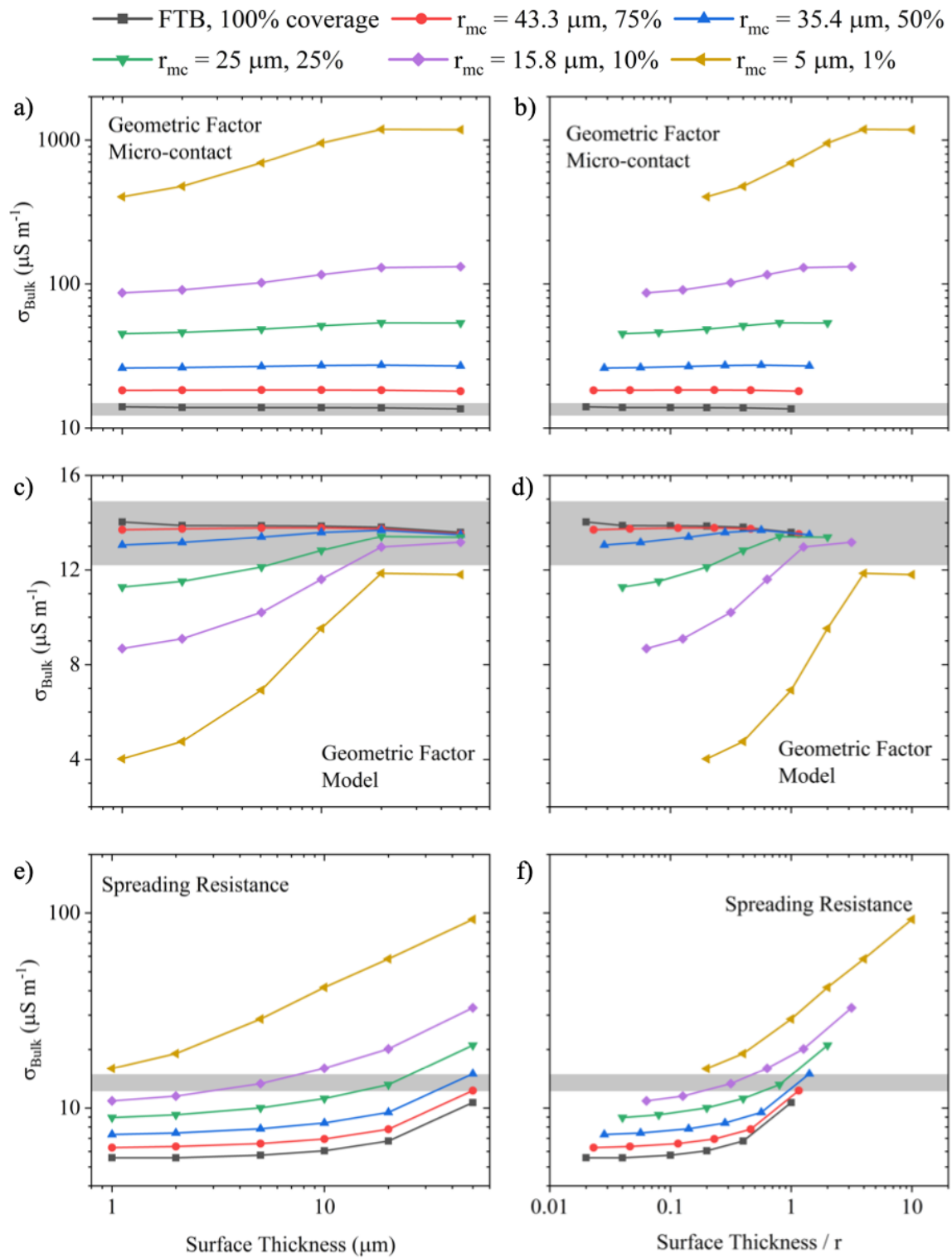


Figure 5.11. Calculated conductivity of the bulk beneath a surface layer that is 100 times more resistive than the bulk for the MTFB models using a, b) the geometric factor using the micro-contact area, c, d) the geometric factor using the model area and e, f) the spreading resistance equation. Each is plotted against the surface layer thickness and the ratio of the thickness over the micro-contact radius. The grey box represents the input conductivity  $\pm 10\%$ . All values are shown on a log scale.

The geometric factor using the micro-contact area returns inaccurate conductivities for all micro-contact sizes modelled and becomes significantly worse as the micro-contact size decreases, Figure 5.11 (a) and (b). This is because the current spreads out in the surface layer so when it reaches the bulk it is already flowing over a larger area than the micro-contact. Further, once the current is in the bulk it will spread even more to fill the model. Because the current flows over a larger area than the micro-contact area, the geometric factor using the micro-contact area overestimates the conductivity.

The geometric factor using the model area gives the most accurate bulk conductivities at large surface layer thicknesses for each micro-contact size modelled, Figure 5.11 (c) and (d). This is because the current is able to spread out in the surface layer and when it reaches the bulk the current is spread over the full model area. As the thickness of the surface layer decreases, the current is unable to spread out to fill the full model area, therefore the current still has to spread when it is in the bulk. It should be noted this would be the case for most measurements in reality as the size of the micro-contacts are generally much smaller than the size of the sample. Because of this, the geometric factor using the model area then underestimates the conductivity as the current flows from a smaller area.

Using the spreading resistance equation, the calculated conductivity converges at small surface layer thicknesses, Figure 5.11 (e) and (f). When the surface layer thickness is small the geometric factor using the micro-contact area gives the best approximation for the surface layer conductivity, Figure 5.9 (a) and (b). This suggests the current will flow into the bulk over an area that is similar to the micro-contact area. Once the current flow enters the bulk, it will spread out to fill the model and as such the spreading resistance equation gives a good approximation. As the micro-contact size increases, the value that the conductivity converges towards decreases. This is due to the increased amount of confinement increasing the resistance (see Chapter 4). At larger surface layer thicknesses, the accuracy of the spreading resistance equation decreases as the current flows over a larger area, meaning the micro-contact radius assumed in the equation is too small.

Analogous plots for the calculated effective permittivity of each region showed similar trends to those for the calculated conductivity and so are not shown here. This shows the permittivity can be calculated to a similar accuracy using the methods discussed above. However, it should be noted that in this case the relative permittivity of both regions was equal. To fully understand how permittivity affects the response, the conductivity of each region should be fixed, and the permittivity should be varied; however, this has not been tested here.

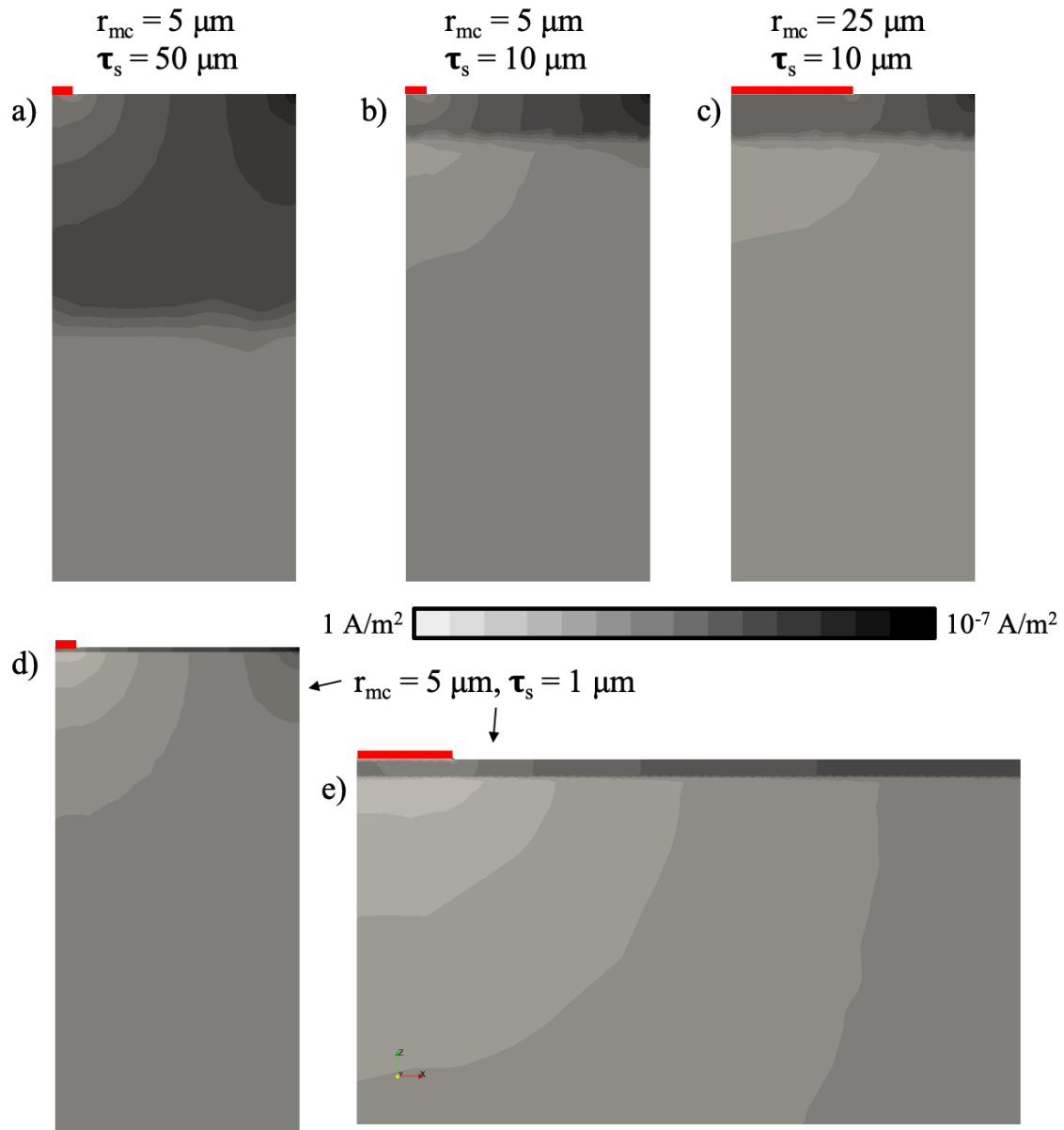


Figure 5.12. Current density plots of a two-layer model using the (quarter) MTFB geometry where the surface layer is 100 times more resistive than the bulk. a)  $r_{mc} = 5 \mu\text{m}$ ,  $\tau_s = 50 \mu\text{m}$ , b)  $r_{mc} = 5 \mu\text{m}$ ,  $\tau_s = 10 \mu\text{m}$ , c)  $r_{mc} = 25 \mu\text{m}$ ,  $\tau_s = 10 \mu\text{m}$ , d)  $r_{mc} = 5 \mu\text{m}$ ,  $\tau_s = 1 \mu\text{m}$ , e) top left corner of d) on a smaller scale. Black and white represents regions of low and high current density, respectively.

Current density plots for a number of the MTFB models where the surface layer is 100 times more resistive than the bulk are shown in Figure 5.12. When the micro-contact has a radius of  $5 \mu\text{m}$ , covering 1% of the top surface, and the surface layer has a thickness of  $\tau_s = 50 \mu\text{m}$ , Figure 5.12 (a), the current is able to spread out to the full model area within the surface layer. The current flow enters the bulk over an area equal to the full model area and so remains homogeneous throughout the bulk. This is consistent for the larger micro-contact sizes modelled and this surface layer thickness.

When  $\tau_s = 10 \mu\text{m}$  and  $r_{mc} = 5 \mu\text{m}$ , Figure 5.12 (b), the current begins to spread out in the surface layer, but the layer is not thick enough for it to spread out to the full model area in this layer such as in Figure 5.12 (a). The current density in the bulk is inhomogeneous and there is a small amount of spreading from directly underneath the micro-contact. For the same thickness but with a larger contact size of  $r_{mc} = 25 \mu\text{m}$ , Figure 5.12 (c), there is a small amount of spreading again, however the current density is homogeneous directly underneath the micro-contact.

When  $\tau_s = 1 \mu\text{m}$  and  $r_{mc} = 5 \mu\text{m}$ , Figure 5.12 (d) and (e), the magnitude of the current density in the surface layer significantly decreases away from the micro-contact. The current density in the bulk is inhomogeneous and is spreading from the region directly beneath the micro-contact. This shows similarities to the current density plots for a single material in Chapter 4.

### 5.3.3 Micro top top (MTT)

Calculations were then performed for the Micro-top-top geometry (MTT). Simulations where the surface layer was 10, 100 and 1000 times more resistive than the bulk were performed, obtaining similar results; however, only the results where the conductivity is 100 times smaller than the bulk are shown for conciseness. The simulated impedance response for a micro-contact radius of  $5 \mu\text{m}$  is shown in Figure 5.13. The data can be compared by fixing the surface layer thickness and changing the micro-contact separation, Figure 5.13 (a) and (b), or by fixing the contact separation and varying the surface layer thickness, Figure 5.13 (c) and (d).

When the surface layer thickness is fixed at  $1 \mu\text{m}$  and the separation of the micro-contacts is varied, the response from the surface layer changes very little in both the modulus and impedance plots, Figure 5.13 (a) and (b), respectively. This demonstrates the current takes the same path through the surface layer and is independent of the micro-contact separation. In contrast, the response from the bulk increases with increasing separation in the modulus plot, Figure 5.13 (a), but the changes are difficult to resolve in the impedance plot as the surface layer dominates the impedance, Figure 5.13 (b).

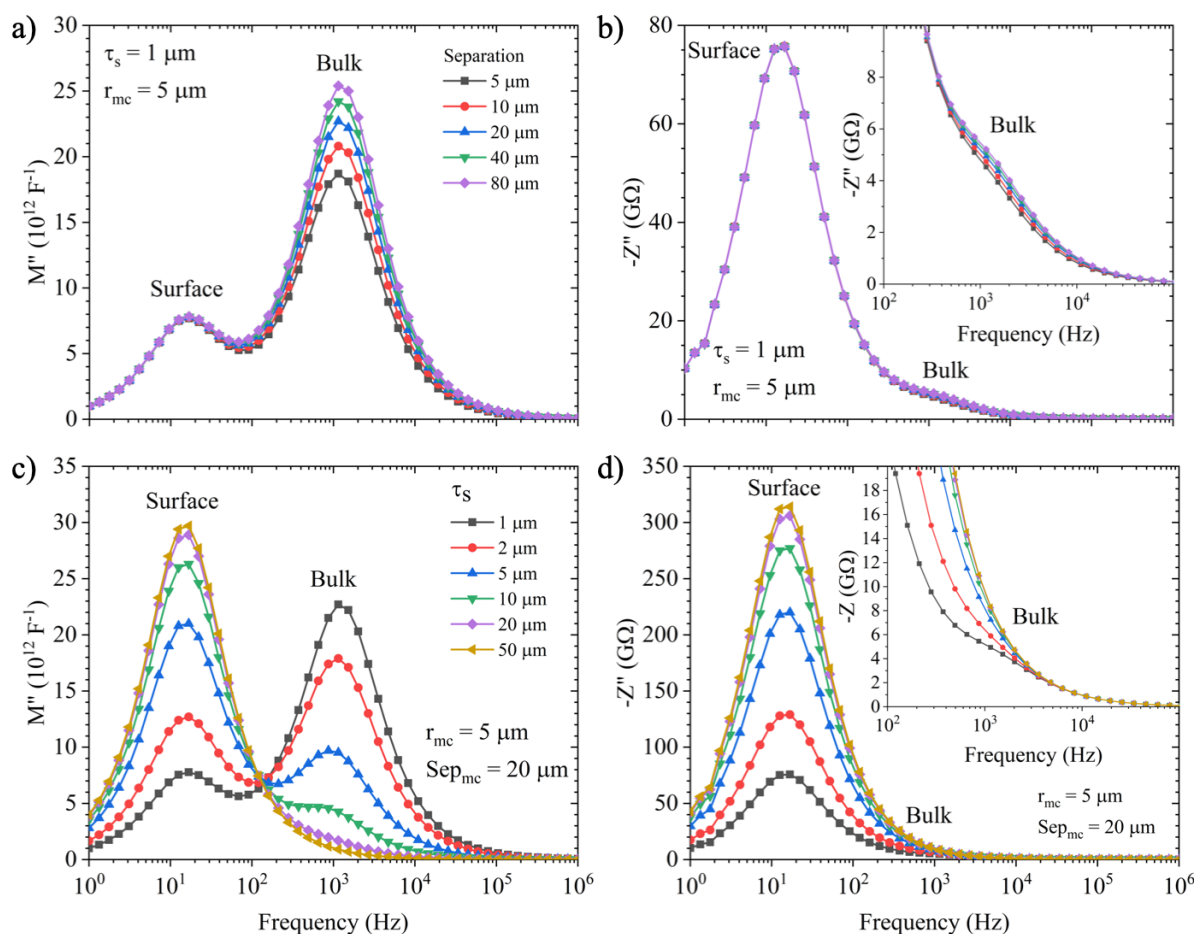


Figure 5.13. Simulated impedance data for a surface layer that is 100 times more resistive than the bulk using the MTT geometry. a)  $M''$  spectroscopic plots and b)  $Z''$  spectroscopic plots for a resistive surface layer that is  $1\ \mu\text{m}$  thick and micro-contact radius of  $5\ \mu\text{m}$  for a range of contact separations. c)  $M''$  spectroscopic plots and d)  $Z''$  spectroscopic plots for a micro-contact radius of  $5\ \mu\text{m}$  and contact separation of  $20\ \mu\text{m}$  for a range of surface layer thicknesses.

For a fixed micro-contact separation, the electrical response changes as a function of the thickness of the surface layer. As the thickness of the surface layer increases, its response increases whilst the response from the bulk decreases. This is observed in both the  $M''$  and  $Z''$  plots, Figure 5.13 (c) and (d), respectively, as expected. When the thickness of the surface layer is  $50\ \mu\text{m}$  (10 times greater than the micro-contact radius), it is difficult to resolve any response from the bulk at all, yellow left triangles in Figure 5.13 (c).

The conductivity of the surface layer was then calculated using both the spreading resistance equation and the geometric factor using the micro-contact surface area and the results are shown in Figure 5.14. For the surface layer analysis, the resistance values were calculated from the magnitude of the low frequency  $Z''$  peaks, although analysis using the  $M''$  peaks produced similar results.

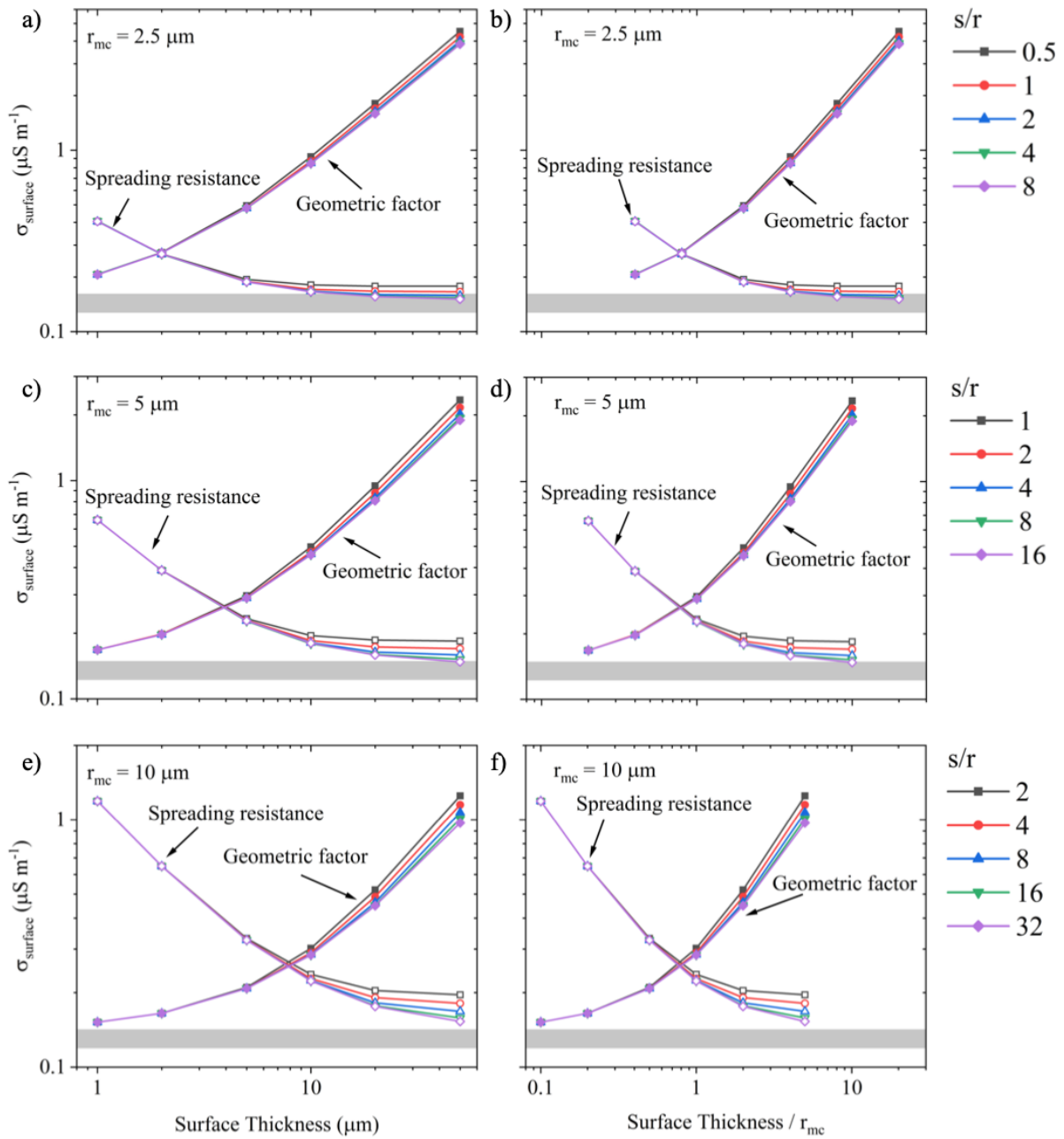


Figure 5.14. Calculated conductivity of a surface layer that is 100 times more resistive than the bulk for the MTT models using the geometric factor using the micro-contact area (solid symbols) or the spreading resistance equation (open symbols). a, b) micro-contact radius =  $2.5 \mu\text{m}$ , c, d) micro-contact radius =  $5 \mu\text{m}$ , e, f) micro-contact radius =  $10 \mu\text{m}$ .  $s/r$  in the legend is the ratio of the micro-contact separation over the micro-contact radius. The grey box represents the input conductivity  $\pm 10\%$ .

The trends observed in Figure 5.14 are consistent throughout all plots. The geometric factor using the micro-contact area provides the best approximation of conductivity if the surface layer thickness is small (filled symbols to the left of plots in Figure 5.14). As the surface layer thickness increases (moving right in Figure 5.14) the accuracy of this equation decreases.

Conversely, the spreading resistance equation overestimates the conductivity at small surface layer thicknesses. As the thickness increases, the accuracy of this equation increases (open symbols in Figure 5.14). The spreading resistance equation becomes a better approximation for the conductivity when the surface layer thickness is  $\sim 0.8$  times the micro-contact radius and this is consistent for all micro-contact sizes modelled, Figure 5.14 (b), (d) and (e). As the surface layer thickness increases further, the accuracy of using the spreading resistance equation increases and converges to within 10% of the input conductivity.

When the surface layer thickness is less than (or equal to) 0.8 times the micro-contact radius, the calculated conductivities overlap and is independent of separation. In contrast, when the surface layer thickness is greater than 0.8 times the micro-contact radius, the calculated conductivities begin to deviate, and are dependent on the separation of the micro-contacts.

The conductivity and effective permittivity were then calculated for the bulk response using the spreading resistance equations and are shown in Figure 5.15. A geometric factor was not used, as in Chapter 4 this was shown to be not valid for similar types of measurements. In this case, the capacitance of the bulk was calculated from the frequency and magnitude of the  $M''$  peak and then converted to resistance, using Equation 5.4 followed by Equation 3.12.

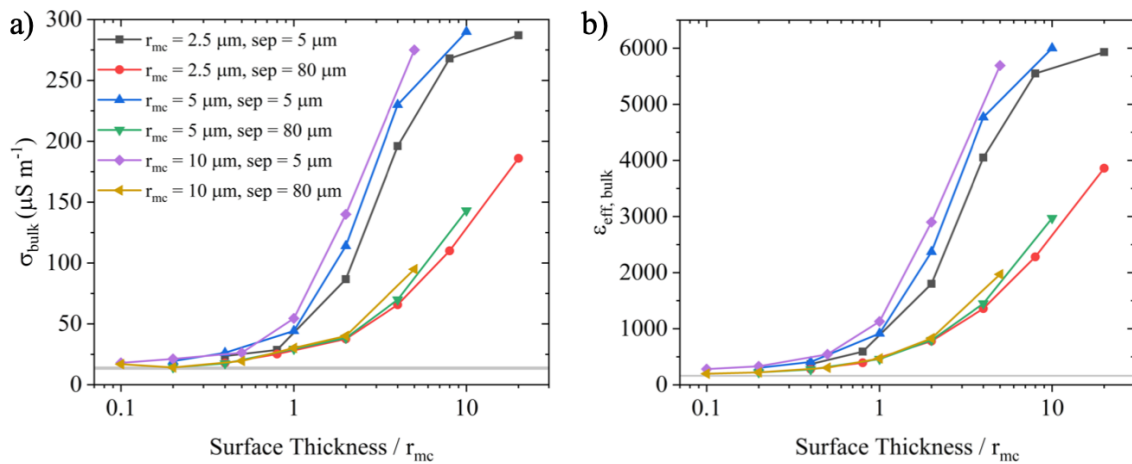


Figure 5.15. a) Calculated conductivity and b) effective permittivity for the bulk beneath a surface layer that is 100 times more resistive than the bulk for the MTT models using the spreading resistance equation. The grey box represents the input values  $\pm 10\%$ .

The spreading resistance equation returns accurate bulk conductivities when the surface layer thickness is much smaller than the micro-contact radius, Figure 5.15 (a). As the surface layer thickness increases, the accuracy of the spreading resistance equation decreases. A similar trend can be observed for the calculated effective permittivity of the bulk, Figure 5.15 (b).

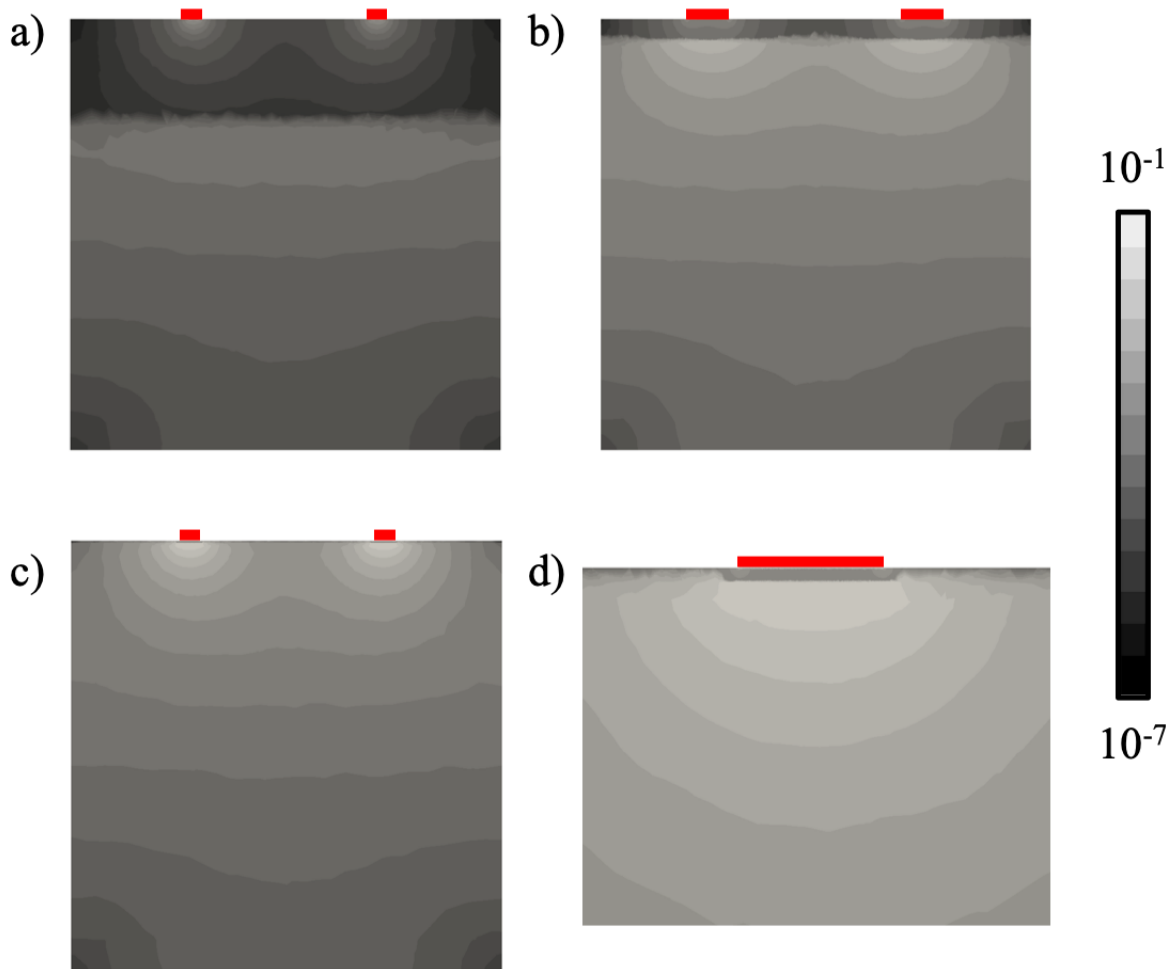


Figure 5.16. Current density plots of a two-layer model using the MTT geometry where the surface layer is 100 times more resistive than the bulk. a)  $r_{mc} = 2.5 \mu\text{m}$ ,  $\tau_s = 50 \mu\text{m}$ , separation =  $80 \mu\text{m}$ , b)  $r_{mc} = 10 \mu\text{m}$ ,  $\tau_s = 10 \mu\text{m}$ , separation =  $80 \mu\text{m}$ , c)  $r_{mc} = 5 \mu\text{m}$ ,  $\tau_s = 1 \mu\text{m}$ , separation =  $80 \mu\text{m}$ , d) a larger scale image of one of the micro-contacts in c). Black and white represents regions of low and high current density, respectively. Red represents the micro-contacts. Scale bar is in units of  $\text{A m}^{-2}$ .

Current density plots for a number of the MTT models where the surface layer is 100 times more resistive than the bulk are shown in Figure 5.16. When the micro-contact radius is  $2.5 \mu\text{m}$  and the surface layer thickness is  $50 \mu\text{m}$ , the surface layer is sufficiently large for the current to spread out freely, Figure 5.16 (a). The current density in the surface layer is similar to the current density in a single homogeneous material using the MTT geometry (see Chapter 4, Figure 4.8).

When the micro-contact radius and the surface layer thickness are both  $10 \mu\text{m}$ , Figure 5.16 (b), the current begins to spread out in the surface layer but cannot spread out as freely as shown in Figure 5.16 (a). The current density in the bulk is inhomogeneous and there is some spreading from the regions directly beneath the micro-contacts.

When the micro-contact radius is 5  $\mu\text{m}$  and the surface layer thickness is 1  $\mu\text{m}$ , Figure 5.16 (c) and (d), spreading occurs in the bulk and looks similar to the current density in the surface layer for large thicknesses (Figure 5.16 (a)) or a single homogeneous material (see Chapter 4, Figure 4.8). The current density in the bulk shows the current is spreading from an area that is similar to the micro-contact, Figure 5.16 (d).

## 5.4 Discussion

Analytical approaches for current flow in FTB contact geometries is relatively simple due to the homogeneous current flow in such systems. This has allowed us to validate our FEM method and the calculated electrical properties from these simulations (Table 5.2) are in agreement with the analytical solution (Table 5.1). However, when micro-contacts are used, current flow is no longer homogeneous and as such a single analytical solution is difficult.

When using the MTFB geometry, if the surface layer thickness is large, the response from the bulk does not change significantly for the different micro-contact sizes modelled, Figure 5.6 (a) and (c). This suggests current flow is similar in this region for each micro-contact size modelled. The current density plot for the smallest micro-contact size modelled (5  $\mu\text{m}$ ) and a surface layer thickness of 50  $\mu\text{m}$ , Figure 5.12 (a), shows the current flow to be homogeneous throughout the bulk. This demonstrates the current has spread out completely to fill the model before it reaches the bulk of the model. This will therefore be true of the larger contact sizes modelled also and is the reason why the bulk response does not change significantly with varying micro-contact sizes.

For the model with the least amount of confinement and a micro-contact radius of 5  $\mu\text{m}$ , the current density spreads from the micro-contact, Figure 5.12 (a). Because of this, the spreading resistance equation obtains the best approximation of the conductivity, Figure 5.9 (f). This model is still rather confined compared to an experimental sample (such as a surface layer on a single crystal where the confinement could be deemed negligible); however, our results demonstrate if the surface layer thickness is at least 10 times greater than the micro-contact radius, the spreading resistance will produce surface layer conductivities within 10% of the input value, Figure 5.10. Calculations of the bulk properties would be complicated in a completely unconfined system as it would be difficult to determine over what area the current enters the bulk from the surface layer and over what area the current then spreads out to.

If the surface layer thickness is similar to the micro-contact radius, calculations of both the surface layer and bulk become difficult, Figure 5.9 and Figure 5.11. The current spreads out in

the surface layer but cannot spread out as freely as for the thicker surface layer, Figure 5.12 (b), causing the accuracy of the spreading resistance equation to reduce. Because the current is spreading out over a larger area than the micro-contact area, the geometric factor using the micro-contact area is also inaccurate, Figure 5.10. At a surface layer thickness of 0.8 times the micro-contact radius there is a cross-over for which equation is most accurate. At thicknesses greater than this value the spreading resistance equation returns the most accurate surface layer conductivity. Lower than this value the geometric factor using the micro-contact area returns the most accurate surface layer conductivity. It is also difficult to calculate the bulk conductivity, as it is unknown over what area the current enters the bulk. Where possible, surface layer thicknesses similar to the micro-contact radius should be avoided.

If the surface layer thickness is 10 times smaller than the micro-contact radius the geometric factor using the micro-contact area gives the best approximation of the surface layer conductivity, Figure 5.9 (b) and Figure 5.10. This is because the current is unable to spread out in the limited thickness of the surface layer and so the area the majority of the current passes through the surface layer is similar to the micro-contact area, Figure 5.12 (d) and (e), i.e. the majority of the current passes through a cylinder that has length of the surface layer thickness and an area of the micro-contact. This means the majority of the current enters the bulk over the same area and as such spreads out from this area, Figure 5.12 (d) and (e); therefore, the spreading resistance equation gives the most accurate bulk conductivities, Figure 5.11 (f). For the larger micro-contact sizes modelled, there is a significant amount of confinement, which as explained in the previous chapter, increases the measured resistance and thus an underestimate of the bulk conductivity is obtained in this case. Where possible, the micro-contact radius should be at least 10 times the surface layer thickness for accurate conductivities of both the surface layer and bulk to be obtained.

Similar trends can be observed when using two micro-contacts on the same surface (MTT). The crossover where either the geometric factor using the micro-contact area or the spreading resistance equation returns the most accurate surface layer conductivity occurs at a surface layer thickness that is 0.8 times the micro-contact radius, Figure 5.14, consistent with the MTFB results.

If the surface layer thickness is greater than this value, the spreading resistance equation is more accurate, Figure 5.14. When this is the case, the calculated surface layer conductivity is also dependent on the contact separation, as in Chapter 4, hence to obtain accurate conductivities one must consider the micro-contact radius, the surface layer thickness and the

contact separation. As a consequence, it is difficult to suggest an ideal experimental setup. From Chapter 4, an  $s/r$  of 8 was proposed to obtain conductivities within 10% of the input value. If the micro-contact radius is 10 times smaller than the surface layer thickness, the spreading resistance equation should obtain surface layer conductivities to a similar accuracy. Current density plots, Figure 5.16 (a), show the current spreads from the two micro-contacts in a similar way to how spreading occurs in a homogeneous material (see Chapter 4, Figure 4.8). The current density in the bulk is inhomogeneous, and greatest near the interface. It is difficult to suggest a geometry that describes this, thus bulk conductivities cannot be calculated with large surface layer thicknesses, Figure 5.15 (a).

If the surface layer thickness is smaller than 0.8 times the micro-contact radius, the geometric factor using the micro-contact area returns the most accurate surface layer conductivity, Figure 5.14, particularly if the thickness is 10 times smaller than the micro-contact radius. When the surface layer thickness is less than 0.8 times the micro-contact radius, the response is independent of the contact separation. This can be seen in Figure 5.13 (a) and (b) where the low frequency response does not change and in Figure 5.14 where the data points overlap for the different  $s/r$  values modelled. This suggests current takes the same path through the surface layer for all contact separations modelled. The current density in the bulk looks similar to that seen for spreading from two micro-contacts in a homogeneous material, Figure 5.16 (c) and (d), and as such the spreading resistance equation returns the most accurate bulk conductivity, Figure 5.15 (a). The bulk response is dependent on the contact separation, Figure 5.13 (a) and (b), in the same way that a homogeneous material is; at small separations, contact interference occurs and therefore conductivity is overestimated.

A summary of this chapter's findings is presented in Figure 5.17 showing the different contact geometries and the method for calculation of the respective conductivities when there is no sample confinement. If the surface layer thickness is greater than 10 times the micro-contact radius, the spreading resistance equation should be used to obtain accurate surface layer conductivities, Figure 5.17 (a) and (b). For MTFB, if there is no confinement, bulk conductivities cannot be obtained, Figure 5.17 (a), and they cannot be obtained for the MTT case either, Figure 5.17 (b).

If the surface layer thickness is at least 10 times smaller than the micro-contact area, the geometric factor using the micro-contact area can be used to obtain accurate surface layer conductivities and the spreading resistance equation can be used to obtain bulk conductivities, Figure 5.17 (c) and (d).

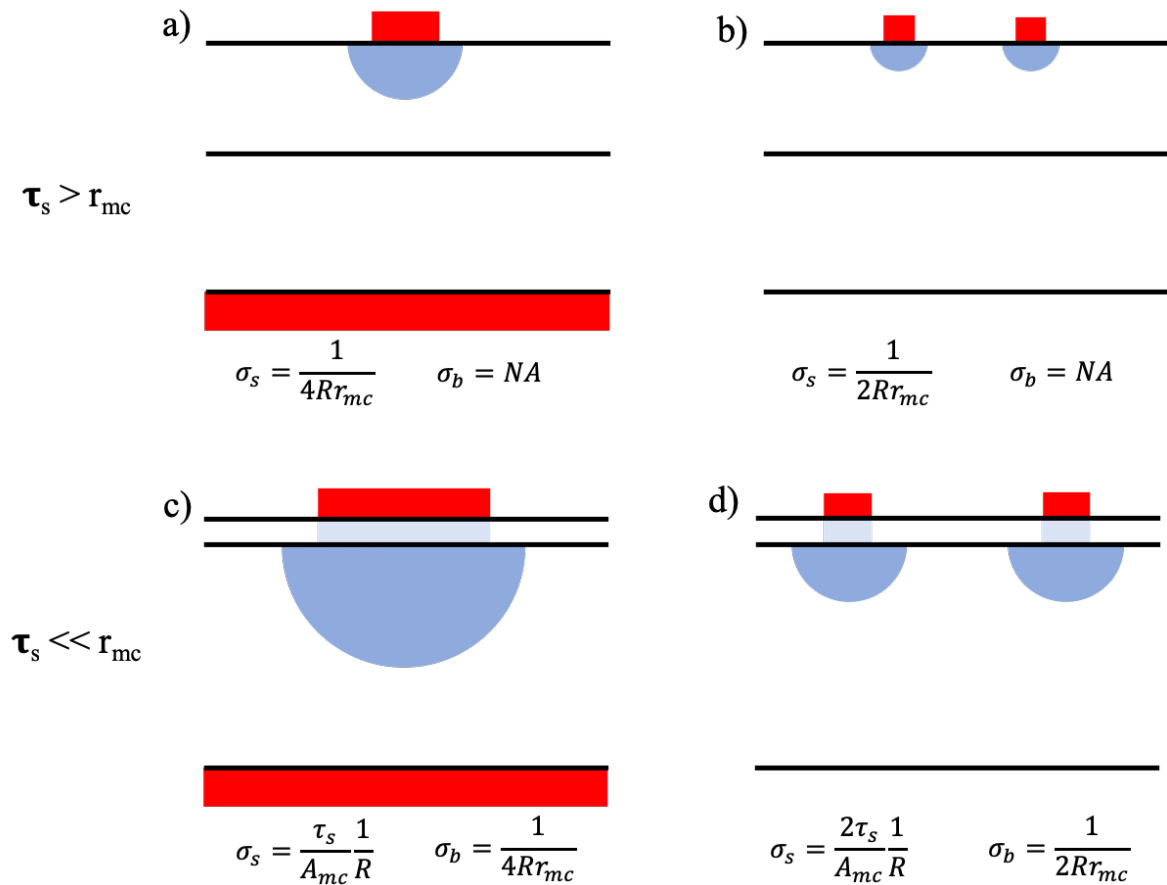


Figure 5.17. a, c) MTFB and b, d) MTT contact geometries for an unconfined case when the surface layer thickness is a, b) greater than the micro-contact radius and c, d) smaller than the micro-contact radius. The equations to be used to calculate the conductivity of each region is also shown.

## 5.5 Conclusions

The electrical response of a sample with a resistive surface layer has been simulated for different micro-contact geometries. If the thickness of the surface layer is  $\sim 10$  times larger than the radius of the micro-contact, the spreading resistance equation provides the most accurate approximation of the surface layer conductivity. For an unconfined sample, the conductivity of the bulk cannot be calculated as the area where current enters the bulk is unknown.

If the thickness of the surface layer is  $\sim 10$  times smaller than the radius of the micro-contact, the geometric factor using the micro-contact area provides the most accurate approximation of the surface layer conductivity. As a consequence, current enters the bulk over an area that is comparable to the micro-contact radius; therefore, the spreading resistance equation provides the most accurate approximation of the bulk conductivity.

When using two micro-contacts on a thin resistive surface layer, the response from the surface layer is independent of the contact separation. The response from the bulk is dependent on the contact separation and at small separations contact interference occurs, in a similar way to that of a single, homogeneous material.

## 5.6 References

1. Fleig, J. & Maier, J. Point contacts in solid state ionics: Finite element calculations and local conductivity measurements. *Solid State Ionics* **86–88**, 1351–1356 (1996).
2. Navickas, E., Gerstl, M., Friedbacher, G., Kubel, F. & Fleig, J. Measurement of the across-plane conductivity of YSZ thin films on silicon. *Solid State Ionics* **211**, 58–64 (2012)

## Chapter 6: Characterisation of Pristine Fe-doped SrTiO<sub>3</sub> Single Crystals prior to Irradiations

### 6.1 Introduction

In this chapter, different levels of Fe-doped SrTiO<sub>3</sub> single crystals are characterised by X-ray Diffraction (XRD and GAXRD) and conventional and micro-contact Impedance Spectroscopy (MCIS). This characterisation was performed prior to 5 MeV Au irradiations.

GAXRD is the initial technique employed to characterise damage in the irradiated samples, however there is little in the literature of pristine single crystal characterisation by this technique. Oyoshi et al.<sup>1</sup> studied undoped SrTiO<sub>3</sub> by this technique and the results reported in this chapter are compared to their findings.

The heating stage used for MCIS measurements has a temperature limit of 580 °C and the resistance limit on the Solartron for impedance measurements is ~ GΩ. Due to the smaller size of the micro-contact, MCIS measurements produce much larger resistances than conventional measurements. As a consequence, samples were selected so their responses could be measured in this temperature and resistance range. SrTiO<sub>3</sub> with different levels of Fe-doping were used because the doping increases the conductivity of SrTiO<sub>3</sub>, allowing samples to be characterised at lower temperatures.

Inductive effects have been reported previously in MCIS measurements<sup>2-5</sup>, and these have been attributed to capacitive coupling of the sample and the heating stage. Increasing the distance between the sample and heating stage by a slab of sapphire decreases these effects. Here we decrease the level of inductance in our measurement system by testing three slabs of sapphire of different thickness.

Finally, the sample under study in the probe station is heated asymmetrically when using a heating stage, meaning there is a temperature gradient between the heating stage, across the piece of sapphire and then across the sample. The surface of the sample then dissipates heat to the surrounding air which is at room temperature. In addition, the tungsten probes attached to micromanipulators at room temperature can also act as heat sinks<sup>6</sup>. As a consequence, the temperature at the surface of the sample can be significantly different to that set at the heating stage. Estimates of the sample temperature have been made using the following equation<sup>6,7</sup>,

$$T_{spr} = \frac{E_a}{k_B \cdot \ln(\sigma_0 4r_{mc}R)} \quad (6.1)$$

where  $E_a$  is the bulk activation energy of the electrical conductivity for the material,  $k_B$  is the Boltzmann constant,  $r_{mc}$  is the micro-contact radius and  $R$  is the measured resistance for a micro-contact and full surface counter electrode. Here we employ a simpler method that operates on the principle of the time constant,  $\tau$ , of the bulk response being independent of the method of measurement,

$$\tau = RC = \frac{GF}{\sigma} \cdot \frac{\epsilon_0 \epsilon_r}{GF} \quad (6.2)$$

$$2\pi f_{max} \tau = 1 \quad (6.3)$$

where  $\sigma$  is the bulk conductivity,  $GF$  is the geometric factor,  $\epsilon_0$  is the permittivity of free space,  $\epsilon_r$  is the relative permittivity and  $f_{max}$  is the frequency of the maximum of the bulk  $M''$  Debye peak. Comparing the frequency of the  $M''$  Debye peak associated with the bulk response from MCIS measurements, where there is a large uncertainty of the sample temperature, to that of conventional impedance measurements, where accurate sample temperatures are obtained ( $\pm 1$  °C), allows the sample temperature(s) for the MCIS measurements to be calibrated.

## 6.2 Results

### 6.2.1 X-ray Diffraction

XRD patterns of the pristine single crystals are shown in Figure 6.1 and the observed diffraction peaks indexed to a unit cell arising from the perovskite structure with space group  $Pm-3m$ . As expected, the two strongest peaks are that of the [001] and [002] planes of the perovskite structure, as this is the orientation the single crystals were grown on. There is a reflection at 42.5 ° attributed to the [002] plane reflection from Cu  $K_\beta$  radiation, consistent with previous studies<sup>8</sup>. No other peaks that would be expected from a polycrystalline sample are observed.

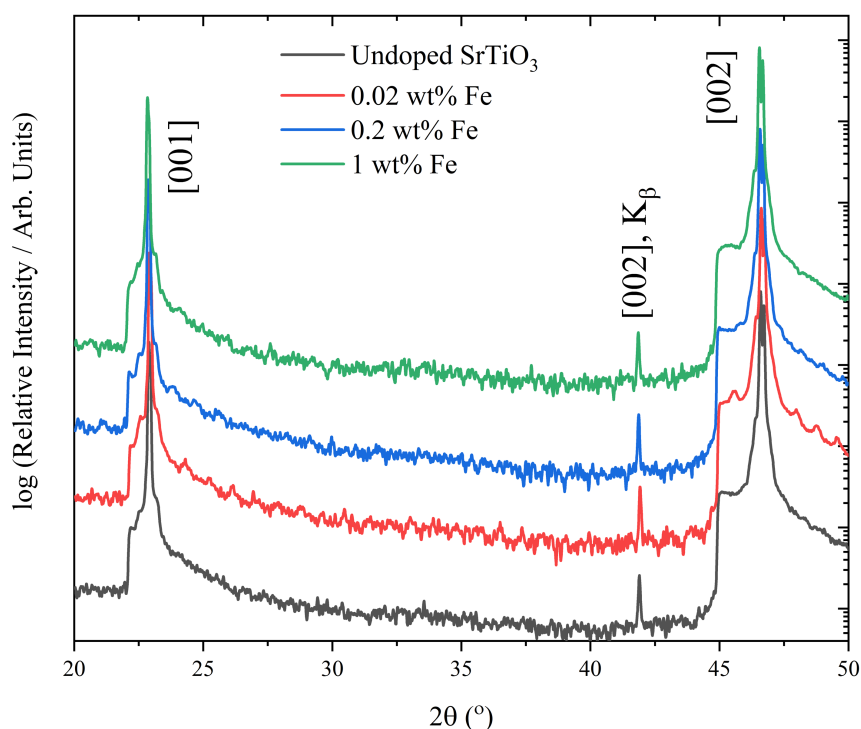


Figure 6.1 XRD patterns of the pristine Fe-doped SrTiO<sub>3</sub> single crystals over the  $2\theta$  range of 20 – 50 °. The relative intensity is on a log scale and the patterns have been stacked for easier comparison.

### 6.2.2 Glancing Angle X-ray Diffraction

GAXRD patterns of the pristine Fe-doped single crystals are shown in Figure 6.2 as this technique will be used initially to identify amorphous regions in the irradiated samples. The penetration depth of the X-rays into the surface plotted against the incidence angle is shown in Figure 6.3 for the undoped sample and the 1 wt% Fe-doped sample. There is very little difference in the penetration depths of the undoped sample and the most heavily Fe-doped sample and so can be assumed to be the same. At an incidence angle of  $\alpha = 0.5^\circ$ , the X-rays penetrate  $\sim 0.46 \mu\text{m}$  into the surface. Only the 0.2 and 1 wt% samples show a reflection at this incidence angle which has been indexed to the [012] peak of the perovskite structure. For an incidence angle of  $\alpha = 10^\circ$ , the X-rays penetrate  $\sim 9.3 \mu\text{m}$  into the surface. Only the 1 wt% sample shows a reflection at this incidence angle which has been indexed to the [001] peak of the perovskite. For all the other incidence angles and compositions, the data are noisy and show no peaks consistent with the perovskite structure. This is most likely a limitation in the technique for highly oriented samples, such as single crystals.

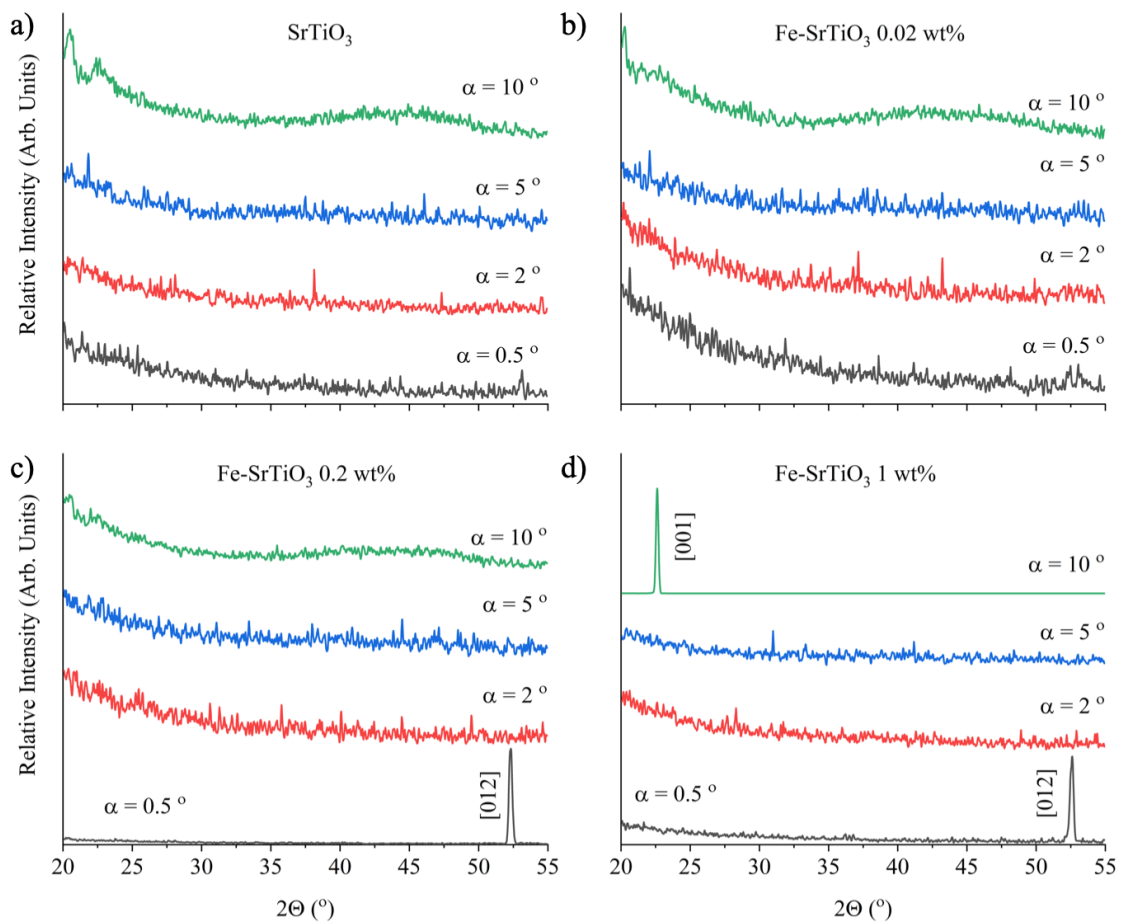


Figure 6.2. GAXRD patterns of the pristine Fe-doped SrTiO<sub>3</sub> single crystals over the 2 $\theta$  range of 20 – 55 ° and at different incidence angles,  $\alpha$ . The patterns have been stacked for easier comparison.

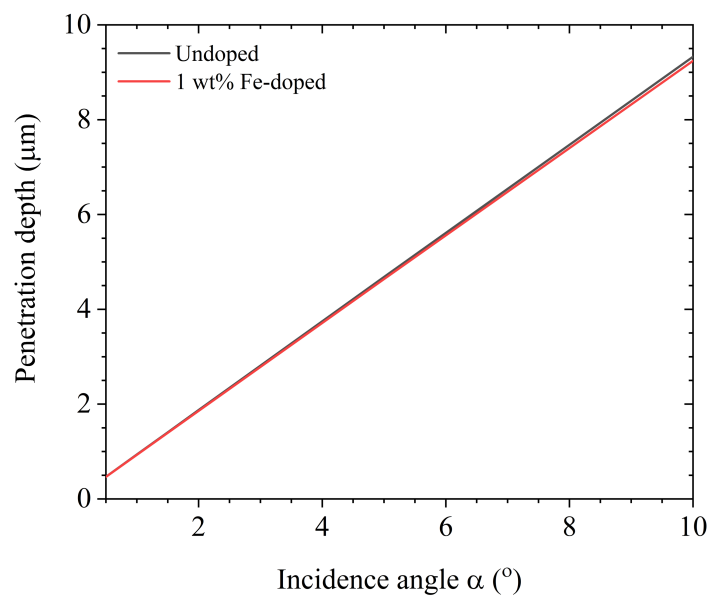


Figure 6.3. Penetration depths of X-rays at different incidence angles,  $\alpha$ , for undoped and 1 wt% Fe-doped SrTiO<sub>3</sub> samples.

### 6.2.3 Conventional Impedance Spectroscopy

Modulus ( $M''$ ) and impedance ( $Z''$ ) spectroscopic plots for the Fe-doped  $\text{SrTiO}_3$  single crystals at 350 °C are shown in Figure 6.4. All compositions show a single Debye peak in the  $M''$  plots which is attributed to the bulk response. The corresponding  $Z''$  plots show an additional feature at lower frequencies which is attributed to an electrode effect, consistent with previous measurements on similar single crystal compositions of  $\text{SrTiO}_3$ <sup>9</sup>.

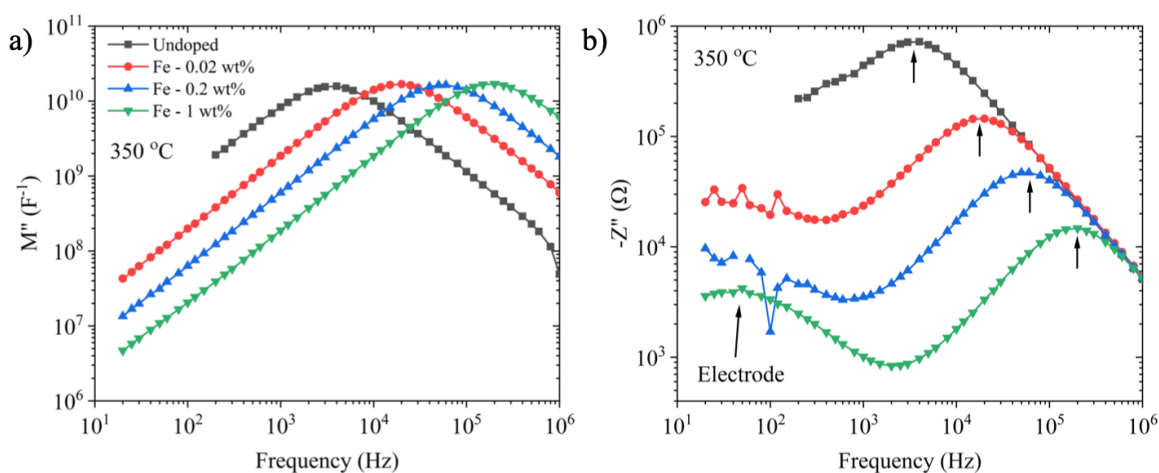


Figure 6.4. a)  $M''$  and b)  $Z''$  spectroscopic plots of Fe-doped  $\text{SrTiO}_3$  single crystals heated at 350 °C. The low frequency data for the undoped sample have been cut-off to remove the noisy measurements. The up arrows at high frequency in b) are attributed to the bulk response of the single crystals.

Arrhenius plots of the bulk conductivity and the inverse relative permittivity as a function of temperature of the pristine Fe-doped single crystals, obtained by conventional Impedance Spectroscopy measurements, are shown in Figure 6.5. These data were calculated using the magnitude and  $f_{\text{max}}$  value of the Debye peak observed in the  $M''$  spectroscopic plots; however, similar calculations based on  $Z''$  spectroscopic peaks were in good agreement. A linear fit has been shown for the Arrhenius data (apart from the 0.02 wt% sample). The calculated activation energies from the gradients of the Arrhenius linear fits were 1.33, 0.87, 1.01 and 1.02 eV for the undoped, 0.02, 0.2 and 1 wt% samples, respectively. As the Fe content increases, the conductivity increases, as shown by the plots shifting to lower temperatures with increasing Fe content, Figure 6.5 (a), and also by the bulk peak shifting to higher frequencies in the spectroscopic plots, Figure 6.4. A linear, Curie-Weiss, fit is shown for the inverse of the bulk permittivity values versus temperature which is reasonably consistent for all samples, Figure 6.5 (b).

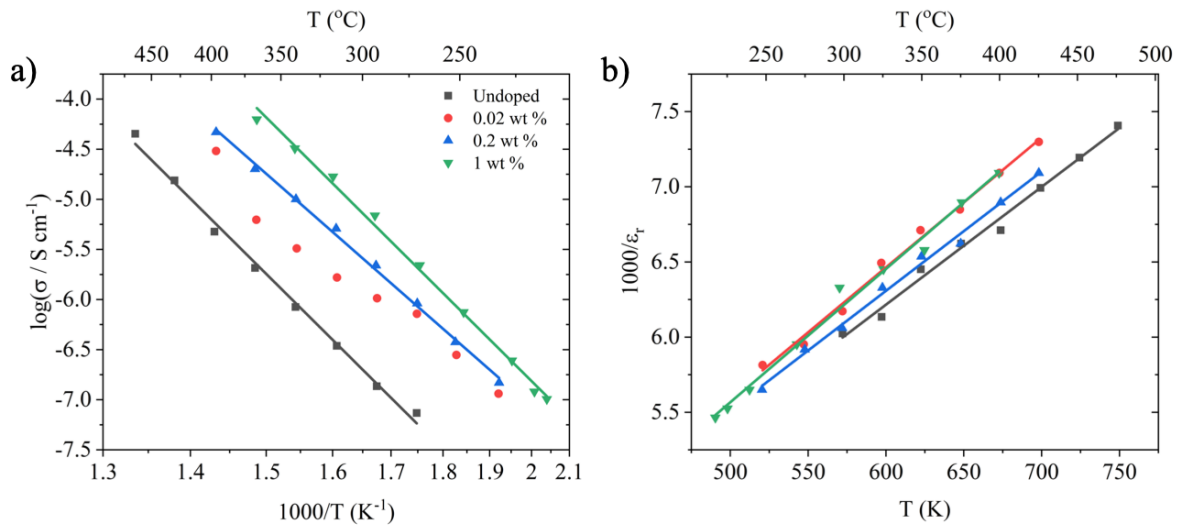


Figure 6.5. a) Arrhenius plots of the bulk conductivity of Fe-doped single crystals measured by conventional impedance spectroscopy and b) the variation in (bulk) reciprocal relative permittivity with temperature.

A frequency-temperature relationship for each sample was obtained by a linear fit through the data with the results shown in Table 6.1. This was required to obtain accurate temperatures for the MCIS measurements. The heating stage is set at a certain temperature, but this is not the same as the sample temperature due to the asymmetric heating set-up. Correction for the position of the M'' peak associated with the bulk response allows the actual sample temperature to be obtained.

Table 6.1. Equations of the frequency vs temperature linear fits for the Fe-doped SrTiO<sub>3</sub> single crystals.

Fe-SrTiO <sub>3</sub> (Fe wt%)	Frequency-Temperature relationship
Undoped	$\log(f_{\max}) = (0.016 \times T(^{\circ}\text{C})) - 2.07$
0.02	$\log(f_{\max}) = (0.013 \times T(^{\circ}\text{C})) - 0.06$
0.2	$\log(f_{\max}) = (0.015 \times T(^{\circ}\text{C})) - 0.35$
1	$\log(f_{\max}) = (0.016 \times T(^{\circ}\text{C})) - 0.54$

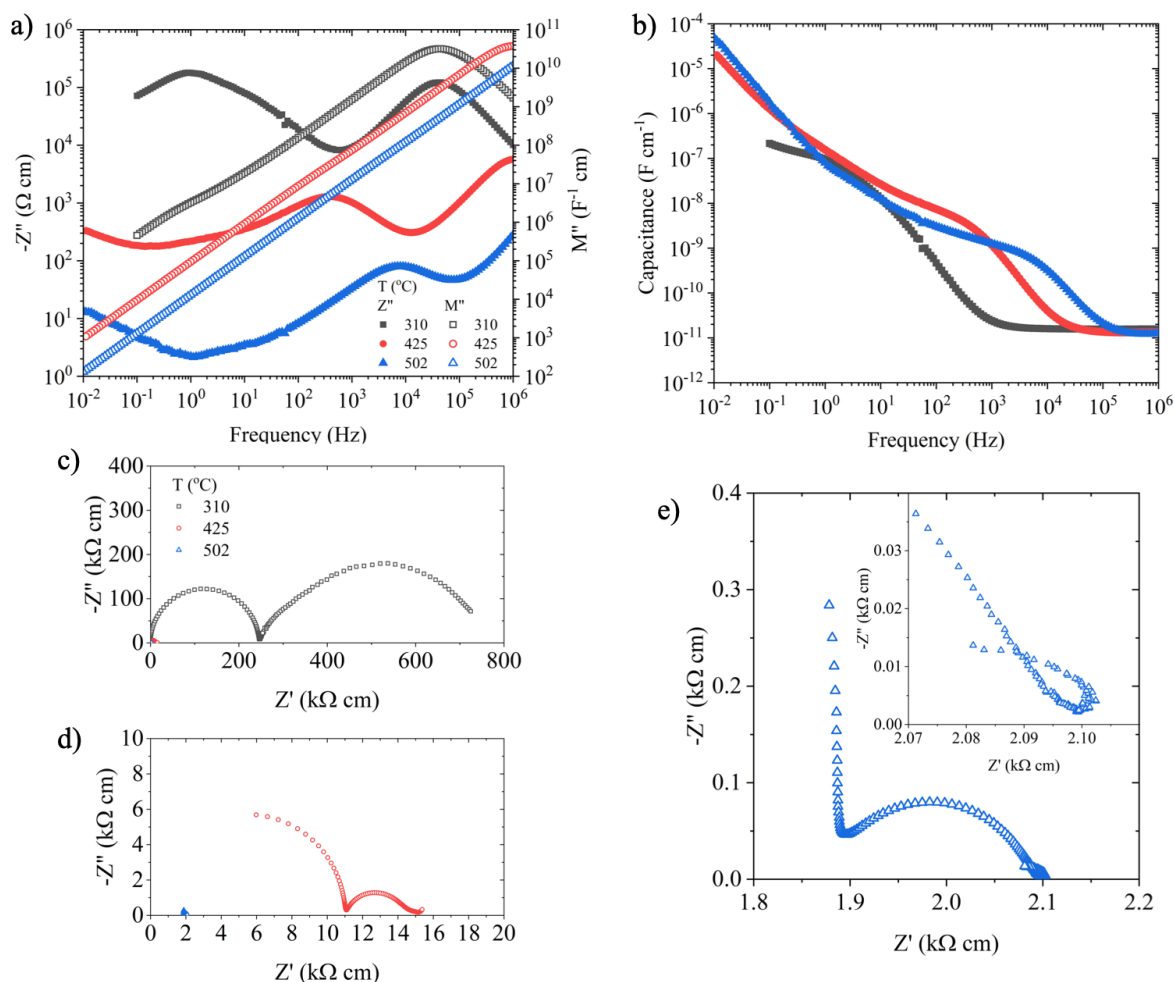


Figure 6.6. a) Combined  $Z''$  and  $M''$  spectroscopic plots, b)  $C'$  spectroscopic plots and c-e)  $Z^*$  plots for the 1 wt% Fe-doped  $\text{SrTiO}_3$  single crystal at temperatures of 310, 425 and 502 °C. Inset of e) is the same data on a smaller scale to highlight the inductive loop.

The impedance response of the 1 wt% Fe-doped sample at multiple temperatures is shown in Figure 6.6. Apart from the bulk,  $M''$  spectroscopic plots show no other response at lower frequencies, whereas  $Z''$  show a number of responses at lower frequencies, Figure 6.6 (a). These extra responses can also be observed in the  $C'$  plots by the presence of plateau at intermediate frequencies and a low frequency incline, Figure 6.6 (b). The bulk response shows a near ideal high frequency arc in  $Z^*$  plots at 310 °C but the lower frequency response appears to be a combination of multiple components that are hard to resolve, Figure 6.6 (c). As the temperature increases, one of these components becomes easier to resolve as the other component significantly decreases, Figure 6.6 (d), until at high enough temperatures there is evidence for induction at low frequencies, Figure 6.6 (e).

## 6.2.4 Micro-contact Impedance Spectroscopy

Inductive loops are common in impedance measurements between two micro-contacts<sup>3,10</sup>. It has previously been stated that these arise because of capacitive coupling of the leads and electrodes to the ground, through the heating stage<sup>10</sup>. These effects can be reduced by increasing the distance between the sample and the heating stage. This has been done previously by placing a piece of sapphire between the sample and the heating stage<sup>2,6</sup>. Complex impedance ( $Z^*$ ) plots and overlaid  $Z''$  and  $M''$  spectroscopic plots for the 1 wt% Fe-doped  $\text{SrTiO}_3$  single crystal with different thicknesses of sapphire (1, 3 and 10 mm) between it and the heating stage are shown in Figure 6.7.

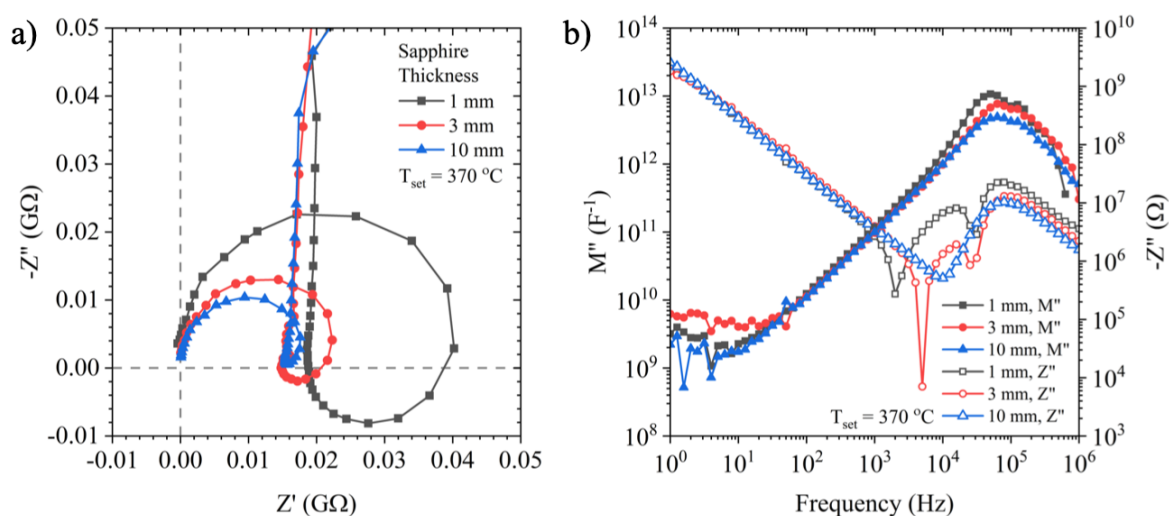


Figure 6.7. a)  $Z^*$  and b) combined  $Z''$  and  $M''$  spectroscopic plots for the 1 wt% Fe-doped  $\text{SrTiO}_3$  single crystal at a set temperature of 370 °C with different thicknesses of sapphire between the sample and the heating stage.

Effects of inductance can be observed for all measurements with the different thicknesses of sapphire, Figure 6.7. In the complex impedance plot, Figure 6.7 (a), inductive loops are observed. The size of the loop is greatest for the 1 mm sapphire and decreases as the thickness of the sapphire increases, increasing the distance between the sample and the heating stage. For the 1 and 3 mm thick sapphire measurements,  $Z''$  is positive where the inductive loop occurs and then increases straight up (spike) at lower frequencies, similar to the response of a pure capacitor. For the 10 mm thick sapphire measurement, the loop still occurs but  $Z''$  is never positive.

Inductive effects can also be observed in the spectroscopic plots, Figure 6.7 (b). Resonance peaks occur between 1 and 100 kHz in the  $Z''$  plots, open symbols in Figure 6.7 (b). The resonance peaks are separated by a large frequency range for the 1 mm sapphire measurement

but the frequency range decreases with increasing thickness. When the sapphire is 10 mm thick this effect is almost negligible. The position of the  $Z''$  peaks occur at a slightly higher frequency than the  $M''$  peaks and this could also be due to the inductance. The following measurements (rest of this chapter and Chapter 7) are taken with 10 mm thick sapphire slabs as these measurements obtained the least amount of inductance.

MCIS measurements were recorded over a range of temperatures between 340 and 550 °C and using micro-contact radii of 60, 50, 40 and 30  $\mu\text{m}$  and  $s/r$  of 2 or 10. The resistance of the bulk response was extracted using the different formalisms and the conductivity calculated. All methods were in reasonably good agreement. For the remainder of this thesis, all measurements will be extracted from the  $M''$  peak height and associated  $f_{\text{max}}$  as  $M''$  seemed to be least affected by inductance effects (see Figure 6.7 (b)) and is most convenient.

Although the temperature at the surface of the sample is unknown, it can be estimated with comparison to macroscopic impedance measurements of the same sample, as the time constant is geometry independent. By using Equation 6.1 or by measuring the frequency of the bulk response, the equations listed in Table 6.1 can be used to estimate the sample temperature. A plot showing the set temperature and the corrected temperature for the three Fe-doped samples is shown in Figure 6.8. At high set temperatures, the 1 wt% Fe doped actual temperature is in worst agreement with the set temperature whereas the 0.02 wt% is in best agreement. In contrast, at lower temperatures the 1 wt% actual temperature is very close to the set temperature and the 0.02 wt% sample in worst agreement. Corrections for the sample temperature are similar using both methods, although the corrected temperature is slightly higher when using Equation 6.1. In the following figures, all temperatures have been corrected using the frequency of the bulk peak from  $M''$  spectroscopic plots and the equations listed in Table 6.1.

In this contact geometry, the spreading resistance equation gives a good approximation for the conductivity. An Arrhenius plot and the inverse effective permittivity as a function of temperature for the 1 wt% Fe-doped sample is compared to the conventional impedance measurements in Figure 6.9.

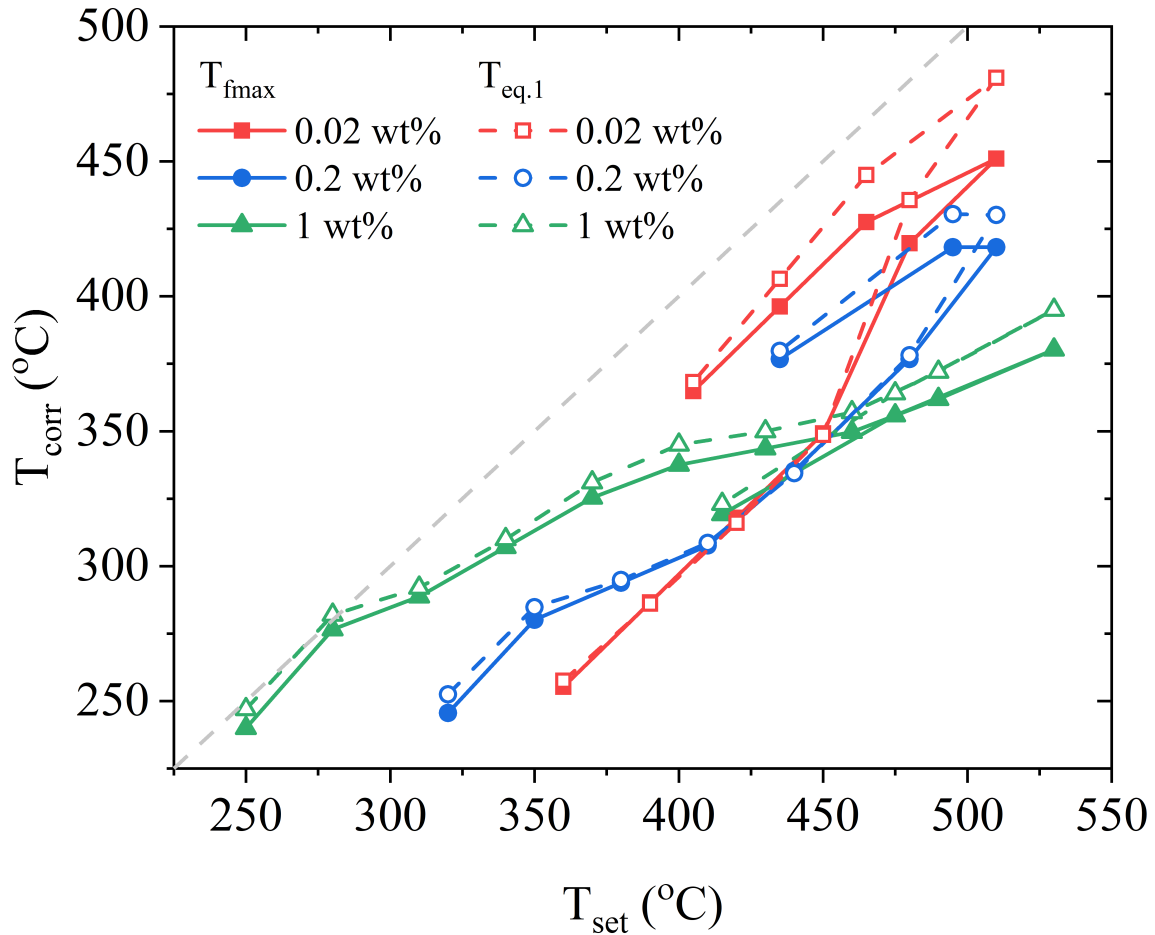


Figure 6.8. Plot showing the heating stage set temperature and the estimated actual sample temperature from taking the position of the  $M''$  peak associated with the bulk and using the equations in Table 6.1 (closed symbols) or using Equation 6.1 (open symbols). The dashed grey line represents where  $T_{set} = T_{corr}$ .

The calculated conductivity is accurate at low temperatures without any corrections, red circles towards the right of Figure 6.9. As the temperature increases, the data points with no corrections deviate significantly from the conventional measurements. After correcting the temperature by using the position of the bulk  $M''$  peaks and the equation in Table 6.1, the data are in much better agreement with the conventional measurements; however, all data points are offset from the conventional measurements. Finally, an  $s/r$  of 2 requires a correction of 0.83 to account for contact interference at small separations (from Chapter 4) and after this correction the data is in better agreement with the conventional measurements. In contrast, the effective permittivity calculations appear to be less accurate with respect to the values from conventional measurements, even after the corrections, Figure 6.9 (b). Different micro-contact sizes and separations were tested and the conductivity Arrhenius plots and inverse effective permittivity as a function of temperature for the 1 wt% Fe-doped sample are shown in Figure 6.10.

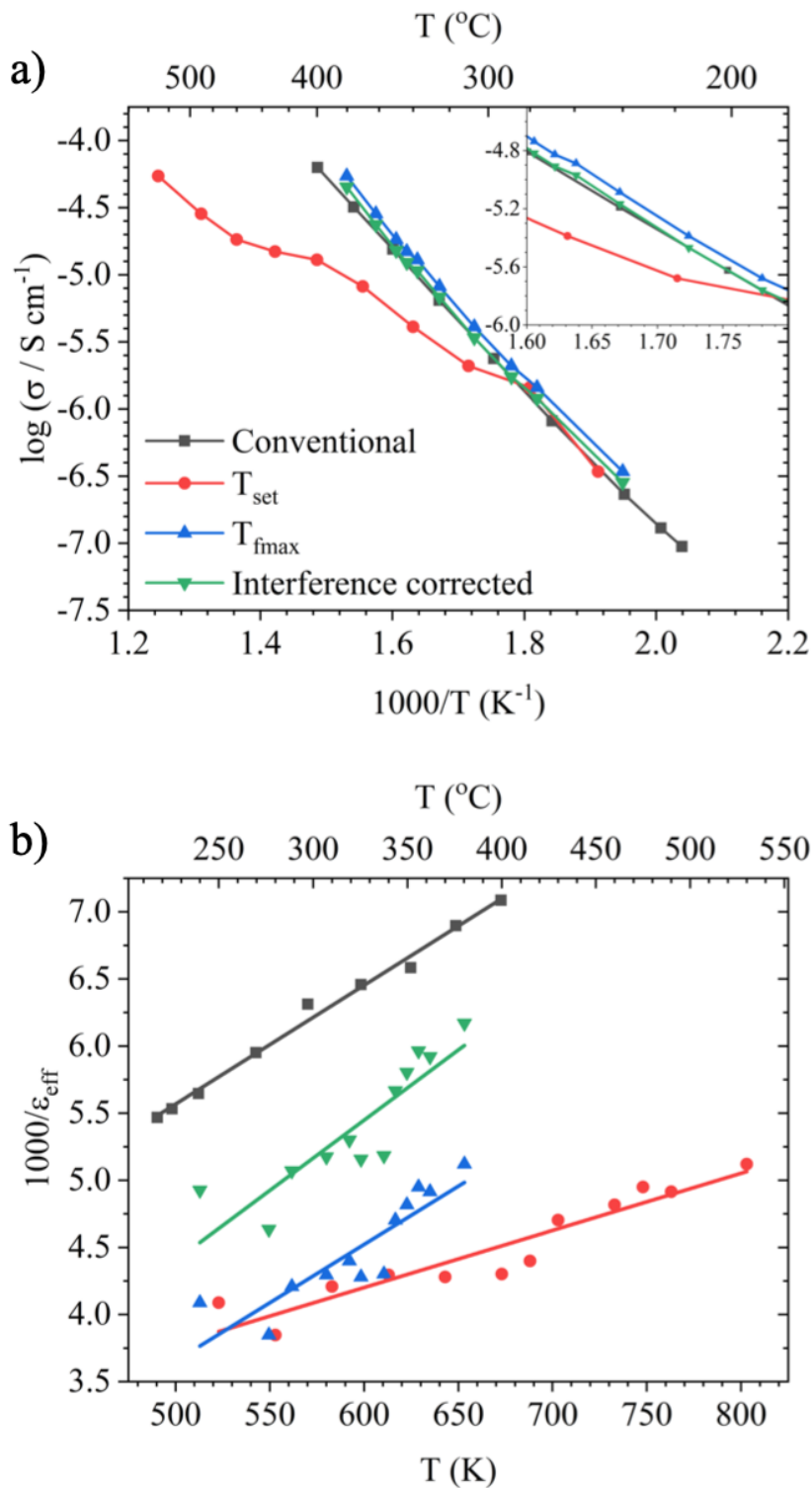


Figure 6.9. a) Conductivity Arrhenius plots and b) the inverse effective permittivity plotted against temperature for the 1 wt% Fe-doped  $\text{SrTiO}_3$  sample by conventional Impedance Spectroscopy measurements and compared to micro-contact measurements with  $r_{mc} = 30 \mu\text{m}$  and  $s/r = 2$ . Data are shown for measurements with no corrections applied (red circles), correction for the temperature using Table 6.1 (blue up triangles), and an additional correction for contact interference from Chapter 4 (green down triangles).

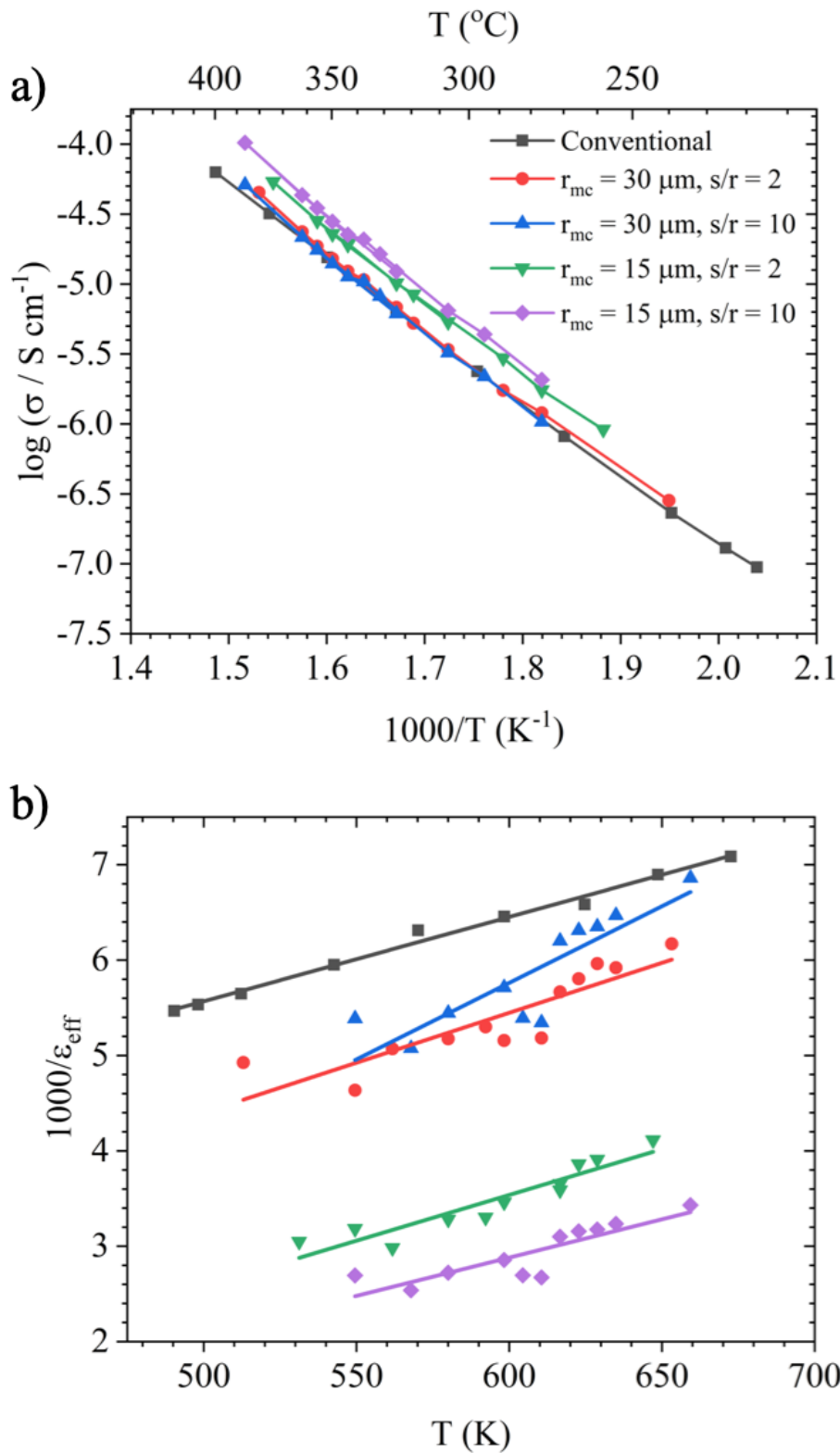


Figure 6.10. a) Conductivity Arrhenius plots and b) the inverse effective permittivity plotted against temperature for the 1 wt% Fe-doped SrTiO<sub>3</sub> sample using a micro-contact radius of 30 and 15  $\mu\text{m}$  and  $s/r$  of 2 and 10. Measurements have both corrections described above applied and are compared to conventional impedance measurements.

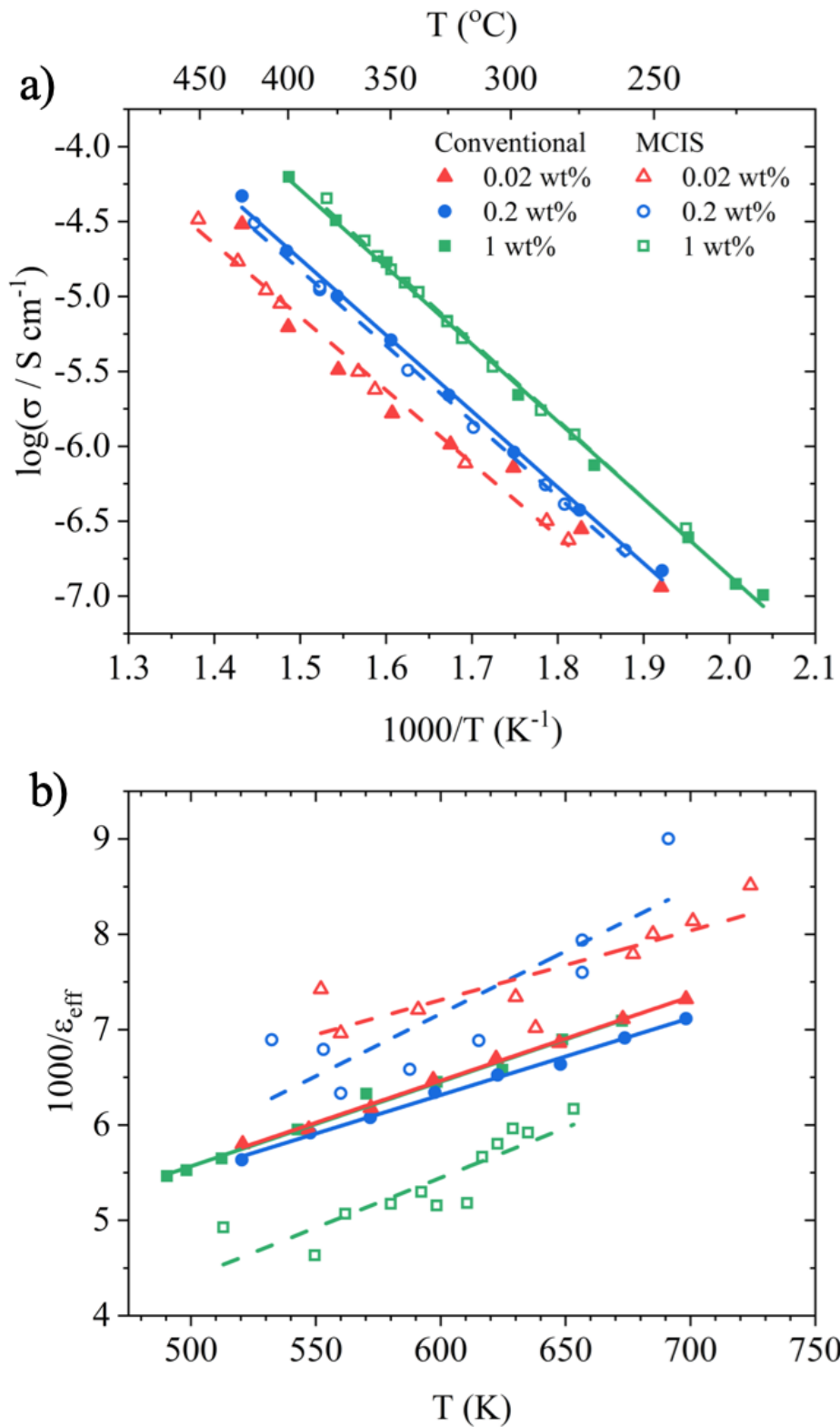


Figure 6.11. a) Conductivity Arrhenius plots and b) inverse permittivity-temperature plots comparing micro-contact measurements with conventional measurements. The MCIS measurements use  $r_{mc} = 30 \mu\text{m}$  and  $s/r = 10$ . Filled and open symbols are conventional and MCIS measurements, respectively.

For both the conductivity and effective permittivity, the larger contact size measurements give values in better agreement with the conventional measurements, Figure 6.10. Using a smaller contact size produces overestimates when using the spreading resistance equation. Similar trends were observed for the other compositions with the larger contact size returning values in best agreement with conventional measurements. Figure 6.11 shows conductivity Arrhenius plots and inverse effective permittivity as a function of temperature plots for the different compositions comparing the micro-contact measurements, with  $r_{mc} = 30 \mu\text{m}$  and  $s/r = 10$ , with conventional measurements.

The MCIS conductivity calculations (open symbols) for each composition are in good agreement with the conventional measurements (solid symbols), Figure 6.11 (a); however, although the values are in poorer agreement for the permittivity calculations the values remain fairly comparable, Figure 6.11 (b).

#### 6.2.5 Micro-contact / conventional Impedance Spectroscopy comparison

A comparison between a conventional and a MCIS measurement after temperature and geometry corrections is shown in Figure 6.12. The high frequency data, attributed to the bulk response, are in good agreement in both impedance and electric modulus formalisms and the capacitance, Figure 6.12 (a) and (b). The Nyquist plots at high frequency are reasonably comparable, with the main difference being the inductive loop, Figure 6.12 (d). In contrast, the lower frequency data show some differences, Figure 6.12 (c).

For the conventional measurement, the  $M''$  plot (black open squares in Figure 6.12 (a)) decreases linearly at frequencies lower than the Debye peak attributed to the bulk response, showing no clear extra responses, whereas the corresponding  $Z''$  plot (black filled squares in Figure 6.12 (a)) shows another response around 60 Hz. This response can also be observed in the  $Z^*$  plot, Figure 6.12 (d), as a lower frequency second arc. The micro-contact measurement shows a similar bulk response in both the  $M''$  and  $Z''$  spectroscopic plots (red circles in Figure 6.12 (a)) and the  $C'$  plateaus at similar values to the conventional measurement; however, the influence of inductance is visibly more apparent in the  $Z''$  and  $C'$  spectroscopic plots. The magnitude of the low frequency  $Z''$  response is 2-3 orders of magnitude greater than the conventional response and can also be observed in the Nyquist plot as a much larger lower frequency arc, red circles in Figure 6.12 (c)).

At lower frequencies, the  $M''$  plot for the conventional measurement shows no response but the  $Z''$  data show a response and can be observed as a small shoulder in the Nyquist plot. The micro-contact measurement is  $\sim 4$  orders of magnitude greater in  $Z''$  and a response is also

observable in the  $M''$  plot, Figure 6.12 (a).  $C'$  increases more in the conventional measurement than the micro-contact measurement, Figure 6.12 (b).

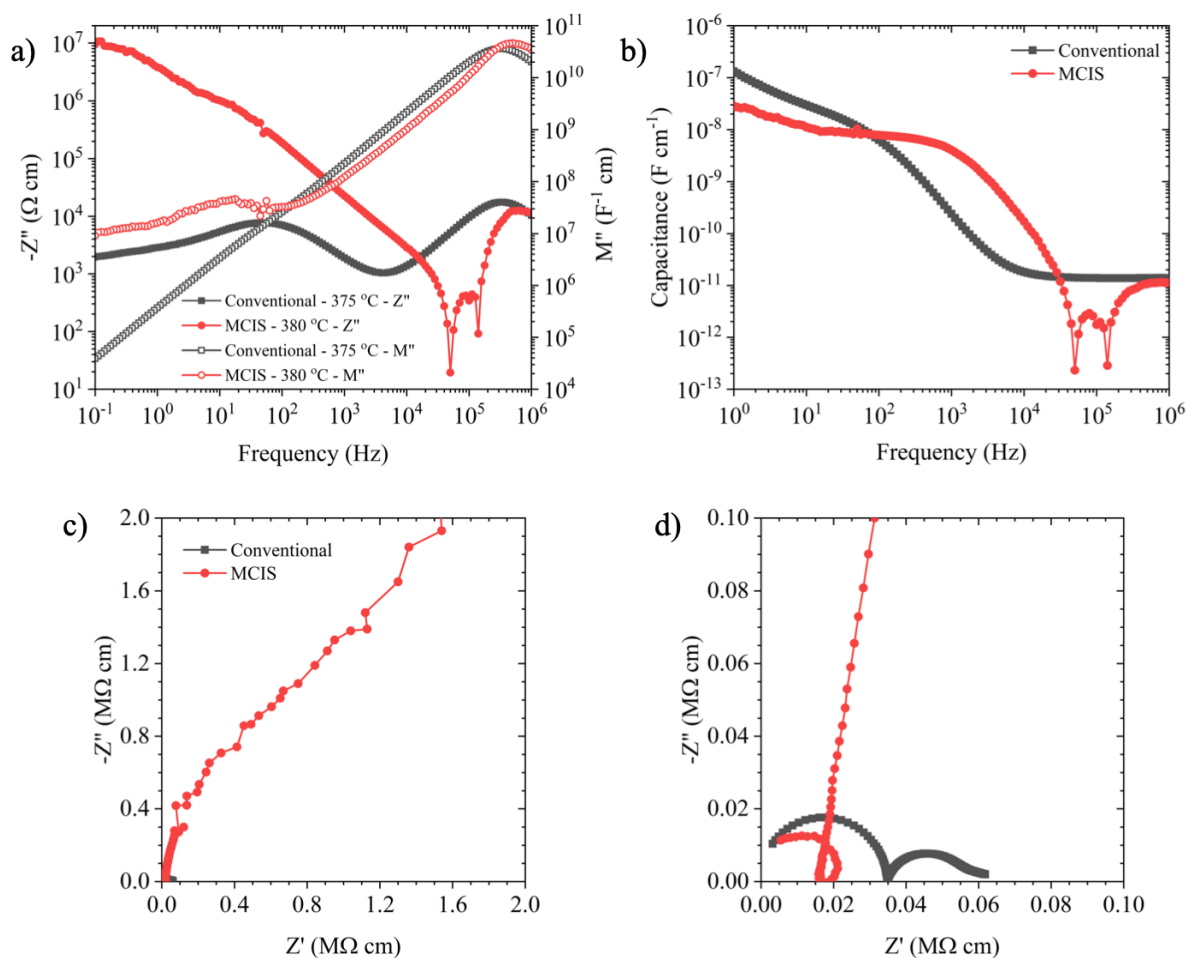


Figure 6.12. Comparison between a conventional measurement at 375 °C and a micro-contact measurement at 380 °C after corrections for geometry and temperature. a)  $Z''$  and  $M''$  spectroscopic plots, b)  $C'$  spectroscopic plots, c) and d)  $Z^*$  plots of the same data but on different scales.

### 6.3 Discussion and Conclusions

XRD patterns of the crystals confirm all are single-phase with the perovskite structure ( $Pm-3m$ ), Figure 6.1, in agreement with previous studies for similar Fe-doping levels<sup>11</sup>. The small peak at  $\sim 42^\circ$  is due to Cu  $K_\beta$  radiation and not an impurity in the samples. It should be noted that the data is shown on a log scale and the most intense peaks obtained counts in the order of  $10^5$ . The Cu  $K_\beta$  Ni filter employed on the D2 phaser is expected to suppress the  $K_\beta$  counts to 0.01%. Considering the counts are so high for the  $K_\alpha$  peaks, it may be expected that the  $K_\beta$  peaks are also significant when plotted on a logarithmic scale.

GAXRD data did not return useful information about the samples, Figure 6.2. Our results are similar to that reported by Oyoshi et al.<sup>1</sup> in that the expected perovskite peaks were not present;

however, for the undoped sample Oyoshi et al. obtained a [012] reflection where we did not. Using GAXRD will help in identifying damage and amorphous regions in samples in the first case after irradiation; however, damage depths will not be obtainable and cross-sectional transmission electron microscopy is required.

Conventional Impedance Spectroscopy showed the bulk conductivity to increase with the Fe content. Fe-doped SrTiO<sub>3</sub> is a mixed conductor. Replacing Ti<sup>4+</sup> with Fe<sup>3+</sup> induces the formation of oxygen vacancies for charge compensation, increasing the ionic conductivity<sup>12</sup>. The electronic conduction contribution also becomes more dominant with increasing Fe content<sup>13</sup>. Our results are in agreement with these studies and Rothschild et al<sup>14</sup>.

Conventional Impedance data at different temperatures identified the bulk response and also the presence of additional responses at low frequencies, Figure 6.6. The bulk response is near-ideal and behaves as expected with temperature. The extra responses at low frequency are very sensitive to temperature and are attributed to processes at the interface of the sample and electrode. The low frequency response gives information about the charge carriers and interactions at the interface but these processes are complex and difficult to resolve. Although the low frequency response was not investigated in detail it provides a signature for a pristine sample response to compare with the damaged sample response and to identify any additional responses that may arise as a result of the irradiations.

Micro-contact impedance measurements are affected by inductance that is assumed to originate from the heating stage. The heating element on the THMS600 heating stage is a single coil of platinum wire. When current passes through a coil, it induces a magnetic field. This magnetic field may be causing the induction in micro-contact measurements and would explain why increasing the distance between the sample and the heating stage decreases the amount of induction, Figure 6.7. The data are affected less by the inductance in the Modulus ( $M''$ ) formalism than in Impedance ( $Z''$ ). At this stage, it is unknown why this is the case but as a consequence of this observation,  $M''$  plots are used for all subsequent data analysis.

The temperature of the sample has been calculated using both Equation 6.1, as in previous studies<sup>6,7</sup> and by  $f_{\max}$  of the  $M''$  Debye associated with the bulk response and the equations listed in Table 6.1. Both methods are in relatively good agreement. Equation 6.1 uses the fit of an Arrhenius plot and determines at what temperature the measured conductivity would be on the linear fit of the Arrhenius plot. Using  $f_{\max}$  of the bulk response in  $M''$  spectroscopic plots and then correcting the temperature uses the fit from the conventional measurement  $f_{\max}$  vs temperature relationship. Ultimately, both methods are calculating the temperature the same

way but from different points in the data and/or different formalisms; however, our method specifies how we extract the resistance. Equation 6.1 doesn't specify where the resistance value is taken from. Intercepts and circle fitting from  $Z^*$  plots or extracting resistance from  $Z''$  spectroscopic plots are susceptible to inductance, as shown in Figure 6.7 (b).  $M''$  spectroscopic plots are less susceptible to inductance effects and so there is more confidence in extracting correct resistances for the bulk using this method. As far as we are aware, comparing  $f_{\max}$  of the  $M''$  bulk response in MCIS measurements to the conventional measurements as a method for obtaining the actual temperature at the surface of the sample has not been used previously. The MCIS measurements without any corrections for the sample temperature are in poor agreement with conventional measurements, especially at high temperatures (for the 1 wt% sample), Figure 6.9. By using the equations in Table 6.1, i.e. comparing the frequency of the bulk response in MCIS measurements to the frequency of the bulk in conventional measurements, the conductivities are in much better agreement with conventional measurements. Using the correction factors to account for contact interference from Chapter 4 further improves the agreement with conventional measurements. The calculated permittivity values are in poorer agreement with the conventional measurements but are reasonably comparable, Figure 6.11.

Comparison between conventional and MCIS measurements after corrections show the high frequency bulk response is comparable, ignoring inductance effects, in all formalisms shown, Figure 6.12. The second response that has been attributed to the electrode/sample interface, has a much larger resistance in the MCIS measurement because of the smaller size of the electrodes. Because of this, the response is easily identifiable in both  $Z''$  and  $M''$  plots by MCIS measurements whereas only  $Z''$  could resolve this response in conventional measurements. As stated previously, these measurements provide a signature of a pristine sample to compare to the irradiated samples considered in the next chapter.

## 6.4 References

1. Oyoshi, K., Hishita, S. & Haneda, H. Study of ion beam induced epitaxial crystallization of SrTiO<sub>3</sub>. *J. Appl. Phys.* **87**, 3450–3456 (2000).
2. Fleig, J., Jamnik, J., Maier, J. & Ludvig, J. Inductive Loops in Impedance Spectroscopy Caused by Electrical Shielding. *J. Electrochem. Soc.* **143**, 3636–3641 (1996).
3. Lee, J. S., Fleig, J., Maier, J., Chung, T. J. & Kim, D. Y. Microcontact impedance spectroscopy in nitrogen-graded zirconia. *Solid State Ionics* **176**, 1711–1716 (2005).

4. Kubicek, M., Taibl, S., Navickas, E., Hutter, E., Fafilek, G. & Fleig, J. Resistive states in strontium titanate thin films: Bias effects and mechanisms at high and low temperature. *J. Electroceramics* **39**, 197–209 (2017).
5. Taibl, S., Fafilek, G. & Fleig, J. Impedance spectra of Fe-doped SrTiO<sub>3</sub> thin films upon bias voltage: Inductive loops as a trace of ion motion. *Nanoscale* **8**, 13954–13966 (2016).
6. Huber, T. M., Opitz, A. K., Kubicek, M., Hutter, H. & Fleig, J. Temperature gradients in microelectrode measurements: Relevance and solutions for studies of SOFC electrode materials. *Solid State Ionics* **268**, 82–93 (2014).
7. Opitz, A. K. & Fleig, J. Investigation of O<sub>2</sub> reduction on Pt/YSZ by means of thin film microelectrodes: The geometry dependence of the electrode impedance. *Solid State Ionics* **181**, 684–693 (2010).
8. Ng, M. F. & Cima, M. J. Heteroepitaxial growth of lanthanum aluminate films derived from mixed metal nitrates. *J. Mater. Res.* **12**, 1306–1314 (1997).
9. Rodewald, S., Fleig, J. & Maier, J. Measurement of conductivity profiles in acceptor-doped strontium titanate. *J. Eur. Ceram. Soc.* **19**, 797–801 (1999).
10. Rodewald, S., Fleig, J. & Maier, J. Microcontact Impedance Spectroscopy at Single Grain Boundaries in Fe-Doped SrTiO<sub>3</sub> Polycrystals. *J. Am. Ceram. Soc.* **84**, 521–530 (2001).
11. Da Silva, L. F., Bernardi, M. I. B., Maia, L. J. Q., Frigo, G. J. M. & Mastelaro, V. R. Synthesis and thermal decomposition of SrTi<sub>1-x</sub>Fe<sub>x</sub>O<sub>3</sub> (0.0 < x < 0.1) powders obtained by the polymeric precursor method. **97**, 173–177 (2009).
12. Da Silva, L. F., M'Peko, J. C., Andres, J., Beltran, A., Gracia, L., Bernardi, M. I. B., Mesquita, A., Antonelli, E., Moreira, M. L. & Mastelaro, V. R. Insight into the effects of Fe addition on the local structure and electronic properties of SrTiO<sub>3</sub>. *J. Phys. Chem. C* **118**, 4930–4940 (2014).
13. Kubacki, J., Kajewski, D., Goraus, J., Szot, K., Koehl, A., Lenser, Ch., Dittman, R. & Szade, J. Impact of Fe doping on the electronic structure of SrTiO<sub>3</sub> thin films determined by resonant photoemission. *J. Chem. Phys.* **148**, 154702 (2018).

14. Rothschild, A., Menesklou, W., Tuller, H. L. & Ivers-Tiffée, E. Electronic structure, defect chemistry, and transport properties of  $\text{SrTi}_{1-x}\text{Fe}_x\text{O}_{3-y}$  solid solutions. *Chem. Mater.* **18**, 3651–3659 (2006).

# Chapter 7: Characterising Radiation Damage in Fe-doped SrTiO<sub>3</sub> Single Crystals using Micro-contact Impedance Spectroscopy

## 7.1 Introduction

In Chapter 6, characterisation of pristine Fe-doped SrTiO<sub>3</sub> single crystals was reported in preparation for radiation damage studies. Impedance Spectroscopy measurements identified this signature to include the bulk response and also low frequency responses that were attributed to the sample/electrode interface. Any deviation(s) from this signature can be concluded to be as a result of the irradiations.

The orientation of the ion beam with respect to the crystallographic axes of the substrate can have a significant effect when irradiating single crystals. If the incident ions are aligned along atomic rows, the positively charged lattice atoms ‘steer’ the positively charged ions down the open space between atomic rows. This effect is called channeling<sup>1</sup> and leads to a lower rate of energy loss,  $\frac{dE}{dx}$ , and a greater range into the material. To minimise this effect the irradiations were performed at an incidence angle that was 7 ° from the normal to the surface.

The irradiated samples were first characterised using commonly used techniques to characterise the structural properties of the sample, such as glancing angle X-ray diffraction (GAXRD) and cross-sectional transmission electron microscopy (XTEM). These are then repeated for annealed/recrystallised samples before conventional Impedance Spectroscopy and Micro-contact Impedance Spectroscopy (MCIS) measurements were performed. Corrections for the sample temperature were made using the methods described in Chapter 6.

As far as we are aware, this is the first time that Impedance Spectroscopy, particularly MCIS, has been used in attempts to characterise radiation damage in ceramics.

## 7.2 Results

### 7.2.1 SRIM Calculations

Prior to irradiations, SRIM<sup>2</sup> (Stopping and Range of Ions in Matter) was used to determine the damage profile for different energy Au irradiations in SrTiO<sub>3</sub> using 50 eV for the displacement energies of Sr, Ti and O. Au was used as it is heavy and can therefore produce a large amount of damage; however, a possible disadvantage is that it could lead to conducting pathways through the sample. The results of the SRIM simulations are shown in Figure 7.1.

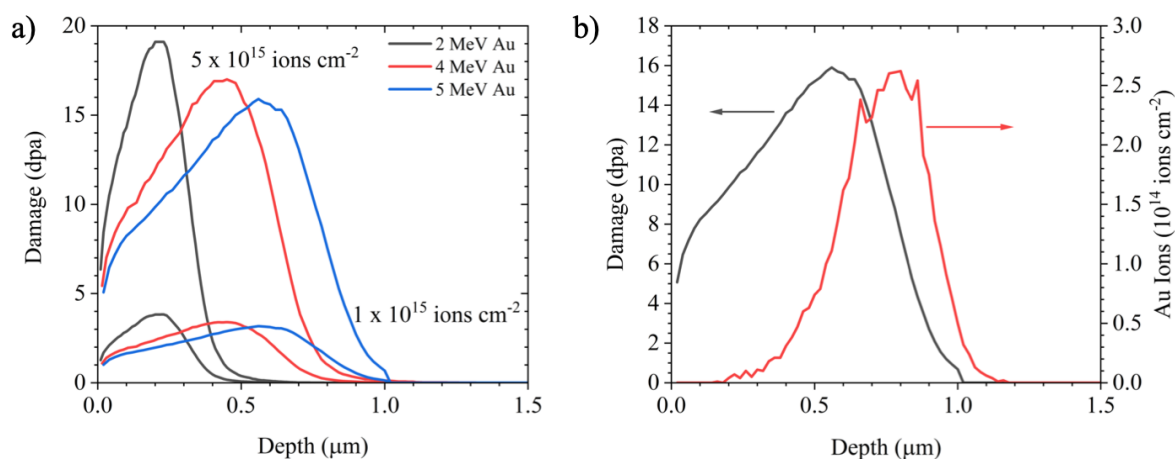


Figure 7.1. a) Damage profiles of different energy and fluence of Au irradiations and b) damage profile and ion range for the chosen irradiations.

As the energy of the irradiations increases, the damage depth also increases whilst the peak damage decreases, Figure 7.1 (a). For a fluence of  $5 \times 10^{15}$  ions  $\text{cm}^{-2}$ , the damage produced is much larger than that required to amorphise the material, which has previously been reported to be  $\sim 1$  dpa<sup>3,4</sup>. For the lower fluence, the damage at the surface is much closer to the damage required to amorphise SrTiO<sub>3</sub>, hence to ensure amorphisation occurs from the surface the higher fluence was chosen. 5 MeV Au irradiations were chosen as the damage extends the furthest into the material and there was a better chance of identifying the amorphised region by Impedance Spectroscopy. The Au ions are expected to come to rest approximately 300 nm deeper than the peak damage, Figure 7.1 (b).

### 7.2.2 Glancing Angle X-ray Diffraction & Recovery

GAXRD patterns of the Fe-doped single crystals after irradiations and after holding at set temperatures for 30 mins are shown in Figure 7.2. For each composition, the irradiated samples prior to any heat treatments show diffuse scattering at  $\sim 30^\circ$ . No peaks associated with any crystalline phase can be observed; however, the pristine samples showed little evidence of crystallinity (see Figure 6.2 in Chapter 6). After heating at 300 °C, the 0.02 wt% sample shows the [011] diffraction peak of SrTiO<sub>3</sub> at  $\sim 32^\circ$ , Figure 7.2 (b), but none of the other samples show a clear presence of this peak. At a temperature of 400 °C, all compositions show diffraction peaks expected from a polycrystalline perovskite ( $Pm-3m$ ); however, there is still a small amount of diffuse scattering at  $\sim 30^\circ$  indicating there are still some amorphous regions present in the samples. It appears the undoped and 0.2 wt% samples have more diffuse scattering than the other two compositions; however, this may be associated with errors in the measurements of the temperature (i.e. the 0.02 and 1 wt% compositions were likely held at a

slightly higher temperature). At a temperature of 500 °C, diffuse scattering is not observed in any sample, therefore the amorphous region has fully recovered.

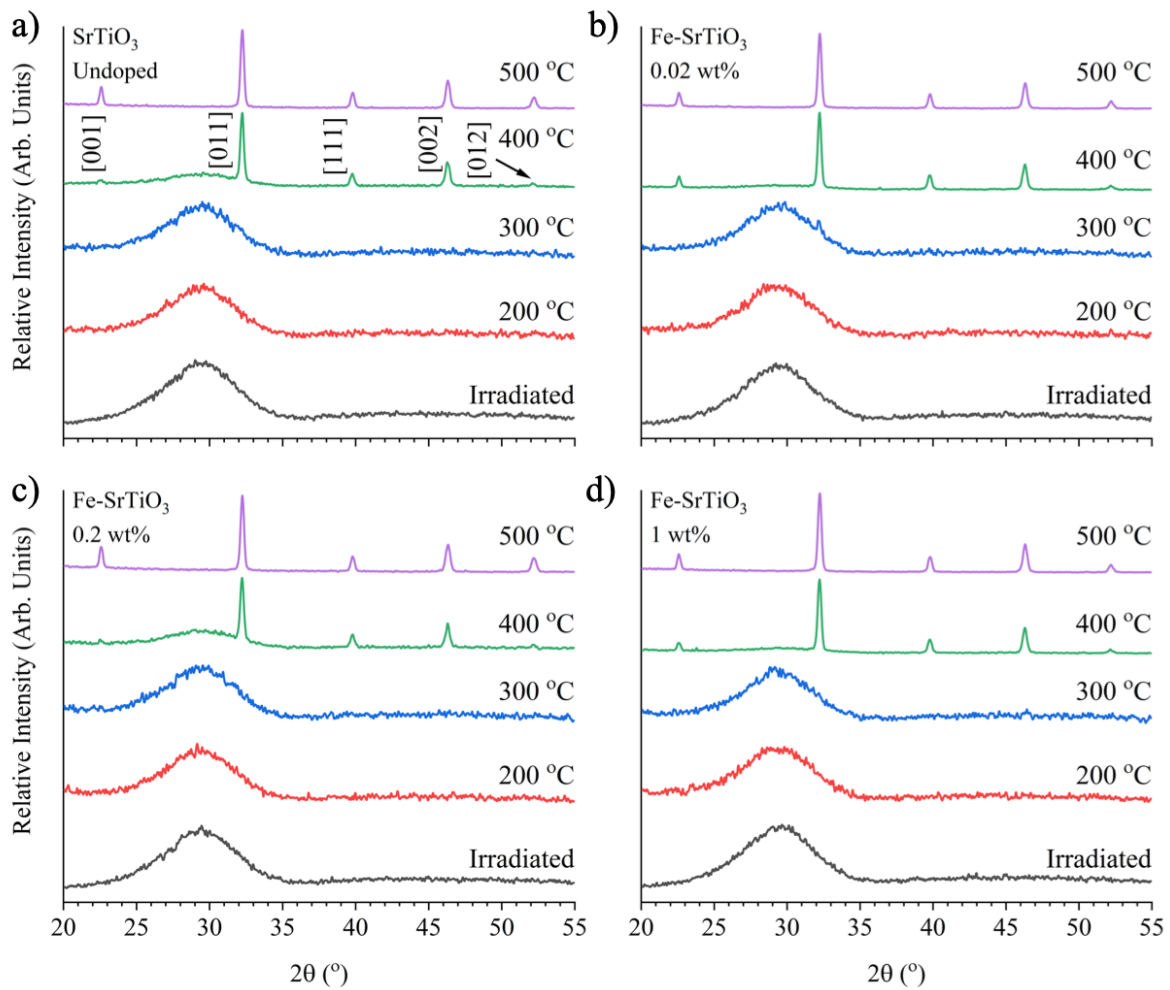


Figure 7.2. GAXRD patterns at an incidence angle of  $\alpha = 2^\circ$  after holding the sample at different temperatures for 30 mins. a) Undoped sample, b) 0.02 wt% Fe-doped sample, c) 0.2 wt% Fe-doped sample and d) 1 wt% Fe-doped sample.

Conventional XRD patterns of the same samples after the 500 °C heat treatment are shown in Figure 7.3. The two most intense reflections are the [001] and [002] peaks which are attributed to the underlying unirradiated single crystal. Peaks associated with polycrystalline perovskite can be observed but are orders of magnitude lower than the two most intense peaks. This suggests these peaks are only associated with the surface.

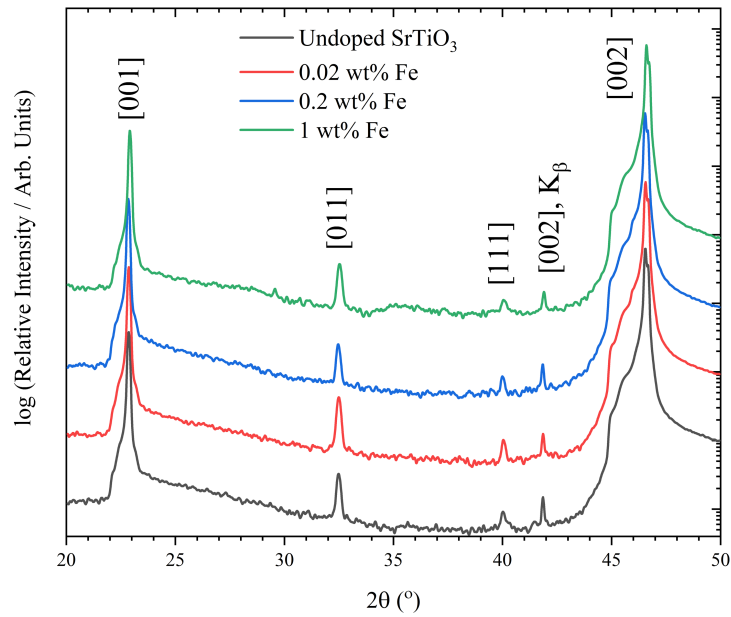


Figure 7.3. XRD patterns of the Fe-doped single crystals after the 500 °C heat treatment.

### 7.2.3 Optical Microscopy

Optical microscope images for a damaged and recovered sample are shown in Figure 7.4. After irradiations and prior to any heat treatment, the sample surface is smooth with no significant features, Figure 7.4 (a). After heat treatment at 500 °C, cracks had formed on the surface which were square or rectangular in shape making the sample appear granular, Figure 7.4 (b). Within these ‘grains’ were other crack-like features. In some regions the cracks appear to converge towards the same point (see bottom left of Figure 7.4 (b)), but generally the ‘grains’ are square or rectangular in shape.

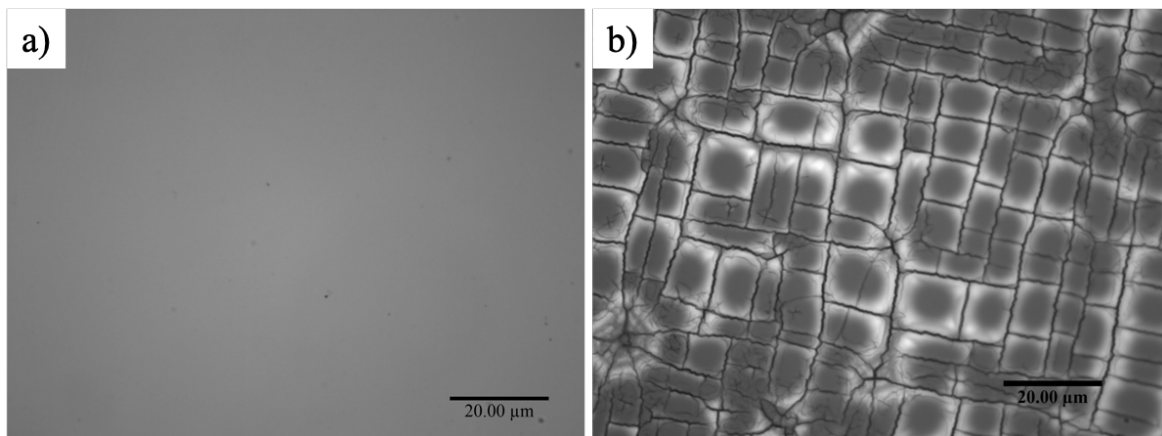


Figure 7.4. Optical microscope image of a) damaged and b) damaged and annealed (at 500 °C) 0.02 wt% Fe-doped single crystal sample at 100x magnification. Other samples showed similar features.

## 7.2.4 Cross-sectional Transmission Electron Microscopy

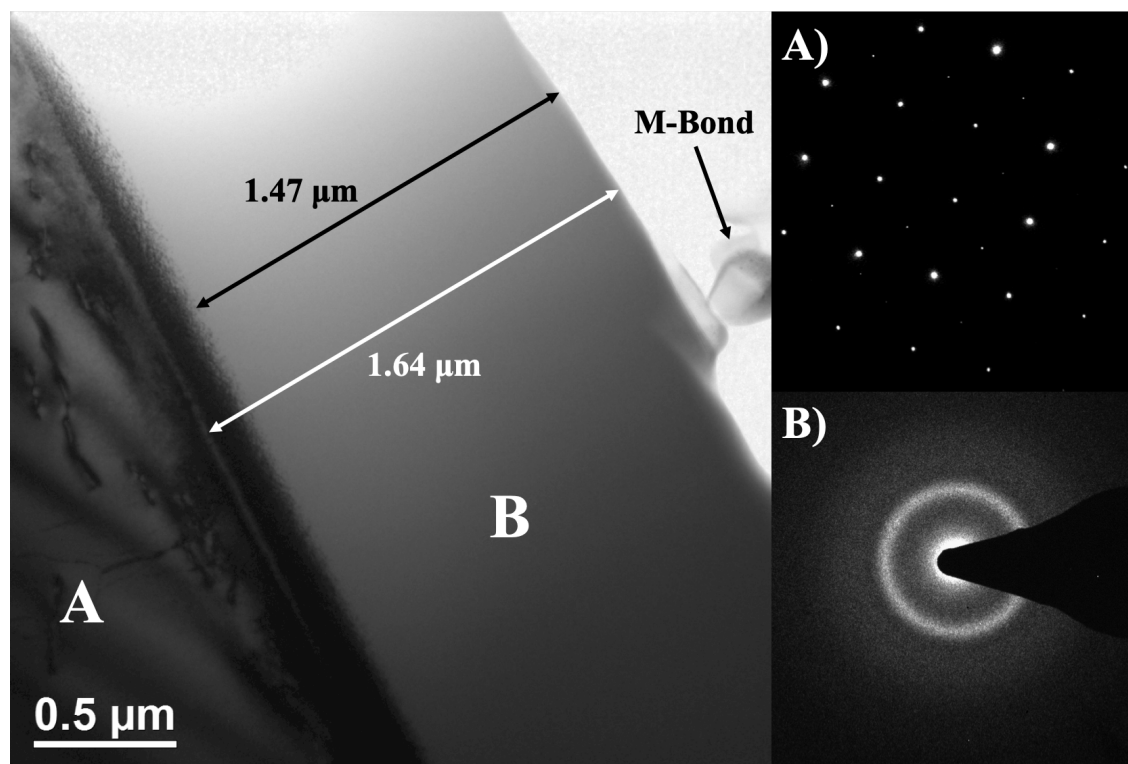


Figure 7.5. Bright-field XTEM micrograph image of a 0.2 wt% Fe-doped  $\text{SrTiO}_3$  sample with the selected area electron diffraction patterns taken from the regions labelled A (crystalline) and B (amorphous surface).

An XTEM micrograph image and selected area electron diffraction patterns (SAEDP) of the 0.2 wt% sample are shown in Figure 7.5. The M-bond epoxy at the top right of the image confirms the image is located at the surface of the cross-section. There are three distinct regions present associated with the sample. A damaged region which extends  $\sim 1.47 \pm 0.04 \mu\text{m}$  from the surface, as evidenced by the loss of diffraction contrast in this region and the SAEDP showing diffuse rings and the absence of any spots arising from any crystalline phase. From this image and SAEDP, region B appears to be completely amorphous, Figure 7.5. There is also a crystalline region, evidenced by the diffraction contrast in this region and the SAEDP which is the [001] zone axis electron diffraction pattern for  $\text{SrTiO}_3$ , space group  $Pm-3m$ , and begins at  $\sim 1.64 \pm 0.04 \mu\text{m}$  into the surface. There does appear to be some defects in this region, however these were not studied further. The depth of this damage region differs from the SRIM simulations by  $\sim 0.5 \mu\text{m}$ , Figure 7.1, which could be as a result of the displacement energies assumed and channelling of the ion beam through the single crystal. The third region is the line of dark, mottled contrast that separates the two previous discussed regions and is attributed to a significant amount of point defects at the crystalline-amorphous interface. A higher magnification XTEM micrograph of this region is shown in Figure 7.6.

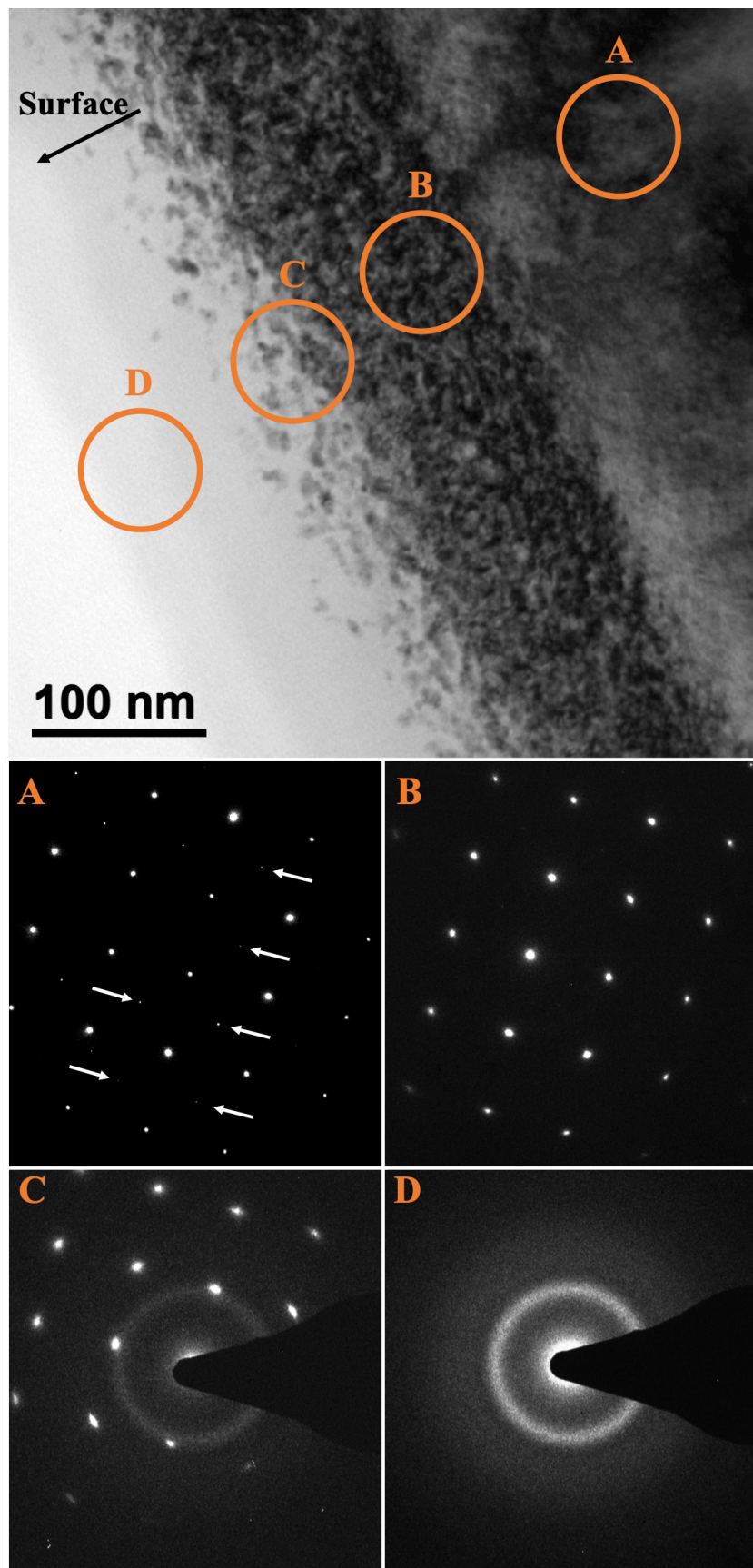
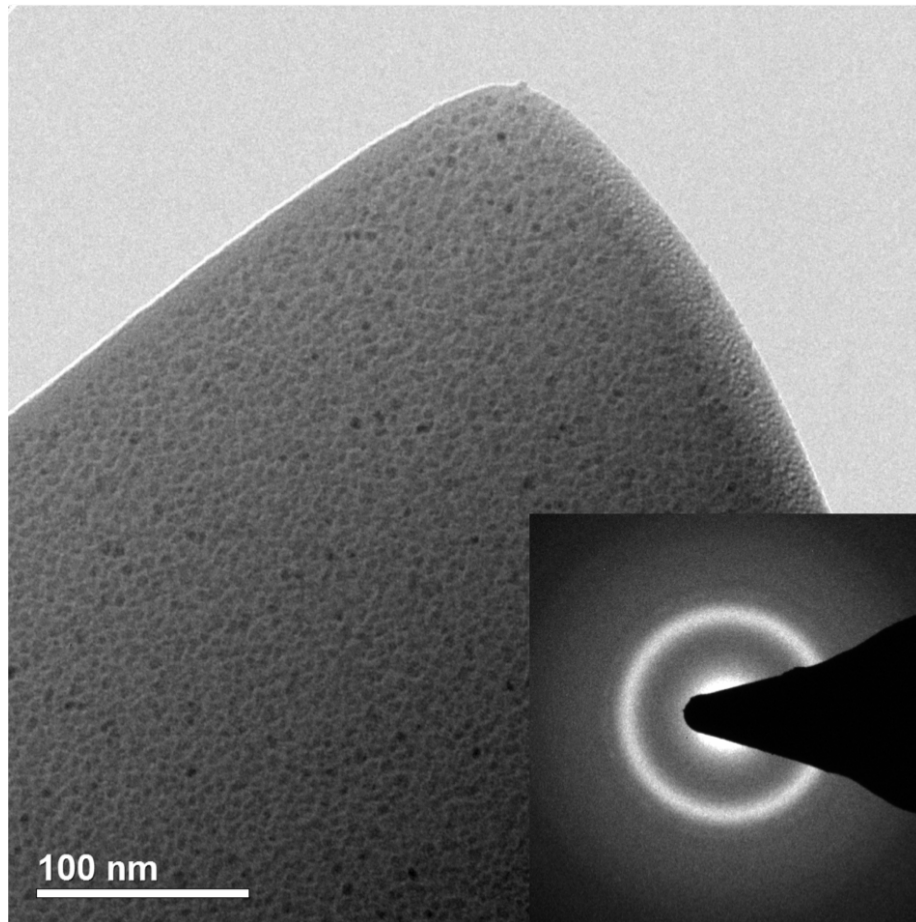


Figure 7.6. (top) Bright-field XTEM micrograph image of the amorphous-crystalline interface with the location of the SAEDPs (bottom) labelled.

The regions marked A and D in Figure 7.6 showed diffraction patterns consistent with those in Figure 7.5. The faint spots in Figure 7.6 A marked by the white arrows are attributed to superstructure reflections that arise due to anti-phase tilting<sup>5</sup>. As the SAEDP moves across the interface, the spots decrease in intensity and are just visible in Figure 7.6 B but are not visible in Figure 7.6 C. The bright spots in B are slightly distorted and become more distorted in C which is indicative of large radiation-induced strain in the material<sup>6</sup>. Also, in Figure 7.6 C there is a halo, suggesting there are amorphous regions present. A higher magnification XTEM image of the amorphous region is shown in Figure 7.7.



*Figure 7.7. Bright-field XTEM image of the amorphous region and (inset) SAEDP from the thinnest region.*

Small regions of dark contrast can be observed in Figure 7.7 and the SAEDP pattern suggests the majority of the material is amorphous from the diffuse ring. However, an extra faint ring can be observed which is typical of polycrystalline material. This additional ring could only be observed at the thinnest regions of sample (top of Figure 7.7) and is likely to be because at the thicker part of the samples, the electrons are passing through more of the amorphous material which is dominating the response. It is unknown whether this is an effect from the irradiations or as a result of the sample preparation.

A bright-field XTEM micrograph image of a 1 wt% sample that has been irradiated and then heated to 500 °C is shown in Figure 7.8. Electron diffraction patterns taken from the regions marked A and B are shown in Figure 7.8 A and B, respectively. SAEDPs confirm that both regions A and B are crystalline and there is no indication of amorphous material. The SAEDP from region B shows double diffraction spots which could be due to overlapping material where the sample has cracked. The cracks at the surface could be assigned to the crack-like features that were observed in the optical microscope image, Figure 7.4. The region that has been damaged and subsequently recovered was measured to be  $1.52 \pm 0.10 \mu\text{m}$  thick, a similar size to that found for the irradiated 0.2 wt% Fe-doped sample, Figure 7.5. The region shown in Figure 7.8 was relatively thick but confirms the position of the surface by the presence of the glue and allowed for the thickness of the surface region to be obtained. A thinner area (and hence more electron transparent) of the same surface region was then observed and through-focus images are shown in Figure 7.9.

The through-focus images indicate the presence of vacancy-type defects which are bright regions in under-focus and dark regions in over-focus, Figure 7.9. It is not clear how these defects have formed or the actual nature of them. They appear to have agglomerated and become larger defects at the surface (towards the bottom of Figure 7.9), whereas further into the sample, the defects are smaller and less sparse. Also observed are regions of dark strain contrast which could be attributed to highly strained regions surrounding defects or dislocation loops.

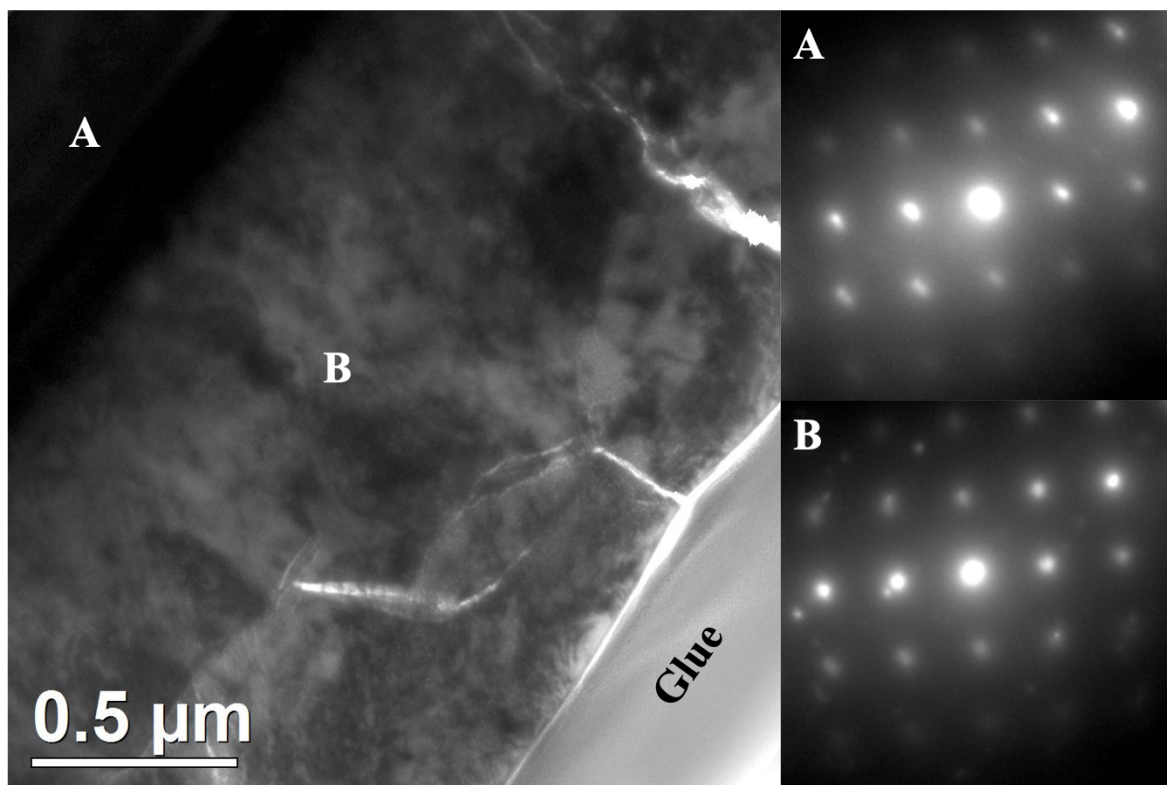


Figure 7.8. Bright-field XTEM micrograph image of a 1 wt% Fe-doped  $\text{SrTiO}_3$  single crystal. SAEDPs are labelled according to their origin with an A or B on the image. Also shown is the M-bond glue used to create the cross-section.

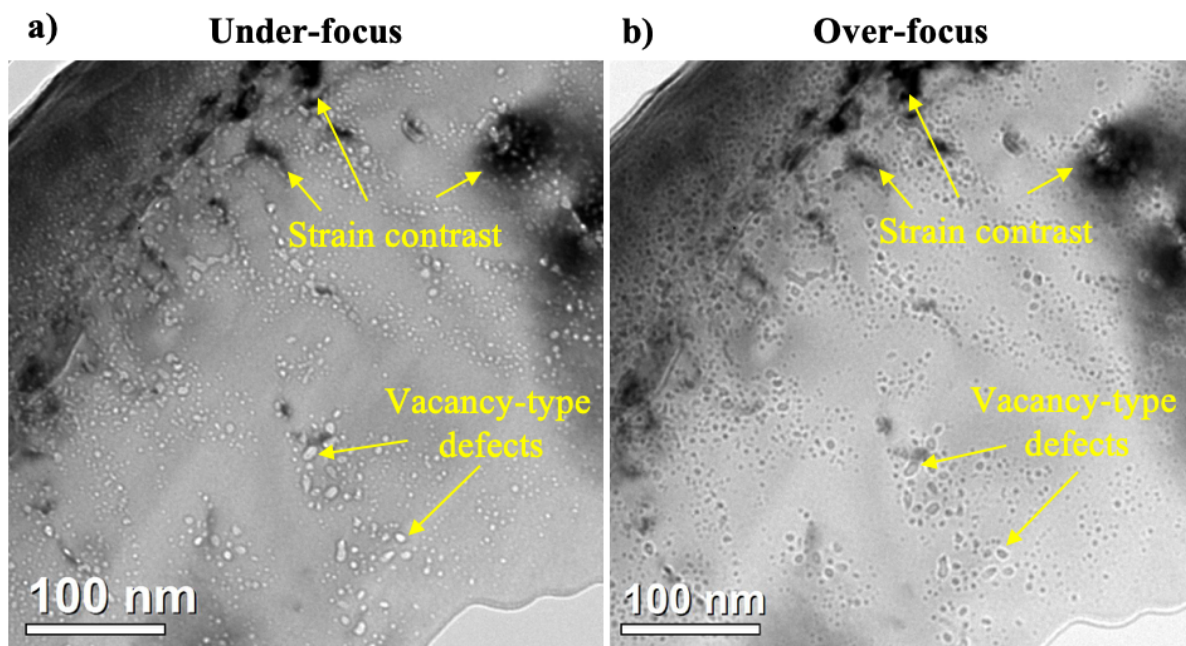


Figure 7.9. Bright-field XTEM micrograph of a 1 wt% Fe-doped  $\text{SrTiO}_3$  single crystal. Through-focus images are presented with a) under-focus and b) over-focus.

## 7.2.5 Conventional Impedance Spectroscopy

For the rest of this chapter the results are all concerned with a 1 wt% Fe-doped sample as the trends were clearer for this sample than the others, probably owing to the fact that this sample was the most conductive. Conventional Impedance Spectroscopy measurements at a temperature of 310 °C are shown in Figure 7.10.

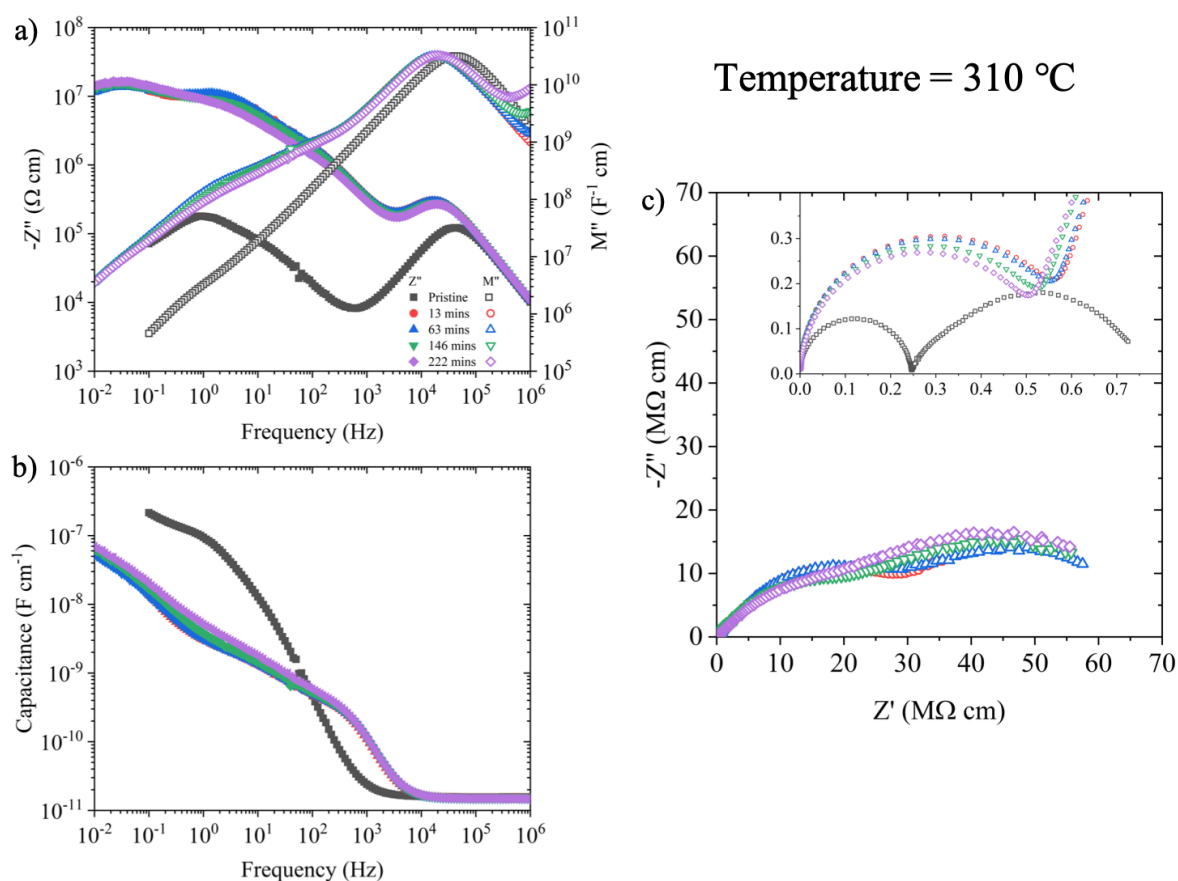


Figure 7.10. a) Combined  $Z''$  and  $M''$  spectroscopic plots, b) capacitance ( $C'$ ) spectroscopic plots and c) complex Impedance ( $Z^*$ ) plots from conventional Impedance Spectroscopy measurements on a damaged 1 wt% Fe-doped SrTiO<sub>3</sub> single crystal as a function of time at a temperature of 310 °C. Inset of c) is the same data on a smaller scale to highlight the high frequency response (bulk). Data for a pristine sample are shown for comparison at the same temperature.

Significant differences can be seen, in each formalism, between a pristine and a damaged sample. The bulk response appears to have changed as a result of radiation damage. In the  $Z''$  and  $M''$  spectroscopic plots, the frequency maximum of the bulk response (high frequency) has shifted to slightly lower frequencies (which if solely due to errors in temperature measurements equates to  $\sim 20$  °C), Figure 7.10 (a), and the magnitude of the impedance has increased, leading to larger arcs (by a factor of  $\sim 2$ ) in the Nyquist plot, inset in Figure 7.10 (c). This could be due to poor resolution of the bulk response due to the dominance of the high impedance lower

frequency response or it may indicate a small change in the electrical properties of the underlying SrTiO<sub>3</sub> close to the damaged region. Between low and intermediate frequencies there are several responses that are not easily resolvable. In Z'' spectra for the damaged sample, data follow the same trend as the pristine sample but are ~ 2 orders of magnitude greater. In M'' spectra for the damaged sample, data deviate from the pristine sample at ~ 1,000 Hz and become ~ 1 order of magnitude greater. The capacitance plateau at high frequencies associated with the bulk response appears unchanged, Figure 7.10 (b), but there are several extra responses at low to intermediate frequencies that were not observed for the pristine sample. Apart from the bulk response, the capacitance data do not plateau at lower frequencies and none of the other responses are well defined. As a consequence, it is difficult to extract meaningful information from this data.

In an effort to try and resolve the responses arising from the surface more clearly, MCIS measurements were performed on the damaged samples.

#### 7.2.6 Micro-contact Impedance Spectroscopy

Three separate samples were used for the MCIS measurements. The first sample was measured by doing a temperature sweep from 340 to 580 °C. The sample was also measured on cooling. The sample was held at the set temperature for at least 30 mins before the measurement was taken. The MCIS measurements described are shown in Figure 7.11.

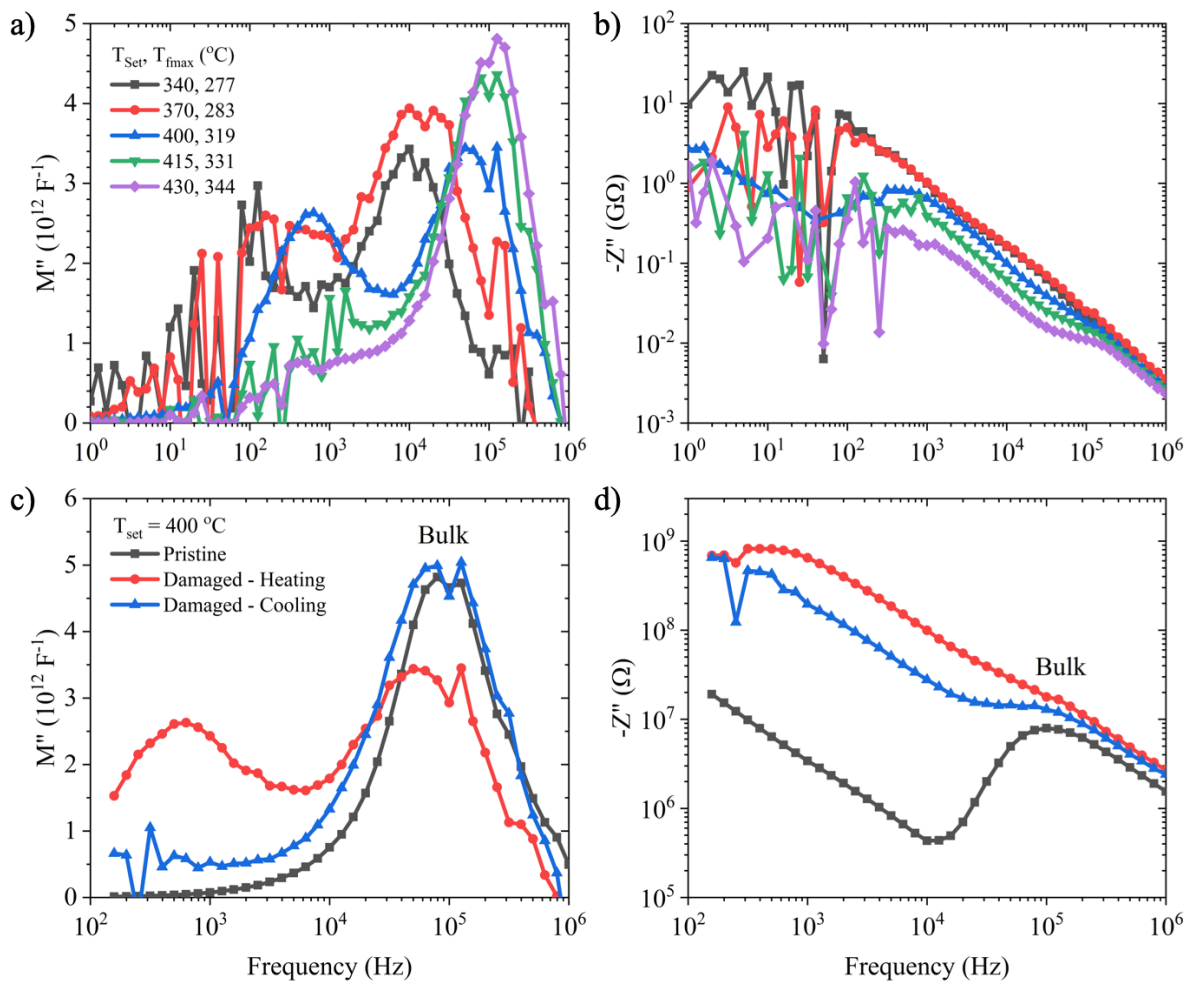


Figure 7.11. MCIS measurements for a 1 wt% Fe-doped SrTiO<sub>3</sub> single crystal. a)  $M''$  and b)  $Z''$  spectroscopic plots on heating between 340 and 430 °C. c)  $M''$  and d)  $Z''$  spectroscopic plots of the sample at the heating stage set temperature of 400 °C on heating and cooling and compared to a pristine sample at the same temperature.

On heating, a high frequency response can be resolved from 370 °C, black squares in Figure 7.11 (a) and (b), and there is a lower frequency response also although the data are noisier at these frequencies. The data become less noisy at 400 °C, blue triangles in Figure 7.11 (a) and (b), and two responses can be resolved. As the sample was heated further, the magnitude of the lower frequency  $M''$  response decreases whilst the higher frequency  $M''$  response increases. There are clear differences between a pristine sample, the damaged sample on heating and the damaged sample on cooling (after MCIS measurements from 400 °C → 580 °C → 400 °C, approximately 10 hrs between the two sets of 400 °C measurements) Figure 7.11 (c) and (d). Both plots show two clear responses for the damaged sample on heating. On cooling, the magnitude of the low frequency response has decreased significantly but is still greater than the pristine sample where there is no significant response present at this frequency. The magnitude of the higher frequency response has increased in  $M''$  after the heating cycle and is

a similar value to that obtained in a pristine sample, Figure 7.11 (c). All samples show the  $Z''$  response increasing to lower frequencies, meaning there are additional features outside the frequency window shown here, and was attributed to the sample/electrode interface in Chapter 6. The conductivity and effective permittivity of the bulk and low frequency response was calculated using the suggested equations in Chapter 5 and are shown in Figure 7.12.

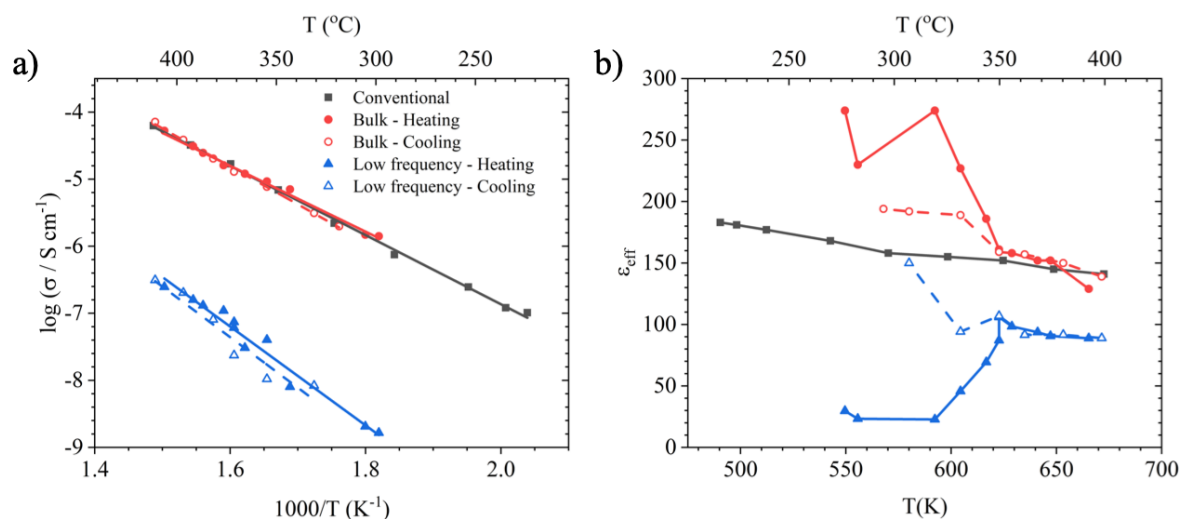


Figure 7.12. a) Arrhenius conductivity and b) permittivity-temperature plots for the bulk (high frequency) and low frequency responses in Figure 7.11. Conductivity and permittivity values were calculated using the equations from Chapter 5. Linear fits are shown in a) with solid lines and dashed lines representing fits to the heating and cooling data, respectively.

The conductivity of the bulk response is in excellent agreement with conventional measurements for a pristine sample, red circles in Figure 7.12 (a), whilst the low frequency response is 2-3 orders of magnitude lower in conductivity, blue triangles in Figure 7.12 (a). The effective permittivity of the bulk is in better agreement with the conventional measurement at higher temperatures, red circles in Figure 7.12 (b). As the temperature increases, the effective permittivity of the low frequency response increases towards the pristine permittivity but seems to saturate at a permittivity that is  $\sim 60$  lower than the bulk.

Recrystallisation of amorphised material is dependent on both temperature and time. Figure 7.13 shows the damaged sample taken to a set temperature of 390 °C and held at this temperature whilst measurements were repeated on two contacts that had a radius of 30  $\mu\text{m}$  and an  $s/r$  of 10.

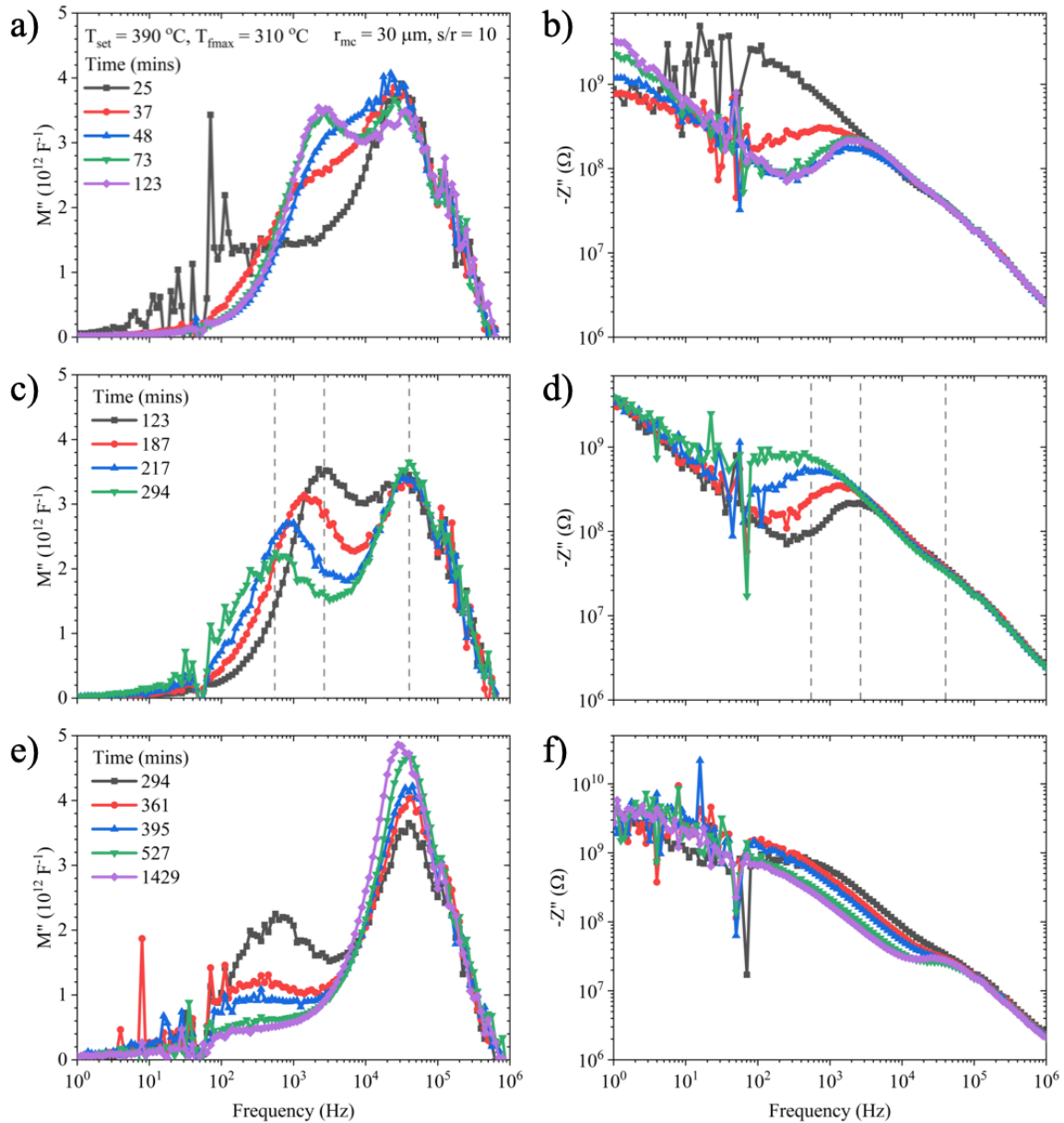


Figure 7.13. MCIS measurements of the damaged 1 wt% Fe-doped SrTiO<sub>3</sub> single crystal at a heating stage set temperature of 390 °C. The a, c, e)  $M''$  and b, d, f)  $Z''$  data are split into 3 ranges of time measurements (shown in the legends). All measurements are taken from two contacts with a radius of 30  $\mu\text{m}$  and an s/r of 10. The grey dashed lines are used to highlight the same frequencies in c) and d).

For most measurements, the peak position of the high frequency response is constant. By assuming this is the bulk response an actual sample temperature can be estimated, using the equations in Table 6.1 from Chapter 6, which was found to be  $\sim 310$  °C. Initially the lower frequency response is broad and resistive, Figure 7.13 (a) and (b). With time it appears to shift to higher frequency and then increases in  $M''$ , whilst its impedance remains fixed. The bulk response is constant in impedance and there are no significant changes in  $M''$ .

Between 123 and 294 mins, Figure 7.13 (c) and (d), the  $M''$  bulk response still remains constant; however, the intermediate frequency  $M''$  response decreases and shifts to lower frequencies. The  $Z''$  response is also shifting to lower frequencies and increasing in magnitude.

For the final stage shown here, the intermediate  $M''$  frequency response continues to decrease in magnitude and then also starts to decrease in  $Z''$ , Figure 7.13 (e) and (f), respectively. The  $M''$  bulk response increases in magnitude and also shifts to slightly lower frequencies, which in turn slightly increases its  $Z''$  response.

Capacitance ( $C'$ ) spectroscopic plots for the same data in Figure 7.13 are compared with those on a pristine sample and a conventional measurement on a damaged sample in Figure 7.14.

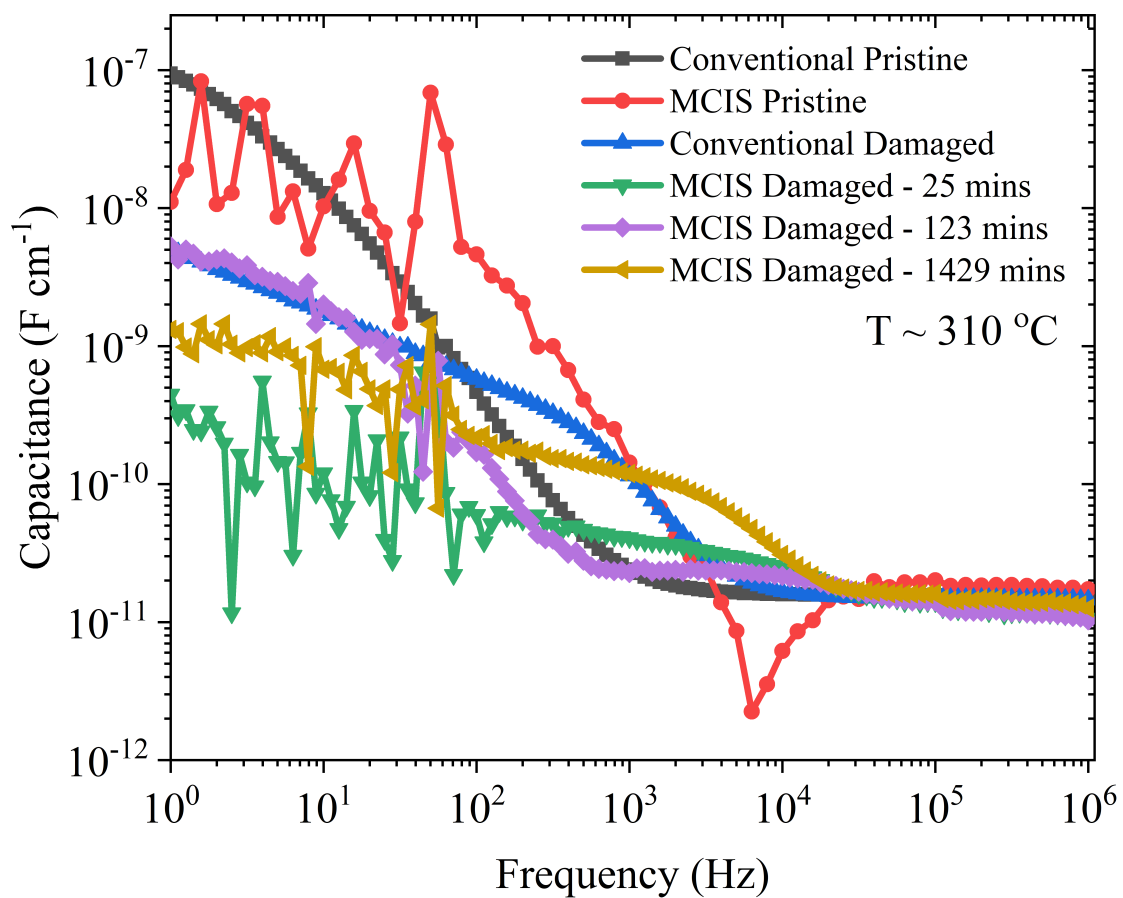


Figure 7.14. Capacitance spectroscopic plots for the MCIS data in Figure 7.13 and compared to a pristine sample and conventional measurements of a damaged sample. The temperature is the actual sample temperature.

For conventional measurements, the capacitance for the damaged sample deviates from the pristine sample at intermediate frequencies, blue triangles in Figure 7.14 but it is hard to resolve this response (Figure 7.10). MCIS measurements allows this response to be better resolved, particularly after 123 mins, purple diamonds in Figure 7.14. With increasing time, the

capacitance of the intermediate frequency response increases, yellow left triangles in Figure 7.14, but it is still some way off reaching the pristine response, red circles in Figure 7.14.

The conductivity and effective permittivity of the bulk and low frequency response was calculated using the suggested equations in Chapter 5 and are shown in Figure 7.15. In agreement with the previous calculations, the lower frequency response remains 2-3 orders of magnitude lower in conductivity over the full time period, Figure 7.15 (a). The permittivity of the bulk is initially in poor agreement with the pristine value, but with increasing time tends towards this value, black squares in Figure 7.15 (b); however, even after 1429 mins the calculated effective permittivity is still not within 10% of the pristine sample value. The low frequency response increases towards the pristine value with increasing time, red circles in Figure 7.15 (b).

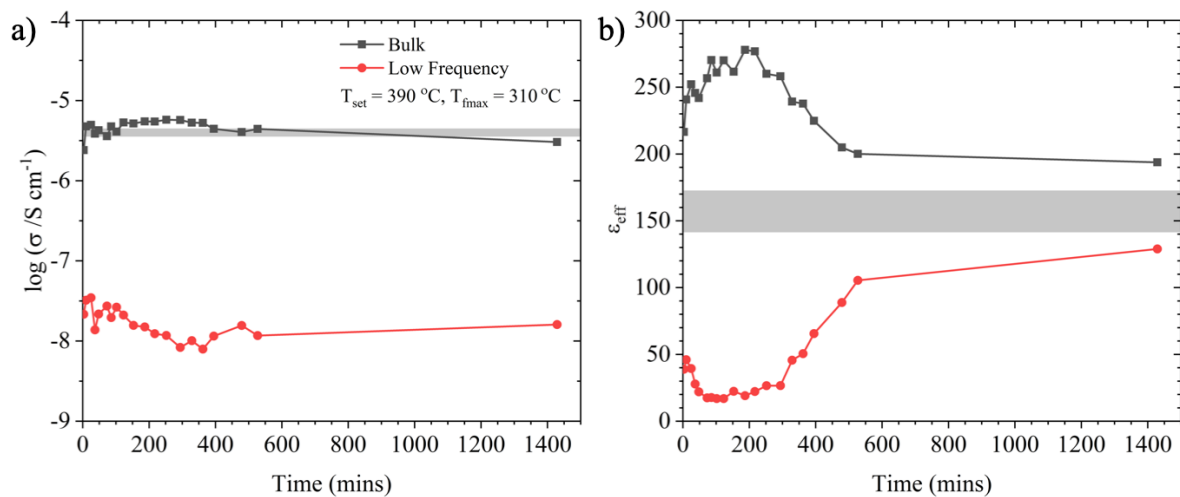


Figure 7.15. Change in a) conductivity and b) effective permittivity of the bulk (high frequency) and low frequency response with time for a damaged 1 wt% Fe-doped SrTiO<sub>3</sub> single crystal at a heating stage set temperature of 390 °C. The grey box represents the conventional pristine sample value  $\pm 10\%$ .

Measurements were also performed on two contacts with a radius of 25  $\mu\text{m}$  and an s/r of 10 and the results are shown in Figure 7.16. Generally, the same trends can be observed for the smaller micro-contact size which is expected. The main differences are that in the first stage the bulk response decreases in magnitude, which is less obvious for the larger micro-contact measurements. Also, the intermediate frequency response increases to a larger magnitude than the bulk response in the  $M''$  plot, Figure 7.16 (a), whereas for the larger contact size the magnitude of the intermediate frequency  $M''$  response was similar to the bulk response, Figure 7.13 (a). Also, the broad response observed after 25 mins in Figure 7.13 (a) is not apparent in

Figure 7.16 (a). Instead the response at  $\sim 2,000$  Hz remains at this frequency whilst increasing in  $M''$  in the first stage.

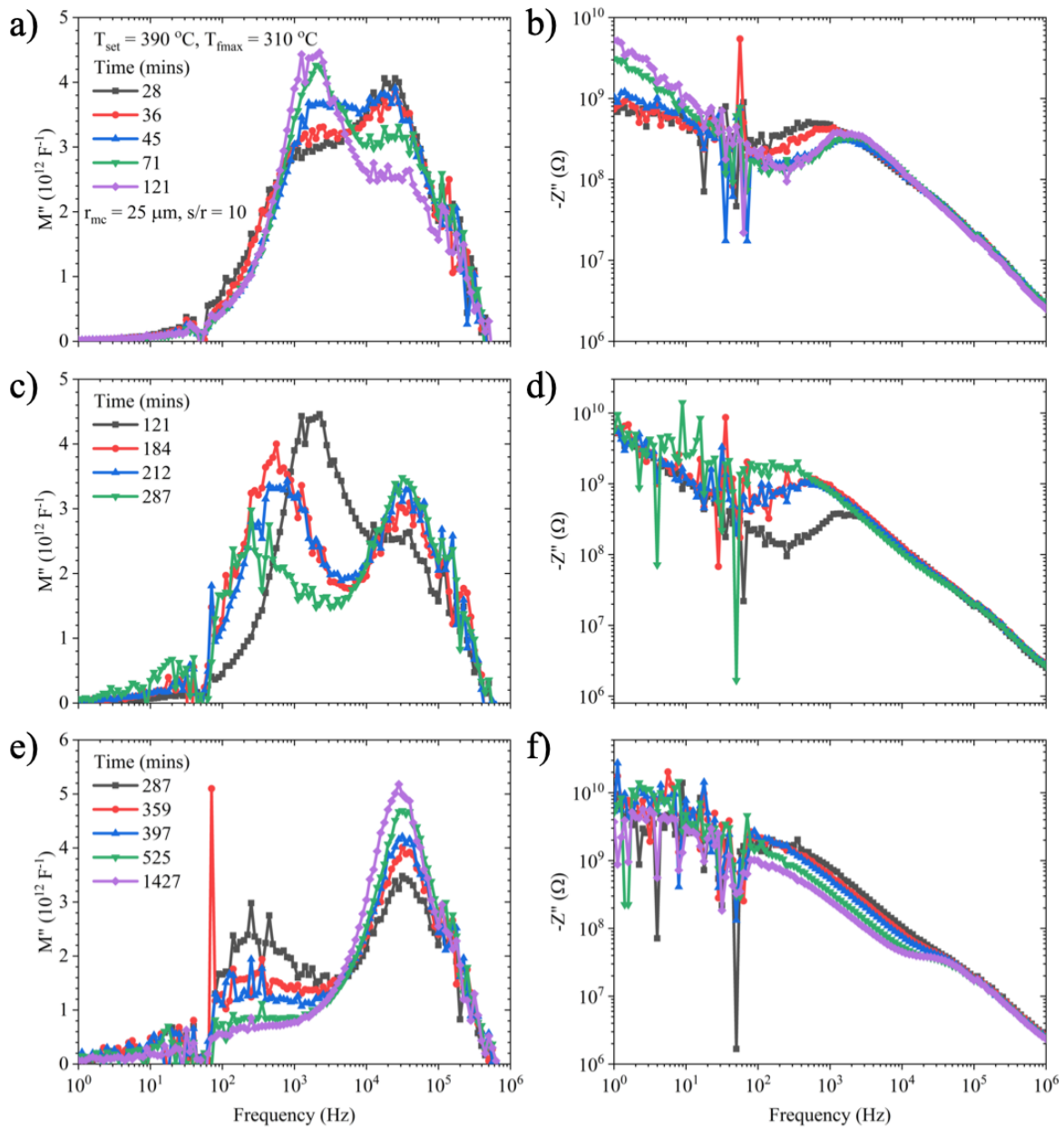
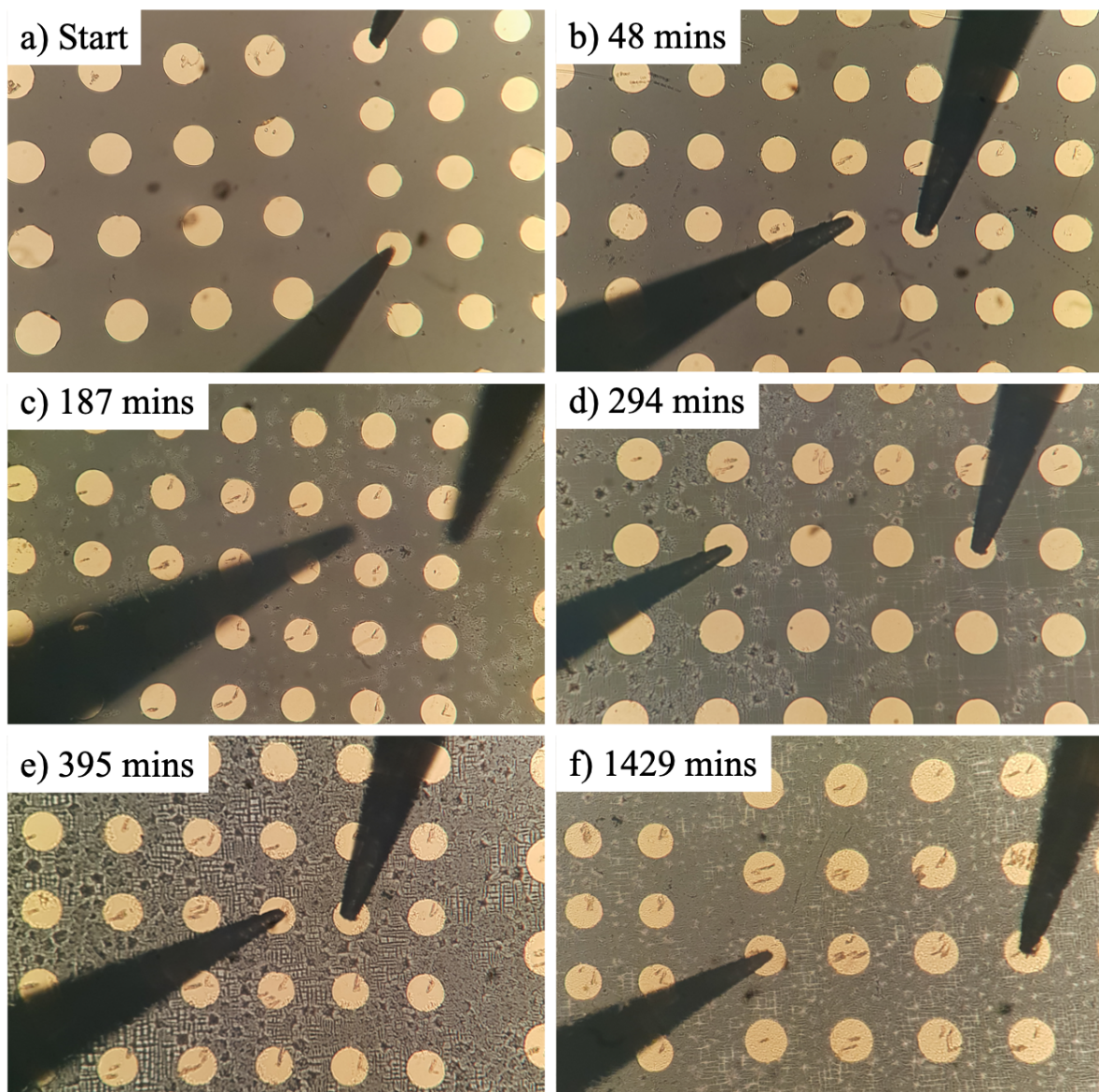


Figure 7.16. MCIS measurements of a damaged 1wt% Fe-doped  $\text{SrTiO}_3$  single crystal at a heating stage set temperature of  $390$  °C. The a, c, e)  $M''$  and b, d, f)  $Z''$  spectra are split into 3 ranges of time measurements (shown in the legends). All measurements are taken from two contacts with a radius of  $25$   $\mu\text{m}$  and an  $s/r$  of  $10$ .

How the surface evolved over time whilst the measurements were performed at a set temperature of  $390$  °C is shown in Figure 7.17. Initially, Figure 7.17 (a), there were no significant features on the surface of the sample except for a few marks that may have been as a result of sample preparation. With increasing time small features start to appear, which can be seen as small white specs in Figure 7.17 (b). The specs grew into crack-like features which

over time progressively worsened until the full sample surface was covered in the crack-like features, Figure 7.17 (f).



*Figure 7.17. Optical microscope images of a 1 wt% Fe-doped SrTiO<sub>3</sub> single crystal during MCIS measurements at a heating stage set temperature of 390 °C (actual temperature of 310 °C) from a) the start to f) the end of the measurements. Time is shown in minutes and represent the measurements shown in Figure 7.13.*

To determine the effect of these cracks on the impedance response, measurements were taken between two micro-contacts where there was a minimal number of cracks forming between the contacts and immediately after measurements were taken between two micro-contacts where there were significantly more cracks. The impedance response from these measurements, and images of the location of the measurements are shown in Figure 7.18.

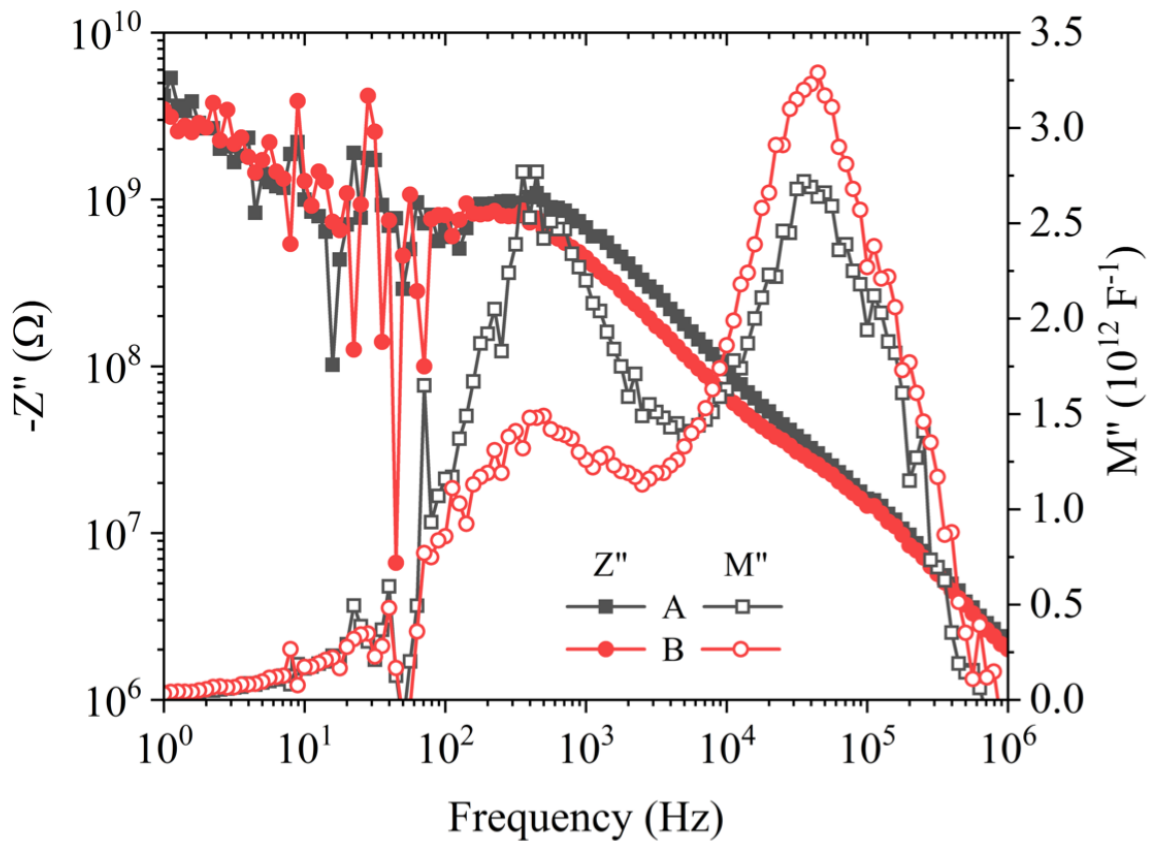
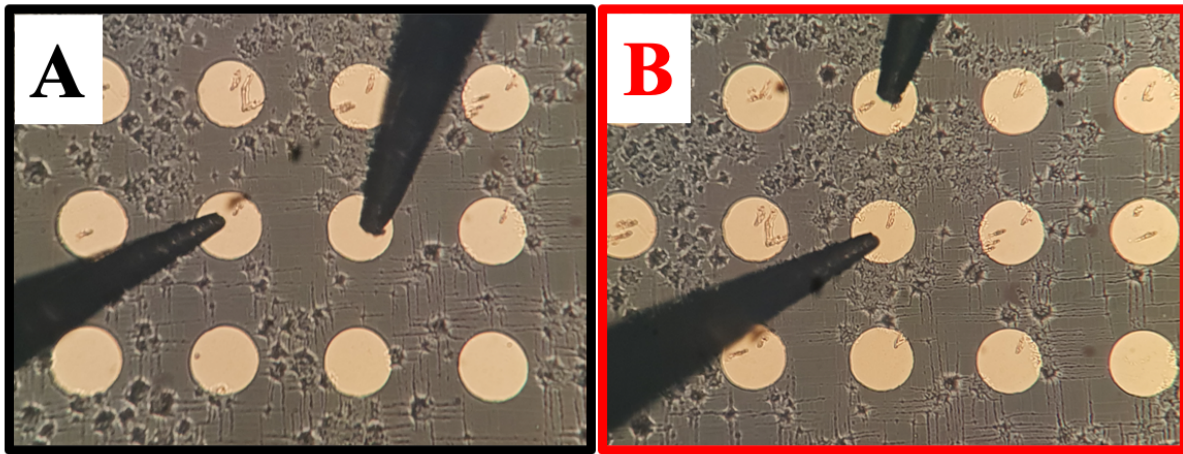


Figure 7.18. Optical microscope images of the surface of a 1 wt% Fe-doped SrTiO<sub>3</sub> single crystal during MCIS measurements between two micro-contacts where there was A) a small number of cracks formed and B) significantly more cracks had formed. Lower – the obtained impedance data shown as Z'' and M'' spectroscopic plots (note Z'' is on a log scale whereas M'' is on a linear scale). The temperature had been held at 390 °C (actual temperature of 310 °C) for 296 mins at the time of the measurements.

Clearly the cracks on the surface of the sample have a significant effect on the impedance measurements. When there is a small number of visible faint cracks between the two micro-contacts the M'' peaks at high and intermediate frequencies are similar in magnitude, Figure 7.18 A. In contrast, if there is a significant number of cracks between the two micro-contacts, the intermediate frequency M'' response has decreased whereas the high frequency response

has increased, Figure 7.18 B. The impedance ( $Z''$ ) is also slightly larger for the measurement with less cracks between the contacts.

To determine whether the intermediate frequency peak could be associated to amorphous material, MCIS measurements were repeated at a set temperature of 440 °C but the sample was removed from the heating stage (after the impedance measurements were complete) thus immediately inhibiting further recrystallisation, before the intermediate  $M''$  frequency response had decreased fully, such as the purple diamond data in Figure 7.13 (e) and Figure 7.16 (e). GAXRD was then performed on the quenched sample and the results are shown in Figure 7.19.

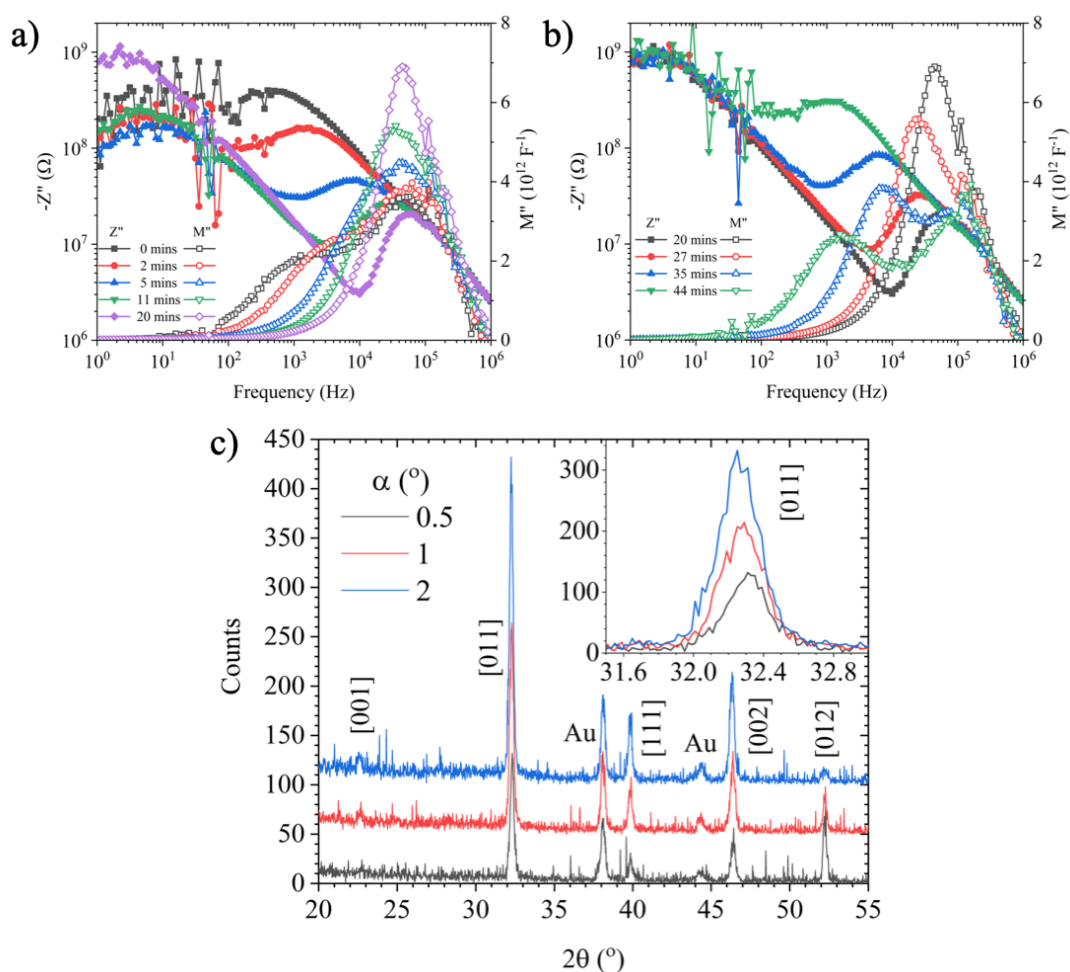


Figure 7.19.  $Z''$  and  $M''$  overlaid spectroscopic plots of a damaged 1 wt% Fe-doped  $\text{SrTiO}_3$  single crystal for times showing a) as the  $M''$  intermediate frequency response reaches a maximum and b) as the  $M''$  intermediate frequency response decreases in magnitude. The sample was removed from the heating stage after a time of 44 mins (green down triangles in b)). C) GAXRD patterns for the quenched sample at three incidence angles where each pattern has been offset by 50 counts. Peaks have been indexed to either the cubic perovskite phase or Au. Inset shows the [011] peak on a smaller scale (note patterns are not offset in inset).

As with the previous measurements, initially the broad intermediate frequency response shifted to higher frequencies and the  $M''$  peak increased in magnitude whilst decreasing in  $Z''$ , Figure 7.19 (a). The  $M''$  response reached a maximum after 20 minutes, after which it began to decrease in magnitude and frequency, whilst increasing in  $Z''$ , Figure 7.19 (b). The sample was removed from the heating stage after 44 mins, green down triangles in Figure 7.19 (b). Comparing Figure 7.19 (b) to Figure 7.13 (e) and Figure 7.16 (e), the intermediate frequency response would decrease even further if held for longer periods of time.

GAXRD results, Figure 7.19 (c), shows the quenched sample had recrystallised to a polycrystalline cubic perovskite structure in agreement with the previous measurements, Figure 7.2. There is no evidence for amorphous material in the GAXRD data at all incidence angles measured. On close inspection of the reflections, inset of Figure 7.19 (c), the position of the peaks had shifted to slightly lower angles in  $2\theta$ , for larger incidence angles. As larger incidence angles penetrate deeper into the surface ( $\alpha = 1^\circ$  penetrates  $\sim 1 \mu\text{m}$  deep (see Figure 6.3 in Chapter 6)), this provides evidence that the material deeper in the amorphous region, and thus towards the position of peak damage, had swelled<sup>7</sup> more than material closer to the surface. Extra peaks have been indexed to Au from the micro-contacts on the surface of the sample.

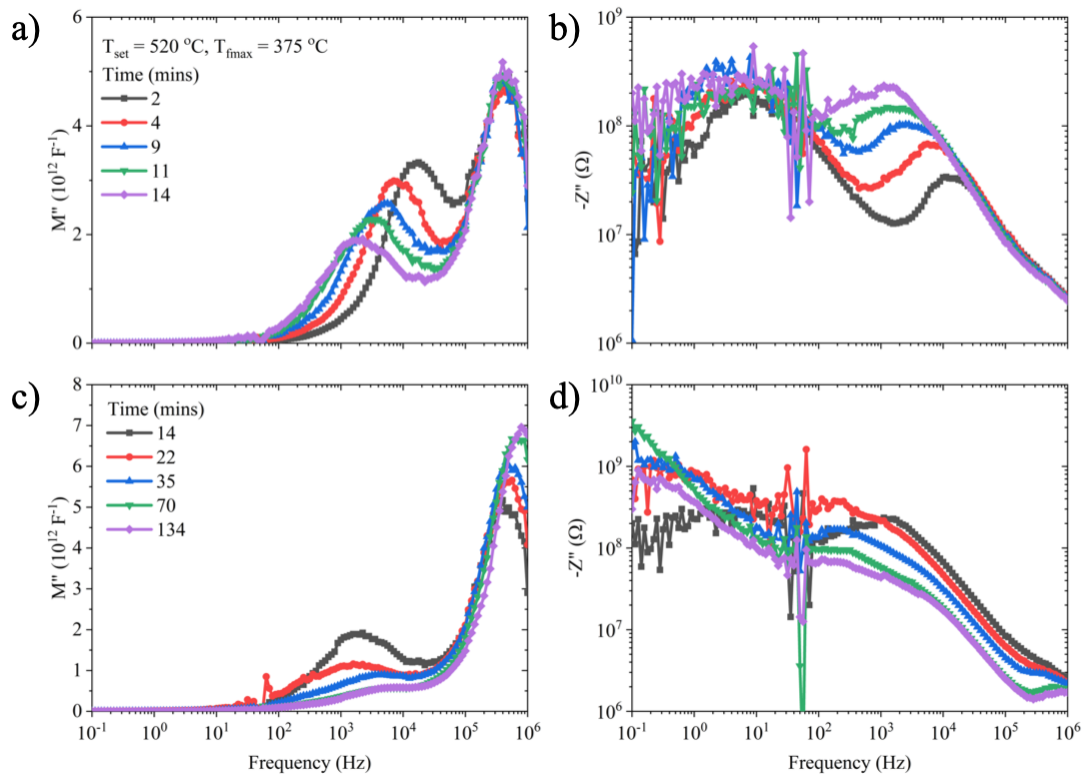


Figure 7.20. MCIS measurements of a damaged 1wt% Fe-doped  $\text{SrTiO}_3$  single crystal at a heating stage set temperature of 520 °C, actual temperature of 375 °C. The a, c)  $M''$  and b, d)  $Z''$  spectra are split into 2 ranges of time measurements (shown in the legends).

To gain a further understanding of the lower frequency impedance data, measurements were repeated for higher temperatures and to a frequency of 0.1 Hz and are shown in Figure 7.20. The cracks on the surface of the sample appeared much quicker than in Figure 7.17 and a significant amount had already formed when the first measurement at 2 mins was performed, Figure 7.20. Using the equations in Table 6.1 of Chapter 6, the actual sample temperature was calculated to be 375 °C. The first stage that was seen holding the heating stage at 390 °C, Figure 7.13 (a) and (b), is not observed at a temperature of 520 °C. This is likely because this stage has already occurred whilst the temperature was increasing towards 520 °C. The second stage that was observed at 390 °C, Figure 7.13 (c) and (d), happens much faster at a temperature of 520 °C, Figure 7.20 (a) and (b). This stage is where the intermediate frequency response decreases in magnitude and shifts to lower frequencies in the  $M''$  plots (Figure 7.20 (a)), which in turn means  $Z''$  increases (Figure 7.20 (b)). At 390 °C this occurs between 123 and 294 mins, whereas at 520 °C this stage takes just 14 mins after reaching the set temperature. The bulk response remains constant whilst this occurs. As time increases further, Figure 7.20 (c) and (d), the intermediate  $M''$  response continues to decrease. The magnitude of the higher frequency  $M''$  peak associated with the bulk response begins to increase in agreement with the 390 °C measurements, but again over a shorter timescale. Similarly, in the  $Z''$  spectra, Figure 7.20 (d), the response at  $\sim 300$  Hz decreases. The response at lower frequencies than those measured here still appeared to be changing, thus the temperature was increased to observe this response and was compared to a pristine sample at the same temperature and is shown in Figure 7.21.

Measurements at 580 °C (which is the highest temperature that the heating stage could be set) show the low and high frequency response for a damaged sample compares well with the pristine sample, Figure 7.21. This confirms that the high frequency response is from the bulk and that the low frequency response can be assigned to electrode effects. Extra responses may be present at even lower frequencies, but this cannot be confirmed from these measurements. The responses at low frequencies were attributed to interactions at the sample/electrode interface in Chapter 6. Between frequencies of 100 and 100,000 Hz there are clearly additional responses in  $Z''$  and  $M''$  spectra in the damaged sample that are not present in the pristine sample, Figure 7.21.

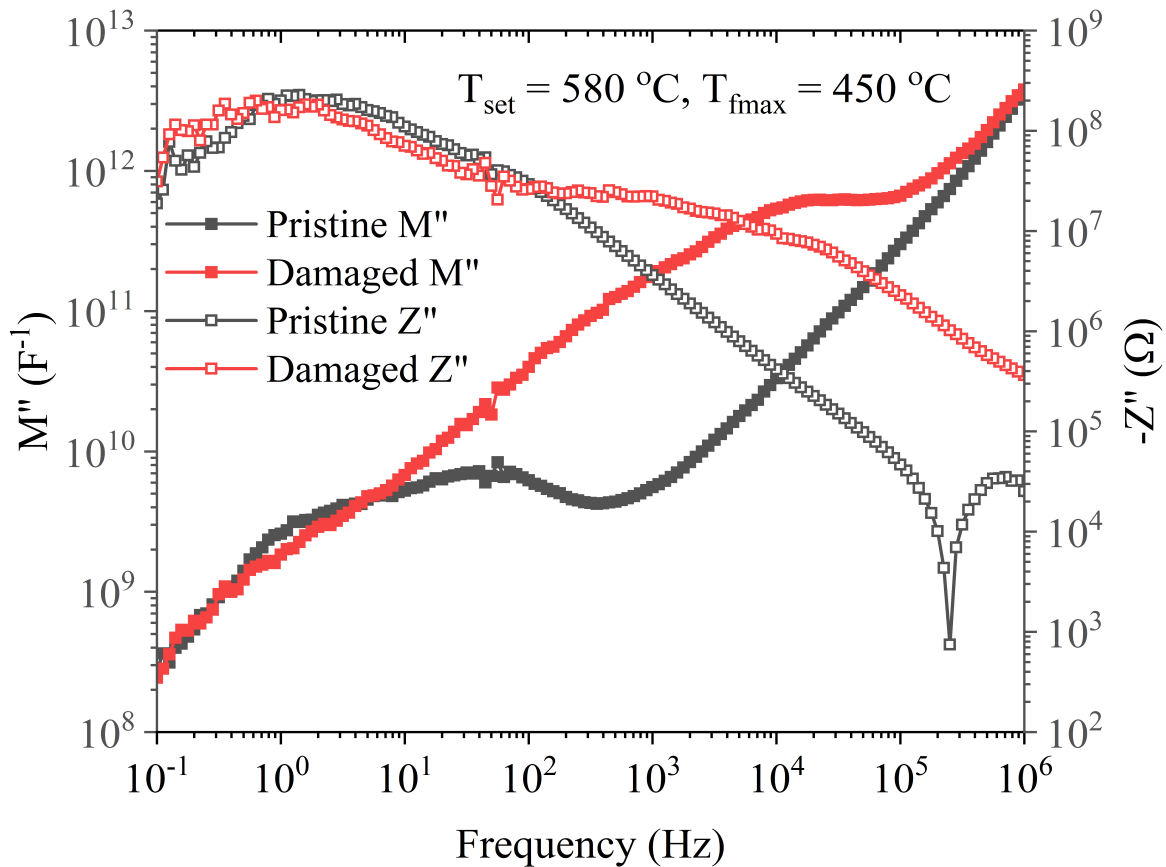


Figure 7.21. MCIS measurements of a damaged and pristine 1wt% Fe-doped SrTiO<sub>3</sub> single crystal at a heating stage set temperature of 580 °C.

## 7.3 Discussion

### 7.3.1 Properties of Damaged Samples

GAXRD patterns of the irradiated samples confirmed the surface of samples were amorphised as a result of 5 MeV Au irradiations to a fluence of  $5 \times 10^{15}$  ions cm<sup>-2</sup>, a damage dose of  $\sim 15$  dpa at the peak value. This is much higher than the reported amorphisation doses for SrTiO<sub>3</sub><sup>3,4</sup>. Such large doses ensured the surfaces were fully amorphous rather than containing regions of highly damaged but still crystalline material, confirmed by XTEM, Figure 7.5. Because of issues presented in Chapter 6, amorphous layer thicknesses were not obtainable by GAXRD. XTEM was able to confirm the thickness of the amorphous region was  $\sim 1.47 \pm 0.04$   $\mu\text{m}$  from the surface of the sample, despite SRIM calculations predicting an amorphous layer extending  $\sim 1$   $\mu\text{m}$  from the surface. It is known that single crystal samples are prone to channelling effects<sup>1</sup>, however the irradiations were conducted at an angle that was  $7^\circ$  off the surface normal to minimise this. Also, the assumed displacement energies of 50 eV may be inaccurate with values ranging from 15 – 80 eV in the literature<sup>4,11,13</sup>.

The crystalline to amorphous transition occurred between 1.47 and  $1.64 \pm 0.04 \mu\text{m}$  from the surface of the sample, Figure 7.6. SAEDPs at different positions across the interface yielded interesting results. The first region was the unirradiated crystalline material, confirmed by the sharp electron diffraction spots expected from the cubic perovskite  $\text{SrTiO}_3$   $Pm-3m$  structure, Figure 7.6 A. As the SAEDP moved over the interface but more towards the crystalline material, the intensity of the faint superstructure spots that arise from anti-phase tilting<sup>5</sup> decreased, Figure 7.6 B. Moving further across the interface, more towards the amorphous material, the superstructure spots completely diminished and diffuse rings appeared suggesting amorphous material was present, Figure 7.6 C, before moving into the amorphous surface where only the diffuse ring was present, Figure 7.6 D. Sabathier et al.<sup>8</sup> detected a phase transformation from  $\text{SrTiO}_3$  to  $\text{Sr}_2\text{TiO}_4$  by XRD and X-ray absorption spectroscopy when they irradiated  $\text{SrTiO}_3$  with Pb ions. The difference in the [001] electron diffraction patterns for these two phases is that  $\text{SrTiO}_3$  show superstructure reflections, Figure 7.6 A, whereas  $\text{Sr}_2\text{TiO}_4$  does not. Hence this phase transformation could be attributed to the results shown here. Existence of a Sr-rich phase means that a Ti-rich phase should also be present, according to the following equation



XTEM images of the thinnest parts of the amorphous region revealed extra features were present and the SAEDP showed this material could have polycrystalline components, Figure 7.7. There may be small regions of  $\text{TiO}_2$  that have resulted from the reaction described above, however this suggestion requires confirmation. Further TEM studies using some form of elemental characterisation (e.g. electron energy loss spectroscopy - EELS) would be able to confirm the nature of these features.

The surfaces of the irradiated samples had no significant features on the surface as a result of irradiation, Figure 7.4 (a).

### 7.3.2 Properties of Damaged and Recrystallised Samples

The only sample to show evidence of crystallinity by GAXRD after heating to 300 °C for 30 mins was a 0.02 wt% Fe-doped sample, Figure 7.2 (b). After heating to 400 °C all samples had peaks that were indexed to a polycrystalline cubic perovskite structure with space group  $Pm-3m$ . There is a substantial amount of evidence in the literature suggesting  $\text{SrTiO}_3$  recrystallises by solid phase epitaxial regrowth<sup>3,9,10</sup>. These studies are either in a TEM on relatively small samples or by using ion channelling techniques. As far as we are aware, a ‘bulk’ annealing

study using GAXRD has not been performed. Oyoshi et al.<sup>11</sup> used GAXRD to study ion beam induced epitaxial recrystallisation of SrTiO<sub>3</sub> and reported the recrystallised sample to recover to the pristine single crystal state, with no evidence of polycrystalline material, in contrast to the results reported here. It should be noted that the temperature for ion beam induced epitaxial recrystallisation is much lower than the temperature required for solid phase epitaxial recrystallisation. Diffuse scattering could be seen in all samples, providing evidence that amorphous regions still existed after this heat treatment. Meldrum et al.<sup>3</sup> determined the recrystallisation temperature of SrTiO<sub>3</sub> to be 800 K (527 °C) by TEM, after amorphising the material using Kr and Xe ions. However, they defined the recrystallisation temperature as that where recrystallisation was observed in a one-minute time frame. As recrystallisation is dependent on temperature and time, they would have obtained lower recrystallisation temperatures if they observed changes over a longer period of time. Similarly, if we had held our samples for longer than 30 mins at temperature, we expect the amount of diffuse scattering to decrease further, and the intensity of the peaks associated with the crystalline phase to increase.

Changing the incidence angles of the GAXRD, measurements penetrate deeper into the material and revealed the peaks had shifted to lower angles deeper into the recrystallised region. Given that SRIM underestimated the damage depth, the peak damage is likely to occur at ~ 1 µm rather than ~ 0.6 µm. The GAXRD measurements provide evidence for lattice expansion at around this depth, Figure 7.19 (c).

An interesting feature on the surface of samples after annealing was the presence of cracks, creating for the majority of the surface, square grain-like features but in some regions the cracks seemed more random, Figure 7.4 (b). The grain-like features could all be orientated in the same direction as the unirradiated crystalline material by solid phase epitaxial recrystallisation but the cracks and ‘grains’ that have formed may slightly offset the orientation from one another. Averaging over the full surface of the sample could make the sample appear polycrystalline by GAXRD. How quickly the cracks appeared on the surface (and subsequently grew) was dependent on the temperature. An example of the evolution for the cracks over time can be seen in Figure 7.17 at a sample temperature of 310 °C but these appeared and evolved much faster at a temperature of 375 °C.

XTEM of a sample that had been heated to 500 °C for 30 mins showed the recrystallised region extended  $\sim 1.52 \pm 0.10$  µm from the surface of the sample, in agreement with the damaged sample where the amorphous region extended  $\sim 1.47 \pm 0.04$  µm from the surface. The SAEDP

confirmed that no diffuse ring was present, Figure 7.8, in agreement with the GAXRD results, Figure 7.2. Cracks could be seen in the recrystallised region, which were normal to the surface at the surface; however, some cracks were observed to deviate away from the normal to the surface within the recrystallised region and away from the surface. It is assumed that the cracks at the surface are consistent with the cracks observed in the optical microscope image, Figure 7.4. In some regions, cracks had formed on the interface between the recrystallised layer and the underlying unirradiated material. This was not observed in samples that had been damaged but not annealed.

Through-focus XTEM images of the recrystallised region revealed the presence of vacancy-type defects. Wang et al.<sup>10,12</sup> observed cavities to form by annealing SrTiO<sub>3</sub> following similar irradiations and suggested they formed by agglomeration of vacancies. They also observed Au clusters were spatially associated with the cavities; however, we saw no evidence of Au clusters in the vacancy-type defects produced here. In regions close to where the peak amount of damage was expected, regions of dark contrast were observed which could be attributed to a region of high strain and/or interstitial-type defect clusters.

To summarise, each region/feature of the sample described above needs to be taken into account when analysing Impedance Spectroscopy data and are listed below:

1. Crystalline, unirradiated material below the damaged surface which has properties unaffected by the irradiations – i.e. same properties as the pristine sample.
2. An amorphous region that is likely to have different electrical properties to its crystalline counterpart.
3. A crystalline to amorphous interface that may have secondary phases of Sr<sub>2</sub>TiO<sub>4</sub> and TiO<sub>2</sub> and is crystalline but highly strained.
4. Au particles or precipitates as a result of the irradiations.
5. A recrystallised surface layer that may or may not have the same electrical properties to the pristine sample.
6. Interstitial-type defects and clusters.
7. Vacancies that agglomerate to create larger vacancy-type defects.
8. Cracks that form in the recrystallised layer and/or at the amorphous crystalline interface.
9. The electrode/sample interface.

Whilst listed regions 1-5 and 9 could influence Impedance Spectroscopy measurements by having their own time constant that relaxes out at different frequencies, features 6-8 could

influence the measurements by manipulating the way current passes through the other regions of the sample. For example, voids and cracks are ‘air gaps’ that confine the current in certain directions.

### 7.3.3 Impedance Spectroscopy Measurements

Conventional Impedance Spectroscopy measurements highlighted differences between a damaged sample and a pristine sample, Figure 7.10. The bulk response had shifted to lower frequencies that would equate to  $\sim 20$  °C if this was an error in temperature readings alone. It is likely that the lower frequency data, which is much more resistive in damaged samples is influencing the bulk response, leading to poorer resolution of the bulk response compared to the pristine sample. Another possibility is that the electrical properties of the underlying SrTiO<sub>3</sub> have changed close to the amorphous interface. The intermediate frequency responses of the damaged sample seem to follow the same trend as the pristine sample in  $Z''$  spectra but are offset by 2 orders of magnitude whereas in  $M''$  spectra the response deviates away from the pristine sample. Capacitance plots show an extra capacitance that was not present in pristine samples which may be attributed to the surface layer. A drawback of conventional Impedance Spectroscopy measurements is that the measurements are averaged across the full sample. Although differences can be seen between damaged and pristine samples, the responses cannot be resolved, highlighting the requirement of a surface sensitive measurement.

The temperature sweep with MCIS measurements showed a lower frequency response than the bulk that decreased quickly with increasing temperature, Figure 7.11. There were clear differences between a pristine sample, and a damaged sample on heating and cooling at the same temperature. In  $M''$  spectra, the lower frequency response observed on heating had decreased substantially on cooling, whereas the bulk  $M''$  response had increased to a comparable magnitude as the pristine sample. However, the  $Z''$  response for the cooled sample remained much more resistive than that of the bulk.

The clearest measurement showing the two responses was at a set temperature of 400 °C. To observe this change in the lower frequency response in more detail, the next sample was heated to 390 °C and measurements repeated for a long period of time. As described previously, recrystallisation is dependent on temperature and time. Before the 400 °C measurement in Figure 7.11, the sample had been held at set temperatures for at least 90 minutes, plus ramp time ( $10$  °C  $\text{min}^{-1}$ ). The GAXRD results suggest that if a sample is held at 400 °C, MCIS measurements would need to be obtained within 30 minutes to observe the amorphous region, Figure 7.2. Taking the sample straight to a set temperature of 390 °C decreased the annealing

time by at least 90 mins and in doing so allowed a previous stage in annealing to be observed, Figure 7.13 (a) and (b). This stage shows an intermediate frequency response shifting to higher frequencies, and increasing in magnitude in  $M''$ , whilst decreasing in  $Z''$ . The capacitance is hard to resolve at the beginning of this stage as there are no plateaus in the  $C'$  spectroscopic plots and  $C'$  slowly rises to lower frequencies; however, at the end of this stage there is a clear plateau. Interestingly, throughout this stage only small features were apparent on the surface, see Figure 7.17 (a) and (b). By 187 mins (2<sup>nd</sup> measurement of second stage), Figure 7.17 (c), significant cracks were forming on the surface. Because cracks on the surface were not significant during this initial stage, it is reasonable to propose this initial intermediate frequency response be associated with the amorphous surface.

The second stage, Figure 7.13 (c) and (d), shows the intermediate frequency response shifting to lower frequencies and decreasing in  $M''$  whilst increasing in  $Z''$ . Throughout this stage, cracks on the surface became substantially more significant, as shown in Figure 7.17 (d). Measurements taken between contacts that had a significant number of cracks between them or between contacts with few cracks between them showed how sensitive the impedance measurements are to the cracks, Figure 7.18. When there were more cracks between the two contacts,  $M''$  had increased for the bulk response and decreased for the intermediate frequency response, compared to the measurement with less cracks present. This suggests an increase in the electrical volume fraction of the bulk response when there are more cracks.

A schematic showing the current flow (blue arrows) through the resistive surface layer (light grey) is shown in Figure 7.22. When no cracks are present, the current is unconfined and so can pass through the surface layer between the electrodes, Figure 7.22 (a). When there are more cracks in the surface layer, the current is confined in that it has to pass around them, Figure 7.22 (b). This leads to less current flowing through the surface layer between the micro-contacts, instead directing the current to the more conductive bulk. The electrical volume fraction is greater in the surface layer in the former case. As the cracks are air gaps, they are unlikely to contribute themselves to the impedance response.

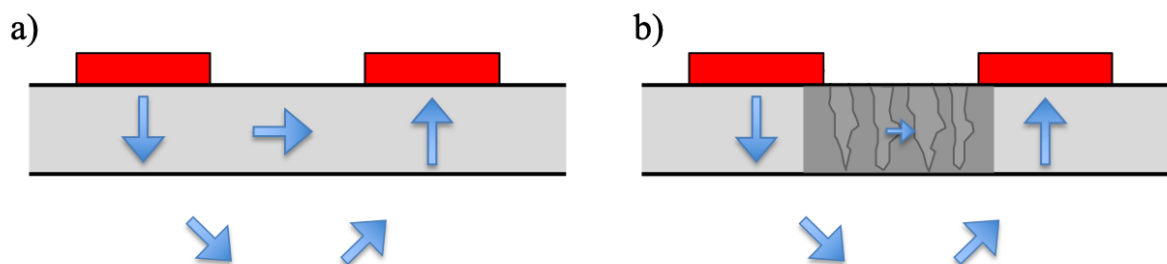


*Figure 7.22. Schematic showing the flow of current through the sample. a) Before the physical microstructure begins to change. The material is composed of the resistive surface (light grey) and the crystalline bulk (white). b) The cracks that form over time produce more resistive regions (dark grey) inhibiting current flow (blue arrows) through the surface layer between the micro-contacts.*

Using the equations from Chapter 5 and the thickness obtained from the TEM images, Figure 7.5, conductivity and effective permittivity values were calculated. Both the temperature cycle (Figure 7.12) and constant temperature measurements (Figure 7.15) obtained similar trends with temperature and/or time. The conductivity of the lower frequency response remained 2-3 orders of magnitude lower than the bulk whilst the permittivity increased at higher temperatures and/or longer times to values more similar to the pristine bulk. Assuming the lower frequency response is related to the surface layer, the effective permittivity shows the surface is recovering to a material more similar to the pristine material. However, these results should be viewed with caution as i) the thickness of the amorphous region changes with temperature and time meaning the thickness assumed may only be accurate at the start of heating and ii) the physical microstructure is changing significantly and the equations from Chapter 5 do not take these changes into account.

GAXRD measurements provided evidence that the intermediate frequency response in the second stage may not be due to amorphous regions in the sample. The measurements showed a fully (poly)crystalline material with no evidence of diffuse scattering, despite the sample being quenched when the impedance measurement showed a significant intermediate frequency response, Figure 7.19. Therefore, it may be reasonable to suggest the intermediate frequency response is the recrystallised surface layer, however as the data are so sensitive to the cracks a geometric factor for this region is hard to obtain.

The final stage showed the increase in the  $M''$  peak for the bulk response, and as described above, may be attributed to the electrical volume fraction of the bulk significantly increasing as substantially more cracks form in the surface layer. The capacitance of the intermediate frequency response had increased nearly an order of magnitude by the end of the measurements, Figure 7.14. Increases in capacitance can occur due to increases in the relative

permittivity or decreases in thickness. Decreases in thickness could be consistent with the epitaxial recrystallisation of an amorphous region.

Measurements at higher temperature and to lower frequencies didn't yield any further information and therefore understanding. The cracks appeared faster and the stages described above occurred much faster. Low frequency measurements of a damaged sample were consistent with that of a pristine sample. These responses were described as interactions at the sample/electrode interface in Chapter 6. The bulk response was also consistent with the pristine sample, leaving the intermediate frequency responses to be the significant difference between a pristine and damaged sample. The damaged sample response never returned to the pristine response for the times and temperatures studied in this project. We attribute these differences to substantial changes in the physical microstructure of the sample, namely the cracks (and voids) that have formed in the recrystallised surface as a result of annealing.

#### **7.4 Conclusions**

Fe-doped SrTiO<sub>3</sub> single crystals have been bulk ion implanted with 5 MeV Au ions to a fluence of  $5 \times 10^{15}$  ions cm<sup>-2</sup>, a damage dose of  $\sim 15$  dpa. GAXRD and XTEM confirmed all samples were fully amorphous to a depth of  $\sim 1.47$   $\mu$ m. The crystalline to amorphous interface showed evidence of superstructure reflections decreasing in intensity and are evidence to support the phase transformation from SrTiO<sub>3</sub> to Sr<sub>2</sub>TiO<sub>4</sub> as a result of radiation damage, first observed by Sabathier et al.<sup>8</sup> Further elemental characterisation is required to confirm this to be the case.

GAXRD confirmed that recrystallisation occurred after a heat treatment of 400 °C for 30 mins, a lower temperature than previously reported by Meldrum et al.<sup>3</sup> Data on recrystallised samples showed reflections expected of a polycrystalline sample, which may be due to slight mismatches in orientation because of cracks producing grain-like features on the surface. XTEM revealed significant vacancy-type defects had formed after annealing which has previously been attributed to agglomeration of vacancies during annealing<sup>10</sup>. The cracks on the surface extend into the recrystallised layer and in some regions, cracks had formed along the recrystallised to unirradiated crystalline interface.

Significant differences are observed between damaged and pristine samples by conventional Impedance Spectroscopy measurements; however, the responses in the damaged samples were not well resolved. MCIS measurements (which are surface sensitive) were able to better resolve these responses. Over time the measured impedance response could be sub-divided into two main stages:

1. An initial stage where the intermediate frequency  $M''$  response shifted to higher frequencies and increased in magnitude. During this stage, the features on the surface of the sample were starting to appear but were not substantial. This stage is attributed to recrystallisation of the amorphous surface layer.
2. The second stage where the intermediate frequency  $M''$  response shifted back to lower frequencies and decreased in magnitude. During this stage, cracks on the surface of the sample were a prominent feature. The  $M''$  spectra were very sensitive to these cracks, leading to an increase in the electrical volume fraction of the underlying unirradiated crystalline material response when there was a significant number of cracks between the micro-contacts.

Ultimately, significant changes in the physical microstructure limited the use of MCIS to probe radiation damage in single crystal  $\text{SrTiO}_3$  samples. The physical micro-structure is more complex than that assumed in Chapter 5 for a simple 2-layer model. In reality there are at least 9 different regions or features (as listed in the discussion) that need to be taken into account.

## 7.5 References

1. Nastasi, M. & Mayer, J. W. *Ion Implantation and Synthesis of Materials*. (Springer, 2006).
2. Ziegler, J. F., Ziegler, M. D. & Biersack, J. P. SRIM - The stopping and range of ions in matter (2010). *Nucl. Instruments Methods Phys. Res. B* **268**, 1818–1823 (2010).
3. Meldrum, A., Boatner, L. A., Weber, W. J. & Ewing, R. C. Amorphization and recrystallization of the  $\text{ABO}_3$  oxides. *J. Nucl. Mater.* **300**, 242–254 (2002).
4. Thevuthasan, S., Jiang, W., Shutthanandan, V. & Weber, W. J. Accumulation of ion beam induced disorder in strontium titanate. *Nucl. Instruments Methods Phys. Res. Sect. B Beam Interact. with Mater. Atoms* **206**, 162–165 (2003).
5. Woodward, D. I. & Reaney, I. M. Electron diffraction of tilted perovskites. *Acta Crystallogr. Sect. B Struct. Sci.* **61**, 387–399 (2005).
6. Zhuo, M. J., Yan, L., Fu, E. G., Wang, Y. Q., Misra, A., Nastasi, M., Uberuaga, B. P. & Jia, Q. X. Phase transformations and defect clusters in single crystal  $\text{SrTiO}_3$  irradiated at different temperatures. *J. Nucl. Mater.* **442**, 143–147 (2013).
7. Li, Y. H., Wang, Y. Q., Valdez, J. A., Tang, M. & Sickafus, K. E. Swelling effects in  $\text{Y}_2\text{Ti}_2\text{O}_7$  pyrochlore irradiated with 400keV  $\text{Ne}^{2+}$  ions. *Nucl. Instruments Methods Phys.*

- Res. B* **274**, 182–187 (2012).
8. Sabathier, C., Chaumont, J., Rouzière, S. & Traverse, A. Characterisation of Ti and Sr atomic environments in SrTiO<sub>3</sub> before and after ion beam irradiation by X-ray absorption spectroscopy. *Nucl. Instruments Methods Phys. Res. Sect. B* **234**, 509–519 (2005).
  9. White, C. W., Boatner, L. A., Rankin, J. & Aziz, M. J. Ion Implantation and Annealing of SrTiO<sub>3</sub> and CaTiO<sub>3</sub>. *Mater. Res. Soc. Symp. Proc.* **93**, 9–14 (1987).
  10. Wang, C. M., Shutthanandan, V., Zhang, Y., Thomas, L. E., Baer, D. R. & Thevuthasan, S. Precipitation of Au nanoclusters in SrTiO<sub>3</sub> by ion implantation. *J. Appl. Phys.* **95**, 5060–5068 (2004).
  11. Oyoshi, K., Hishita, S. & Haneda, H. Study of ion beam induced epitaxial crystallization of SrTiO<sub>3</sub>. *J. Appl. Phys.* **87**, 3450–3456 (2000).
  12. Wang, C. M., Shutthanandan, V., Zhang, Y., Thevuthasan, S. & Duscher, G. Direct observation of substitutional Au atoms in SrTiO<sub>3</sub>. *Phys. Rev. B - Condens. Matter Mater. Phys.* **70**, 1–4 (2004).
  13. Zhang, Y., Wang, C. M., Engelhard, M. H. & Weber, W. J. Irradiation behavior of SrTiO<sub>3</sub> at temperatures close to the critical temperature for amorphization. *J. Appl. Phys.* **100**, 113533 (2006).

## Chapter 8: Conclusions

The overarching aim of this thesis was to determine whether micro-contact Impedance Spectroscopy could be used to characterise radiation damage in ceramics. The work contained finite element modelling to aid in understanding the technique and to provide a method of data analysis followed by experimental work to determine the feasibility of the technique to characterise radiation damage.

Finite element modelling was used to determine the influence of contact geometry and sample confinement on the electrical response of a single crystal sample based on  $\text{SrTiO}_3$ . The geometric factor gives the best approximation for the conductivity when there is homogeneous current flow. In contrast, the spreading resistance equation gives the best approximation when there is heterogeneous current flow. When there is a micro-contact on one surface and a full contact on the other surface, confinement can occur at very large or very small separations. At very small separations, there is not enough space for the current to spread from the micro-contact and therefore the majority of current flows over an area that is the micro-contact area. When the separation is very large, spreading does occur from the micro-contact but the majority of the model showed homogeneous current flow across the same area as the model area. In these cases, the geometric factor using the respective areas can be used to calculate the conductivity. At intermediate separations, typical of experimental geometries, current flow remains heterogeneous and the spreading resistance equation provides the best approximation of the conductivity.

For two micro-contacts on the same surface and when there is no confinement the spreading resistance provides an overestimate of the conductivity at small separations due to contact interference. Increasing the separation increases the accuracy of the approximation and a separation that is 8 times the micro-contact radius is required to obtain conductivity values within 10% error. Further increases in accuracy require increasingly larger distances and a separation of 28 times the micro-contact radius is required to obtain conductivity values within 5% error. Such separations may not be feasible. Instead we suggest applying correction factors to the calculated conductivity to account for contact interference at small separations. For example, for a separation that is 2 and 4 times the micro-contact radius, we suggest correction factors of 0.81 and 0.87, respectively. Confinement can occur for two contacts on the same surface and can be provided by a resistive secondary phase such as a grain boundary or epoxy. Confinement decreases the calculated conductivity and, in some cases, a correction factor may

not be required if the enhancement from contact interference counter balances the decrease from confinement.

The modelling was then extended to contain a resistive surface layer, to aid in determining how to analyse experimental data; however, this work could also be applied to thin films. The thickness of the surface layer was varied so it was  $\sim$  either 10 times smaller or larger than the micro-contact radius. Similar results were obtained for when there was one micro-contact on one surface and a full contact on the other, and when there were two micro-contacts on the same surface. If the surface layer thickness is small compared to the micro-contact radius, there is not enough space for current to spread from the micro-contact meaning the majority of the current in the surface layer flows over an area equal to the micro-contact area. This result is analogous to the homogeneous material in Chapter 4 and the geometric factor using the micro-contact area provides accurate values for the surface layer conductivity. Current spreads in the bulk from the same area, meaning the spreading resistance provides an accurate value for the bulk conductivity. When the surface layer thickness is large, there is enough space for current spreading to occur from the micro-contact meaning the spreading resistance equation provides a good approximation for the surface conductivity. Similar to in a homogeneous material, contact interference generates an overestimation of the conductivity. As it is difficult to define the current flow in the bulk, a bulk conductivity cannot be calculated.

Fe-doped SrTiO<sub>3</sub> single crystals were characterised using X-ray diffraction (XRD), glancing angle X-ray diffraction (GAXRD), conventional and micro-contact Impedance Spectroscopy (MCIS). XRD revealed reflections arising from the [001] and [002] planes only. As, for the most part, no reflections were observed in GAXRD data, this suggests a limitation in the technique for highly orientated samples such as single crystals. Impedance Spectroscopy results showed the bulk conductivity of SrTiO<sub>3</sub> increases with increasing Fe content. Due to temperature gradients through the hot-stage/sample arrangement in the probe station set-up, the actual sample temperature in MCIS was obtained by comparing the frequency maximum for the M<sup>2</sup> Debye peak of the bulk response to that with conventional measurements where temperature could be measured with an accuracy of  $\pm 1$  °C. Arrhenius plots of the bulk conductivity were in much better agreement with that obtained from conventional measurements after correction. Using the correction factors for contact interference proposed in Chapter 4 further enhanced the agreement. The signature obtained in Z\* plots contained a high frequency arc response, attributed to the pristine bulk, and multiple low frequency responses, attributed to processes at the electrode/sample interface.

Bulk 5 MeV Au ion implantation on Fe-doped SrTiO<sub>3</sub> single crystals was undertaken to a fluence of  $5 \times 10^{15}$  ions cm<sup>-2</sup>, a dose of  $\sim 15$  dpa. The high dose was chosen to ensure complete amorphisation of the surface, with no highly damaged but still crystalline regions present. GAXRD and cross-sectional transmission electron microscopy (XTEM) confirmed the material had amorphised to a depth of  $\sim 1.5$   $\mu\text{m}$  from the surface. The amorphous to crystalline interface was  $\sim 0.15$   $\mu\text{m}$  and contained a large amount of point defects and the crystalline material was highly strained. Selected area electron diffraction patterns across the interface provided evidence for a phase transformation to Sr<sub>2</sub>TiO<sub>4</sub>, in agreement with previous studies<sup>1</sup>. Large cracks formed on the surface after annealing, producing what appear to be square or rectangular shaped grains. GAXRD revealed the annealed surface layer was polycrystalline. Vacancy-type defects and highly strained regions were also observed to exist after annealing by XTEM. Conventional Impedance Spectroscopy measurements provided evidence of differences between the damaged and pristine samples; however, as the response is averaged over the full sample, and the differences were not easily resolved. MCIS significantly improved the resolution. Initially, an intermediate frequency M'' Debye peak response increased in height and frequency, approaching the high frequency M'' Debye peak associated with the bulk response (stage one); followed by the intermediate frequency M'' Debye peak decreasing in height and frequency (stage two). The cracks were not a significant feature on the surface during stage one, therefore the intermediate frequency M'' Debye peak could be attributed to in-situ crystallisation of the amorphous region. The impedance response was very sensitive to the number of cracks on the surface during the second stage. Conductivity and effective permittivity values were calculated using the equations suggested in Chapter 5; however, these results should be viewed with caution as our models do not contain the level of complexity observed by XTEM. Ultimately, the changes in the physical microstructure, and especially the development of cracks, limit the use of MCIS to characterise radiation damage in the samples investigated in this thesis.

## 8.1 Future Work

The results obtained in this thesis present several interesting conclusions; however, scope for future work is suggested for each of the results chapters.

In Chapter 4, we showed confinement can be produced by a resistive grain boundary or epoxy. In our models we used a single grain. This could be extended to contain surrounding grains to observe the current flow through grain boundaries and into adjacent grains and the results for ceramics or epoxy embedded single crystal samples could then be compared to early work by

Fleig<sup>2</sup>. The work can then be extended to determine the effects of confinement in the z-axis as this is an unknown quantity when making MCIS measurements in a probe station.

In Chapter 5, we concentrated on a resistive surface layer as this is how we interpreted our results in Chapter 7. To fully understand micro-contact measurements on surface layers a more conductive surface layer should also be modelled. Preliminary results for a model containing a surface layer that is 1000 times more conductive than the bulk is shown in Figure 8.1.

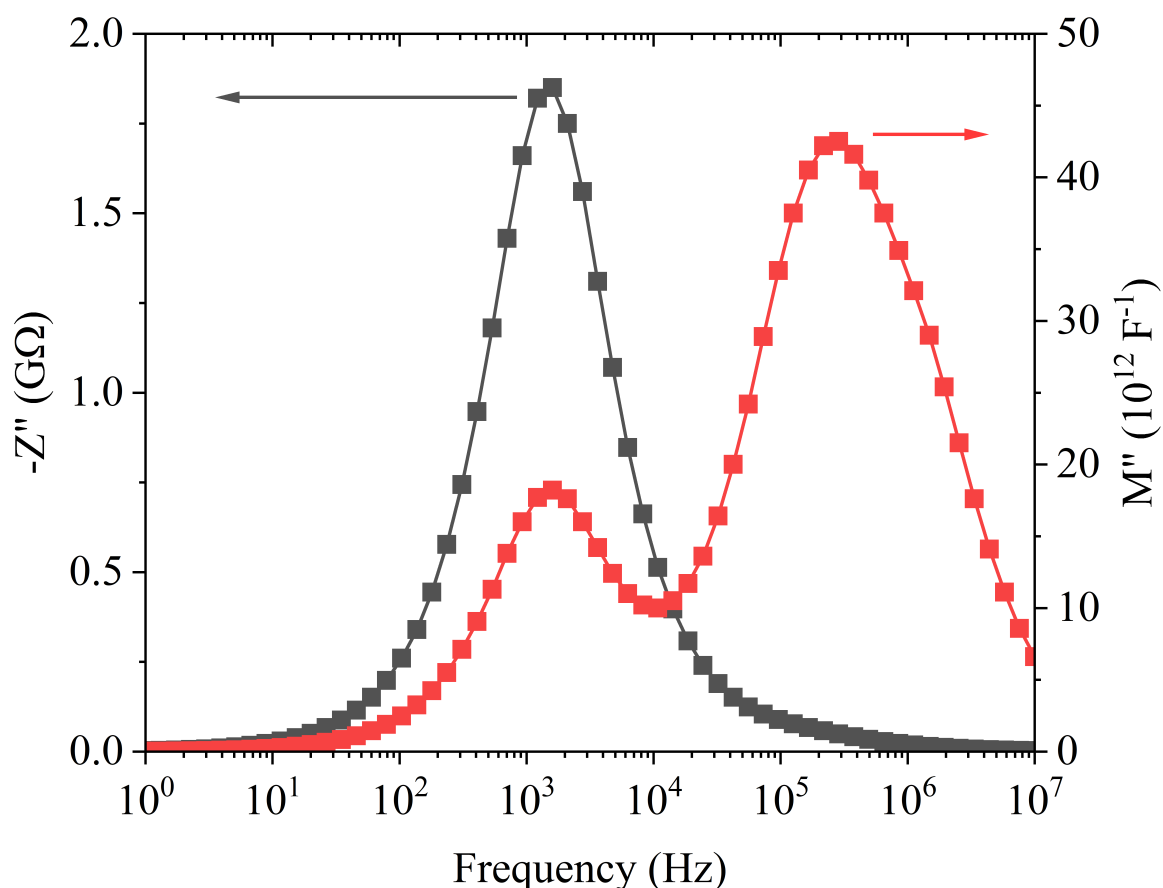


Figure 8.1. Combined  $Z''$  and  $M''$  spectroscopic plots for a  $50\ \mu\text{m}$  radius and  $100\ \mu\text{m}$  thick cylinder with a  $1\ \mu\text{m}$  thick surface layer that is 1000 times more conductive than the bulk. The bottom surface was a full surface contact and the micro-contact connected to the surface layer had a radius of  $5\ \mu\text{m}$ .

The lower frequency Debye peaks associated with the bulk response appears to be near-ideal whereas the higher frequency  $M''$  Debye peak attributed to the conductive surface layer is not ideal. The response appears to have a high frequency shoulder. Considering the model has only two material properties, the presence of a third component is unusual. To interpret this data, a better understanding of confinement is required. A wider range of conductivity, relative permittivity and separations should be investigated.

To confirm the results reported in Chapter 4, further experiments on a pristine sample should be conducted. Micro-contacts with different separations should be studied further to determine whether the suggested correction factors are appropriate, even at very small separations where contact interference is greatest.

Finally, the cracks that appeared on the surface of our samples during annealing limited the use of MCIS for characterising radiation damage. These cracks may not form for all samples or irradiation conditions. The dose we used was  $\sim 15$  dpa, but the required dose for amorphisation of SrTiO<sub>3</sub> has been shown to be  $\sim 1$  dpa<sup>3</sup>. Due to the high doses used in this study, the total strain in the surface layer may have carried on accumulating despite the surface layer already being amorphous. This higher strain may be the reason for the crack formation. We suggest further experiments at significantly lower doses to alleviate this level of strain. Previous recrystallisation studies have irradiated to a dose that is twice the amorphisation dose<sup>4</sup>, so we suggest irradiating to  $\sim 2$  dpa and repeating our experiments. Cracks may have formed because we also used single crystal samples. In a polycrystalline sample, grain boundaries can act as defect sinks and regions where stresses may be relieved. Because of this, cracks may not form within the grain. Rodewald et al.<sup>5</sup> achieved grain sizes of  $\sim 140$   $\mu\text{m}$  in Fe-doped SrTiO<sub>3</sub>, meaning a large number of micro-contacts could fit within the same grain, which would be better for our experiments. Unfortunately, we were unable to reproduce such large grain sizes in the same compositions but this approach of studying ceramics with exaggerated grain growth is also worthy of further study.

## 8.2 References

1. Sabathier, C., Chaumont, J., Rouzière, S. & Traverse, A. Characterisation of Ti and Sr atomic environments in SrTiO<sub>3</sub> before and after ion beam irradiation by X-ray absorption spectroscopy. *Nucl. Instruments Methods Phys. Res. Sect. B* **234**, 509–519 (2005).
2. Fleig, J., Rodewald, S. & Maier, J. Spatially resolved measurements of highly conductive and highly resistive grain boundaries using microcontact impedance spectroscopy. *Solid State Ionics* **136–137**, 905–911 (2000).
3. Thevuthasan, S., Jiang, W., Shutthanandan, V. & Weber, W. J. Accumulation of ion beam induced disorder in strontium titanate. *Nucl. Instruments Methods Phys. Res. Sect. B Beam Interact. with Mater. Atoms* **206**, 162–165 (2003).
4. Meldrum, A., Boatner, L. A., Weber, W. J. & Ewing, R. C. Amorphization and

recrystallization of the  $ABO_3$  oxides. *J. Nucl. Mater.* **300**, 242–254 (2002).

5. Rodewald, S., Fleig, J. & Maier, J. Microcontact Impedance Spectroscopy at Single Grain Boundaries in Fe-Doped  $SrTiO_3$  Polycrystals. *J. Am. Ceram. Soc.* **84**, 521–530 (2001).